Threshold Resummation and Higher Order Effects in QCD

Dissertation

der Mathematisch-Naturwissenschaftlichen Fakultät
der Eberhard Karls Universität Tübingen
zur Erlangung des Grades eines
Doktors der Naturwissenschaften
(Dr. rer. nat.)

vorgelegt von
Felix Maximilian Ringer
aus Herrenberg

Tübingen
2015

Gedruckt mit Genehmigung der Mathematisch-Naturwissenschaftlichen Fakultät der Eberhard Karls Universität Tübingen.

Tag der mündlichen Qualifikation:	26.06.2015
Dekan:	Prof. Dr. Wolfgang Rosenstiel
1. Berichterstatter:	Prof. Dr. Werner Vogelsang
2. Berichterstatter:	Prof. Dr. Thomas Gutsche
3. Berichterstatter:	Prof. Dr. Andreas Schäfer

SUMMARY

The main focus of my PhD thesis is on calculations of QCD threshold resummation for various processes. The infrared cancellation between virtual and real emission diagrams in higher orders leaves behind logarithmic contributions. These "threshold logarithms" become large when the available phase space for real gluon emission shrinks. In this case, they have to be taken into account to all orders which yields a much better behaved perturbative expansion. This procedure is known as threshold resummation. We investigated resummation effects beyond the next-to-leading logarithmic (NLL) order for di-hadron production in hadronic collisions $H_1H_2 \to h_1h_2X$ at high invariant mass of the produced pair. This may only be achieved by taking into account the non-trivial color structure of the underlying partonic hard-scattering cross sections. We determined explicitly the relevant hard and soft matrices in color space. We found significant improvements at next-to-next-to-leading logarithmic (NNLL) accuracy compared to previous phenomenological results for both fixed-target and collider regimes. In particular, the scale dependence of the resummed cross section is greatly reduced.

In related work, we also considered single-inclusive hadron production in hadronic collisions $H_1H_2 \to hX$. We have derived all necessary ingredients for the extension of the resummation framework toward NNLL. Our theoretical results allow future phenomenological studies along these lines.

Furthermore, we derived approximate next-to-next-to-leading order (NNLO) results for single-inclusive jet production $H_1H_2 \to \mathrm{jet}X$ based on threshold resummation. Starting at NLL accuracy, we included for the first time the three leading classes of logarithmic terms. In addition, we took into account the dependence of the cross section on the jet parameter R and our results are adapted to the full kinematics in jet transverse momentum p_T and rapidity η. There is a great phenomenological interest in single-inclusive jet production. On the one hand, fits of parton distribution functions (PDFs) rely on jet data constraining in particular the gluon PDF at large x. On the other hand, large p_T jets are an important observable for the search of new physics at the LHC. A recent full NNLO calculation in the all-gluon channel allowed us to assess the region, where our approximation is valid. Having extended di-hadron production beyond NLL accuracy, we also applied the same techniques to single-inclusive jet production. We found good agreement in the central region with $\eta \lesssim 2$, where

our NNLO-NNLL results match with the full calculation to better than 10%. With the lessons learnt at NNLO, we were able to deduce approximate N^{3}LO results which are again a significant contribution.

Recently, data sets with unprecedented precision were published for semi-inclusive deep-inelastic scattering (SIDIS) $\ell N \to \ell h X$ and semi-inclusive annihilation (SIA) $e^+e^- \to hX$. This motivated us to study the effects of threshold resummation on hadron multiplicities for these two color-singlet processes. A solid theoretical understanding of higher order effects is crucial for the extraction of fragmentation functions in a global analysis. Indeed, we found modest but significant enhancements.

Part of my work so far was in the field of spin physics in which the main goal is to disentangle the various contributions to the nucleon spin. For example, we extended our work on resummation for processes with identified hadrons in the final state to double spin asymmetries for inclusive deep-inelastic scattering (DIS) and SIDIS. In general, we found rather small enhancements for the asymmetries in comparison to the hadron multiplicities in the unpolarized case. Nevertheless, higher order effects derived from resummation are not negligible and will be particularly relevant for experiments at JLab where polarized valence PDFs $\Delta u/u$, $\Delta d/d$ will be probed at very large x.

Another phenomenologically relevant effect on top of the standard NLO framework for (unpolarized) DIS and SIA are hadron mass corrections. Relying on a relatively recent approach of target mass corrections (TMC) for DIS developed within collinear factorization, we proposed a way of consistently combining TMC with threshold resummation. For DIS, both effects are most relevant for the extraction of PDFs at large x and we found a non-trivial interplay between resummation and TMC. In addition, we extended this framework to SIA, where it turns out that the two effects are essentially independent.

The production of W bosons in hadronic collisions plays an important role at past and present-day collider experiments. We calculated analytically at NLO in QCD the cross section for the single-inclusive process $pp \to \ell^\pm X$, where the produced charged lepton has a large transverse momentum p_T and results from the decay of a W boson. In addition, we considered the related processes with an intermediate Z, γ and γZ interference. The transverse momentum distribution of the decay lepton has been measured at the Tevatron and the LHC. By analyzing the region of the "Jacobian peak", the W boson mass is determined to a very high precision. Around the Jacobian peak QCD (and electroweak) corrections are particularly relevant. Our analytical results shed light on the general role and size of higher-orders. We found different large logarithmic enhancements that affect the shape of the lepton's p_T spectrum. We found a double peak structure around the Jacobian peak which may result in an instability of the NLO calculation which is generally overlooked in Monte-Carlo based results.

Due to the parity violating vertex structure of the W boson, a non-zero longitudinal single spin asymmetry may be obtained which is presently measured at RHIC. The W program at RHIC offers a unique possibility to obtain new constraints on polarized PDFs in a different kinematical region than the usual (SI)DIS measurements. Already first results indicate surprising insights into the size of the polarized sea quark distributions $\Delta\bar{u}$ and $\Delta\bar{d}$. We extended our calculation for W boson production to the polarized case $\vec{p}p \to \ell X$. In order to incorporate the results from RHIC in a global analysis of polarized PDFs, fast numerical codes are needed which are now available with our analytical results at hand.

ZUSAMMENFASSUNG

Der Schwerpunkt meiner Doktorarbeit liegt auf QCD threshold resummation Rechnungen für verschiedene Prozesse. Aufgrund des gegenseitigen Aufhebens infraroter Divergenzen zwischen virtuellen und reellen Diagrammen treten in der QCD Störungsentwicklung logarithmische Terme auf. Diese "threshold" Logarithmen werden groß, wenn der verfügbare Phasenraum für reelle Gluon Abstrahlung abnimmt. In diesem Fall müssen die Logarithmen in allen Ordnungen der störungstheoretischen Entwicklung aufsummiert werden. Diese Technik ist bekannt als "threshold resummation". Wir haben die Effekte der "resummation" analysiert jenseits der nächst-führenden logarithmischen (NLL) Ordnung für die Produktion von Hadron Paaren in hadronischen Kollisionen $H_1H_2 \to h_1h_2X$ bei einer großen invarianten Masse des produzierten Paares. Dies kann nur erreicht werden, indem man die nicht-triviale Farbstruktur des zugrundeliegenden harten partonischen Streuprozesses in Betracht zieht. Wir haben explizit die relevanten "hard" und "soft" Matrizen bestimmt. Wir fanden eine wesentliche Verbesserung bei nächst-zu-nächst-zu führender logarithmischer (NNLL) Ordnung im Vergleich zu früheren phänomenologischen Ergebnissen für die kinematischen Regionen bei "fixed target" Experimenten als auch für Hadronen collider. Insbesondere reduziert sich die Skalenabhängigkeit des resummierten Wirkungsquerschnitts deutlich.

In einer damit verbundenen Arbeit haben wir single-inclusive Hadron Produktion in hadronischen Kollisionen $H_1H_2 \to hX$ betrachtet. Wir haben alle relevanten Beiträge berechnet für die Erweiterung der Resummation in Richtung NNLL. Dies ermöglicht es in Zukunft detaillierte numerische Studien dafür durchzuführen.

Darüberhinaus haben wir näherungsweise Ergebnisse für "single-inclusive" Jet Produktion $H_1H_2 \to \text{jet}X$ in nächst-zu-nächst-zu führender Ordnung berechnet basierend auf "threshold resummation". Beginnend mit NLL haben wir erstmals die drei wichtigsten Klassen logarithmischer Terme mit einbezogen. Zusätzlich haben wir die Abhängigkeit des Wirkungsquerschnitts von dem Jet Parameter R berücksichtigt und unsere Ergebnisse sind an die volle Kinematik des Jets angepasst, d.h. doppelt differenziell in Rapidität η und Transversalimpuls p_T. Es gibt ein großes phänomenologisches Interesse an "single-inclusive" Jet Produktion. Einerseits werden Parton Verteilungsfunktionen (PDFs) under

anderem anhand von Jet Daten bestimmt. Dies ist besonders relevant für die Gluon PDF bei großen x. Andererseits sind hohe p_T Jets eine wichtige Observable für die Suche nach neuer Physik am LHC. Eine neue volle NNLO Rechnung im "all-gluon" Kanal erlaubt es uns die Region zu bestimmen, wo unsere Näherung gültig ist. Nachdem wir Di-Hadron Produktion auf jenseits der nächst-führenden logarithmischen Ordnung erweitert hatten, haben wir dieselben Techniken für Jet Produktion angewendet. Wir fanden eine gute Übereinstimmung in der zentralen Region mit $\eta \lesssim 2$, wo unsere NNLO-NNLL Ergebnisse mit der vollen Rechnung besser als 10% übereinstimmen. Mit den gelernten Lektionen auf dem Level von NNLO waren wir in der Lage näherungsweise N^{3}LO Korrekturen zu berechnen welche wieder ein wichtiger Beitrag darstellen.

In letzter Zeit wurden Daten veröffentlicht mit noch nie da gewesener Präzision für semi-inklusive tief-inelastische Streuung (SIDIS) $\ell N \to \ell h X$ und semi-inklusive Annihilation (SIA) $e^+e^- \to hX$. Dies hat uns motiviert für diese beiden Prozesse die Effekte von "threshold resummation" für Hadron Multiplizitäten zu analysieren. Ein verlässliches theoretisches Verständnis von Korrekturen höherer Ordnung ist äußerst wichtig für die Bestimmung von Fragmentations Funktionen in einer globalen Analyse. Tatsächlich fanden wir moderate aber signifikante Erhöhungen der Wirkungsquerschnitte.

Ein Teil meiner Doktorarbeit war auf dem Gebiet der Spin Physik. Das Hauptziel ist es dabei die verschiedenen Beiträge zum Spin des Nukleons zu entschlüsseln. Zum Beispiel haben wir unsere Arbeiten zu "resummation" für Prozesse mit identifizierten Hadronen im Endzustand ausgedehnt auf doppelte Spin Asymmetrien in der inklusiven tief-inelastischen Streuung (DIS) und SIDIS. Im Allgemeinen fanden wir relativ geringe änderungen der Asymmetrien im Vergleich zu den Hadron Multiplizitäten im unpolarisierten Fall. Dennoch sind Effekte von höheren Ordnungen entsprechend der "resummation" nicht vernachlässigbar und werden besonders relevant sein für Experimente am JLab, wo polarisierte Valenz-PDFs $\Delta u/u$, $\Delta d/d$ bei sehr großen x getestet werden.

Ein weiterer phänomenologisch relevanter Effekt zusätzlich zum dem üblichen NLO Rahmen für (unpolarisierte) DIS und SIA sind Korrekturen, welche durch die Massen der beobachteten Hadronen auftreten (HMCs). Mit einem relativ neuen Zugang zu HMCs für DIS, der innerhalb der kollinearen Faktorisierung entwickelt wurde, haben wir eine Möglichkeit ausgearbeitet um HMCs und "threshold resummation" zu kombinieren. Für DIS sind beide Effekte besonders relevant für die Bestimmung von PDFs bei großen x und wir haben eine nicht triviale Wechselwirkung der beiden Effekte gefunden. Darüberhinaus haben wir analoge Betrachtungen für SIA gemacht, wo es sich herausstellt, dass die beiden Effekte im Wesentlichen unabhängig sind.

Die Produktion von W Bosonen in hadronischen Kollisionen spielt heutzutage eine wichtige Rolle bei Teilchenbeschleunigern. Wir haben analytisch bis NLO in QCD den Wirkungsquerschnitt berechnet für $pp \to \ell^{\pm} X$, wobei das produzierte geladene Lepton einen großen Transversalimpuls hat und von dem Zerfall eines W Bosons stammt. Darüberhinaus haben wir ähnlichen Prozesse betrachtet mit einem Z oder γ als auch die γZ Interferenz. Die p_T Verteilung des durch den W Zerfall entstehenden Leptons wurde am Tevatron und beim LHC gemessen. Durch die Analyse der Region des "Jacobian Peaks" ist es möglich die Masse des W Bosons mit sehr hoher Genauigkeit zu bestimmen. Um den "Jacobian peak" herum sind QCD (und elektroschwache) Korrekturen besonders wichtig. Unsere analytischen Ergebnisse ermöglichen es ein besseres Verständnis von der Rolle und der Größe höherer

Ordnungen zu bekommen. Wir fanden verschiedene Arten von logarithmischen Erhöhungen, welche die Form des p_T Spektrums stark beeinflussen. Wir haben eine Struktur mir zwei Spitzen entdeckt, die sogar zu einer Instabilität der gesamten NLO Rechnung werden kann. Dies wird im Allgemeinen übersehen bei Monte-Carlo gestützten Ergebnissen.

Aufgrund der paritätsverletzenden Vertex Struktur des W Bosons, erhält man eine nicht verschwindende longitudinale "single-spin" Asymmetrie, die zur Zeit bei RHIC gemessen wird. Das W Programm von RHIC erlaubt eine einzigartige Möglichkeit neue Datensätze für die Bestimmung von polarisierte PDFs zu erhalten, die in einer ganz anderen kinematischen Region liegen, als die üblichen Daten von (SI)DIS. Bereits erste Messungen deuten auf überraschende Einsichten hin bezüglich der Größe der polarisierten See Quark Verteilungen $\Delta\bar{u}$ and $\Delta\bar{d}$. Wir haben unsere Rechnung für W Boson Produktion auf den polarisierten Fall erweitert $\vec{p}p \to \ell X$. Um die Ergebnisse von RHIC in einer globalen NLO Analyse für polarisierte PDFs implementieren zu können braucht man schnelle numerische Verfahren, die jetzt verfügbar sind dank unseren analytischen Rechnungen.

LIST OF PUBLICATIONS

Journal papers

[*i*] Daniele P. Anderle, Felix Ringer, Werner Vogelsang,
"QCD Resummation for Semi-Inclusive Hadron Production Processes",
Phys. Rev. D **87**, 034014 (2013), arXiv: 1212.2099.

[*ii*] Daniele P. Anderle, Felix Ringer, Werner Vogelsang,
"Threshold resummation for Polarized (Semi-)Inclusive Deep-Inelastic Scattering",
Phys. Rev. D **87**, 094021 (2013), arXiv: 1304.1373.

[*iii*] Alberto Accardi, Daniele P. Anderle, Felix Ringer,
"Interplay of Threshold Resummation and Hadron Mass Corrections in Deep Inelastic Processes",
Phys. Rev. D. **91**, 034008 (2015), arXiv: 1411.3649.

[*iv*] Patriz Hinderer, Felix Ringer, George F. Sterman, Werner Vogelsang,
"Toward NNLL Threshold Resummation for Hadron Pair Production in Hadronic Collisions",
Phys. Rev. D. **91**, 014016 (2015), arXiv: 1411.3149.

[*v*] Patriz Hinderer, Felix Ringer, George F. Sterman, Werner Vogelsang,
"Toward NNLL Threshold Resummation for Single-Inclusive Hadron Production,
in Hadronic Collisions",
in preparation.

[*vi*] Daniel de Florian, Patriz Hinderer, Asmita Mukherjee, Felix Ringer, Werner Vogelsang,
"Approximate next-to-next-to-leading Order Corrections to Hadronic Jet Production",
Phys. Rev. Lett. **112**, 082001 (2014), arXiv: 1310.7192.

[*vii*] Daniel de Florian, Patriz Hinderer, Asmita Mukherjee, Felix Ringer, Werner Vogelsang,
"Improved Approximate NNLO and N^3LO *Results for Hadronic Jet Production"*,
in preparation.

[*viii*] Felix Ringer, Werner Vogelsang,
"Single-Spin Asymmetries in W *Boson Production at NLO"*,
submitted for publication to Phys. Rev. D., arXiv: 1503.07052.

[*ix*] Felix Ringer, Werner Vogelsang,
"Analytical Results for Hadronic W *Production at NLO"*,
in preparation.

Conference Proceedings

[*x*] Daniele P. Anderle, Felix Ringer, Werner Vogelsang,
"QCD Resummation in Hadron Production",
Nuovo Cim. C **036**, 153-157 (2013), arXiv: 1307.0701.

CONTENTS

INTRODUCTION

Quantum chromodynamics (QCD) is a quantum field theory describing the strong interaction between quarks and gluons which are the building blocks of hadrons. Being developed in the 1970s, it is nowadays one of the most established theories in physics. Alongside electro-magnetic and weak forces, QCD is one of the cornerstones of the standard model of particle physics which aims at describing all fundamental forces in nature except gravitation. QCD offers an enormously rich phenomenology even though it is based on a rather simple Lagrangian as a starting point.

The experimental tool of choice are several types of collider experiments. At high energies, the inner structure of hadrons can be probed. in 1968, pointlike partons, which turned out to be the quarks and gluons of QCD, were observed for the first time in Deep-Inelastic Scattering (DIS) experiments carried out at SLAC [1]. Since then, there have been many dedicated experiments such as the Tevatron at Fermilab, HERA at DESY or LEP at CERN. Nowadays, there are experiments like RHIC at BNL, BELLE at KEK, COMPASS at CERN and the most prominent one, which is the LHC at CERN.

Besides the experimental progress in the last decades, there has been an ever growing need for QCD calculations with a very high precision in order to confront theory with data. The most precise predictions from QCD are obtained in the framework of perturbative QCD (pQCD). This approach relies on a key feature of QCD which is asymptotic freedom. At high energies (or short distances) quarks and gluons interact weakly with each other, which was found by Wilczek, Gross [2] and Politzer [3] in 1973. Besides asymptotic freedom, another key concept is factorization [4, 5] which allows QCD predictions derived from perturbation theory. As an example, we illustrate factorization for hadronic scattering in Fig. 1. We are considering proton-proton collisions and in the final state one might observe for example pions, photons or jets. In the middle of Fig. 1, the partonic hard scattering process is shown, where the two incoming partons a, b interact and some final state configuration is produced. When writing down such a cross section within pQCD we have to include parton distribution functions (PDFs) $f_{a/p}$ for the incoming protons and fragmentation functions (FFs) $D_{h/c}$ in case that we are considering identified particles in the final state. Other than that we consider an inclusive cross section in the sense that we are summing over any additional hadronic final state X. Using factorization, one

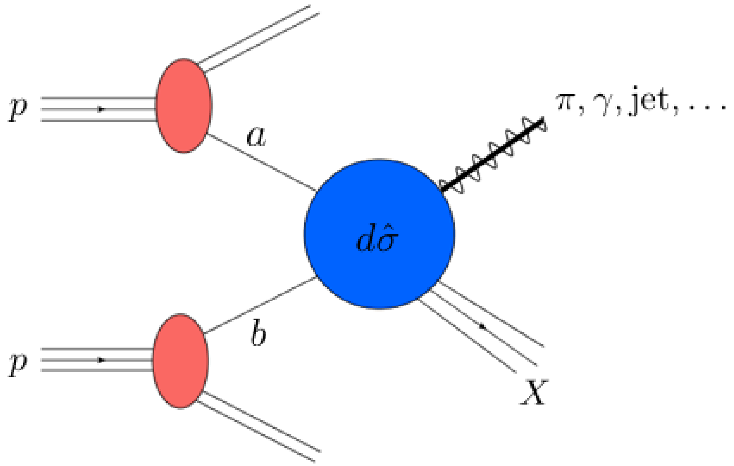

Figure 1: Factorization for hadronic scattering.

can write down such a cross section schematically as

$$d\sigma = f_{a/p} \otimes f_{b/p} \otimes D_{h/c} \otimes d\hat{\sigma} \ , \tag{0.1}$$

where $\otimes$ denotes a convolution product which will be defined below. Factorization theorems state that this structure of the cross section holds up to power suppressed corrections. The PDFs and FFs are non-perturbative but universal objects which may be determined from a global analysis of various reference processes. The hard-scattering cross section $d\hat{\sigma}$ is process dependent but it may be calculated perturbatively as a power series in the strong coupling constant

$$d\hat{\sigma} = \omega^{\mathrm{LO}} + \frac{\alpha_s}{\pi}\omega^{\mathrm{NLO}} + \left(\frac{\alpha_s}{\pi}\right)^2 \omega^{\mathrm{NNLO}} + \ldots \tag{0.2}$$

The current state of the art are fixed order calculations at next-to-leading order (NLO), next-to-next-to-leading oder (NNLO) and sometimes even partial N^{3}LO depending on the complexity of the process under consideration. Potentially large logarithmic corrections appear in the coefficient functions $\omega^{\mathrm{N^kLO}}$ at every order in perturbation theory. In case that they are dominant, a reliable prediction from pQCD may only be obtained if these logarithms are taken into account to all orders. An important type of logarithmic corrections are threshold corrections. For a given fixed order k of the partonic cross section $d\hat{\sigma}$, they appear as

$$\alpha_s^k \left(\frac{\ln^n(1-x)}{1-x}\right)_+ , \qquad \text{with} \ \ n < 2k-1 \, . \tag{0.3}$$

Here x is a process dependent kinematic variable and $x \to 1$ is called the partonic threshold. The plus distribution will be defined below. Threshold logarithms become large when the phase space for real gluon radiation shrinks. The technique to take these corrections into account to all orders in α_s is called "threshold resummation" [6–8], which is the main topic of this thesis.

The first run at the LHC in 2010, at a center of mass (c.m.s.) energy of $\sqrt{s} = 7\,\mathrm{TeV}$, kicked off a new

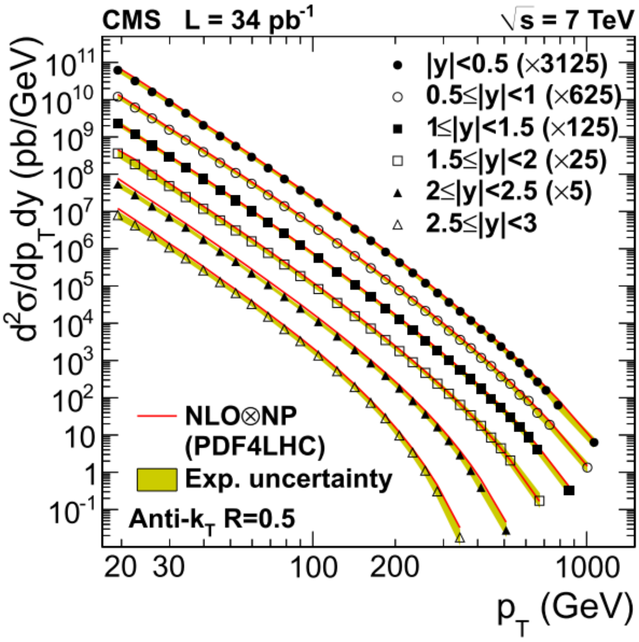

Figure 2: Single-inclusive jet production at the LHC, Figure taken from [9].

era of high energy precision phenomenology in particle physics. Besides the prominent discovery of a scalar boson that is very likely to be the expected Higgs particle, it was found that the vast majority of the observed collisions are extremely well described within the framework of perturbative QCD. As an example, in Fig. 2 the success of pQCD is illustrated. We show the measured cross section of single-inclusive jet production at the LHC for several different rapidity intervals along with the corresponding predictions from pQCD at NLO. The theoretical calculations fit very well with the experimental data spanning over more than twelve orders of magnitude. Another example of experiments which recently reported on data sets with very high precision are BELLE [10] and BaBar [11]. Their new measurements of single-inclusive pion and kaon production in e^+e^- annihilation at a c.m.s energy of $\sqrt{s} \approx 10$ GeV allow QCD studies in unprecedented detail.

Besides various experiments and theoretical efforts that are made in order to learn more about the strong interaction itself, pQCD also plays a role of fundamental importance in the search for physics beyond the standard model especially in the era of the LHC. For example, the discovery of the Higgs particle and the identification of its properties relies heavily on our understanding of QCD. The same argument holds for the search of supersymmetry, extra dimensions etc. As it is illustrated in Fig. 3, most of the collisions at the LHC can be described using only the standard model or QCD in particular. In order to single out the very few events that might be a signal for new physics, the huge background from QCD interactions has to be subtracted. Therefore, a sophisticated quantitative understanding of QCD is necessary. In particular, knowledge about higher order corrections in perturbation theory and the non-perturbative PDFs is required.

The structure of this thesis is as follows. In the first Chapter we introduce the theoretical concepts

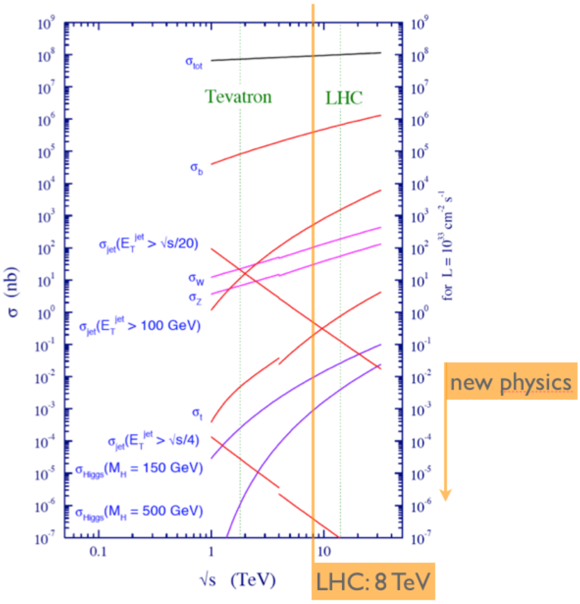

Figure 3: Comparison of cross sections for standard model processes and beyond at a luminosity of $\mathcal{L} = 10^{33}\text{cm}^{-1}s^{-1}$. Figure adapted from [12].

of perturbative QCD. We choose to give a general overview as the subsequent Chapters cover rather separate topics within perturbative QCD. We discuss the running of the strong coupling constant α_s, infrared safe observables, factorization and evolution. Along the way, we introduce some of the most important processes

- e^+e^- Annihilation,
- Deep-inelastic scattering,
- Hadron-hadron collisions.

Finally, we introduce the concept of threshold resummation which plays an important role in this thesis.

The subsequent Chapters are structured according to the papers listed above on page IX. In general, this thesis can be categorized in three main parts.

Resummation and Hadron Mass Corrections for Color Singlet Processes: In Chapter 2, we present resummation calculations for hadron-multiplicities in lepton-hadron processes. This Chapter is based on publications [i] and [x]. Based on publication [ii], we extend this framework to double longitudinal spin asymmetries in Chapter 3. We investigate the interplay of threshold resummation and hadron mass corrections for deep inelastic processes in Chapter 4 which is based on publication [iii].

Hadronic QCD Hard Scattering: In Chapter 5, we present threshold resummation studies beyond next-to-leading logarithmic (NLL) accuracy for di-hadron production in hadron-hadron collisions based on publication [iv]. In Chapter 6, we derive all necessary ingredients for the extension of resummation toward next-to-next-to-leading logarithmic (NNLL) accuracy for single-inclusive hadron production based on publication [v]. Following similar steps in Chapter 7, we present approximate next-to-next-to(-next-to) leading order results for hadronic jet production. This Chapter is based on publications [vi] and [vii].

Heavy Gauge Boson Production: In the Chapter 8, we present an analytical next-to-leading order calculation for single-spin asymmetries in W boson production in hadronic collisions. Our calculation will be used for the analysis of experiments presently carried out at the BNL RHIC. This Chapter is based on publication [viii]. In the subsequent Chapter 9, we continue to analyze our results for the unpolarized case. A solid theoretical understanding is crucial for the extraction of the W boson mass M_W from collider data. This Chapter is based on publication [ix].

CHAPTER 1

PERTURBATIVE QCD

In this Chapter, we introduce the main theoretical concepts of perturbative quantum chromodynamics. Starting from the basic Lagrangian density, we are going to outline the key steps necessary to write down an expression for a measurable cross section obtained in the framework of perturbative QCD. We focus on the basic concepts such as infrared safety, factorization, evolution and we give an introduction to threshold resummation.

1.1 Quantum Chromodynamics

Early theoretical work was carried out by Yang and Mills [13] in 1954 who wrote down a Lagrangian density invariant under local $SU(N_c)$ gauge transformations, with $N_c = 3$ in the case of QCD. After the concept of colored particles was introduced in hadron spectroscopy, this idea was extended to a gauge theory by Fritzsch, Gell-Mann and Leutwyler [14] in 1973. Finally, Gross, Wilczek and Politzer found that quarks and gluons interact weakly at high energies, as mentioned above. For this discovery, they were awarded the Nobel Prize in 2004.

1.1.1 QCD Lagrangian

We start with the classical Lagrangian density invariant under the local color gauge group $SU(N_c)$ describing the interaction of quarks ψ_f and gluons A^a_μ

$$\mathcal{L}_{cl} = \sum_f \bar{\psi}_f (i\not{D} - m_f)\psi_f - \frac{1}{4} F^a_{\mu\nu} F^{\mu\nu}_a \,. \tag{1.1}$$

where we sum over N_f quark flavors. D_μ is the covariant derivative given by

$$D_\mu = \partial_\mu - i g_s A^a_\mu T^a \,. \tag{1.2}$$

The factor g_s is the coupling strength in QCD and the T^a are the $N_c^2 - 1$ hermitian and traceless generators of $SU(N_c)$. The field strength tensor $F^a_{\mu\nu}$ in Eq. (1.1) is defined as

$$F^a_{\mu\nu} = \partial_\mu A^a_\nu - \partial_\nu A^a_\mu + g_s f^{abc} A^b_\mu A^c_\nu \,. \tag{1.3}$$

The third term here is due to the fact, that QCD is a non-abelian gauge theory leading to self-interaction terms for the gluon fields. This marks the crucial peculiarity of QCD in comparison to quantum electrodynamics (QED). The antisymmetric structure constants f^{abc} are defined via the relation

$$[T^a, T^b] = i f^{abc} T^c \quad \Leftrightarrow \quad i f^{abc} = 2\,\mathrm{tr}([T^a, T^b] T^c) \,. \tag{1.4}$$

When quantizing QCD using the path integral formalism [15], we have to fix the gauge. For covariant gauges, this is done by implementing the condition $\partial^\mu A^a_\mu = 0$. This is achieved by adding the following term to the Lagrangian

$$\mathcal{L}_{gf} = -\frac{1}{2\lambda} (\partial^\mu A^a_\mu)^2 \,. \tag{1.5}$$

Where λ denotes an arbitrary gauge parameter which has to drop out at the end when a physical observable is calculated. However, due to this extra term, we are able to write down a propagator for the gluon field. Feynman gauge corresponds to $\lambda = 1$ whereas Landau gauge is obtained by setting $\lambda \to 0$. With this type of gauge fixing term, we also have to add a term to our Lagrangian density involving anti-commuting complex scalar fields η^a also known as Faddeev-Popov ghost fields [16]. The extra term is given by

$$\mathcal{L}_{gh} = \partial_\mu \bar{\eta}^a D^\mu_{ab} \eta^b \,, \tag{1.6}$$

where now the covariant derivative D^μ_{ab} has to be taken in the adjoint representation. The additional ghost fields cancel unphysical degrees of freedom which otherwise would be present in the polarization sum for gluons, see [17].

Summing up everything, we end up with the final QCD Lagrangian density

$$\begin{aligned} \mathcal{L} &= \mathcal{L}_{cl} + \mathcal{L}_{gf} + \mathcal{L}_{gh} \\ &= \bar{\psi}(i\not{\partial} - m)\psi - \frac{1}{4}(\partial_\mu A^a_\nu - \partial_\nu A^a_\mu)^2 - \bar{\eta}\Box\eta - \frac{\xi}{2}(\partial_\mu A^\mu_a)^2 \\ &\quad - g_s\, \bar{\psi} T^a \not{A}^a \psi + \frac{g_s}{2}(\partial_\mu A^a_\nu - \partial_\nu A^a_\mu) f^{abc} A^\mu_b A^\nu_c \\ &\quad - \frac{1}{4} g_s^2 f^{abc} f^{ade} A^\mu_b A^\nu_c A^d_\mu A^e_\nu - g_s f^{abc} \bar{\eta}_a \partial^\mu (A^c_\mu \eta^b) \end{aligned} \tag{1.7}$$

where the sum over N_f quark flavors is implicit. From the Lagrangian density, we can directly see the difference between QCD and QED, which is given by terms that lead to the existence of 3 and 4-gluon vertices. This can be traced back to the non-abelian nature of its gauge group, as mentioned above. The QCD Feynman rules can be derived from Eq. (1.7). They are summarized for covariant gauges in the Appendix A.

Alternatively to covariant gauges, we may also choose non-covariant ones such as Coulomb gauge or axial gauges. In the context of parton distribution functions and resummation axial gauges are of special interest. Choosing a fixed gauge vector n^μ, we implement the condition $n^\mu A^a_\mu = 0$ by adding the following gauge fixing term to the QCD Lagrangian

$$\mathcal{L}_{gf} = -\frac{1}{2\lambda}\left(n^\mu A^a_\mu\right)^2 \tag{1.8}$$

instead of the one given in Eq. (1.5). Choosing the square of n^μ positive, i.e. $n^2 > 0$, is called a temporal gauge, whereas the condition $n^2 = 0$ is called light-cone gauge and $n^2 < 0$ is called pure axial gauge. It turns out that no ghost fields are required for an axial gauge. However, in return we obtain a more complicated gluon propagator $D^{ab}_{\mu\nu}(k)$ which takes the form

$$D^{ab}_{\mu\nu}(k) = \frac{-i\delta^{ab}}{k^2 + i\varepsilon} N_{\mu\nu}(k)\,, \qquad N_{\mu\nu}(k) = g_{\mu\nu} - \frac{n_\mu k_\nu + n_\nu k_\mu}{n \cdot k} + \frac{(n^2 + \lambda k^2) k_\mu k_\nu}{(n \cdot k)^2}\,. \tag{1.9}$$

Special care has to be taken when loop integrations are performed in axial gauges [18].

1.1.2 Asymptotic Freedom

As mentioned already, the crucial difference between the non-abelian gauge theory QCD and the abelian QED are the self-interaction terms for gluons in the Lagrangian which is in contrast to photons in QED. As a result, quarks and gluons interact weakly at high energies or small distance scales. This is a crucial requirement for the applicability of perturbative calculations in QCD. In analogy to the fine structure constant in QED, we define

$$\alpha_s = \frac{g_s^2}{4\pi}\,. \tag{1.10}$$

The renormalization of divergences introduces an arbitrary mass scale μ_R in the calculations. However, physical observables should not depend on whatever choice we make for μ_R. Hence, we can derive a differential equation that describes the dependence of α_s on μ_R which is called the renormalization group equation

$$\mu_R^2 \frac{d\alpha_s}{d\mu_R^2} = \beta(\alpha_s) = -\alpha_s^2\left(b_0 + b_1\,\alpha_s + b_2\,\alpha_s^2 + \ldots\right)\,. \tag{1.11}$$

Here $\beta(\alpha_s)$ is the QCD beta function where the coefficients b_i are calculable in perturbation theory. The first few coefficients in the $\overline{\text{MS}}$ scheme are given by [19, 20]

$$\begin{aligned} b_0 &= \frac{1}{12\pi}\left(11C_A - 2N_f\right)\,, \qquad b_1 = \frac{1}{24\pi^2}\left(17C_A^2 - 5C_A N_f - 3C_F N_f\right)\,, \\ b_2 &= \frac{1}{64\pi^3}\left(\frac{2857}{54}C_A^3 - \frac{1415}{54}C_A^2 N_f - \frac{205}{18}C_A C_F N_f + \frac{78}{54}C_A N_f^2 + \frac{11}{9}C_F N_f^2\right)\,. \end{aligned} \tag{1.12}$$

Note that the more commonly used coefficients β_i for the QCD beta function are related to the b_i used here by $\beta_i = b_i(4\pi)^{i+1}$. Asymptotic freedom or, in other words, a negative QCD beta function in Eq. (1.11), follows from the fact that b_0 is positive for $N_f \leq 16$ quark flavors. A negative beta function implies that the coupling strength decreases for higher energies. At leading order (LO), we can solve

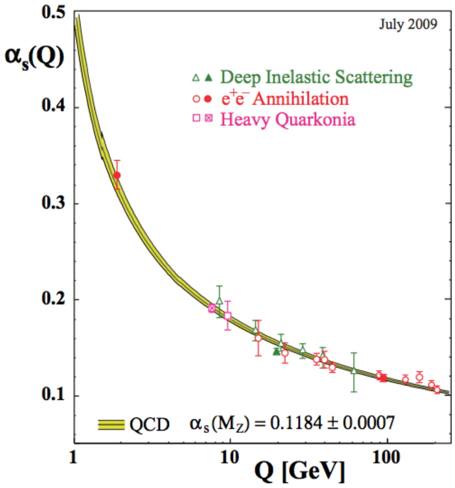

Figure 1.1: Scale dependence of the strong coupling constant $\alpha_s(Q^2)$. Figure taken from [21].

Eq. (1.11) exactly

$$\alpha_s(\mu_R^2) = \frac{\alpha_s(\mu_0^2)}{1 + b_0\, \alpha_s(\mu_0^2) \log(\mu^2/\mu_0^2)} \,. \tag{1.13}$$

For example at NNLO, including the coefficients b_1, b_2, we can derive an implicit equation for α_s which can be solved approximately, see [22] for example. One finds

$$\alpha_s(\mu_R^2) = \frac{\alpha_s(\mu_0^2)}{X}\left[1 - \frac{b_1}{b_0}\alpha_s(\mu_0^2)\frac{\log X}{X} + \alpha_s^2(\mu_0^2)\left(\frac{b_2}{b_0}\frac{1-X}{X^2} + \frac{b_1^2}{b_0^2}\frac{\log^2 X - \log X + X - 1}{X^2}\right)\right] \,, \tag{1.14}$$

with

$$X = 1 + b_0\, \alpha_s(\mu_0^2) \log(\mu_R^2/\mu_0^2) \,. \tag{1.15}$$

With these relations at hand, we can compute the strong coupling constant α_s at scale μ_R in case that it is known at some reference scale μ_0. Hence, from perturbative QCD we may compute the scale variation of α_s but the “non-perturbative” input has to be determined from experiment. Fig. 1.1 illustrates the running of α_s obtained from QCD with a starting value for α_s at the Z mass which is consistent with data from several experiments. On the right side of Fig. 1.1, we see that α_s becomes small which implies that a perturbative methods are a valid approach. However, at low energies we find that α_s increases which implies that quarks and gluons start to interact strongly with each other. This is the region where confinement sets in which means that the partons are bound into colorless hadrons.

As a side remark, we would like to point out that solving the renormalization group equations sums up logarithms to all orders in perturbation theory. This can be seen most easily by considering the LO solution for α_s given in Eq. (1.13). Writing it as a series in powers of the strong coupling constant, we

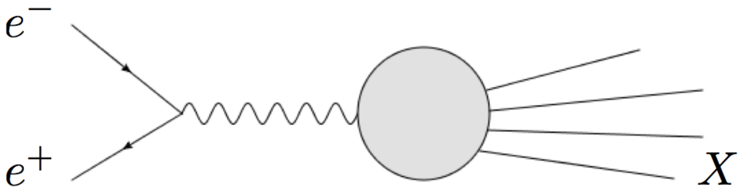

Figure 1.2: e^+e^- Annihilation to hadrons, summing over everything in the final state X.

obtain

$$\begin{aligned}\alpha_s(\mu_R^2) &= \frac{\alpha_s(\mu_0^2)}{1+b_0\,\alpha_s(\mu_0^2)\log(\mu_R^2/\mu_0^2)} \\ &= \alpha_s(\mu_0^2) - b_0\log(\mu_R^2/\mu_0^2)\,\alpha_s^2(\mu_0^2) + (b_0\log(\mu_R^2/\mu_0^2))^2\,\alpha_s^3(\mu_0^2) + \dots \end{aligned} \tag{1.16}$$

This is the first example of an all order "resummation" that we come across. It is so called because we first perform an expansion in α_s and afterwards, we sum up to all orders a certain type of terms, here logarithms of the ratio of two different scales.

QCD Renormalization Scale Uncertainties

The arbitrary scale parameter μ introduces an uncertainty into any prediction obtained from pQCD. As an example, we consider the fully inclusive cross section $e^+e^- \to X$ which we are going to discuss further in the next Sections. The Feynman diagram is shown in Fig. 1.2, where we sum over everything in the final state X. The grey circle represents any kind of hard interaction that has to be computed to a given order in perturbation theory. Leaping ahead, we can write down the cross section in the following form

$$\sigma = \sigma_0\,(1+\Delta_{\mathrm{QCD}})\,, \tag{1.17}$$

where σ_0 is the leading-order cross section which will be discussed below, cf. Eq. (1.22). The quantity Δ_{QCD} denotes contributions from higher order QCD corrections. In principle, Δ_{QCD} is of the form

$$\Delta_{\mathrm{QCD}} = \sum_{n=1}^{\infty} c_n(\mu_R^2)\left(\frac{\alpha_s(\mu_R^2)}{\pi}\right)^n . \tag{1.18}$$

Using the $\overline{\mathrm{MS}}$-scheme, the result up to third order in α_s is given by [17, 23]

$$\begin{aligned}\Delta_{\mathrm{QCD}} &= \frac{\alpha_s(\mu_R^2)}{\pi} + \left[1.4092 + 1.9167\log\left(\mu_R^2/s\right)\right]\left(\frac{\alpha_s(\mu_R^2)}{\pi}\right)^2 \\ &\quad + \left[-12.805 + 7.8186\log\left(\mu_R^2/s\right) + 3.674\log^2\left(\mu_R^2/s\right)\right]\left(\frac{\alpha_s(\mu_R^2)}{\pi}\right)^3 + \dots\end{aligned} \tag{1.19}$$

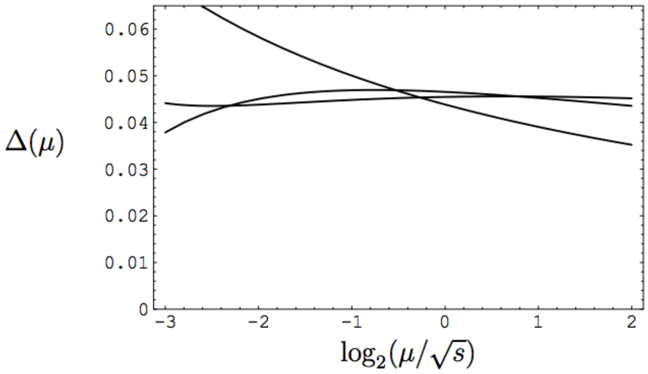

Figure 1.3: Renormalization scale dependence of $\Delta_{\text{QCD}}(\mu_R)$ for the first three QCD corrections to inclusive $e^+e^- \to X$. Here, we have $\mu = \mu_R$. Figure taken from [17].

The requirement that the physical cross section has to be independent of μ_R can be formulated as

$$\frac{d}{d\log\mu_R^2}\Delta_{\text{QCD}} = 0\,. \tag{1.20}$$

This equation would hold exactly if we have a prediction for Δ_{QCD} from the full theory, *i.e.* including all higher order corrections. However, in practice we always have a finite order approximation which means that we can only compute the first few coefficients $c_n(\mu_R^2)$ in Eq. (1.18). Assuming that we can compute N terms in the perturbative series, one finds that the obtained cross section exhibits a scale uncertainty of the order of α_s^{N+1}

$$\frac{d}{d\log\mu_R^2}\sum_{n=1}^{N} c_n(\mu_R^2)\left(\frac{\alpha_s(\mu_R^2)}{\pi}\right)^n = -\frac{d}{d\log\mu_R^2}\sum_{n=N+1}^{\infty} c_n(\mu_R^2)\left(\frac{\alpha_s(\mu_R^2)}{\pi}\right)^n \sim \mathcal{O}(\alpha_s(\mu_R^2)^{N+1})\,. \tag{1.21}$$

Therefore, the scale uncertainty is reduced when higher order corrections are computed. This behavior is illustrated in Fig. 1.3, where the scale dependence is shown when various higher order corrections for Δ_{QCD} are included. In that sense, the scale uncertainty can be viewed as a way of quantifying uncertainties introduced in the calculation by the lack of knowledge about higher order terms starting at α_s^{N+1}. The question that remains is how to choose the scale. The only requirement is that the terms involving a $\log(\mu_R^2/s)$ in Eq. (1.19) should not be too big. Otherwise, we have to worry about the convergence of the perturbative series. Therefore, we may choose $\mu_R^2 = s$ for example.

Given the fact that α_s becomes small at high energies and since for example the energy of the LHC is in the TeV range, perturbative methods should work perfectly fine. However, in the view of confinement, there is still some way to go in order to apply perturbative methods in QCD. Even though, we can compute the interactions of quarks and gluons at short distances there is still a problem since the protons colliding at the LHC have a rich inner structure. In addition, detectors are placed at “long distance scales” compared to the hard interaction point in the sense that they observe hadrons instead of free quarks and gluons. In order to overcome these issues, *i.e.* making perturbation theory in QCD a valid approach, we have to consider observables which are either

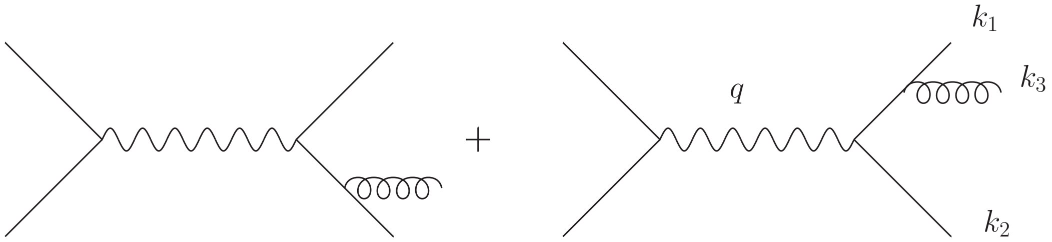

Figure 1.4: Real gluon emission diagrams at NLO.

- insensitive to long-distance physics or
- observables for which we can systematically separate long-distance and short-distance phenomena.

This observation leads to two key concepts of perturbative QCD which are infrared safety (IR safety) and factorization. We introduce them in the next two Sections along with several applications to QCD phenomenology.

1.2 Infrared Safety

In this Section we introduce the fundamental concept called infrared safety. In order to obtain sensible answers from QCD for a given observable, this observable has to be independent of long-distance or low energy physics, *i.e.* it has to be infrared safe. We choose to start with e^+e^- annihilation because it is a clean process in the sense that we do not need to worry about hadrons in the initial state. Lepton-hadron and hadron-hadron processes will be discussed in Sections 1.3 and 1.4. However, the conclusions we can draw here are of general nature. We start by considering the totally inclusive rate of $e^+e^- \to X$ annihilation to hadrons, where we sum over everything in the final state. Afterwards, we also extend our analysis to event shapes and jets.

1.2.1 Totally Inclusive Annihilation $e^+e^- \to$ hadrons

In this Section, we are going to follow roughly the steps outlined in [17, 24, 25]. Starting at leading order, we only have to consider the production of a $q\bar{q}$ pair resulting in the following expression for the LO cross section

$$\sigma_0 = \frac{4\pi\alpha^2}{3s} N_c \sum_{q=u,d,s,\dots} e_q^2 \,. \tag{1.22}$$

Here, $\alpha = e^2/4\pi$ denotes the electromagnetic fine structure constant, $s = q^\mu q_\mu$ is total energy in the c.m.s. and we sum over all active quark flavors.

Next-to-Leading Order

At next-to-leading order, we have to consider the process, where there is one additionally radiated gluon in the final state $e^+e^- \to q\bar{q}g$. The relevant Feynman diagrams are displayed in Fig. 1.4. Here

q^μ is the momentum of the virtual photon with $s = q^2$ and the k_i^μ are the momenta $i = 1, 2, 3$ of the outgoing partons $q, \bar{q}, g$ respectively. It is convenient to define the corresponding energy fractions x_i as

$$x_i = \frac{2E_i}{\sqrt{2}} = \frac{2k_i \cdot q}{s} \,. \tag{1.23}$$

These are bounded by $0 \leq x_i \leq 1$ and they satisfy $x_1 + x_2 + x_3 = 2$ due to momentum conservation $q = k_1 + k_2 + k_3$ which implies that there are only two independent x_i. Calculating the cross section at NLO according to Fig. 1.4, we find the following result

$$\sigma(e^+e^- \to q\bar{q}g) = \sigma_0 \frac{\alpha_s}{2\pi} C_F \int_0^1 dx_1 \int_{1-x_1}^1 dx_2 \frac{x_1^2 + x_2^2}{(1-x_1)(1-x_2)} \tag{1.24}$$

where σ_0 is given in Eq. (1.22). The lower boundary of the integration region for x_2 is directly obtained from momentum conservation and the requirement $x_3 \leq 1$. We find that the cross section diverges as $x_1 \to 1$ and/ or $x_2 \to 1$. In order to pin down the origin of these divergences, we need to examine the structure of the NLO result. We can relate the energy fractions x_i to the angles θ_{ij} between the respective partons i and j via

$$\begin{aligned} &2k_1 \cdot k_2 = (k_1 + k_2)^2 = (q - k_3)^2 = s - 2q \cdot k_3 \\ &2E_1 E_2 (1 - \cos\theta_{12}) = s(1 - x_3) \,. \end{aligned} \tag{1.25}$$

This result generalizes to

$$x_i x_j (1 - \cos\theta_{ij}) = 2(1 - x_k) \,, \tag{1.26}$$

for $i, j, k = 1, 2, 3$ as well as cyclic permutations. Hence, the divergences in Eq. (1.24) correspond to kinematic situations where the emitted gluon becomes parallel to the antiquark or quark (“collinear divergence”)

$$\begin{aligned} &x_1 \to 1 \;\Leftrightarrow\; \theta_{23} \to 0 \,, \\ &x_2 \to 1 \;\Leftrightarrow\; \theta_{13} \to 0 \,. \end{aligned} \tag{1.27}$$

In addition, we obtain a singularity, when the emitted gluon becomes soft $x_3 \to 0$ (“soft” or “infrared divergence”). Written in terms of the integration variables $x_{1,2}$, this situation corresponds to both $(1 - x_1) \to 0$ and $(1 - x_2) \to 0$ which directly follows from Eq. (1.26).

Before continuing the discussion of the origin of the singularities, we present the final result at NLO. After including virtual corrections as well, all singularities cancel and we obtain a finite result for the totally inclusive cross section

$$\sigma(e^+e^- \to X) = \frac{4\pi\alpha^2}{3s} N_c \sum_{q=u,d,s,\ldots} e_q^2 \left(1 + \frac{\alpha_s}{\pi}\right) \,. \tag{1.28}$$

Here, we evaluate the strong coupling constant as $\alpha_s(s)$ which is due to higher order corrections, cf. Eq (1.19). Therefore, we end up with a moderate correction which is typically of the order of ten percent at NLO. The process $e^+e^- \to X$ is the first and most simple example of an infrared safe quan-

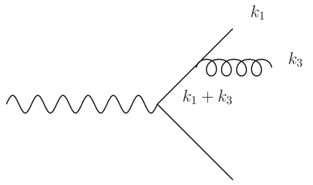

$$\Rightarrow \qquad \frac{1}{(k_1 + k_3)^2} = \frac{1}{2E_1E_3\,(1-\cos\theta_{13})}$$

Figure 1.5: Collinear, soft gluon radiation.

tity. In fact, the Kinoshita-Lee-Nauenberg theorem [26, 27] guarantees the cancellation of infrared singularities to all orders in perturbation theory. A detailed calculation of both the real and virtual corrections at NLO can be found in [24].

The occurrence of these types of divergences is a general feature of perturbative methods in field theories. They indicate sensitivity to long-distance physics which, however, should be avoided since perturbation theory is out of control in this case, as discussed in Section 1.1.2. Going back to the process $e^+e^- \to q\bar{q}g$, we find that the singularities at the phase space boundaries are due to internal propagators that go on-shell, as shown in Fig. 1.5. We find the following double logarithmic structure for the total cross section

$$\sigma \sim \int \frac{dE_3}{E_3}\frac{d\theta_{13}}{\sin\theta_{13}}d\phi\,. \tag{1.29}$$

We obtain a divergence for $E_3 \to 0$ and $\theta_{13} \to 0,\ \pi$. Note that the factor $1/E_1$ in the propagator given in Fig. 1.5 does not produce a similar divergence because it will be cancelled by an appropriate factor in the numerator. It was found in [28, 29] that this generalizes also to more complicated diagrams in pQCD.

Definition of Infrared Safe Observables

Having identified the origin of collinear and soft divergences, there still remains the question of how to generally get rid of them in order to be left with a sensible answer from perturbation theory. In pQCD, we can only compute observables that are independent of long-distance physics.

We start with the formal definition of an infrared safe quantity following the notation of [30]. Let us consider an inclusive observable $\mathcal{I}$ in e^+e^- annihilation. The symmetric "measurement functions" $\mathcal{S}_n$ specify how the observable $\mathcal{I}$ is constructed

$$\begin{aligned}\mathcal{I} = \quad & \frac{1}{2!}\int d\Omega_2 \frac{d\sigma[2]}{d\Omega_2}\mathcal{S}_2(p_1^\mu, p_2^\mu) \\ & + \frac{1}{3!}\int d\Omega_2 dE_3 d\Omega_3 \frac{d\sigma[3]}{d\Omega_2 dE_3 d\Omega_3}\mathcal{S}_3(p_1^\mu, p_2^\mu, p_2^\mu) \\ & + \ldots\,, \end{aligned} \tag{1.30}$$

where the

$$\frac{d\sigma[n]}{d\Omega_2 dE_3 d\Omega_3 \cdots dE_n d\Omega_n} \tag{1.31}$$

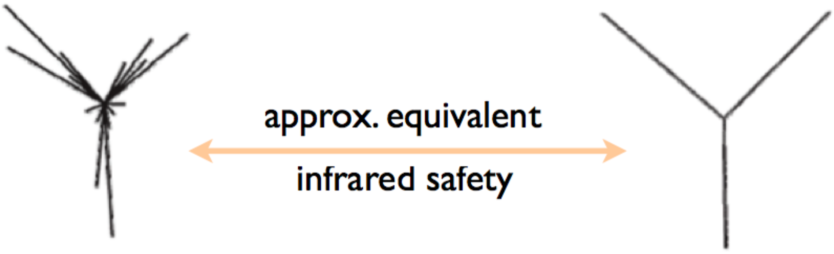

Figure 1.6: Infrared safety illustrated for a three jet event. Figure adapted from [17].

denote cross sections with n hadrons in the final state. For the observable to be infrared safe, the functions $\mathcal{S}_n$ have to satisfy

$$\mathcal{S}_{n+1}(p_1^\mu, \ldots, (1-\lambda)p_n^\mu, \lambda p_n^\mu) = \mathcal{S}_n(p_1^\mu, \ldots, p_n^\mu) \tag{1.32}$$

for $0 \leq \lambda \leq 0$. This means that an infrared safe observable is insensitive to whether we have $n+1$ or n contributing particles in the final state in the case that the $n+1$ particles have n-particle kinematics [30]. The physical meaning is that the observable is insensitive to soft ($\lambda = 0$) and collinear ($0 < \lambda \leq 1$) splittings which is equivalent to the statement that the observable has to be insensitive to long-distance physics.

This requirement can be interpreted in the way that experiments are not able to resolve collinear and soft partons. Hence, we have to require the approximate equivalence of the two situations displayed in Fig. 1.6 where a three jet event is shown as an example. Removing soft partons and combining collinear ones does not affect an infrared safe observable. From the mathematical point of view, infrared safety manifests itself in the way that IR singularities which appear at intermediate steps of the calculation drop out at the end, as we have seen it already for the process $e^+e^- \to X$ in Eq. (1.28). This brings us to the question of how the measurement functions look like for a given observable. The simplest example is the just mentioned process of inclusive $e^+e^- \to X$ annihilation. The measurement functions are given by

$$\mathcal{S}_n(p_1^\mu, \ldots, p_n^\mu) = 1\,, \tag{1.33}$$

which trivially fulfill the requirements in Eq. (1.32). For the totally inclusive cross section we sum over everything in the final state X and all produced partons hadronize with unit probability. A formal argument can be made using unitarity, cf. [17].

Other examples for infrared safe observables are event shapes. The thrust distribution $d\sigma/dT$ is one of the most prominent ones [31]. The measurement functions are given by

$$\begin{aligned} \mathcal{S}(p_1^\mu, \ldots, p_n^\mu) &= \delta(T - T_n(p_1^\mu, \ldots, p_n^\mu))\,, \\ T_n(p_1^\mu, \ldots, p_n^\mu) &= \max_{\boldsymbol{n}} \frac{\sum_{i=1}^n |\boldsymbol{p}_i \cdot \boldsymbol{n}|}{\sum_{i=1}^n |\boldsymbol{p}_i|}\,, \end{aligned} \tag{1.34}$$

where the maximum is taken over the unit vector $\boldsymbol{n}$. Varying between 1 and 1/2, the thrust gives a

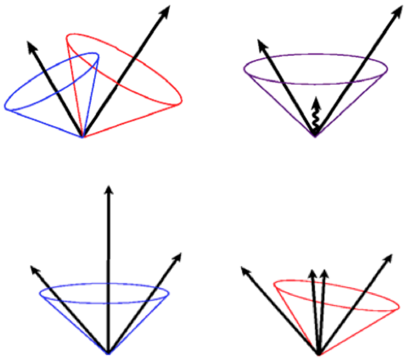

Figure 1.7: Illustration of IR safety requirements for jet definitions, see text. Figure taken from [25].

measure of how back-to-back or pencil-like an event is. We find

$$|(1-\lambda)\,\boldsymbol{p}_i\cdot\boldsymbol{n}| + |\lambda\,\boldsymbol{p}_i\cdot\boldsymbol{n}| = |\boldsymbol{p}_i\cdot\boldsymbol{n}|\,, \tag{1.35}$$

which confirms its infrared safety according to Eq. (1.32). Nowadays, one of the most important examples of infrared safe observables are jet cross sections which we are going to discuss in the next Section.

1.2.2 Jets

Generally speaking, jets are bunches of collimated particles seen in the detectors. Observables involving jets are an invaluable tool in present day collider experiments where they are used as high precision probes of QCD and for the search of BSM physics. There is no unique way to define a jet. In general, the jet definitions given here apply to both e^+e^- and proton-proton (pp) collisions. In Chapter 7, we consider single-inclusive jet production in pp collisions. The first NLO IR safe jet definition was given by Sterman and Weinberg [32]. Nowadays [33], most of the existing jet algorithms can be grouped into cone algorithms on the one hand [34] and successive recombination algorithms ("k_t algorithms") on the other hand [35–38]. In addition to the jet definition, one also needs to specify a recombination scheme which specifies how the momentum of the jet is obtained from the momenta of the particles that make up the jet.

The requirements for any jet definition are illustrated in Fig. 1.7. Firstly, adding a soft parton should not change the number of jets found by the algorithms (upper row in Fig. 1.7). Secondly, replacing one parton by a pair of collinear partons should also not alter the number of jets (lower row in Fig.1.7). Those two requirements basically reflect the concept of IR safety discussed above. Finally, the jet definition needs to be resilient to detector effects. Cone type jet algorithms cluster particles according to their distance in the rapidity and the azimuthal angle plane. Particles are clustered in cones along the dominant directions of momentum. This is done such that the direction of the sum of the momenta points into the center of the cone. However, in general, there are potential problems with IR safety for this type of jet algorithms.

Nowadays, the standard choice for jet cross sections are k_t-type algorithms. For each pair of objects in the final state j, k, one defines a distance d_{jk} as

$$d_{jk} \equiv \min(k_{Tj}^{2p}, k_{Tk}^{2p}) \frac{R_{jk}^2}{R} \,, \tag{1.36}$$

where k_{Tj} denotes the transverse momentum of the object j and the exponent p defines the specific algorithm under consideration. For the k_t algorithm [35, 36] one has $p = 1$, for the Cambridge/ Aachen algorithm [37] one has $p = 0$ and for the most commonly used anti-k_t algorithm [38], one has $p = -1$. Furthermore, in Eq. (1.36) one defines

$$R_{jk} \equiv (\eta_j - \eta_k)^2 + (\phi_j - \phi_k)^2 \,. \tag{1.37}$$

Here η_j and ϕ_j are the pseudo-rapidity and the azimuthal angle of objekt j. Finally, the parameter R in Eq. (1.36) is some fixed value which is called the jet parameter or jet radius. In addition, an object-beam distance is defined as

$$d_{jB} \equiv k_{Tj}^{2p} \,. \tag{1.38}$$

The algorithm combines successively objects by identifying the smallest of the distances d_{jk} and d_{jB}. When two objects are merged the sum of both four momenta is assigned to the new object following the most commonly used recombination scheme, see [34] for example. In case that a d_{jB} is the smallest distance, the object j is called a jet and removed from the list.

Often jet cross sections are calculated using Monte-Carlo integrators. However, an analytical form of the partonic hard-scattering cross section may be achieved within the “Narrow Jet Approximation” (NJA) developed in [39–42]. Assuming that the jet is a rather narrow object, one may expand the partonic cross section around $R = 0$ as

$$\mathcal{A} \log R + \mathcal{B} + \mathcal{O}(R^2) \,. \tag{1.39}$$

The functions $\mathcal{A}$ and $\mathcal{B}$ are perturbatively calculable and we neglect terms of the order $\mathcal{O}(R^2)$ and beyond. The NJA approximation was found to work very well for all kinematical regions at present-day collider experiments [40, 43]. Indeed, this statement holds true even for very large values of $R \sim \mathcal{O}(1)$. In Chapter 7, we apply this technique to single-inclusive jet production in hadronic collisions $pp \to \text{jet}X$.

1.3 Factorization and Evolution

Different to the observables discussed so far, another class of cross sections involve identified hadrons in the final state. For example, $e^+e^- \to hX$ requires the use of “fragmentation functions” (FFs) describing the non-perturbative effects of a parton fragmenting into an observed hadron h. Such processes will be discussed further in subsequent Chapters. Instead, here we choose to present the necessary concepts of factorization and evolution using DIS $\ell N \to \ell' X$ as an example as it is one of the most prominent processes. It was this process, where pointlike partons were discovered for the first time. Within pQCD, we need parton distribution functions (PDFs) describing the distribution of quarks and gluons

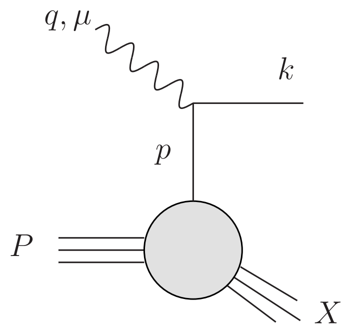

Figure 1.8: Diagrammatic expression for the DIS amplitude at LO.

in a nucleon N. To some extent PDFs may be viewed as the initial state analogue of FFs.

1.3.1 Deep Inelastic Scattering at LO

We consider the process where a lepton is scattering inelastically off a nucleon target $\ell N \to \ell' X$. For simplicity, we assume for now that the interaction with the nucleon (momentum P) is mediated only via the exchange of a virtual photon with momentum q. We may separate the DIS cross section into a leptonic part and a hadronic one, *i.e.* $d\sigma \sim L_{\mu\nu} W^{\mu\nu}$. In general, we may write the hadronic tensor $W^{\mu\nu}$ as [44, 45]

$$\begin{aligned} W^{\mu\nu} &= \frac{1}{8\pi} \int d^4 z \, e^{iq\cdot z} \sum_X \langle P | j^\mu(z) | X \rangle \langle X | j^\nu(0) | P \rangle \\ &= \left(-g^{\mu\nu} + \frac{q^\mu q^\nu}{q^2} \right) F_1(x, Q^2) + \frac{1}{P\cdot q} \left(P^\mu - q^\mu \frac{P\cdot q}{q^2} \right) \left(P^\nu - q^\nu \frac{P\cdot q}{q^2} \right) F_2(x, Q^2) \,, \end{aligned} \tag{1.40}$$

where $j^\mu(x)$ is the electromagnetic current and $Q^2 = -q_\mu q^\mu$. In the second line we introduced the structure functions $F_{1,2}(x, Q^2)$.

The scattering amplitude of the virtual photon with the nucleon at LO is shown in Fig. 1.8, where all the relevant momenta are shown. The struck quark has momentum p. For the corresponding mathematical expression, we obtain

$$\begin{aligned} \mathcal{M}_0^\mu &= \bar{u}_i(k) \, (ie\,\gamma^\mu_{ij}) \int \frac{d^4 p}{(2\pi)^4} \left(\int d^4 z \, \langle X | \psi_j(z) | P \rangle \, e^{ip\cdot x} \right) \\ &= \bar{u}_i(k) \, (ie\,\gamma^\mu_{ij}) \int \frac{d^4 p}{(2\pi)^4} \int d^4 z \, \langle X | \psi_j(0) | P \rangle \, e^{i(p-P+P_X)\cdot z} \\ &= \bar{u}_i(k) \, (ie\,\gamma^\mu_{ij}) \, \langle X | \psi_j(0) | P \rangle \;. \end{aligned} \tag{1.41}$$

The indices i, j are in Dirac space, whereas color and flavor indices are left implicit. The grey circle in Fig. 1.8 is expressed by the Fourier transform of a hadronic matrix element where a quark of flavor

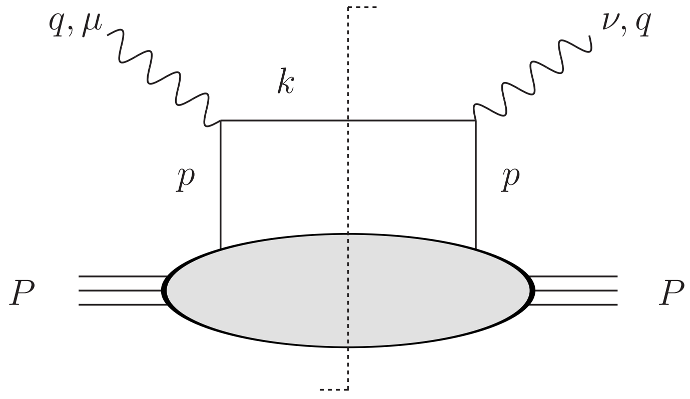

Figure 1.9: Leading order cut diagram for DIS, where the sum is taken over all states/ lines crossing the final state cut.

f and momentum p is created. This is achieved by acting with the operator $\psi_j(z)$ on the initial state proton with momentum P, see also Appendix B. In the final state we have labeled any additional hadronic state by X with momentum P_X. In addition, we integrate over all possible momenta p as it is an internal momentum variable. In the first step, we made use the translation relation that is generally satisfied by field operators

$$\mathcal{O}(z) = e^{i\mathcal{P}\cdot z}\, \mathcal{O}(0)\, e^{-i\mathcal{P}\cdot z}\,, \tag{1.42}$$

where $\mathcal{P}^\mu$ is the momentum operator. for the complex conjugate amplitude $\mathcal{M}_0^{*\mu}$, we obtain

$$\mathcal{M}_0^{*\mu} = \langle P|\bar{\psi}_i(0)|X\rangle\, (-ie\gamma^\mu_{ij})\, u_j(k)\,. \tag{1.43}$$

We can now write down the hadronic tensor which corresponds to the cut diagram shown in Fig. 1.9 as

$$\begin{aligned} W^{\mu\nu} \;\; &= \;\; \frac{1}{8\pi} \sum\!\!\!\!\!\!\!\int_X \int \frac{d^3k}{2E_k(2\pi)^3}\, \bar{u}_i(k)\, (ie\gamma^\mu_{ij})\, \langle X|\psi_j(0)|P\rangle\, \langle P|\bar{\psi}_k(0)|X\rangle\, (-ie\gamma^\nu_{kl})\, u_l(k) \\ &\quad\;\; (2\pi)^4\, \delta^{(4)}(P + q - k - P_X)\,, \end{aligned} \tag{1.44}$$

where the factor $1/8\pi$ is due to normalization and the delta function ensures momentum conservation. We integrate over the phase space of the outgoing partons that cross the final state cut. This includes both the parton with momentum k and any additional final state X. The summation over X and the integration over its phase space is given by

$$\sum\!\!\!\!\!\!\!\int_X = \sum_{i=0}^{n} \prod_{j=0}^{i} \int \frac{d^3p_j}{2E_j(2\pi)^3}\,. \tag{1.45}$$

We rewrite Eq. (1.44) as

$$
\begin{aligned}
W^{\mu\nu} &= \frac{e^2}{4}\int \frac{d^4k}{(2\pi)^4}\delta(k^2)\,\bar{u}_i(k)\,\gamma^{\mu}_{ij}\,\sum\!\!\!\!\!\!\int_X \langle P|\bar{\psi}_k(0)|X\rangle\,\langle X|\psi_j(0)|P\rangle\;\gamma^{\nu}_{kl}\,u_l(k)\\
&\quad (2\pi)^4\delta^{(4)}(P+q-k-P_X)\cdot\int\frac{d^4p}{(2\pi)^4}\int d^4z\,e^{-i(p+P_X-P)\cdot z}\,, \qquad (1.46)
\end{aligned}
$$

where we introduced a factor of unity in the second line. We now define the so-called quark correlator as the Fourier transform of an hadronic matrix element

$$
\Phi_{ij}(p) = \int \frac{d^4z}{(2\pi)^4}\,\langle P|\bar{\psi}_j(z)\,\psi_i(0)|P\rangle\,e^{-ip\cdot z}\,. \qquad (1.47)
$$

Hence, making again use of (1.42), we obtain for the hadronic tensor

$$
W^{\mu\nu} = \frac{e^2}{4}\int d^4p\,d^4k\,\delta(k^2)\,\delta^{(4)}(p+q-k)\,\mathrm{tr}[\not{k}\gamma^{\mu}\Phi(p)\gamma^{\nu}]\,, \qquad (1.48)
$$

where we used

$$
\sum\!\!\!\!\!\!\int_X |X\rangle\,\langle X| = 1\,. \qquad (1.49)
$$

We may expand the correlator $\Phi(p)_{ij}$ in terms of Dirac matrices and determine its components which is known as Fierz rearrangement

$$
\Phi(p) = \phi_1(p)\,\mathbb{1} + \phi_2(p)\not{p} + \phi_3(p)\gamma_5 + \phi_4(p)\not{p}\gamma_5\,. \qquad (1.50)
$$

The first term is a mass term which we neglect for now. However, in Chapter 4 when we are considering hadron mass corrections, we will include a non-zero mass for the nucleon target in DIS as well as for the observed final-state hadron in semi-inclusive annihilation (SIA) $e^+e^- \to hX$. The third and forth terms vanish when we compute an unpolarized cross section. Therefore, we are only left with the second term $\phi_2(p)\not{p}$. Acting on both sides of Eq. (1.50) with $\mathrm{tr}[\ldots\not{n}]$, where n is defined such that in general $n\cdot a = a^+$, we obtain

$$
\begin{aligned}
\phi_2(p) &= \frac{1}{4p^+}\mathrm{tr}[\not{n}\,\phi(p)]\\
&= \frac{1}{4p^+}\int\frac{d^4z}{(2\pi)^4}\,\langle P|\bar{\psi}(z)\gamma^+\psi(0)|P\rangle\,e^{ip\cdot z}\,. \qquad (1.51)
\end{aligned}
$$

Using the delta function in (1.48) to perform the d^4k integration, we can now write the hadronic tensor as

$$
W^{\mu\nu} = \frac{e^2}{4}\int dp^+dp^-d^2\boldsymbol{p}_T\,\delta((p+q)^2)\,\mathrm{tr}[(\not{p}+\not{q})\gamma^{\mu}\not{p}\gamma^{\nu}]\phi_2(p)\,. \qquad (1.52)
$$

Using light-cone coordinates, we can write the momentum of the incoming proton as $P=(P^+,0,\mathbf{0}_T)$. Within the framework of collinear factorization, we write the momentum of the struck quark only as $p^+ = xP^+$. Hence, in the trace term of Eq. (1.48), we only keep the contribution with $\not{p} = p^+\gamma^-$. In addition, only the plus component of p is kept when writing the remaining delta function as

$$\delta((p+q)^2) = \delta(q^2 + 2p\cdot q) = \frac{x_B}{Q^2}\delta(x - x_B)\,, \tag{1.53}$$

where the Bjorken scaling variable is given by $x_B = Q^2/2P\cdot q$. Therefore, we are only left with p^+ components for the integral and the $dp^- d^2\boldsymbol{p}_T$ act directly on the quark correlator which then is denoted as the integrated correlator without any dependence on the transverse momentum of the quarks inside the proton. Keeping the dependence on the transverse momentum component, we would obtain transverse momentum dependent PDFs. As discussed above, we only keep the $\phi_2(p)$ component for the unpolarized cross section without mass corrections. In order to be consistent with the rest of this thesis, we denote the unpolarized quark PDF from now on with $f(x)$ instead of $\phi_2(p)$, where f denotes a parton of flavor $f = q, \bar{q}, g$. Two delta functions $\delta(z^+)\delta^2(\boldsymbol{z}_T)$ are obtained after carrying out the $dp^- d^2\boldsymbol{p}_T$ integrals which yields the final result for the quark PDF in a hadron with momentum P [46]

$$q(x) = \frac{1}{4}\int \frac{dz^-}{2\pi} e^{-ixP^+z^-} \,\langle P|\bar{\psi}(z^-)\gamma^+\psi(0)|P\rangle \,. \tag{1.54}$$

Note that this is only valid in axial gauge $n\cdot A = 0$ gauge. PDFs are non-perturbative but universal ingredients and may be extracted from experiment. In general, we need to introduce a Wilson line between the two quark fields, which is given by the following ordered exponential

$$\mathcal{P}\exp\left(-ig\int_0^{z^-} d\eta\, n\cdot A(\eta n)\right)\,. \tag{1.55}$$

For completeness, we also give here the operator definition for corresponding gluon PDF $g(x)$ in $n\cdot A = 0$ gauge

$$g(x) = \frac{1}{2xP^+}\int \frac{dz^-}{2\pi} e^{-ixP^+z^-} \,\langle P|F^+_\mu(z^-)F^{\mu+}(0)|P\rangle \,, \tag{1.56}$$

where $F^{\mu\nu}$ is the gluon field strength tensor. Finally, we note that for helicity PDFs $\Delta f(x)$, as discussed further in Chapters 3 and 9, we need to make the replacement $\gamma^+ \to \gamma^+\gamma_5$ in (1.54).

Returning to the calculation of the hadronic tensor for DIS in (1.52), we may now use the following two operators to project onto the structure functions $F_{1,2}(x, Q^2)$

$$\begin{aligned} P^1_{\mu\nu} &= \frac{1}{2}\left[-g_{\mu\nu} + \frac{Q^2}{(P\cdot q)^2}P_\mu P_\nu\right]\,, \\ P^2_{\mu\nu} &= \frac{Q^2}{2P\cdot q}\left[-g_{\mu\nu} + 3\frac{Q^2}{(P\cdot q)^2}P_\mu P_\nu\right]\,. \end{aligned} \tag{1.57}$$

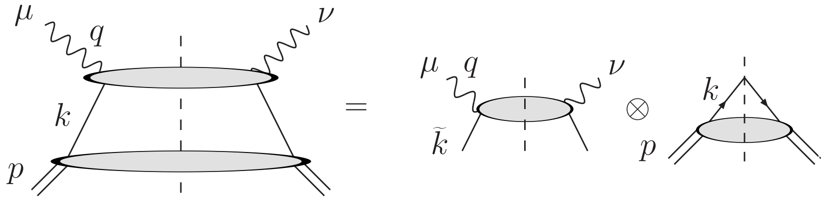

Figure 1.10: Collinear factorization for the hadronic tensor in DIS. Figure taken from [47].

We end up with the LO result

$$\begin{aligned} F_2(x_B) &= \sum_f \frac{e_f^2}{4} \int \frac{dx}{x} \frac{x_B}{Q^2}\, \delta(x - x_B)\, 4Q^2 x\, f(x) \\ &= \sum_f e_f^2\, x_B\, f(x_B) \\ &= 2x_B\, F_1(x_B)\,, \end{aligned} \tag{1.58}$$

where now we introduced an explicit sum over the different quark flavors $f = q, \bar{q}$. The relation between the two structure functions is known as Callan-Gross relation. The Q^2 independence of the structure functions at LO is referred to as Bjorken-x_B scaling.

1.3.2 Deep Inelastic Scattering at NLO

Factorization theorems developed in [5] state how to extend the leading-order result for DIS to higher orders. The leading-order diagram in Fig. 1.9 is extended as shown on the left hand side of Fig. 1.10. The upper grey ellipse corresponds to any higher order correction with real and virtual corrections. According to factorization theorems, we may separate short-distance from long-distance physics. This is illustrated on the right hand side of Fig. 1.10, where we have the product, or the convolution, of the hard-scattering part and the PDF which now both depend on the factorization scale μ_F, see discussion below. Both of which need to be calculated to a given order in perturbation theory. Collinear initial state singularities are absorbed into the bare parton distribution functions. Note that this is only valid up to corrections that are suppressed by $1/Q^2$. Mathematically, this statement manifests itself in the following structure of the corresponding structure functions at NLO

$$2F_1(x, Q^2) = \sum_f \int_x^1 \frac{d\hat{x}}{\hat{x}} f\left(\frac{x}{\hat{x}}, \mu_F^2\right) \mathcal{C}_f^1\left(\hat{x}, \frac{Q^2}{\mu_R^2}, \frac{Q^2}{\mu_F^2}, \alpha_s(\mu_R^2)\right)\,, \tag{1.59}$$

and similarly for $F_2(x, Q^2)$ for $f = q, \bar{q}, g$. Here, $\mathcal{C}_f^1$ is the coefficient function which at LO, according to the last Section, is simply given by $\mathcal{C}_f^1 = e_f^2\, \delta(1 - \hat{x})$ for $f = q, \bar{q}$. Note that beyond LO, the PDFs also depend on the factorization scale μ and we need to include a gluon contribution. In this Section, we show explicitly how the factorization and the cancellation of collinear singularities is achieved at NLO using the operator definition of the PDF in Eq. (1.54). The hard-scattering part does not depend on the choice of the hadron but only on parton type f. Therefore, we may calculate $\mathcal{C}^1$ with the simplest choice, where the “external hadron” is actually a parton [5]. We now apply the factorization formula

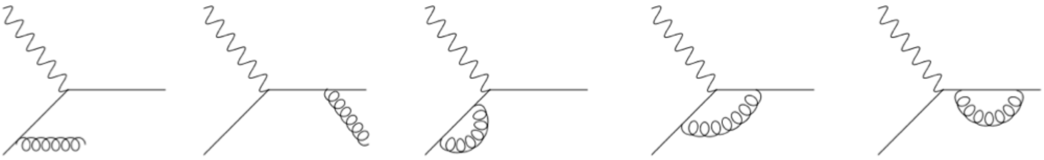

Figure 1.11: NLO real- and virtual corrections for the DIS LO process $\gamma^* q \to q$.

to incoming partons instead of hadrons. We denote the corresponding structure function as G_1 and we find

$$2G_{1,b}(x,Q^2) = \sum_a \int_x^1 \frac{d\hat{x}}{\hat{x}} \phi_{a/b}\left(\frac{x}{\hat{x}}, \mu_F^2\right) \mathcal{C}_a^1\left(\hat{x}, \frac{Q^2}{\mu_R^2}, \frac{Q^2}{\mu_F^2}, \alpha_s(\mu_R^2)\right) , \tag{1.60}$$

where we label the corresponding PDF for finding parton a in parton b with $\phi_{a/b}(x)$. The important difference to the version in (1.59) is the fact, that the $\phi_{a/b}(x)$ are calculable perturbatively up to a given order in α_s, whereas the $f(x)$ are non-perturbative. Both $G_{1,a}$ and $\mathcal{C}_a^1$ allow a perturbative expansion in α_s

$$\begin{aligned} G_{1,a} &= G_{1,a}^{(0)} + \frac{\alpha_s}{\pi} G_{1,a}^{(1)} + \mathcal{O}(\alpha_s^2) , \\ \mathcal{C}_a^1 &= C_a^{1,(0)} + \frac{\alpha_s}{\pi} C_a^{1,(1)} + \mathcal{O}(\alpha_s^2) . \end{aligned} \tag{1.61}$$

What we want to calculate here is the coefficient function $\mathcal{C}_a^1$ up to first order in α_s which is the same function in Eqs. (1.59) and (1.60).

Starting with the first order correction for G_1, we need to compute the real- and virtual corrections diagrams for the process $\gamma^* q \to q$ shown in Fig. 1.11. In addition, we also need to consider gluon initiated processes which are not shown here. The explicit calculation may be found in [45]. Working in dimensional regularization with $d = 4 - 2\varepsilon$ dimensions, $G_1^{(1)}$ has ultraviolet (UV) poles $1/\varepsilon$ due to the virtual corrections. They are removed following the standard $\overline{\text{MS}}$ scheme. Soft poles cancel between real- and virtual corrections and we are left with collinear $1/\varepsilon$ poles, cf. Section 1.2.1. In order to obtain the finite result for $\mathcal{C}_a^1$ from G_1, we also need to know the functions $\phi_{a/b}(x)$ up to $\mathcal{O}(\alpha_s)$. Using their definition given in Eq. (1.54), with the corresponding hadron replaced by a parton, we may evaluate it as described in the Appendix B. After removing UV poles again in the $\overline{\text{MS}}$ scheme, one finds the following result [5, 46]

$$\phi_{a/b}(x) = \delta_{ab}\,\delta(1-x) - \frac{1}{2\varepsilon}\frac{\alpha_s}{\pi} P_{a/b}^{(0)}(x) + \mathcal{O}(\alpha_s^2) , \tag{1.62}$$

where $P_{a/b}^{(0)}(x)$ is the LO Altarelli-Parisi splitting function [48–50], see below in Eq. (1.72) and in the Appendix B. Inserting this result together with the first order expansions for G_1 and $\mathcal{C}_a^1$ in Eq. (1.61) in the factorized formula in Eq.(1.60), we obtain

$$2G_{1,b}^{(0)} + \frac{\alpha_s}{\pi} 2G_{1,b}^{(1)} = C_b^{1,(0)} + \frac{\alpha_s}{\pi} C_b^{1,(1)} - \frac{1}{2\varepsilon} \frac{\alpha_s}{\pi} \sum_a \int_x^1 \frac{d\hat{x}}{\hat{x}} P_{a/b}^{(0)} \left(\frac{x}{\hat{x}}\right) C_a^{1,(0)}(\hat{x}) + \mathcal{O}(\alpha_s^2)\,, \tag{1.63}$$

where, for ease of notation, we omitted various variables that the individual functions depend on. At LO, the correspondence is trivial $2G_{1,b}^{(0)} = C_b^{1,(0)}$. At $\mathcal{O}(\alpha_s)$, we obtain

$$C_b^{1,(1)} = 2G_{1,b}^{(1)} + \frac{1}{2\varepsilon} \frac{\alpha_s}{\pi} \sum_a \int_x^1 \frac{d\hat{x}}{\hat{x}} P_{a/b}^{(0)} \left(\frac{x}{\hat{x}}\right) C_a^{1,(0)}(\hat{x})\,, \tag{1.64}$$

which yields a finite expression for $C_b^{1,(1)}$. In summary, up to NLO, we find the following result for the DIS coefficient function [45, 51]

$$\begin{aligned} \mathcal{C}_q^1(x) \quad = \quad & e_q^2 \delta(1-x) + e_q^2 \frac{\alpha_s}{2\pi} C_F \left[(1+x^2) \left(\frac{\ln(1-x)}{1-x}\right)_+ - \frac{3}{2} \frac{1}{(1-x)_+} - \frac{1+x^2}{1-x} \ln x + 3 \right. \\ & \left. - \left(-\frac{9}{2} + \frac{\pi^2}{3}\right) \delta(1-\hat{x}) + \left(\frac{1+x^2}{1-x}\right)_+ \ln\left(\frac{Q^2}{\mu_F^2}\right) \right]\,, \end{aligned} \tag{1.65}$$

where now we explicitly denoted the factorization scale by μ_F. The results for all DIS coefficient functions at NLO can be found in the Appendix C. Here the so-called "plus distributions" are defined as

$$\int_0^1 dx\, f(x) [g(x)]_+ \equiv \int_0^1 dx\, [f(x) - f(1)] g(x)\,. \tag{1.66}$$

1.3.3 Evolution Equations

From Eqs. (1.59) and (1.65), we already see that due to the factorization procedure, both the PDF and the coefficient function dependent on an arbitrary scale μ_F. However, the measured physical quantity $2F_1(x_B, Q^2)$ can not depend on this scale, *i.e.*

$$\mu_F^2 \frac{d}{d\mu_F^2} 2F_1(x_B, Q^2) = 0\,. \tag{1.67}$$

In the case that we would have a full prediction from QCD to all orders, the dependence on μ_F cancels out between the PDF and the coefficient function. For a finite order calculation $\mathcal{O}(\alpha_s^k)$, the dependence on μ_F is of order $\mathcal{O}(\alpha_s^{k+1})$. This is similar to the dependence on the renormalization scale μ_R in Section 1.1.2. By imposing the condition in Eq. (1.67), we find that the DGLAP (Dokshitzer, Gribov, Lipatov, Altarelli, Parisi) evolution equations for the PDFs take the following form [48–50]:

$$\mu_F^2 \frac{d}{d\mu_F^2} f_i(x, \mu_F^2) = \left[\mathcal{P}_{ij} \otimes f_j(\mu_F^2)\right](x)\,, \tag{1.68}$$

where the so-called splitting functions $\mathcal{P}_{ij}(x)$ can be calculated perturbatively and $\otimes$ denotes an appropriate convolution integral. The splitting functions represent the probability that a parton j splits into a parton i carrying a momentum fraction x. For any cross section within perturbative QCD, we need to calculate both the coefficient function and the splitting function for the evolution equations to a given order in the strong coupling constant α_s. With these two ingredients at hand, we obtain the following accuracy for fixed order calculations $\mathrm{N^kLO}$

$$\begin{aligned}
\mathcal{P}_{ij} &= \qquad \frac{\alpha_s}{2\pi} P_{ij}^{(0)} + \left(\frac{\alpha_s}{2\pi}\right)^2 P_{ij}^{(1)} + \left(\frac{\alpha_s}{2\pi}\right)^3 P_{ij}^{(2)} + \ldots \\
\mathcal{C}_i &= \left(\frac{\alpha_s}{\pi}\right)^{n_0} \left(C_i^{(0)} \; + \; \frac{\alpha_s}{\pi} C_i^{(1)} \; + \; \left(\frac{\alpha_s}{\pi}\right)^2 C_i^{(2)} \; + \; \ldots \right) \\
& \qquad\qquad \text{LO} \qquad\quad \text{NLO} \qquad\qquad \text{NNLO}
\end{aligned} \tag{1.69}$$

where the exponent n_0 depends on the LO of the process under consideration. For example, for DIS, we have $n_0 = 0$. The factor of 1/2 for the $P_{ij}^{(i)}$ is the usual convention. Nowadays, the splitting functions are known up to three loops $P_{ij}^{(2)}$ [52–54]. We write the full DGLAP equations at LO in terms of the gluon PDF (g), a non-singlet (q^{NS}) and a singlet (q^{S}) quark combination

$$q^{\mathrm{NS}} = q - \bar{q}\,, \qquad q^{\mathrm{S}} = \sum_q (q + \bar{q})\,. \tag{1.70}$$

One has [55]

$$\begin{aligned}
\frac{\partial q^{\mathrm{NS}}}{\partial \ln \mu^2} &= \frac{\alpha_s(\mu^2)}{2\pi} P_{qq}^{(0)} \otimes q^{\mathrm{NS}} \\
\frac{\partial}{\partial \ln \mu^2} \begin{pmatrix} q^{\mathrm{S}} \\ g \end{pmatrix} &= \frac{\alpha_s(\mu^2)}{2\pi} \begin{pmatrix} P_{qq}^{(0)} & 2N_f P_{qg}^{(0)} \\ P_{gq}^{(0)} & P_{gg}^{(0)} \end{pmatrix} \otimes \begin{pmatrix} q^{\mathrm{S}} \\ g \end{pmatrix} \,,
\end{aligned} \tag{1.71}$$

where the Altarelli-Parisi splitting functions in the $\overline{\mathrm{MS}}$ scheme at LO [45, 56] are given by

$$\begin{aligned}
P_{qq}^{(0)} &= C_F \left(\frac{1+x^2}{1-x}\right)_+ = C_F \left((1+x^2) \frac{1}{(1-x)_+} + \frac{3}{2} \delta(1-x) \right) \\
P_{qg}^{(0)} &= \frac{1}{2} \left(x^2 + (1-x)^2 \right) \\
P_{gq}^{(0)} &= C_F \left(\frac{1 + (1-x)^2}{x} \right) \\
P_{gg}^{(0)} &= 2\, C_A \left(\frac{1-x}{x} + x(1-x) + \frac{x}{(1-x)_+} \right) + \left(\frac{11}{6} C_A - \frac{1}{3} N_f \right) \delta(1-x) \;.
\end{aligned} \tag{1.72}$$

At LO the evolution equations may be directly solved in Mellin space, where the convolution structure turns into ordinary products. Choosing $\mu_F = \mu_R = \mu$, we can schematically write the PDF in Mellin space q^N at some scale μ in terms of the PDF at scale μ_0 via [57]

$$q^N(\mu^2) = \left(\frac{\alpha_s(\mu^2)}{\alpha_s(\mu_0^2)} \right)^{-2\, P^{(0),N}/\beta_0} q^N(\mu_0^2)\,. \tag{1.73}$$

Here, $P^{(0),N}$ denotes the appropriate LO splitting function in Mellin space. Hence, solving the evolution equations resums single logarithms of the form $\alpha_s^k \ln^k(\mu_F^2/\mu_0^2)$ as can be seen directly by expanding the exponential in (1.73) in powers of α_s. Note that solving the evolution equations at NLO resums terms of the form $\alpha_s^k \ln^{k-1}(\mu_F^2/\mu_0^2)$. See for example [57] of how the evolution equations can be solved at higher orders using Mellin space techniques.

1.4 Threshold Resummation

In this Section, we start by introducing the generic structure for threshold resummation using DIS as an example. In the following parts we go further into the details of how resummation can be derived also in the case that four colored partons are taking part in the scattering process at LO. Here, the underlying color structure of the partonic scattering needs to be taken into account.

1.4.1 Resummation for DIS

In the expression for the DIS coefficient function at NLO in Eq. (1.65), we find several distributions singular at threshold $x \to 1$. Only the singular part at NLO is given by

$$C_{q,\mathrm{th}}^{1,(1)}(x) = C_F \left[(1+x^2) \left(\frac{\ln(1-x)}{1-x} \right)_+ - \frac{3}{2} \frac{1}{(1-x)_+} - \left(\frac{9}{2} + \frac{\pi^2}{3} \right) \delta(1-x) \right] , \tag{1.74}$$

where we chose $\mu_F = Q$ for simplicity. The appearance of these large corrections may spoil the perturbative convergence of the power series in α_s for $x \to 1$ even if we are well in the perturbative regime where $\alpha_s \ll 1$. These so-called threshold distributions become large near the exclusive phase space boundary, where any higher order gluon radiation from the Born process $\gamma^* q \to q$ becomes soft. The logarithms become large as real gluon emission is suppressed and virtual corrections remain. The potentially large logarithms originate from the cancellation of soft singularities between virtual and real corrections and, hence, are directly related to the IR structure of QCD. It can be shown that these logarithmic enhancements do appear at all orders in perturbation theory. For a given order k, we have

$$\alpha_s^k \left(\frac{\ln^n(1-x)}{1-x} \right)_+ , \qquad \text{with } n \leq 2k-1 \,. \tag{1.75}$$

Therefore, in order to obtain a reliable result from perturbation theory, the threshold logarithms need to be taken into account to all orders in the strong coupling constant α_s. This is achieved by a technique called "threshold resummation" [6–8]. We note that in general, the whole cross section may be dominated by the threshold terms, as the region of the partonic threshold is enhanced due to the steeply falling PDFs for large parton momentum fractions. This is a general result and can be seen directly from the convolution structure of the hadronic cross section

$$d\sigma \sim \int_\tau^1 \frac{dx}{x} \mathcal{L}\left(\frac{\tau}{x}\right) d\hat{\sigma}(x) \,. \tag{1.76}$$

Here $\mathcal{L}$ is the "the parton luminosity" which involves the PDFs and τ is a hadronic variable which, for example, is given by x_B for DIS or $\tau = Q^2/S$ for the Drell-Yan process. Given the fact that

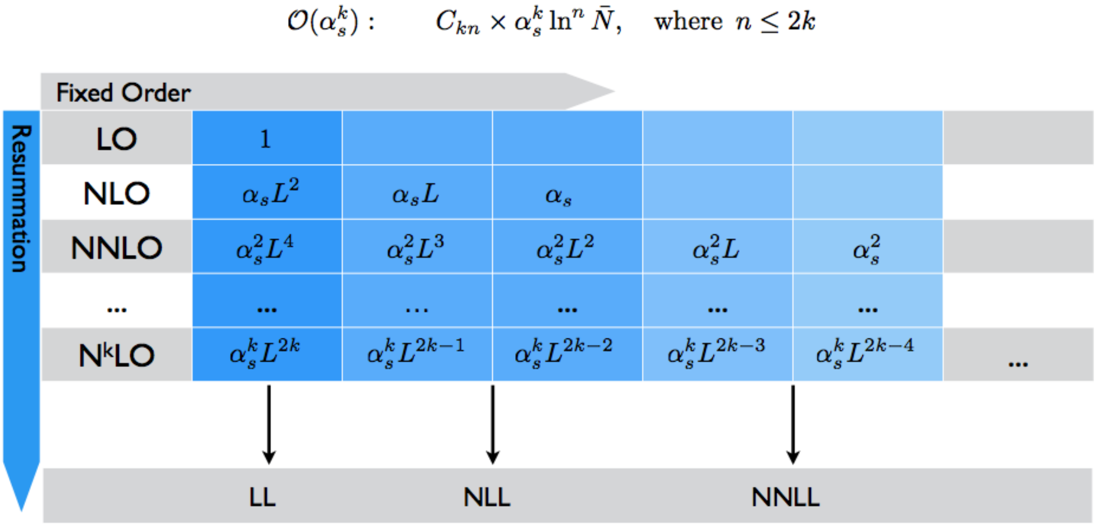

Figure 1.12: Illustration for the accuracy of threshold resummation.

the PDFs are becoming extremely small toward large τ/x, the coefficient function evaluated around $x = 1$ is dominant. This becomes even more relevant as the hadronic threshold is approached for $\tau \to 1$.

Threshold resummation may be derived in Mellin transform space. Taking moments in the scaling variable x_B of the structure function $2F_1$, we find

$$\int_0^1 dx_B\, x_B^{N-1}\, 2F_1(x_B, Q^2) = \left(\int_0^1 dx\, x^{N-1}\, \mathcal{C}_f^1\left(x, \frac{Q^2}{\mu_R^2}, \frac{Q^2}{\mu_F^2}, \alpha_s(\mu_R^2)\right)\right)\left(\int_0^1 dy\, y^{N-1} f(y, \mu_F^2)\right), \tag{1.77}$$

where the convolution structure in has been turned into a product of the moments of the PDF and moments of the coefficient function. The threshold logarithms appearing in the coefficient function turn into large logarithms of the Mellin variable N:

$$\alpha_s^k \left(\frac{\ln^{2k-1}(1-x)}{1-x}\right)_+ \qquad \to \qquad \alpha_s^k \ln^{2k} \bar{N}\,, \tag{1.78}$$

where $\bar{N} = e^{\gamma_E} N$. One finds a Sudakov double logarithmic structure, *i.e.* there two powers of $\ln \bar{N}$ for one power of α_s. The generic all order structure of threshold logarithms in Mellin space is illustrated in Fig. 1.12. Threshold resummation takes into account whole classes or towers of logarithms. For a leading logarithmic (LL) approximation, only the most dominant logarithm is taken into account for every given fixed order. This corresponds to the first column in Fig. 1.12. At the level of next-to leading logarithmic (NLL) accuracy two more subleading towers are taken into account and five towers at next-to-next-to-leading logarithmic (NNLL) accuracy.

Resummation generally relies on two basic concepts. Firstly the QCD matrix elements for n-gluon emissions factorizes into a product of n times the single gluon emission in the soft limit. Secondly, we need the phase space to factorize, which may only be achieved in Mellin transform space. With these two ingredients at hand, the exponentiation of eikonal diagrams can be achieved. In the following Sections, we will get back to how this result can be derived. For now, we simply state the resummed coefficient function for DIS

$$\mathcal{C}^{1,N}_{q,\mathrm{res}}\left(\alpha_s(\mu^2),\frac{\mu_R^2}{Q^2},\frac{\mu_F^2}{Q^2}\right)=e_q^2 H_q\left(\alpha_s(\mu^2),\frac{\mu_R^2}{Q^2},\frac{\mu_F^2}{Q^2}\right)\Delta_q^N\left(\alpha_s(\mu^2),\frac{\mu_R^2}{Q^2},\frac{\mu_F^2}{Q^2}\right)J_q^N\left(\alpha_s(\mu^2),\frac{\mu_R^2}{Q^2}\right),\tag{1.79}$$

where the two exponentials Δ_q^N and J_q^N in the $\overline{\mathrm{MS}}$ scheme are given by

$$\begin{aligned}\ln\Delta_q^N\left(\alpha_s(\mu_R^2),\frac{\mu_R^2}{Q^2},\frac{\mu_F^2}{Q^2}\right) &\equiv \int_0^1 d\xi\frac{\xi^{N-1}-1}{1-\xi}\int_{\mu_F^2}^{(1-\xi)^2Q^2}\frac{dk_\perp^2}{k_\perp^2}A_q(\alpha_s(k_\perp^2)),\\ \ln J_q^N\left(\alpha_s(\mu_R^2),\frac{\mu_R^2}{Q^2}\right) &\equiv \int_0^1 d\xi\frac{\xi^{N-1}-1}{1-\xi}\left[\int_{(1-\xi)^2Q^2}^{(1-\xi)Q^2}\frac{dk_\perp^2}{k_\perp^2}A_q(\alpha_s(k_\perp^2))+\frac{1}{2}B_q(\alpha_s((1-\xi)Q^2))\right].\end{aligned}\tag{1.80}$$

The radiative factor Δ_q^N takes into account soft and collinear gluon emissions associated with the incoming parton. The exponential J_q^N is due to collinear (soft and hard) emissions from the unobserved parton in the final state. The functions A_q and B_q allow a perturbative expansion in α_s:

$$\begin{aligned}A_q(\alpha_s) &= \frac{\alpha_s}{\pi}A_q^{(1)}+\left(\frac{\alpha_s}{\pi}\right)^2A_q^{(2)}+\dots\,,\\ B_q(\alpha_s) &= \frac{\alpha_s}{\pi}B_q^{(1)}+\left(\frac{\alpha_s}{\pi}\right)^2B_q^{(2)}+\dots\,.\end{aligned}\tag{1.81}$$

The relevant coefficients for resummation at NLL accuracy are given by

$$\begin{aligned}A_q^{(1)} &= C_F,\quad A_q^{(2)}=\frac{1}{2}C_F\left[C_A\left(\frac{67}{18}-\frac{\pi^2}{6}\right)-\frac{5}{9}N_f\right],\\ B_q^{(1)} &= -\frac{3}{2}C_F,\end{aligned}\tag{1.82}$$

where $C_F=4/3$, $C_A=3$ and N_f is the number of active flavors. Finally, the coefficient H_q in Eq. (4.30) reads

$$H_q\left(\frac{Q^2}{\mu_R^2},\frac{Q^2}{\mu_F^2},\alpha_s(\mu_R^2)\right)=1+\frac{\alpha_s}{2\pi}C_F\left(-\frac{9}{2}-\frac{\pi^2}{6}+\frac{3}{2}\ln\frac{Q^2}{\mu_F^2}\right)+\mathcal{O}(\alpha_s^2)\,,\tag{1.83}$$

taking into account contributions from hard-virtual contributions. Let us consider the exponential Δ_q^N as an example. We still need to evaluate the integrals in (1.80) which are given by integrations over the strong coupling constant α_s. We substitute the solution for α_s with a required accuracy, cf. Eqs. (1.14) and (1.16). For the expansion of the exponent up to a given N^{k}LL (with $k=0,1,2\dots$) accuracy, we introduce the new expansion parameter $\lambda = \alpha_s(\mu_R^2) b_0 \ln \bar{N}$. Up to N^{3}LL, we can write the result as

$$\begin{aligned} \ln \Delta_q^N \left(\alpha_s(\mu_R^2), \frac{\mu_R^2}{Q^2}, \frac{\mu_F^2}{Q^2}\right) &= h_q^{(1)}(\lambda) \ln \bar{N} + h_q^{(2)}\left(\lambda, \frac{\mu_R^2}{Q^2}, \frac{\mu_F^2}{Q^2}\right) + \alpha_s\, h_q^{(3)}\left(\lambda, \frac{\mu_R^2}{Q^2}, \frac{\mu_F^2}{Q^2}\right) \\ &\quad + \alpha_s^2\, h_q^{(4)}\left(\lambda, \frac{\mu_R^2}{Q^2}, \frac{\mu_F^2}{Q^2}\right) . \end{aligned} \tag{1.84}$$

This is achieved by fixing λ after the integrations are performed and by expanding the result as a series in α_s. See Chapter 6 for a more detailed derivation up to NNLL. The explicit form of the functions $h_q^{(i)}$ will be given below up to NLL and up NNLL in later Chapters when necessary. The classification of the terms into N^{k}LL depends on the prefactors of the functions $h^{(i)}$ in (1.84). The LL term has a prefactor of $\ln \bar{N}$, the NLL has none and the following terms are multiplied by increasing powers of α_s. Note here we count the logarithms in the exponent which fixes the classification of towers in Fig. 1.12. For example, the NNLL function $h_q^{(3)}$ starts to contribute in the fourth tower but not in the third tower.

Note that for a fixed order expansion as shown in Fig. 1.12, we have double logarithms, *i.e.* two powers of logarithms per α_s: $(\alpha_s \ln^2 \bar{N})^k$. However, in the exponent we have a single logarithmic structure, *i.e.* one logarithm per α_s which can be directly seen from $\lambda \sim \alpha_s \ln \bar{N}$. In principle, each of the functions $h_q^{(i)}$ can be written as a power series in λ. Counting each $h^{(i)}$ as λ^k and including the prefactors, we find the following classification

$$\alpha_s^k \ln^{k+1} \bar{N}, \quad \alpha_s^k \ln^k \bar{N}, \quad \alpha_s^k \ln^{k-1} \bar{N}, \quad \alpha_s^k \ln^{k-2} \bar{N}\,, \tag{1.85}$$

where each term corresponds to the respective term in the sum found for the exponent in Eq. (1.84).

In this Section, we consider DIS up to NLL accuracy. Expanding both exponents in Eq. (1.80), we find [58–63]

$$\begin{aligned} \ln \Delta_q^N &= \ln \bar{N} h_q^{(1)}(\lambda) + h_q^{(2)}\left(\lambda, \frac{Q^2}{\mu_R^2}, \frac{Q^2}{\mu_F^2}\right) , \\ \ln J_q^N &= \ln \bar{N} f_q^{(1)}(\lambda) + f_q^{(2)}\left(\lambda, \frac{Q^2}{\mu_R^2}\right) . \end{aligned} \tag{1.86}$$

The two functions $h_q^{(1)}$, $f_q^{(1)}$ ($h_q^{(2)}$, $f_q^{(2)}$) collect all leading logarithmic (next-to-leading logarithmic) contributions in the exponent of the type $\alpha_s^k \ln^n \bar{N}$ with $n = k+1$ ($n = k+2$). The functions $h^{(1)}$ and

$h^{(2)}$ for Δ_q^N are given by

$$\begin{aligned}
h_q^{(1)}(\lambda) &= \frac{A_q^{(1)}}{2\pi b_0 \lambda}\left[2\lambda + (1-2\lambda)\ln(1-2\lambda)\right], \\
h_q^{(2)}\left(\lambda, \frac{Q^2}{\mu_R^2}, \frac{Q^2}{\mu_F^2}\right) &= -\frac{A_q^{(2)}}{2\pi^2 b_0^2}\left[2\lambda + \ln(1-2\lambda)\right] + \frac{A_q^{(1)} b_1}{2\pi b_0^3}\left[2\lambda + \ln(1-2\lambda) + \frac{1}{2}\ln^2(1-2\lambda)\right] \\
&\quad + \frac{A_q^{(1)}}{2\pi b_0}\left[2\lambda + \ln(1-2\lambda)\right]\ln\frac{Q^2}{\mu_R^2} - \frac{A_q^{(1)}}{\pi b_0}\lambda \ln\frac{Q^2}{\mu_F^2}. \qquad (1.87)
\end{aligned}$$

Here, the b_0, b_1 are the coefficients of the QCD beta function cf. (1.12). The functions $f^{(1)}$ and $f^{(2)}$ for J_q^N are given by

$$\begin{aligned}
f_q^{(1)}(\lambda) &= h_q^{(1)}\left(\frac{\lambda}{2}\right) - h_q^{(1)}(\lambda), \\
f_q^{(2)}\left(\lambda, \frac{Q^2}{\mu_R^2}\right) &= 2h_q^{(2)}\left(\frac{\lambda}{2}, \frac{Q^2}{\mu_R^2}, 1\right) - h_q^{(2)}\left(\lambda, \frac{Q^2}{\mu_R^2}, 1\right) + \frac{B_q^{(1)}}{2\pi b_0}\ln(1-\lambda). \qquad (1.88)
\end{aligned}$$

In the end, we go back to x-space by numerically performing the Mellin inverse, which is given by

$$2F_1^{\mathrm{res}}(x_B, Q^2) = \int_{\mathcal{C}_N} \frac{dN}{2\pi i}\, x_B^{-N} \times \mathcal{C}_{q,\mathrm{res}}^{1,N}\left(\frac{Q^2}{\mu_R^2}, \frac{Q^2}{\mu_F^2}, \alpha_s(\mu_R^2)\right) f^N(\mu^2)\,. \qquad (1.89)$$

The contour $\mathcal{C}_N$ in the complex N plane is taken to run between the rightmost pole of the moments of the PDFs and the Landau pole N_L following the minimal prescription of [64], see Fig. 1.13. In addition, we choose a tilted contour for better numerical convergence. Note that for more involved processes such as single-inclusive deep-inelastic scattering or di-hadron production discussed in subsequent Chapters, we take double Mellin or combined Mellin and Fourier moments respectively. This will make it more difficult to parametrize the appropriate contour in the complex plane. However, the general idea for the inverse transformation using the Minimal Prescription remains the same.

Finally, we match the resummed result to a full fixed order calculation which is still a good approximation further away from threshold. Hence, the most accurate prediction form QCD is obtained by adding both the resummed N$^{\mathrm{k}}$LL result and, in case it is available, the corresponding full N$^{\mathrm{k}}$LO result. In order to avoid double counting of threshold logarithms up to order k, we subtract the $\mathcal{O}(\alpha_s^k)$ expansion of the resummed result:

$$d\sigma^{\mathrm{match}} = \left(d\sigma^{\mathrm{res,\,N^kLL}} - d\sigma^{\mathrm{res,\,N^kLL}}\Big|_{\mathcal{O}(\alpha_s^k)}\right) + d\sigma^{\mathrm{full,\,N^kLO}}\,. \qquad (1.90)$$

Numerical results for DIS and other processes will be presented in subsequent Chapters. In the remaining part of this Chapter, we focus on how the all order threshold resummation may be derived. Due to its complexity, we only focus on giving a rather rough outline of the basic concepts and we

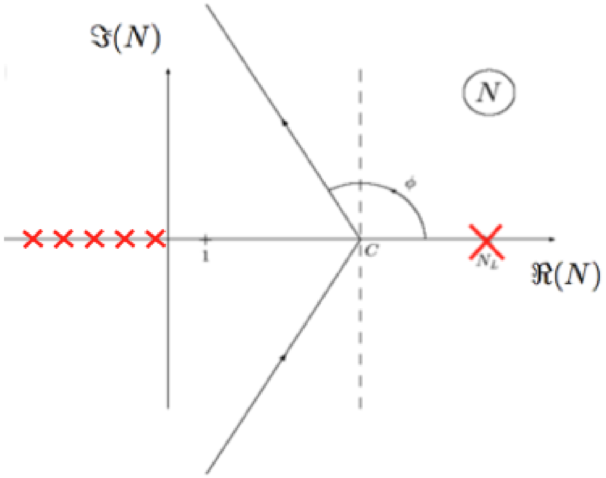

Figure 1.13: Integration contour following the Minimal Prescription of [64]. The red crosses denote poles in the complex N plane.

refer to the literature for further details.

1.4.2 IR structure of QCD

This Section and the following one will only give a brief overview of the basic concepts of resummation. The approach for threshold resummation developed in [7] relies on additional factorization properties of the partonic cross section near threshold. Solving corresponding renormalization group equations leads to the exponentiation of threshold logarithms. As already mentioned, these logarithmic enhancements are directly linked to the IR structure of QCD. Therefore, we first analyze the structure of soft and collinear singularities of scattering amplitudes or Green's functions which will bring us to the Landau equations, power counting techniques and finally will allow us to identify regions of dominant momentum which are directly linked to the additional factorization properties near threshold mentioned above. We roughly follow the discussions outlined in [7, 22, 65–67].

Landau Equations

We consider the complex function G for a Feynman diagram with L loops and I internal lines. The line momenta are labelled by k_i which are functions of the external momenta p_s and the loop momenta l_i

$$G = \prod_{i=1}^{L} \int d^d l_i \; N(k, p_s) \prod_{j=1}^{I} \frac{1}{k_j^2 - m_j^2 + i\varepsilon} \tag{1.91}$$

where $N(k, p_s)$ is some numerator factor containing all relevant prefactors. Introducing I Feynman parameters, we may rewrite G as

$$G = (I-1)! \prod_{j=1}^{I} \int_0^1 d\alpha_j \, \delta(1 - \alpha_1 - \ldots - \alpha_I) \prod_{i=1}^{L} d^d l_i \; N(k, p_s) \; D^{-I} \,, \tag{1.92}$$

where the denominator D is given by

$$D = \sum_{j=1}^{I} \alpha_j \left(k_j^2(l_i, p_s) - m_j^2 \right) + i\varepsilon \,. \tag{1.93}$$

A singularity occurs when the internal lines go on-shell, *i.e.* for $D = 0$. Note that D is quadratic in momenta and linear in Feynman parameters. Due to the "$i\varepsilon$", no l_i^μ contour will go exactly through such a pole. Due to Cauchy's theorem, the contour may be deformed and moved away from the pole. This is the case, unless two poles coalesce and the contour is trapped and cannot be moved around the poles anymore. This situation, where G may develop a singularity, is called a "pinch". Hence, the necessary conditions for a pinch are

$$D = 0 \,, \quad \frac{\partial D}{\partial l_i^\mu} = 0 \quad \forall \, i, \mu \,, \tag{1.94}$$

where the second condition reflects the fact that two poles need to coalesce. In analogy to that, one can find conditions for the α_j. Given the fact that D is linear in α_i, the contour cannot be trapped. However, at the endpoint $\alpha_j = 0$, the contour cannot be moved away. Alternatively, we may have $k_j^2 - m_j^2 = 0$ such that D is independent of α_j. All these conditions are summarized by the Landau equations

$$\begin{aligned} k_j^2 = m_j^2 \quad &\text{or} \quad \alpha_j = 0 \\ \sum_{j \in \text{loop}\, s} &\alpha_j k_j \varepsilon_{js} = 0 \,, \end{aligned} \tag{1.95}$$

where $\varepsilon_{js} = \pm 1$ depending on whether line momentum k_j is flowing in or opposite to the direction of the loop momentum l_s. The standard example is the 1-loop correction to the quark electromagnetic vertex in QCD as shown in Fig. 1.14 a). In this case, we can write the denominator D as

$$D = \alpha_1 l^2 + \alpha_2 (p_1 + l)^2 + \alpha_3 (p_2 - l)^2 + i\varepsilon \,. \tag{1.96}$$

The corresponding (four) Landau equations are given by

$$\alpha_1 l^\mu + \alpha_2 (p_1 + l)^\mu - \alpha_3 (p_2 - l)^\mu = 0 \,. \tag{1.97}$$

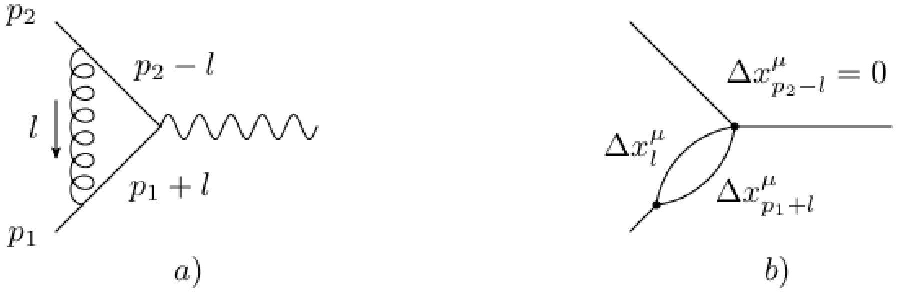

Figure 1.14: a) Electromagnetic vertex at 1-loop order. b) Reduced diagram according to the second line in Eq. (1.98).

In the massless case $p_1^2 = p_2^2 = 0$, there are three solutions

$$\begin{aligned} &l^\mu = 0, \quad \alpha_2 = \alpha_3 = 0 \ ; \\ &l^\mu = -z p_1^\mu, \quad \alpha_3 = 0, \quad \alpha_1 z = \alpha_2(1-z) \ ; \\ &l^\mu = z' p_2^\mu, \quad \alpha_2 = 0, \quad \alpha_1 z' = \alpha_3(1-z') \ , \end{aligned} \tag{1.98}$$

where the first one corresponds to a soft singularity, whereas the second and third are collinear configurations. Note that the double soft and collinear situation is obtained for $z \to 0$ or $z' \to 0$.

Coleman and Norton Picture

Pinch surfaces for higher orders in QCD can be obtained by using the graphical interpretation of the Landau equations by Coleman and Norton [68] which greatly simplifies the analysis. One defines space-time vectors for the terms in the Landau equations $\Delta x_j^\mu = \alpha_j k_j^\mu$. Interpreting the Feynman parameter α_j as the Lorentz invariant ratio $\alpha_j = \Delta x_j^0 / k_j^0$, we obtain

$$\Delta x_j^\mu = \Delta x_j^0 v_j^\mu, \quad \text{where} \quad v_j^\mu = \left(1, \frac{\boldsymbol{k}_j}{k_j^0}\right) . \tag{1.99}$$

Hence, Δx_j^μ may be viewed as a four-vector which describes the free propagation of an on-shell classical particle with momentum k_j^μ. In other words, a direct consequence of the Landau equations is that every singularity is associated with a classical picture of propagation.

Let us see how this works for the simple 1-loop example discussed above. Considering the collinear pinch in the second line of Eq. (1.98), we find

$$\Delta x_l^\mu = \Delta x_{p_1+l}^\mu \, , \quad \Delta x_{p_2-l}^\mu = 0 \, . \tag{1.100}$$

Writing each vertex of the original diagram in Fig. 1.14 a) as a spacetime point separated by the distance Δx_j^μ, we obtain the "reduced" diagram for this collinear pinch. The corresponding diagram is shown in Fig. 1.14 b), where the off-shell line corresponding to $\Delta x_{p_2-l}^\mu = 0$ has been contracted to a point. Note that we suppressed the particle type in the reduced diagram in Fig. 1.14 b), which is the standard convention snce only topological features matter here. Note that what we found here for the 1-loop electromagnetic vertex is completely general. Any IR singularity is described by physical processes of freely moving particles.

IR Power Counting

The Coleman and Norton picture will be an excellent tool to understand the IR structure to all orders. However, it is only a necessary condition for soft and collinear divergencies at a pinch surface. The singularity might still be cancelled by corresponding factors in the numerator. This is where IR power counting comes into play [5, 65]. For each pinch surface in loop momentum space, we will be able to determine the degree of divergence which is in fact very similar to UV power counting. For a given pinch surface, we may separate its coordinates into intrinsic and normal variables. The particular choice of the normal variables depends on the type of pinch. The intrinsic ones only parametrize the surface, whereas the normal variables contain the information about the singularity. In general, it turns out to be convenient to introduce a scaling variable λ according to $\kappa_j = \lambda^{a_j}\kappa'_j$, where the surface is approached for $\lambda \to 0$. In general, the denominators in Eq. (1.91), which correspond to the propagators of the line momenta, are a polynomial in λ, where we only keep the lowest power A_j in λ times some function $f(\kappa'_j, m_j)$, *i.e.*

$$\frac{1}{k_j^2(\kappa_j,\lambda) - m_j^2} \to \frac{1}{\lambda^{A_j} f(\kappa'_j, m_j)} \,. \tag{1.101}$$

The overall degree of divergence for a given pinch surface is obtained by analyzing the corresponding "homogenous integral". It is obtained by introducing normal and intrinsic variables for the volume element and the integrand. The volume element contributes powers B_j in λ and the numerator additional C factors of λ. In summary, we obtain for the homogenous integral [65, 67]

$$\left(\prod_j \int d\kappa'_j \frac{N(\kappa'_j, p_s)}{D(\kappa'_j, m_j)}\right) \lambda^{\sum_j B_j - \sum_j A_j + C} \,, \tag{1.102}$$

where the degree of divergence is given by $n_s = \sum_j B_j - \sum_j A_j + C$. For $n_s = 0$ a logarithmic divergence is obtained, whereas for $n_s > 0$ the result is finite and for $n_s < 0$ a power divergence is obtained.

As an example, we analyze the degree of divergence for the collinear pinch surface shown in Fig. 1.14 b) which corresponds to the second line in Eq. (1.98). We choose the frame $q^\mu = (Q, \vec{0})$, where $(p_1+p_2)^2 = 2p_1\cdot p_2 = Q^2$ and we write $p_{1,2}$ as

$$p_1^\mu = \delta^{\mu +}\frac{Q}{\sqrt{2}}, \qquad p_2^\mu = \delta^{\mu -}\frac{Q}{\sqrt{2}} \,. \tag{1.103}$$

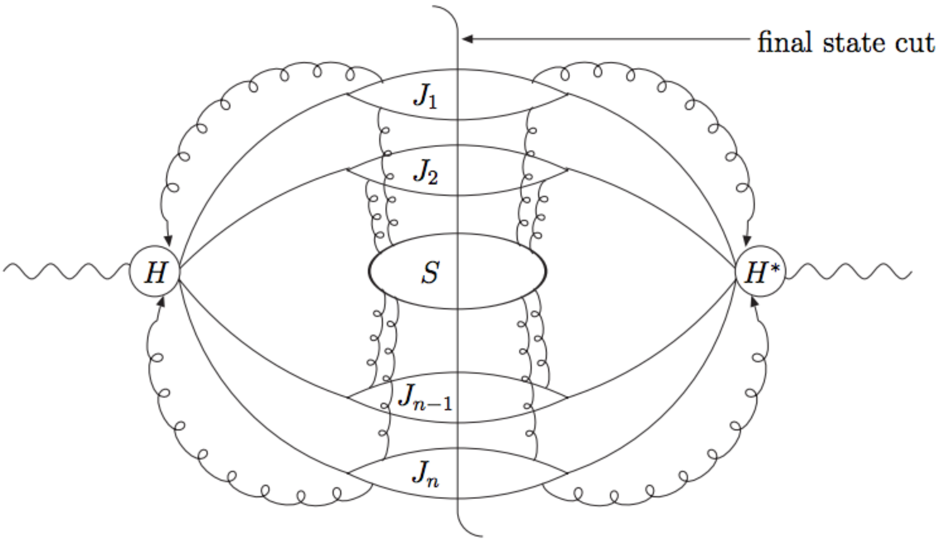

Figure 1.15: Cut diagram illustration of the dominant momentum regions or pinch surfaces for a generic n jet final state originating from the decay of a virtual photon γ^*. Figure taken from [67].

Using light cone coordinates, we may then write the three denominators, cf. Fig. 1.14 a), as

$$\begin{aligned} l^2 &= 2l^+l^- - \boldsymbol{l}_T^2\,, \\ (p_1+l)^2 &= 2p_1^+l^- + 2l^+l^- - \boldsymbol{l}_T^2\,, \\ (p_2-l)^2 &= -2p_2^-l^+ + 2l^+l^- - \boldsymbol{l}_T^2\,. \end{aligned} \tag{1.104}$$

Following the solution in line two of Eq. (1.98), we choose l^-, $\boldsymbol{l}_T^2$ as normal coordinates and l^+, ϕ as intrinsic coordinates, where ϕ is the azimuthal angle in the transverse plane. Hence, using $l^- = \lambda l'^-$ and $\boldsymbol{l}_T^2 = \lambda \boldsymbol{l}'^2_T$, we find the following scaling behaviour

$$l^2 \sim \lambda\,, \qquad (p_1+l)^2 \sim \lambda\,, \qquad (p_1-l)^2 \sim \lambda^0\,. \tag{1.105}$$

In addition, we obtain $d^dl = dl^+dl^-d|\boldsymbol{l}_T||\boldsymbol{l}_T|^{d-3}d\Omega \sim \lambda^{d/2}$. In summary, a logarithmic divergence is obtained as expected with $G \sim \lambda^{d/2-2}$ or equivalently $n_s = 0$. For the soft pinch surface, cf. the first line in Eq. (1.98), one may directly choose the components of the soft momentum $l^\mu = \lambda l'^\mu$ as normal coordinates. Again, a logarithmic divergence is obtained.

Identification of Dominant Momentum Regions

As an example, we consider the decay of a virtual photon γ^* ($Q^2 > 0$) into n jets. For two final state jets this would correspond to the crossed version of the electromagnetic vertex discussed above. According to the picture by Coleman and Norton, we may directly write down the all order structure. All pinch surfaces or reduced diagrams look like the diagram shown in Fig. 1.15. This is called the picture of leading regions or dominant regions of momentum. Here we choose the cut diagram no-

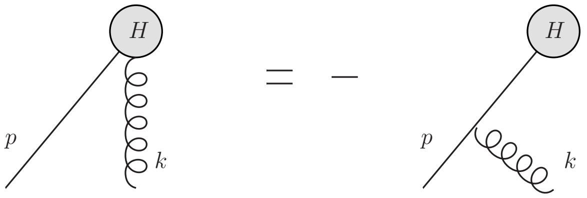

Figure 1.16: Decoupling a single longitudinal collinear gluon from the hard-scattering part using non-abelian Ward identities. Figure adapted from [67].

tation. In principle, it can be obtained by looking for the physical picture. At least, there have to be two jets since $Q^2 > 0$ and $m_{\text{jet}}^2 = 0$. However, in principle there can be n jets $J_{1\ldots n}$ originating from the hard-scattering. The jets represent sets of particles traveling in the same direction. The hard scattering part is shown as H and H^* on the two sides of the final state cut. The Jets fly apart freely at the speed of light thinking in the classical picture of propagation. Therefore, they can never rejoin at a later point. However, the jets can interact with each other by exchanging zero-momentum particles which is generally allowed by the Landau equations. In fact, this can already be seen in from first line of Eq. (1.98) which corresponds to the soft pinch surface at the 1-loop order. The interaction via soft particles is illustrated in Fig. 1.15 by the soft ellipse S in the middle and its attachments to the jets which can be realized in all possible ways. These lines have momenta that vanish at the pinch surface in all four components. A priori, the jets can have multiple attachments to the hard-scattering part which for better readability is only shown for the jets $J_{1,n}$.

There are many lessons to be learnt from IR power counting here. In principle, it works exactly along the lines discussed above. However, the extension to higher orders involves a lot of bookkeeping [65, 67]. Therefore, we only summarize its main results here. One finds only logarithmic divergences which corresponds to $n_s \geq 0$ in Eq. (1.102). The regions of jets and the soft function are only connected by soft gluons but not by soft fermions. There is no direct line connecting the hard-scattering function with the soft function. And as already found within the Coleman and Norton picture, all jets must originate directly from the hard-scattering vertex.

Thus, we were able to deduce the generic structure for the pinch surfaces to all orders. In the following, we briefly discuss the basic concepts of how to decouple J from H and J from S. It will be possible to obtain a factorized form with only scalar functions with one function for each of the pinch surfaces in Fig. 1.15. Afterwards, we move on to discuss a more complicated process which is single-inclusive hadron production in hadronic collisions.

Decoupling J from H

In axial gauge the Jets J_i and the hard-scattering function H are only connected by a single line. However, in Feynman gauge one needs to consider multiple attachments by longitudinal collinear gluons. The situation of a single additional gluon which is attached to H is shown on the left hand side of Fig. 1.16. Making use of non-abelian QCD Ward identities, we can relate it to the diagram shown on the right hand side of Fig. 1.16. Following [65, 69], the sum over all attachments has to vanish.

Therefore, the two diagrams shown in Fig. 1.16 are the same up to a minus sign. We choose the quark to be moving in the "+" direction. Using Feynman rules and omitting color factors, we obtain the following expression

$$g_s H \frac{\not{p}+\not{k}}{(p+k)^2}\gamma^\alpha\, u(p)\, \varepsilon^\beta(k)\, g_{\alpha\beta}\,, \tag{1.106}$$

where the polarization vector of the longitudinal gluon is given by $\varepsilon^\beta = (\varepsilon^+, 0^-, \mathbf{0}_T)$. We define a vector pointing into the opposite direction of the quark momentum $v^\alpha = (0^+, 1^-, \mathbf{0}_T)$. We can rewrite (1.106) as

$$\begin{aligned} g_s H \frac{\not{p}+\not{k}}{(p+k)^2}\gamma^-\, u(p)\, \varepsilon^+ \frac{k^+}{k^+} &= g_s H \frac{\not{p}+\not{k}}{(p+k)^2}\not{k}\, u(p) \frac{\varepsilon\cdot v}{k\cdot v} \\ &= g_s H\, u(p) \frac{\varepsilon\cdot v}{k\cdot v}\,, \end{aligned} \tag{1.107}$$

where in the last equality, we wrote $\not{k} = \not{p}+\not{k}-\not{p}$ and we made use of the massless Dirac equation $\not{p}u(p) = 0$.

Hence, we found a decoupling of J and H at the level of a single gluon. Applying Ward identities at higher orders leads to an increasing level of complexity. However, the same techniques are applicable and eventually one obtains a Wilson line taking into account multiple longitudinal and collinear gluons.

Decoupling J from S

So far, the jets and the soft function still couple to each other with a non trivial Lorentz index structure

$$J_1^{\mu_1\dots\mu_k} J_2^{\nu_1\dots\nu_l} \dots J_n^{\rho_1\dots\rho_m} S_{\mu_1\dots\mu_k\nu_1\dots\nu_l\,\dots\,\rho_1\dots\rho_m}\,. \tag{1.108}$$

A factorization in terms of scalar functions is obtained in the following way, where again we choose to present only the basic concepts. In addition, one finds that only one momentum component and one polarization state are relevant. In Fig. 1.17, a fast moving particle with momentum $p = (p^+, 0^-, \mathbf{0}_T)$ is shown which is part of a jet. Note that in Fig. 1.17 we are omitted the particle type for the solid lines. After splitting into two particles, the two particles have again a large + momentum component. For the lower particle we have $l^+ = xp^+$. The soft gluon with momentum k^μ is coupling to the jet. Firstly, we note that only the k^- component matters for the propagator of the jet line after the gluon is attached

$$\frac{1}{(l+k)^2} \approx \frac{1}{2xp^+k^- + l^2}\,. \tag{1.109}$$

Secondly, we note that the coupling of the soft gluon to the jet may be expressed as $N_{\mu\nu}/(k^2+i\varepsilon)$ ($N_{\mu\nu}$ is given in Eq. (1.9)), multiplied with the jet for which we write $J^\mu(p)$ here. For the jet only the large "+" component of p^μ matters because all momenta of the particles inside the jet are basically collinear to p^+. We define the two vectors $u^\mu = (1^+, 0^-, \mathbf{0}_T)$ and $v^\mu = (0^+, 1^-, \mathbf{0}_T)$ that point in opposite directions. One finds for the coupling of the soft gluon to the jet

$$J^\mu(p) N_{\mu\nu}(k) = \left(J(p)\cdot v\right)\left(u^\mu N_{\mu\nu}(k)\right)\,. \tag{1.110}$$

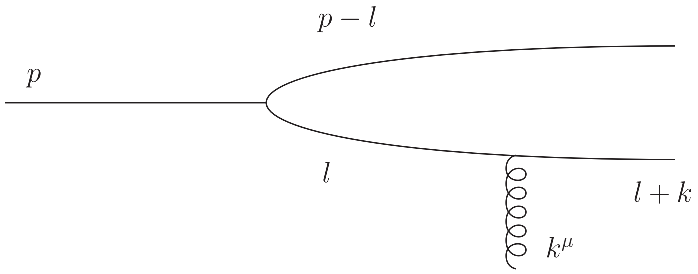

Figure 1.17: Coupling of a soft gluon to a particle inside the jet.

This leads directly to the factorization into separate scalar functions. We leave out the details of how this can be extended to higher orders.

To summarize this Section, we note that in the end, we obtain a factorization into scalar functions: a soft function, the hard function and n jet functions. Most of these concepts were originally developed for the proof of QCD factorization theorems [4, 5, 70]. This would bring us back to the concept of IR safe observables as discussed above. See for example [66, 67] for an introduction. However, here we are interested in the resummation of threshold logarithms which to some extent comes as a by product after a factorized form is obtained following the concept of leading regions or pinch surfaces.

1.4.3 Resummation for Single-Inclusive Hadron Production

We consider the single-inclusive process $H_1H_2 \to hX$ at large transverse momentum of the final state observed hadron. This process will be discussed further in Chapter 6. It is one example, where at LO we have four colored partons taking part in the scattering. Other examples of resummation for QCD hard scattering are di-hadron production and single-inclusive jet production in hadronic collisions which will be discussed in Chapters 5 and 7 respectively. Before we continue to investigate threshold resummation, we briefly introduce the concept of hadronic scattering in pQCD and fragmentation functions.

Hadronic Scattering and Fragmentation Functions

Proton-proton collisions with one identified hadron in the final state are described in pQCD in the following way. For the two incoming protons, we need to include two PDFs. The final state hadronization (parton-to-hadron) is also non-perturbative and it is described by a fragmentation function $D_c^h(z_c, \mu_F^2)$. The fragmentation function depends on the fraction of the parton's momentum transferred to the hadron and the (final state) factorization scale μ_F. Analogously to the discussion for PDFs in Section 1.3.2, FFs absorb final state collinear singularities obtained in perturbative calculations. Similar to the PDFs, fragmentation functions have to be obtained from data [71–76]. For example, the DSS global NLO analysis of FFs in [72] involves data for single-inclusive hadron production in SIA, SIDIS and pp collisions. Analogously to the DGLAP evolution equations discussed in Section 1.3.3, pQCD predicts the scale evolution of FFs allowing predictions within pQCD once the FFs are determined. In summary, the cross section for the single-inclusive production of hadrons in hadronic collisions can be

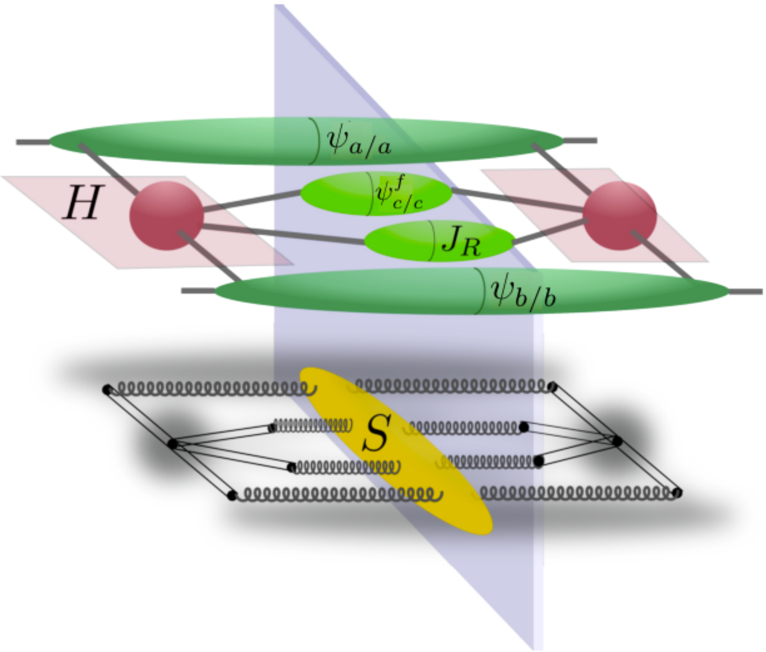

Figure 1.18: Refactorized cross section near threshold for single-inclusive hadron production. Figure taken from [22, 77].

written as

$$\frac{E\, d^3\sigma^{H_1H_2\to hX}}{d^3P_c} = \sum_{abcd} \int dx_a\, dx_b\, dz_c\, f_a^{H_1}(x_a,\mu_F^2)\, f_b^{H_2}(x_b,\mu_F^2)\, D_c^{h_1}(z_c,\mu_F^2) \frac{E\, d^3\hat{\sigma}^{ab\to cd}}{d^3P_c}\,, \tag{1.111}$$

where the $d\hat{\sigma}^{ab\to cd}$ denote the partonic cross sections that can be calculated perturbatively in QCD.

Refactorization near Threshold

We consider the process $H_1(P_a)H_2(P_b) \to h_1(P_c)X$. We define the usual Mandelstam variables

$$S = (P_a+P_b)^2\,, \qquad T = (P_a-P_c)^2\,, \qquad U = (P_b-P_c)^2\,. \tag{1.112}$$

In addition, we define the invariant mass squared of the system recoiling against the observed hadron $S_4 = S+T+U$. Analogously, we define the momenta at the parton level $a(p_a)b(p_b) \to c(p_c)X$ which are related to the hadronic ones via $p_{a,b} = x_{a,b}P_{a,b}$ and $p_c = P_c/z_c$ and we have $s_4 = s+t+u$. The partonic threshold, where all the available energy is used to produced the observed final state parton, is set by $s_4 = 0$. In the perturbative expansion of the partonic cross sections $d\hat{\sigma}^{ab\to cd}$, we obtain threshold logarithms of the form $\alpha_s^k(\ln^n(z)/z)$ with $n \le 2k-1$ and $z = s_4/s$, see also Sections 6 and 7. Following the discussion in the previous Section 1.4.2, we may directly obtain a refactorized version of the cross section near threshold. Following the method of identifying dominant momentum regions, we obtain the structure shown in Fig. 1.18. The plane in the middle symbolizes the final state cut separating the amplitude and its complex conjugate. The function $H_{ab\to cd}$ is given by the hard-scattering amplitude h_I and its complex conjugate h_J^* which contains momentum configurations that are far off shell. The indices I, J refer to a certain color basis. Collinear and soft dynamics of gluon emissions associated with the incoming partons a, b and the outgoing observed parton c are summarized in the jet functions $\psi_{a/a}$, $\psi_{b/b}$ and $\psi^f_{c/c}$ respectively. The jet function J_R for the unobserved final state parton is associated with collinear gluon emissions in the direction of the recoiling jet. Finally, the soft function $S_{ab\to cd}$ takes into account the emission of soft gluons. We denote the total momentum of soft gluons by k_S. As can be seen from Fig. 1.18, the soft function can be separated completely from the rest. Both the hard-scattering function $H_{ab\to cd}$ and the soft function $S_{ab\to cd}$ are matrices in color space [78–83] which is a characteristic feature of processes where four colored partons are taking part in the LO scattering process. The structure of the refactorized cross section here is a direct consequence of the concepts discussed in the previous Section 1.4.2.

We continue by analyzing the kinematics of the underlying parton level process in order to find a decomposition that matches the refactorized cross section discussed above. We introduce the vector $\hat{p}_R$ which denotes the momentum of the recoiling jet at threshold. In the c.m.s, we define the dimensionless vector ζ^μ as $\hat{p}^\mu_R = (p_c, -\boldsymbol{p}_c) \equiv \sqrt{S}\zeta^\mu$ which will be used for the kinematical analysis in Eq. (1.113) below. Momentum conservation implies $x_a p_a + x_b p_b = p_c/z_c + p_R + k_S$, where p_R is the momentum recoiling against the observed parton and k_S denotes any soft radiation. By squaring this relation and omitting corrections of the order S_4^2, we obtain the following relations near threshold [84]

$$\begin{aligned} S_4 &= (1-x_a)2p_a\cdot\hat{p}_R + (1-x_b)2p_b\cdot\hat{p}_R + 2k_S\cdot\hat{p}_R + p_R^2 + p_c^2 z_c^2 \\ &= \left[(1-x_a)\left(\frac{u}{t+u}\right) + (1-x_b)\left(\frac{t}{t+u}\right) + \frac{s_4}{S}\right] S \\ &\equiv \left[w_a\left(\frac{u}{t+u}\right) + w_b\left(\frac{t}{t+u}\right) + w_S + w_R + w_c\right] S\,, \end{aligned} \tag{1.113}$$

where each term in the first line may be identified with one of the functions shown in Fig. 1.18. In the third line, we define dimensionless weights w_i measuring the contribution of the various functions shown in Fig. 1.18 [85]. The weights are additive and vanish at threshold. The refactorized cross section may be written as [84, 85]

$$\begin{aligned} \frac{E_p\, d\sigma_{ab\to cX}}{d^3p} &= \mathrm{Tr}\Bigg\{H_{ab\to cd}(t,u)\int dw_a dw_b dw_S dw_R dw_c \\ &\times\ \delta\left(\frac{S_4}{S} - w_a\left(\frac{u}{t+u}\right) - w_b\left(\frac{t}{t+u}\right) - w_S - w_R - w_c\right) \\ &\times\ \psi_{a/a}(w_a,p_a,\zeta,n)\,\psi_{b/b}(w_b,p_b,\zeta,n)\,\psi^f_{c/c}(w_c,p_c,\zeta,n) \\ &\times\ J^{(d)}(w_R,p_R,\zeta,n)\,S_{ab\to cd}\left(\frac{Sw_S}{\mu^2},\beta_i,\zeta,n\right)\Bigg\}\,, \end{aligned} \tag{1.114}$$

where the kinematical constraint in Eq. (1.113) was taken into account by the delta function. The various functions are evaluated in axial $n\cdot A = 0$, see the discussion in Section 1.4.2. The soft function also depends on the four-velocities β^μ_i of the partons which are defined by $p^\mu_i = \beta^\mu_i\sqrt{s/2}$. Note that the functions $\psi_{a/a}$ also have an operator definition similar to the one for the light cone parton-in-parton distribution functions $\phi_{a/a}$ in Eq. (B.1), see [7, 22, 46, 84]. Also the soft function has an operator definition which is discussed further in the Appendix D in the context of di-hadron production.

We modify the cross section in Eq. (1.111) in the following way. Similarly to the discussion in Section 1.3.2, we replace the initial and final state hadrons with partons and calculate the partonic cross section in IR-regulated perturbation theory. We denote the corresponding diagonal parton-in-parton PDFs (and FFs) by $\phi_{a/a}$, $\phi_{b/b}$ and $\phi^f_{c/c}$. As usual, we derive the all order resummation of threshold logarithms in Mellin moment space where the convolution structure in Eq. (1.114) gets transformed into simple products and the threshold logarithms are then given by $\alpha_s^k \ln^n \bar{N}$ with $n \leq 2k$. Comparing the cross section written with external partons and the refactorized cross section in Eq. (1.114), we find [84]

$$\begin{aligned} \tilde{\Omega}_{abcd}\left(N, \frac{t}{\mu^2}, \frac{u}{\mu^2}, \alpha_s(\mu^2)\right) &= \frac{\tilde{\psi}_{a/a}(N\frac{u}{t+u}, p_a \cdot \zeta)}{\tilde{\phi}_{a/a}(N\frac{u}{t+u}, \mu^2)} \frac{\tilde{\psi}_{b/b}(N\frac{t}{t+u}, p_b \cdot \zeta)}{\tilde{\phi}_{b/b}(N\frac{t}{t+u}, \mu^2)} \frac{\tilde{\psi}^f_{c/c}(N, p_c \cdot \zeta)}{\tilde{\phi}^f_{c/c}(N, \mu^2)} J^{(d)}(N, p_R \cdot n) \\ &\times \widetilde{\mathrm{Tr}}\left\{H(t,u)\, \tilde{S}\left(\frac{S}{N\mu^2}, \beta_i, \zeta, n\right)\right\}_{ab\to cd}, \end{aligned} \tag{1.115}$$

with scale μ and where the tildes indicate that we are considering moment space functions here and $\tilde{\Omega}_{abcd}$ is the perturbative hard-scattering part in Mellin space. This form holds up to corrections of the order $\mathcal{O}(1/N)$. Note the kinematical factors $u/(t+u)$ and $t/(t+u)$ which are a characteristic feature of the single-inclusive kinematics and reflect the kinematical constraint found in Eq. (1.113).

Exponentiation

In the next step, we have to solve evolution equations for each of the functions that appear in Eq. (1.115) which eventually leads to the resummation of threshold logarithms [7, 66]. Each of the ratios $\tilde{\psi}/\tilde{\phi}$ leads to factor of Δ^N which is the same exponential as in Section 1.4.1 where it was found for the observed initial state parton in DIS. Here, the Δ^N for the two initial state partons have to be evaluated for $N_a = N(-u/s)$ and $N_b = N(-t/s)$. Similarly, the function $\tilde{J}^{(d)}$ leads to the same exponential in the resummed formula which we also found for the unobserved final state parton in DIS. As an example, we discuss the evolution equations for the soft function before we present the final resummed result. We write the soft function as $S^{(f)}_{LI}$ and hard function as $H^{(f)}_{IL}$ where we write the color indices IL explicitly and the superscript refers to a parton of flavor f. The soft function is defined such that collinear divergences are absent, cf. the definition of the soft function given in the Appendix D. However, UV divergences due to virtual corrections still need renormalization. Both the hard function and the soft function are renormalized multiplicatively, where we need to take into account that they are matrices in color space [78, 80, 81, 86]

$$\begin{aligned} H^{(f)(B)}_{IL} &= \prod_{i=a,b,c,d} Z_i^{-1} \left(Z_S^{(f)^{-1}}\right)_{IC} H^{(f)}_{CD} \left[\left(Z_S^{(f)\dagger}\right)^{-1}\right]_{DL}, \\ S^{(f)(B)}_{LI} &= \left(Z_S^{(f)\dagger}\right)_{LB} S^{(f)}_{BA} \left(Z_S^{(f)}\right)_{AI}. \end{aligned} \tag{1.116}$$

The Z_i are the renormalization constants of the parton's wave functions and $(Z_S^{(f)})_{IC}$ is a matrix of renormalization constants associated with the soft function. The superscript B on the left side of Eq. (1.116) denotes the bare, *i.e.* unrenormalized functions. From here the renormalization group equation for the soft function may be derived [80, 81]

$$\mu_R^2 \frac{d}{d\mu_R^2} S^{(f)}_{LI} = \left(\mu_R^2 \frac{\partial}{\partial \mu_R^2} + \beta(\alpha_s) \frac{\partial}{\partial \alpha_s}\right) S^{(f)}_{LI} = -\left(\Gamma_S^{(f)}\right)^{\dagger}_{LB} S^{(f)}_{BI} - S^{(f)}_{LA} \left(\Gamma_S^{(f)}\right)_{AI} . \tag{1.117}$$

The matrices $(\Gamma_S^{(f)})_{LB}$ are the so-called soft anomalous dimension matrices which have to be calculated for every partonic process separately. They are obtained from the matrix of renormalization constants of the soft function $(Z_S^{(f)})_{IC}$. Working in dimensional regularization in the $\overline{\text{MS}}$ scheme, one obtains UV poles in the matrix $(Z_S^{(f)})_{IC}$. Hence, the soft anomalous dimension matrices are obtained by taking the residue

$$\left(\Gamma_S^{(f)}\right)_{LI}(g_s) = -\frac{g_s}{2} \frac{\partial}{\partial g_s} \mathrm{Res}_{\varepsilon \to 0} \left(Z_S^{(f)}\right)_{LI}(g_s, \varepsilon) . \tag{1.118}$$

A detailed calculation of the one loop soft anomalous dimension matrices can be found in [22]. Finally, we may solve Eq. (1.117) and we end up with the final result for the resummed cross section [77–82, 84, 87]

$$\begin{aligned}
\tilde{\Omega}^{\text{res}}_{abcd}\left(v, N, \alpha_s(\mu_R^2), \frac{\mu_R^2}{s}, \frac{\mu_F^2}{s}\right) \quad = \quad & \xi_R\left(\alpha_s(\mu_R^2), \frac{\mu_R^2}{s}\right) \xi_F^{abc}\left(\alpha_s(\mu_R^2), \frac{\mu_R^2}{s}, \frac{\mu_F^2}{s}\right) \\
\times \Delta_a^{N_a}\left(\alpha_s(\mu_R^2), \frac{\mu_R^2}{s}, \frac{\mu_F^2}{s}\right) & \Delta_b^{N_b}\left(\alpha_s(\mu_R^2), \frac{\mu_F^2}{s}, \frac{\mu_R^2}{s}\right) \Delta_c^{N}\left(\alpha_s(\mu_R^2), \frac{\mu_R^2}{s}, \frac{\mu_F^2}{s}\right) J_d^N\left(\alpha_s(\mu_R^2), \frac{\mu_R^2}{s}\right) \\
\times \mathrm{Tr}\left\{ H\left(v, \alpha_s(\mu_R^2)\right) \mathcal{S}_N^{\dagger}\left(v, \alpha_s(\mu_R^2), \frac{\mu_R^2}{s}\right) \right. & \left. S\left(\alpha_s(s/\bar{N}^2), v\right) \mathcal{S}_N\left(v, \alpha_s(\mu_R^2), \frac{\mu_R^2}{s}\right) \right\}_{ab \to cd} ,
\end{aligned} \tag{1.119}$$

where we now use the variable v defined as $t = -s(1-v)$, $u = -sv$ and we explicitly distinguish between factorization and renormalization scales μ_F and μ_R respectively. The additional matrices $\mathcal{S}_N$ and $\mathcal{S}_N^{\dagger}$ inside the trace in color space are obtained when solving the renormalization group equation for the soft function in Eq. (1.117). They are given by

$$\mathcal{S}_N\left(v, \alpha_s(\mu_R^2), \frac{\mu_R^2}{s}\right) = \mathcal{P} \exp\left[\frac{1}{2} \int_s^{s/\bar{N}^2} \frac{d\mu^2}{\mu^2} \Gamma_{ab \to cd}(v, \alpha_s(\mu^2))\right] , \tag{1.120}$$

where the soft anomalous dimension matrices appear in the exponent and $\mathcal{P}$ denotes path ordering. Note that the second line in (1.119) directly corresponds to the first line in Eq. (1.115). See Chapter 6 for an explicit evaluation of the hard-scattering function H and the soft function S up to NLO. In addition, we will expand the exponentials Δ^N, J^N and the additional functions $\xi_{R,F}$ explicitly up to NNLL accuracy.

CHAPTER 2

QCD RESUMMATION FOR SEMI-INCLUSIVE HADRON PRODUCTION PROCESSES

We investigate the resummation of large logarithmic perturbative corrections to hadron production in electron-positron annihilation and semi-inclusive deep-inelastic scattering. We find modest, but significant, enhancements of hadron multiplicities in the kinematic regimes accessible in present high-precision experiments. Our results are therefore relevant for the determination of hadron fragmentation functions from data for these processes. This Chapter is based on publications [i] and [x].

2.1 Introduction

Processes with identified final-state hadrons play important roles in QCD. Foremost, they provide crucial information on fragmentation functions and hence, ultimately, the hadronization mechanism. Modern analyses [71, 73–75, 88] of fragmentation functions variously use data for single-inclusive annihilation $e^+e^- \to hX$, semi-inclusive deep-inelastic scattering, $\ell p \to \ell hX$, and $pp \to hX$, where h denotes a final-state hadron. Hadron production observables also serve as powerful probes of nucleon or nuclear structure. In particular, SIDIS measurements with polarized beams and/or targets have by now become indispensable tools for investigations of the spin structure of the nucleon in terms of helicity parton distribution functions and transverse-momentum dependent distributions [89]. Finally, hadron production data also test some of our key concepts in the theoretical analysis of QCD at high energies, among them factorization, universality, and perturbative calculations.

In the present chapter, we address higher-order perturbative corrections to two of the key hadron production processes, SIA $e^+e^- \to hX$ and SIDIS $\ell p \to \ell hX$. Our study is very much motivated by the recent advent of data for these reactions with unprecedented high precision. The BELLE collaboration at KEK has presented preliminary data [90] for pion and kaon multiplicities in SIA that extend over a wide range in values of the fragmentation variable $x_E = 2E^h/\sqrt{s}$, where E^h is the energy of the produced hadron in the e^+e^- center-of-mass system, and $\sqrt{s} = 10.52$ GeV the collision energy. The BELLE data cover the region $0.2 \leq x_E \leq 0.97$, with a very fine binning and extremely high precision partly at the sub-1% level. New preliminary high-statistics SIDIS data have been shown by the HERMES [91] and COMPASS [92] collaborations over the past year or so.

In the kinematic regimes accessed by these experiments, perturbative-QCD corrections are expected to be fairly significant. In case of $e^+e^- \to hX$ at BELLE, as x_E increases toward unity, the phase space for real-gluon radiation is very restricted, since most of the initial leptonic energy is used to produce the observed hadron and a recoiling unobserved final state. When this happens, the infrared cancellations between virtual and real-emission diagrams leave behind large logarithmic higher-order corrections to the basic $e^+e^- \to q\bar{q}$ cross section. These logarithms are very similar in nature to the "threshold logarithms" encountered in hadronic scattering processes when the energy of initial partons is just large enough to produce a given final state. Near $x_E = 1$, it then becomes necessary to take the large corrections into account to all orders in the strong coupling, a technique known as threshold resummation. The SIDIS measurements, on the other hand, are characterized by two scaling variables, Bjorken-x and a variable z given by the energy of the produced hadron over the energy of the virtual photon in the target rest frame. The cross section is typically defined to be differential in both. Large logarithmic corrections to the SIDIS cross section arise when either one of the corresponding partonic variables becomes large. The most important effects arise when both are large, which is typically the case for the presently relevant fixed-target kinematics. As we shall discuss, in this case the logarithmic terms can be simultaneously resummed to all orders within the threshold resummation framework.

Previous work [93] has established a close correspondence between threshold resummation for the Drell-Yan process, double-inclusive annihilation $e^+e^- \to h_1h_2X$, and a variant of SIDIS for which one considers the cross section differential in the *product* xz of the two scaling variables mentioned above, rather than in each of them separately. For this set of observables, the structure of the threshold logarithms turns out to be identical, up to trivial differences in the hard scattering functions that multiply the logarithms. One therefore can derive the resummation for each of the processes in the same manner, using exponentiation of eikonal diagrams in color-singlet processes [6, 94–98]. This approach was termed *crossed threshold resummation* in [93] and will be the framework for our present analysis of SIDIS.

Resummation for $e^+e^- \to hX$ was addressed in detail in Refs. [99–102]. In [99] the next-to-leading logarithm (NLL) expressions were presented, while extensions to next-to-next-to-leading logarithm and even next-to-next-to-next-to-leading logarithm were provided in Refs. [100] and [101], respectively. The global analysis of fragmentation functions of Ref. [73] in fact includes NLL threshold resummation effects for $e^+e^- \to hX$ for the lower-energy data. They are found to improve the theoretical description and the quality of the fit to the data. Given the very high precision of the new BELLE data, a new phenomenological analysis of resummation effects is now timely and will be presented in this work. For now, we will restrict ourselves to resummation at NLL, which captures the main effects. As for SIDIS, an expression for the NLL resummed cross section was stated in [99], which turns out to be analogous to the related expressions for the rapidity-differential Drell-Yan cross section in terms of double-Mellin moments (see also [8, 103]). Phenomenological studies of resummation effects in SIDIS have never really been presented in the literature, except briefly in [104]. In the present chapter, we derive the NLL resummed expression for SIDIS, making use of the techniques of [93]. We also present numerical results as relevant for comparisons to the recent SIDIS data.

Sections 2.2 and 2.3 collect our technical derivations. Since the resummation for SIDIS is the main new result, we mostly focus on this process and only briefly review the well-known results for $e^+e^- \to hX$ and inclusive deep-inelastic scattering (DIS). Section 2.4 presents our phenomenological results.

2.2 Resummation for SIDIS multiplicities

We consider semi-inclusive deep-inelastic scattering, $\ell(k)p(P) \to \ell(k')h(P_h)X$, where we have indicated the momenta of the involved particles. The momentum q of the highly virtual photon exchanged between the incoming electron and proton is given by $q = k - k'$. We define the usual variables

$$\begin{aligned} Q^2 &\equiv -q^2 = -(k-k')^2, \qquad & x \equiv \frac{Q^2}{2P\cdot q}, \\ y &\equiv \frac{P\cdot q}{P\cdot k}, \qquad & z \equiv \frac{P\cdot P_h}{P\cdot q}. \end{aligned} \tag{2.1}$$

We have $Q^2 = xys$, with $\sqrt{s}$ the ℓp center-of-mass energy. In the current fragmentation region that we will consider here, the SIDIS cross section may be written as [51, 51, 105–109]:

$$\frac{d^3\sigma^h}{dxdydz} = \frac{4\pi\alpha^2}{Q^2}\left[\frac{1+(1-y)^2}{2y}\mathcal{F}_T^h(x,z,Q^2) + \frac{1-y}{y}\mathcal{F}_L^h(x,z,Q^2)\right], \tag{2.2}$$

where α is the fine structure constant. $\mathcal{F}_T^h$ and $\mathcal{F}_L^h$ are the transverse and the longitudinal structure functions; they are related to the more customary structure functions F_1^h and F_L^h by $\mathcal{F}_T^h \equiv 2F_1^h$ and $\mathcal{F}_L^h \equiv F_L^h/x$.

SIDIS hadron multiplicities are defined by

$$R^h_{\text{SIDIS}} \equiv \frac{d^3\sigma^h/dxdydz}{d^2\sigma/dxdy}, \tag{2.3}$$

where $d^2\sigma/dxdy$ is the cross section for inclusive DIS, $\ell p \to \ell X$, given by

$$\frac{d^2\sigma}{dxdy} = \frac{4\pi\alpha^2}{Q^2}\left[\frac{1+(1-y)^2}{2y}\mathcal{F}_T(x,Q^2) + \frac{1-y}{y}\mathcal{F}_L(x,Q^2)\right]. \tag{2.4}$$

Here $\mathcal{F}_T \equiv 2F_1$ and $\mathcal{F}_L \equiv F_L/x$, with the standard inclusive structure functions F_1, F_L. Usually, the numerator and denominator of (2.3) are averaged over suitable bins in x and y. In order to investigate higher-order effects on SIDIS multiplicities, we have to consider QCD corrections to both the SIDIS and the inclusive DIS cross section. Since the latter has been treated very extensively in the literature, we will focus here on $d^3\sigma^h/dxdydz$ and only briefly summarize some of the known results for $d^2\sigma/dxdy$.

2.2.1 SIDIS cross section at next-to-leading order, and Mellin moments

Using factorization, the transverse and longitudinal structure functions $\mathcal{F}_T^h \equiv 2F_1^h$ and $\mathcal{F}_L^h \equiv F_L^h/x$ in (2.2) are given by $(i = T, L)$

$$\mathcal{F}_i^h(x,z,Q^2) \;=\; \sum_{f,f'} \int_x^1 \frac{d\hat{x}}{\hat{x}} \int_z^1 \frac{d\hat{z}}{\hat{z}} f\left(\frac{x}{\hat{x}},\mu^2\right) D_{f'}^h\left(\frac{z}{\hat{z}},\mu^2\right) \times \mathcal{C}_{f'f}^i\left(\hat{x},\hat{z},\frac{Q^2}{\mu^2},\alpha_s(\mu^2)\right), \quad (2.5)$$

where $f(\xi,\mu^2)$ denotes the distribution of parton $f = q,\bar{q},g$ in the nucleon at momentum fraction ξ and scale μ, while $D_{f'}^h\left(\zeta,\mu^2\right)$ is the corresponding fragmentation function for parton f' going to the observed hadron h. For simplicity, we have set all factorization and renormalization scales equal and collectively denoted them by μ. The hard-scattering coefficient functions $\mathcal{C}_{f'f}^i$ can be computed in perturbation theory:

$$\mathcal{C}_{f'f}^i \;=\; C_{f'f}^{i,(0)} + \frac{\alpha_s(\mu^2)}{2\pi} C_{f'f}^{i,(1)} + \mathcal{O}(\alpha_s^2), \quad (2.6)$$

where, again, $i = T, L$. To lowest order (LO), only the process $\gamma^* q \to q$ contributes, and we have

$$\begin{aligned} C_{qq}^{T,(0)}(\hat{x},\hat{z}) &= e_q^2\,\delta(1-\hat{x})\delta(1-\hat{z}), \\ C_{qq}^{L,(0)}(\hat{x},\hat{z}) &= 0, \end{aligned} \quad (2.7)$$

with the quark's fractional charge e_q. Beyond LO, also gluons in the initial or final state contribute. The full set of the first-order coefficient functions [51, 105–109] $C_{f'f}^{i,(1)}$ are collected in Appendix C.

Since threshold resummation can be derived in Mellin-moment space, it is useful to take Mellin moments of the structure functions $\mathcal{F}_T^h$ and $\mathcal{F}_L^h$. Since x and z are independent variables, we take moments separately in both [105, 110]. We define

$$\tilde{\mathcal{F}}_i^h(N,M,Q^2) \equiv \int_0^1 dx\, x^{N-1} \int_0^1 dz\, z^{M-1}\, \mathcal{F}_i^h(x,z,Q^2). \quad (2.8)$$

We then readily find from (2.5)

$$\tilde{\mathcal{F}}_i^h(N,M,Q^2) \;=\; \sum_{f,f'} \tilde{f}^N(\mu^2) \tilde{D}_{f'}^{h,M}(\mu^2) \times \tilde{\mathcal{C}}_{f'f}^i\left(N,M,\frac{Q^2}{\mu^2},\alpha_s(\mu^2)\right), \quad (2.9)$$

where

$$\begin{aligned} &\tilde{f}^N(\mu^2) \equiv \int_0^1 dx\, x^{N-1} f(x,\mu^2), \\ &\tilde{D}_{f'}^{h,M}(\mu^2) \equiv \int_0^1 dz\, z^{M-1} D_{f'}^h(z,\mu^2), \\ &\tilde{\mathcal{C}}_{f'f}^i\left(N,M,\frac{Q^2}{\mu^2},\alpha_s(\mu^2)\right) \equiv \int_0^1 d\hat{x}\, \hat{x}^{N-1} \int_0^1 d\hat{z}\, \hat{z}^{M-1}\, \mathcal{C}_{f'f}^i\left(\hat{x},\hat{z},\frac{Q^2}{\mu^2},\alpha_s(\mu^2)\right) \end{aligned} \quad (2.10)$$

Thus, the Mellin moments of the structure functions are obtained from ordinary products of the moments of the parton distribution functions and fragmentation functions, and double-Mellin moments of the partonic hard-scattering functions. For the perturbative expansion given in (3.5), we have for the latter in lowest oder according to (2.7):

$$\begin{aligned}\tilde{C}_{qq}^{T,(0)}(N,M) &= e_q^2, \\ \tilde{C}_{qq}^{L,(0)}(N,M) &= 0. \end{aligned} \tag{2.11}$$

The corresponding moments of the next-to-leading order (NLO) terms $C_{f'f}^{i,(1)}$ [110] are also provided in Appendix C.

2.2.2 Resummation of the SIDIS coefficient function

As one can see from Eq. (C.1), the NLO coefficient function $C_{qq}^{T,(1)}(\hat{x},\hat{z})$ receives large corrections near $\hat{x},\hat{z}\to 1$. Choosing for simplicity $\mu_F = Q$, we have

$$\begin{aligned}C_{qq}^{T,(1)}(\hat{x},\hat{z}) \;\sim\; e_q^2 C_F\Bigg[& -8\delta(1-\hat{x})\delta(1-\hat{z}) + 2\delta(1-\hat{x})\left(\frac{\ln(1-\hat{z})}{1-\hat{z}}\right)_+ + 2\delta(1-\hat{z})\left(\frac{\ln(1-\hat{x})}{1-\hat{x}}\right)_+ \\ & + \frac{2}{(1-\hat{x})_+(1-\hat{z})_+}\Bigg], \end{aligned} \tag{2.12}$$

corresponding in moment space to

$$\tilde{C}_{qq}^{T,(1)}(N,M) \;\sim\; e_q^2 C_F\left[-8 + \frac{\pi^2}{3} + \left(\ln\bar{N} + \ln\bar{M}\right)^2\right], \tag{2.13}$$

where $\bar{N} \equiv N\mathrm{e}^{\gamma_E}$, $\bar{M} \equiv M\mathrm{e}^{\gamma_E}$, with γ_E the Euler constant. Here we have only kept contributions that are neither suppressed as $1/N$, nor as $1/M$ in moment space. The terms given in (3.10) therefore always contain two distributions, one in $\hat{x}$ and one in $\hat{z}$.

Threshold resummation addresses the logarithms in $\bar{N}$ and $\bar{M}$ to all orders in the strong coupling constant α_s. More precisely, it captures terms of the form $\alpha_s^k \ln^n N \ln^m M$, with $n + m \leq 2k$. We now discuss the derivation of the resummed expression for the SIDIS coefficient function $\tilde{C}_{qq}^{T,(1)}(N,M)$. Since the leading-order process is $\gamma^* q \to q$ scattering, and since both the incoming and the outgoing quark are "observed", the treatment has much in common with that for the total Drell-Yan cross section, or for its "crossed" versions considered in Ref. [93]. A significant difference is, however, that in the present case two independent Mellin moments, N and M, have to be considered. At large N and M, or equivalently $\hat{x}$ and $\hat{z}$, all gluon radiation from the basic process $\gamma^* q \to q$ becomes soft, since we have the relation [93]

$$(1-\hat{x}) + (1-\hat{z}) \approx \frac{2k^0}{Q}, \tag{2.14}$$

where k^0 is the total energy of gluon radiation. The coefficient function may then be evaluated in the eikonal approximation for the quarks and/or antiquarks involved in the hard scattering. In moment space, the eikonal hard scattering functions exponentiate, leading to [6, 93–98]

$$\tilde{C}_{qq}^{T,\mathrm{res}}\left(N, M, \alpha_s(\mu^2), \frac{Q^2}{\mu^2}\right) \quad\propto\quad \exp\left[\int_0^{Q^2}\frac{dk_\perp^2}{k_\perp^2}A_q\left(\alpha_s(k_\perp^2)\right)\left\{\int_{\frac{k_\perp^2}{Q^2}}^1\frac{d\xi}{\xi}\left[\mathrm{e}^{-N\xi - M\frac{k_\perp^2}{\xi Q^2}}-1\right]+\ln\bar{N}+\ln\bar{M}\right\}\right], \tag{2.15}$$

which is valid to next-to-leading logarithmic (NLL) accuracy. Here, $A_q(\alpha_s)$ is a perturbative function:

$$A_q(\alpha_s) = \frac{\alpha_s}{\pi}A_q^{(1)} + \left(\frac{\alpha_s}{\pi}\right)^2 A_q^{(2)} + \ldots, \tag{2.16}$$

with

$$A_q^{(1)} = C_F, \quad A_q^{(2)} = \frac{1}{2}C_F\left[C_A\left(\frac{67}{18}-\frac{\pi^2}{6}\right)-\frac{5}{9}N_f\right], \tag{2.17}$$

where $C_F = 4/3$, $C_A = 3$ and N_f is the number of active flavors.

Up to corrections that are exponentially suppressed at large N, M, the integral over ξ in (2.15) can be carried out analytically, and one finds

$$\int_{\frac{k_\perp^2}{Q^2}}^1\frac{d\xi}{\xi}\left[\mathrm{e}^{-N\xi - M\frac{k_\perp^2}{\xi Q^2}}-1\right]+\ln\bar{N}+\ln\bar{M} \approx 2\left[K_0\left(\sqrt{NM}\,\frac{2k_\perp}{Q}\right)+\ln\left(\frac{k_\perp}{Q}\sqrt{\bar{N}\bar{M}}\right)\right], \tag{2.18}$$

where K_0 is a Bessel function. It arises when we extend the ξ integral to $0 < \xi < \infty$. It is instructive to confront this with the analogous expression for the Mellin-N moments of the partonic total Drell-Yan cross section, which reads [93, 97, 98]:

$$\int_{\frac{k_\perp^2}{Q^2}}^1\frac{d\xi}{\xi}\left[\mathrm{e}^{-N\left(\xi-\frac{k_\perp^2}{\xi Q^2}\right)}-1\right]+2\ln\bar{N} \approx 2\left[K_0\left(N\,\frac{2k_\perp}{Q}\right)+\ln\left(\frac{k_\perp}{Q}\bar{N}\right)\right]. \tag{2.19}$$

From this comparison one can immediately see that the result for the resummed SIDIS cross section can be obtained from the one for the total Drell-Yan cross section by simply setting $\bar{N}\to\sqrt{\bar{N}\bar{M}}$. In the case of SIDIS, the moments N and M independently fix the light-cone plus component ξ and the minus component $\zeta = k_\perp^2/(\xi Q^2)$ of the soft gluon momentum, resulting in the slightly more elaborate form of the exponent in (2.18). Likewise, the $\overline{\mathrm{MS}}$-subtraction of collinear divergencies in the initial and the final state in SIDIS yields the terms $\ln\bar{N}$ and $\ln\bar{M}$, respectively, whereas in Drell-Yan one has the contribution $2\ln\bar{N}$ from the two initial partons.

With (2.18), the final resummed coefficient function becomes in the $\overline{\mathrm{MS}}$ scheme:

$$\begin{aligned}\tilde{C}_{qq}^{T,\mathrm{res}}\left(N, M, \alpha_s(\mu^2), \frac{Q^2}{\mu^2}\right) \;=\; e_q^2 H_{qq}\left(\alpha_s(\mu^2), \frac{Q^2}{\mu^2}\right)\exp\left[2\int_0^{Q^2}\frac{dk_\perp^2}{k_\perp^2}A_q\left(\alpha_s(k_\perp^2)\right)\left\{K_0\left(\sqrt{NM}\,\frac{2k_\perp}{Q}\right)\right.\right.\\ \left.\left.+\ln\left(\frac{k_\perp}{Q}\sqrt{\bar{N}\bar{M}}\right)\right\}\right].\end{aligned} \tag{2.20}$$

Here we have included a perturbative function H_{qq} that collects the hard virtual corrections to $\gamma^* q \to q$

scattering. For resummation at NLL, one needs to know H_{qq} to first order in the strong coupling, which may be derived by expanding (2.20) to $\mathcal{O}(\alpha_s)$ (keeping only logarithmic terms in the exponent) and comparing to the explicit NLO expression (2.13) for large N, M. One finds:

$$H_{qq}\left(\alpha_s(\mu^2), \frac{Q^2}{\mu^2}\right) = 1 + \frac{\alpha_s}{2\pi} C_F \left(-8 + \frac{\pi^2}{3} + 3\ln\frac{Q^2}{\mu^2}\right) + \mathcal{O}(\alpha_s^2)\,. \tag{2.21}$$

We note that an alternative, but equivalent, form of the resummed result is [8, 99]

$$\begin{aligned}\tilde{\mathcal{C}}_{qq}^{T,\mathrm{res}}\left(N, M, \alpha_s(\mu^2), \frac{Q^2}{\mu^2}\right) \;&=\; e_q^2 H_{qq}\left(\alpha_s(\mu^2), \frac{Q^2}{\mu^2}\right) \times \exp\left[\int_0^1 dx \frac{\xi^N - 1}{1-\xi} \int_{Q^2}^{(1-\xi)Q^2} \frac{dk_\perp^2}{k_\perp^2} A_q(\alpha_s(k_\perp^2))\right.\\ &\left.+ \int_0^1 d\zeta \frac{\zeta^M - 1}{1-\zeta} \int_{Q^2}^{(1-\zeta)Q^2} \frac{dk_\perp^2}{k_\perp^2} A_q(\alpha_s(k_\perp^2)) + \int_0^1 dx \frac{\xi^N - 1}{1-\xi} \int_0^1 d\zeta \frac{\zeta^M - 1}{1-\zeta} A_q\left(\alpha_s(Q^2(1-\xi)(1-\zeta))\right)\right].\end{aligned} \tag{2.22}$$

This expression can be obtained from (2.15) by first writing the integrand as

$$\mathrm{e}^{-N\xi - M\frac{k_\perp^2}{\xi Q^2}} - 1 \;=\; \left(\mathrm{e}^{-N\xi} - 1\right)\left(\mathrm{e}^{-M\frac{k_\perp^2}{\xi Q^2}} - 1\right) + \mathrm{e}^{-N\xi} - 1 + \mathrm{e}^{-M\frac{k_\perp^2}{\xi Q^2}} - 1. \tag{2.23}$$

Including the integrals over ξ and $k_\perp$ and substituting $k_\perp^2 = \zeta\xi Q^2$, the first term on the right-hand-side of (2.23) yields

$$\int_0^1 \frac{d\xi}{\xi}\left(\mathrm{e}^{-N\xi} - 1\right) \int_0^1 \frac{d\zeta}{\zeta}\left(\mathrm{e}^{-M\zeta} - 1\right) A_q\left(\alpha_s(\zeta\xi Q^2)\right). \tag{2.24}$$

Next, we deal with the term containing $\left(\mathrm{e}^{-N\xi} - 1\right)$ in (2.23). Combining with the logarithm $\ln\bar{N}$ in (2.15) we find, up to corrections suppressed as $1/N$:

$$\int_0^{Q^2} \frac{dk_\perp^2}{k_\perp^2} A_q\left(\alpha_s(k_\perp^2)\right)\left\{\int_{\frac{k_\perp^2}{Q^2}}^1 \frac{d\xi}{\xi}\left(\mathrm{e}^{-N\xi} - 1\right) + \ln\bar{N}\right\} \approx \int_0^1 \frac{d\xi}{\xi}\left(\mathrm{e}^{-N\xi} - 1\right) \int_{Q^2}^{\xi Q^2} \frac{dk_\perp^2}{k_\perp^2} A_q\left(\alpha_s(k_\perp^2)\right). \tag{2.25}$$

Likewise,

$$\int_0^{Q^2} \frac{dk_\perp^2}{k_\perp^2} A_q\left(\alpha_s(k_\perp^2)\right)\left\{\int_{\frac{k_\perp^2}{Q^2}}^1 \frac{d\xi}{\xi}\left(\mathrm{e}^{-\frac{Mk_\perp^2}{\xi Q^2}} - 1\right) + \ln\bar{M}\right\} \approx \int_0^1 \frac{d\zeta}{\zeta}\left(\mathrm{e}^{-M\zeta} - 1\right) \int_{Q^2}^{\zeta Q^2} \frac{dk_\perp^2}{k_\perp^2} A_q\left(\alpha_s(k_\perp^2)\right). \tag{2.26}$$

Adding the expressions in Eqs. (2.24),(2.25),(2.26), and changing $\xi \to 1-\xi$, $\zeta \to 1-\zeta$, we recover (2.22). Our expression (2.20) is however simpler and makes the close connection to the resummed expression for the total Drell-Yan cross section more transparent.

2.2.3 Expansion to NLL

At small argument, the Bessel function K_0 behaves as

$$K_0(x) = -\ln\left(x e^{\gamma_E}/2\right) + \mathcal{O}(x^2 \ln x) \, .$$

Therefore, logarithmic behavior of the integral in (2.20) in N and M occurs only when $k_\perp$ is bounded from below, and the K_0 function effectively acts as step function. To NLL, one finds the condition $k_\perp \geq Q/\sqrt{\bar{N}\bar{M}}$ [97, 98]:

$$\tilde{\mathcal{C}}_{qq}^{T,\mathrm{res}}\left(N, M, \alpha_s(\mu^2), \frac{Q^2}{\mu^2}\right) = e_q^2 H_{qq}\left(\alpha_s(\mu^2), \frac{Q^2}{\mu^2}\right) \times \exp\left[2\int_{\frac{Q^2}{\bar{N}\bar{M}}}^{Q^2} \frac{dk_\perp^2}{k_\perp^2} A_q\left(\alpha_s(k_\perp^2)\right) \ln\left(\frac{k_\perp}{Q}\sqrt{\bar{N}\bar{M}}\right)\right] . \tag{2.27}$$

The explicit NLL expansion of the right-hand side is straightforward after inserting the standard expression for the running strong coupling and, anyway, the result can be directly obtained from the well-known one [64] for Drell-Yan, setting $\bar{N} \to \sqrt{\bar{N}\bar{M}}$ there. In the exponent in (3.15) we obtain

$$\int_{\frac{Q^2}{\bar{N}\bar{M}}}^{Q^2} \frac{dk_\perp^2}{k_\perp^2} A_q\left(\alpha_s(k_\perp^2)\right) \ln\left(\frac{k_\perp}{Q}\sqrt{\bar{N}\bar{M}}\right) \approx h_q^{(1)}\left(\frac{\lambda_{NM}}{2}\right) \frac{\lambda_{NM}}{2b_0\alpha_s(\mu^2)} + h_q^{(2)}\left(\frac{\lambda_{NM}}{2}, \frac{Q^2}{\mu^2}, \frac{Q^2}{\mu_F^2}\right) , \tag{2.28}$$

where

$$\begin{aligned}
\lambda_{NM} &\equiv b_0\alpha_s(\mu^2)\left(\log\bar{N} + \log\bar{M}\right) , \\
h_q^{(1)}(\lambda) &= \frac{A_q^{(1)}}{2\pi b_0 \lambda}\left[2\lambda + (1-2\lambda)\ln(1-2\lambda)\right] , \\
h_q^{(2)}\left(\lambda, \frac{Q^2}{\mu^2}, \frac{Q^2}{\mu_F^2}\right) &= -\frac{A_q^{(2)}}{2\pi^2 b_0^2}\left[2\lambda + \ln(1-2\lambda)\right] + \frac{A_q^{(1)} b_1}{2\pi b_0^3}\left[2\lambda + \ln(1-2\lambda) + \frac{1}{2}\ln^2(1-2\lambda)\right] \\
&\quad + \frac{A_q^{(1)}}{2\pi b_0}\left[2\lambda + \ln(1-2\lambda)\right]\ln\frac{Q^2}{\mu^2} - \frac{A_q^{(1)}}{\pi b_0}\lambda \ln\frac{Q^2}{\mu_F^2} ,
\end{aligned} \tag{2.29}$$

where the b_i are defined in Eq. (1.12). The functions $h_q^{(1)}$, $h_q^{(2)}$ collect all leading-logarithmic and NLL terms in the exponent, which are of the form $\alpha_s^k \ln^n \bar{N} \ln^m \bar{M}$ with $n + m = k + 1$ and $n + m = k$, respectively. Note that we have kept the factorization and renormalization scales arbitrary in the above expressions. The standard Drell-Yan result is recovered by setting $\lambda_{NM}/2 \to \lambda_{\mathrm{DY}}$, where $\lambda_{\mathrm{DY}} = b_0\alpha_s(\mu^2)\log\bar{N}$.

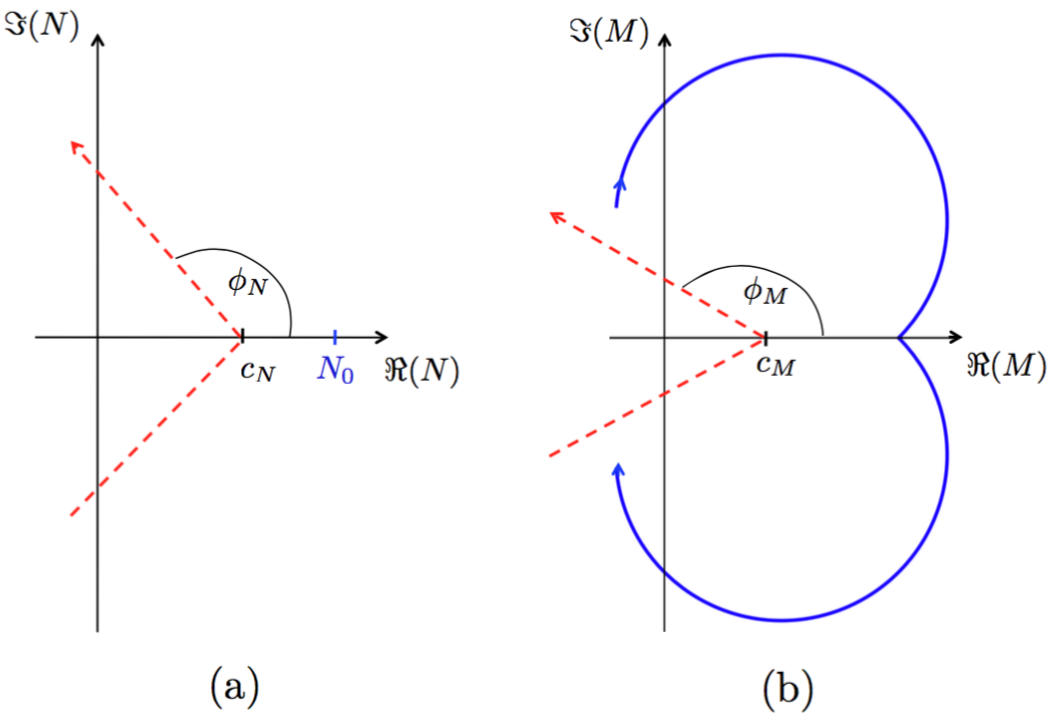

Figure 2.1: Contours for the inverse Mellin transforms, (a) for $\mathcal{C}_N$, (b) for $\mathcal{C}_M$. We have defined $N_0 = L_0/c_M$, with L_0 given in (2.31). In (b), the solid line depicts the location of the Landau pole as N moves along a part of its contour (see text).

2.2.4 Inverse Mellin transforms

As the exponentiation of soft-gluon corrections is achieved in Mellin moment space, the hadronic structure function is obtained by taking the inverse Mellin transforms of Eq. (2.8):

$$\mathcal{F}_i^h(x,z,Q^2) = \int_{\mathcal{C}_N} \frac{dN}{2\pi i} x^{-N} \int_{\mathcal{C}_M} \frac{dM}{2\pi i} z^{-M} \tilde{\mathcal{F}}_i^h(N,M,Q^2), \tag{2.30}$$

where $\mathcal{C}_N$ and $\mathcal{C}_M$ denote integration contours in the complex plane, one for each Mellin inverse. When performing an inverse Mellin transform, the contour usually has to be chosen in such a way that all singularities of the integrand lie to its left. However, as can be seen from Eq. (2.28),(2.29), the resummed cross section has a Landau singularity at $\lambda_{NM} = 1$ or

$$N\,M = \mathrm{e}^{1/(\alpha_s b_0) - 2\gamma_E} \equiv L_0, \tag{2.31}$$

as a result of the divergence of the running coupling α_s in Eq. (2.20) for $k_\perp \to \Lambda_{\mathrm{QCD}}$. For the Mellin inversions, we adopt the *minimal prescription* developed in Ref. [64] to deal with the Landau pole. For this prescription the contours are chosen to lie to the *left* of the Landau singularity. In order to achieve this, we first choose the contour for the N-integration in the upper complex half plane in the standard way (see Fig. 2.1(a)) as

$$N = c_N + z_N \, \mathrm{e}^{i\phi_N} , \tag{2.32}$$

where c_N is a postive real constant, $\phi_N \sim 3\pi/4$ and $z_N \in [0, \infty]$. For the lower branch of the contour, one simply uses the complex conjugate of N. The contour for the M-integration is parameterized in a similar fashion, with a constant c_M, an integration parameter z_M and an angle ϕ_M that we will address shortly. The fact that both contours are tilted into the half-plane with negative real part improves the numerical convergence of the integration, since contributions with negative real part are exponentially suppressed by the factors x^{-N}, z^{-M} in Eq. (2.30).

In accordance with the minimal prescription [64], the parameter c_N is chosen to be smaller than $N_0 \equiv L_0/c_M$. As N moves along its contour from a point with large negative imaginary part to a point with large positive one, the Landau pole given by Eq. (2.31) describes a trajectory shown by the solid line in Fig. 2.1(b). The angle ϕ_M is now chosen in such a way that the M-integration contour (shown by the dashed line) avoids this trajectory. The larger the imaginary part of N, the larger the angle ϕ_M needs to become. Of course, ultimately as $\Im(N) \to \pm\infty$, the Landau pole moves to the origin in the M-plane, and the contour falls onto the real M-axis. However, as described above, the contributions from such large values of N are extremely suppressed. We note that a similar approach to the choice of contours was discussed in Ref. [111], where combined inverse Mellin and Fourier transforms were considered. An alternative approach is to expand the resummed formula to high perturbative orders. At each finite order, the Landau pole is not present and, therefore, standard Mellin contours can be chosen.

We match the resummed cross section to the NLO one by subtracting the $O(\alpha_s)$ expansion of the resummed expression and adding the full NLO cross section. This "matched" cross section consequently not only resums the large threshold logarithms to all orders, but also contains the full NLO results for the $q \to q$, $q \to g$ and $g \to q$ channels. We will occasionally also consider a resummed cross section that has not been matched to the NLO one. We will refer to such a cross section as "unmatched".

2.2.5 Resummation for inclusive DIS

In order to obtain resummed predictions for the SIDIS hadron multiplicities defined in (2.3), we also need the resummation for the inclusive cross section. In this case, there is only one variable x, and standard Mellin-moment resummation techniques [58–62, 112, 113] may be applied. The inclusive structure functions $\mathcal{F}_T$ and $\mathcal{F}_L$ introduced in Eq. (2.4) can be written as

$$\mathcal{F}_i(x, Q^2) = \sum_f \int_x^1 \frac{d\hat{x}}{\hat{x}} f\left(\frac{x}{\hat{x}}, \mu^2\right) \mathcal{C}_f^i \left(\hat{x}, \frac{Q^2}{\mu^2}, \alpha_s(\mu^2)\right) . \tag{2.33}$$

The expressions for the NLO coefficient functions $\mathcal{C}_f^i$ may also be found in Appendix C. Alternatively, see [51] for example. Resummation may be performed by again introducing Mellin moments in x. The resummed DIS coefficient function for the structure function $\mathcal{F}_T$ reads to NLL in moment space:

$$\begin{aligned}\tilde{C}_q^{T,\mathrm{res}}\left(N,\alpha_s(\mu^2),\frac{Q^2}{\mu^2}\right) &= e_q^2 H_q\left(\alpha_s(\mu^2),\frac{Q^2}{\mu^2}\right)\exp\left[\int_0^1 d\xi\frac{\xi^N-1}{1-\xi}\right.\\ &\quad\times\left.\left\{\int_{Q^2}^{(1-\xi)Q^2}\frac{dk_\perp^2}{k_\perp^2}A_q(\alpha_s(k_\perp^2))+\frac{1}{2}B_q\left(\alpha_s((1-\xi)Q^2)\right)\right\}\right],\end{aligned} \tag{2.34}$$

where the function $A_q(\alpha_s)$ is as in (3.16). The perturbative function $B_q(\alpha_s)$ is given by

$$B_q(\alpha_s)=\frac{\alpha_s}{\pi}B_q^{(1)}+\mathcal{O}(\alpha_s^2), \tag{2.35}$$

with

$$B_q^{(1)}=-\frac{3}{2}C_F. \tag{2.36}$$

Finally, the hard-scattering coefficient reads

$$H_q\left(\alpha_s(\mu^2),\frac{Q^2}{\mu^2}\right)=1+\frac{\alpha_s}{2\pi}C_F\left(-\frac{9}{2}-\frac{\pi^2}{6}+\frac{3}{2}\ln\frac{Q^2}{\mu^2}\right)+\mathcal{O}(\alpha_s^2). \tag{2.37}$$

The exponential in (4.30) can evidently be written as $\Delta_q^N \times J_q^N$, see Eq. (1.80) in Chapter 1, where also their evaluation up to NLL accuracy is given.

2.3 Resummation for $e^+e^- \to hX$

Hadron multiplicities in $e^+e^- \to hX$ are defined by

$$R^h_{e^+e^-}\equiv\frac{1}{\sigma^{\mathrm{tot}}}\frac{d^2\sigma^h}{dx_E d\cos\theta}, \tag{2.38}$$

where $d^2\sigma^h/dx_E d\cos\theta$ is the differential cross section for the production of the hadron h at angle θ relative to the initial positron. Furthermore,

$$x_E\equiv\frac{2P_h\cdot q}{Q^2}, \tag{2.39}$$

where P_h and q are the momenta of the produced hadron and the intermediate virtual photon respectively and $Q^2=q^2$. σ^{tot} is the total cross section for $e^+e^- \to$ hadrons. To first order in α_s it reads:

$$\sigma^{\mathrm{tot}}=\frac{4\pi\alpha^2}{3Q^2}N_c\sum_q e_q^2\left(1+\frac{\alpha_s}{\pi}\right), \tag{2.40}$$

where $N_c=3$ is the number of colors.
As in the case of SIDIS, one can write the cross section $d^2\sigma^h/dx_E d\cos\theta$ in terms of structure func-

tions [51, 106]:

$$\frac{d^2\sigma^h}{dx_E d\cos\theta} = \frac{\pi\alpha^2}{Q^2} N_c \left[\frac{1+\cos^2\theta}{2}\hat{\mathcal{F}}_T^h(x_E,Q^2) + \sin^2\theta\,\hat{\mathcal{F}}_L^h(x_E,Q^2)\right], \tag{2.41}$$

where

$$\hat{\mathcal{F}}_i^h(x_E,Q^2) = \sum_f \int_{x_E}^1 \frac{d\hat{z}}{\hat{z}} D_f^h\left(\frac{x_E}{\hat{z}},\mu^2\right)\hat{\mathcal{C}}_f^i\left(\hat{z},\frac{Q^2}{\mu^2},\alpha_s(\mu^2)\right), \tag{2.42}$$

with the fragmentation functions D_f^h introduced in subsection 2.2.1. To lowest order, only the partonic channel $e^+e^- \to qX$ contributes, for which

$$\begin{aligned}\hat{C}_q^{T,(0)}(\hat{z}) &= e_q^2\,\delta(1-\hat{z}),\\ \hat{C}_q^{L,(0)}(\hat{z}) &= 0.\end{aligned} \tag{2.43}$$

Again, the NLO expressions may be found in Appendix C. Alternatively, we refer the reader to the previous literature [51, 105, 114]. After taking Mellin moments in x_E, the resummed result for the corresponding hard-scattering function turns out to be identical to that in (4.30) [99–101], except for a change $-\pi^2/6 \to 5\pi^2/6$ in the coefficient H_q in (2.37).

2.4 Phenomenological Results

We now investigate the numerical size of the threshold resummation effects for the two semi-inclusive hadron production processes discussed above, SIDIS and $e^+e^- \to hX$. We focus entirely on pion production in this work, for which the theory is expected to be under best control. We also consider a proton target throughout this work. For the parton distribution functions we use the NLO "Martin–Stirling–Thorne–Watt" (MSTW 2008) set of [115], whereas we choose the NLO "de Florian–Sassot–Stratmann" (DSS) [71, 74] pion fragmentation functions. In this set, fragmentation functions for charged pions $\pi^\pm$ are separately available. We note that the parton distributions and fragmentation functions are provided in x (or z) space, whereas according to Eq. (2.9) we need their Mellin moments. To obtain the latter, we first fit suitable functions of the form $Ax^\alpha(1-x)^\beta$ times a polynomial in x to the distributions. It is then straightforward to take Mellin moments of the fitted functions analytically and use them in the numerical code. We have checked that the accuracy of the fit is overall very good.

2.4.1 Results for SIDIS

We start by examining the overall effects of threshold resummation for SIDIS, using the kinematics relevant for the COMPASS SIDIS measurements [92] as an example. COMPASS uses a muon beam of energy 160 GeV incident on a proton fixed target. The resulting center-of-mass energy is $\sqrt{s} \approx 17.4$ GeV. The kinematic cuts employed by COMPASS are $0.041 < x < 0.7$, $0.1 < y < 0.9$, $Q^2 > 1$ GeV^2 and $W^2 = Q^2(1-x)/x + m_p^2 > 49$ GeV^2, where m_p is the proton mass. We choose the renormalization and factorization scales as Q and consider the SIDIS multiplicity for neutral pions π^0 as a function of z, but integrating numerator and denominator of Eq. (2.3) over x and y. We observe that the range of x probed by the full COMPASS data sample extends down to fairly low values, where one could

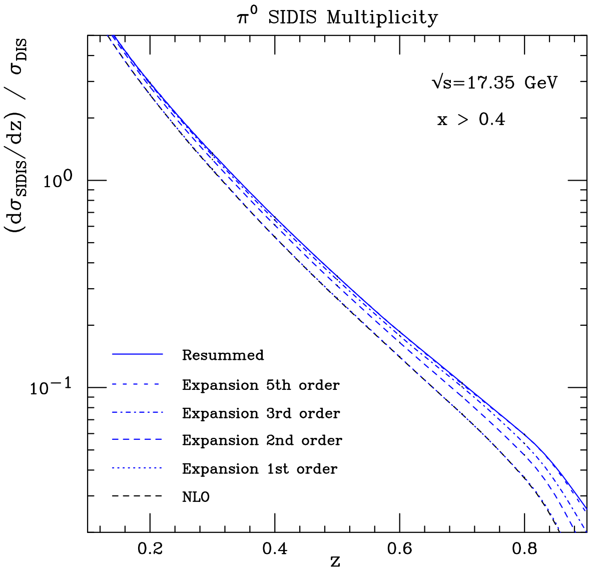

Figure 2.2: SIDIS multiplicity for π^0. Kinematics are as for the COMPASS measurements [92] (see text) with, however, an additional cut $x > 0.4$ to enhance the contribution from the threshold regime. The lower two lines which are almost indistinguishable show the NLO result and the first-order expansion of the resummed result (without matching). The top line shows the full NLL resummed result; the lines in between display various fixed-order expansions of the latter.

be quite far from the threshold regime. We therefore first consider a lower cut of $x > 0.4$. Figure 2.2 shows our results for the NLO and the resummed multiplicities, along with those for expansions of the resummed cross section to various finite orders in α_s. In each case, the denominator of the multiplicity, the inclusive-DIS cross section, has been treated in the same fashion as the SIDIS one in the numerator. With the exception of the first-order expansion, all beyond-NLO results have been matched to the NLO one (separately in the numerator and the denominator) as described at the end of Sec.2.2.4. We first of all note that the first-order expansion of the resummed cross section agrees very well with the full NLO one, which demonstrates that for the chosen kinematics the threshold regime strongly dominates the NLO cross section. The full resummed result shows a marked increase over the NLO one, in particular at high z, and the higher-order expansions converge nicely to the resummed result. Clearly, the α_s^2 and α_s^3 contributions generated by resummation are still significant.

The results can also be studied as ratios $(\mathrm{Th}' - \mathrm{NLO})/\mathrm{NLO}$, where Th' denotes any of the higher-order SIDIS multiplicities generated by resummation. Figure 2.3 shows these ratios for the unmatched first-order expansion, the matched higher-order expansions and the full resummed result. The good agreement of NLO and the first-order expansion is evident, as are the large resummation effects at high z.

We now extend the x-range to the full region $0.041 < x < 0.7$ covered by COMPASS. The Figures in 2.4 show the corresponding results, where all lines directly correspond to the ones shown in Figs. 2.2 and 2.3 for the case $x > 0.4$. One can see that the resummation effects are generally smaller now,

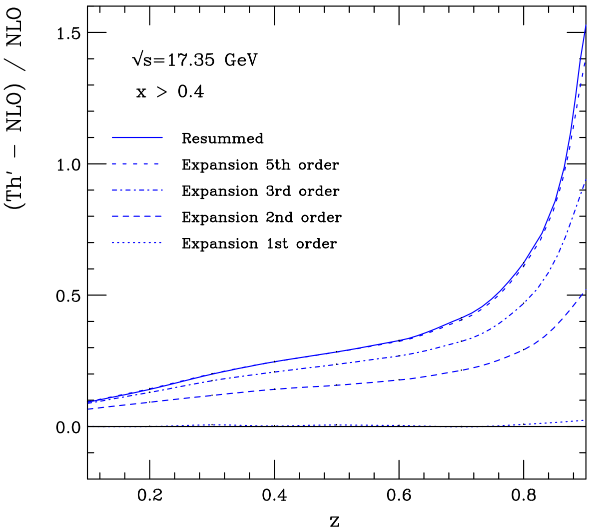

Figure 2.3: Ratios $(\mathrm{Th}' - \mathrm{NLO})/\mathrm{NLO}$, where Th' corresponds to the SIDIS multiplicity at higher orders as generated by resummation. The first-order expansion of the resummed cross section has not been matched since it would otherwise be identical to NLO.

even though they remain significant at high z. As expected, the agreement between NLO and the first-order expansion of the resummed cross section is worse now, but it typically remains at the 10% level or better. The second-order expansion captures most of the full resummation effects; the yet higher orders converge somewhat more slowly now to the resummed result. The Figure on the right side of 2.4 shows the corresponding ratios $(\mathrm{Th}' - \mathrm{NLO})/\mathrm{NLO}$, where again Th' denotes any of the SIDIS multiplicities computed at higher orders.

Preliminary precise data from COMPASS for charged-pion and kaon multiplicities are available for a wide range of kinematics [92]. The full data set, which evidently has the best statistics, covers the range used above for Figs. 2.4. The Figures in 2.5 show comparisons of our NLO and NLL resummed calculations for charged pions to the COMPASS data. As one can see, resummation leads to a moderate, but significant, enhancement of the multiplicities. It is interesting to note that such an enhancement is in fact preferred by the π^- data. However, we do not assign much importance to this observation. The fragmentation functions are presently still not very well determined and a different set (or a new fit) might well describe the data also at NLO. Our main point is that inclusion of resummation effects in an analysis of fragmentation functions could make a significant difference for the extracted functions.

The Figure in 2.6 shows similar comparisons to the HERMES preliminary data [91]. For this data set, the center-of-mass energy is $\sqrt{s}$ ≈17.4 GeV. The kinematic cuts employed by HERMES are $0.023 < x < 0.6$, $0.1 < y < 0.85$, $Q^2 > 1$ GeV^2 and $W^2 = 10$ GeV^2. The results are qualitatively similar to those shown for COMPASS kinematics.

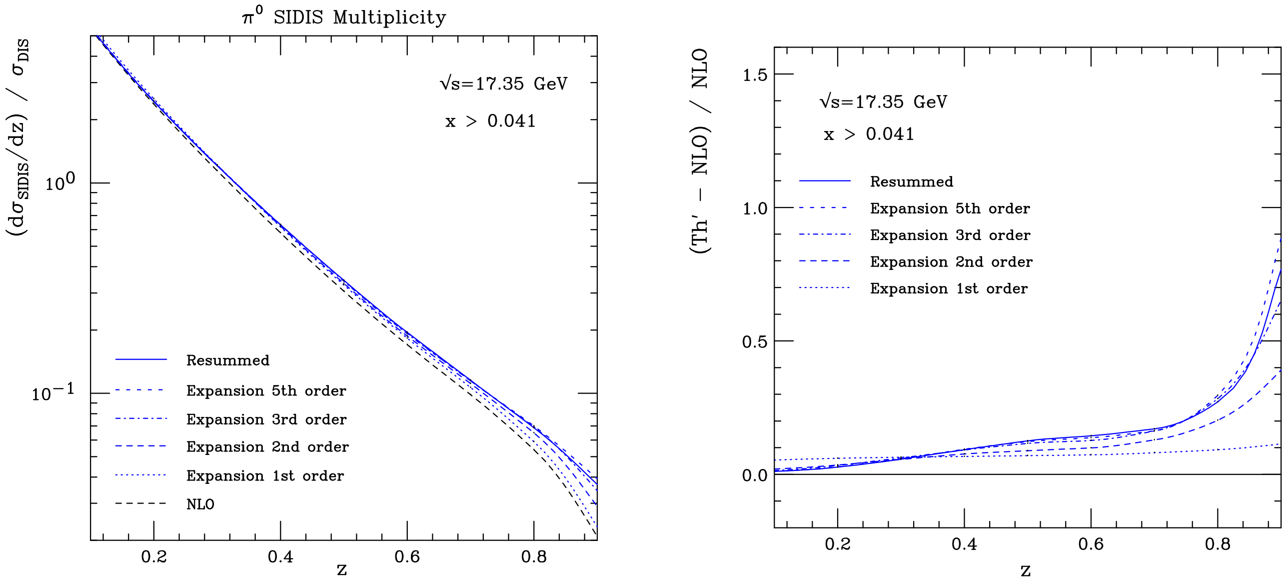

Figure 2.4: Analogously to Figs. 2.2 and 2.3, but for $x > 0.041$.

2.4.2 Results for single-inclusive e^+e^- annihilation

Figure 2.7 (on the left side) presents our results for the π^- multiplicity in e^+e^- annihilation at $\sqrt{s} = 10.52$ GeV and for $-1 < \cos\theta < 1$, as appropriate for comparison to the forthcoming BELLE data [90]. The π^+ multiplicity is identical thanks to charge conjugation symmetry. We have chosen the factorization and renormalization scales as $\sqrt{s}$. As for SIDIS, we show NLO and NLL resummed results, along with various fixed-order expansions of the resummed multiplicity. One first of all observes the excellent agreement between the NLO result and the first-order expansion of the resummed one. This clearly demonstrates that the threshold regime strongly dominates for the BELLE kinematics. We can therefore be confident that also the resummed result reliably captures the important higher-order terms. Resummation leads to a significant enhancement of the π^- multiplicity. This enhancement becomes particularly strong at high x_E, but is present also at moderate values. Figure 2.7 (on the right side) shows the corresponding ratios $(\mathrm{Th}' - \mathrm{NLO})/\mathrm{NLO}$, where Th' denotes any of the higher-order multiplicities generated by resummation and shown on the left side of Fig. 2.7. Since the precision of the preliminary BELLE data is typically much better than 10%, it will be important to include the enhancements we find in future global analyses of fragmentation functions, similar to what has been done in the past in Ref. [73]. In Fig. 2.8, we compare our results to the recent data sets from BELLE [10] and BaBar [11]. We are going to revisit this comparison in more detail in Chapter 4.

2.5 Conclusions

We have derived threshold-resummed expressions for the coefficient functions for single-inclusive hadron production in semi-inclusive lepton scattering and e^+e^- annihilation. We have presented phenomenological results for pion multiplicities for these processes in the kinematic regimes presently accessed by the COMPASS, HERMES, BELLE and BaBar experiments. We have found that resummation

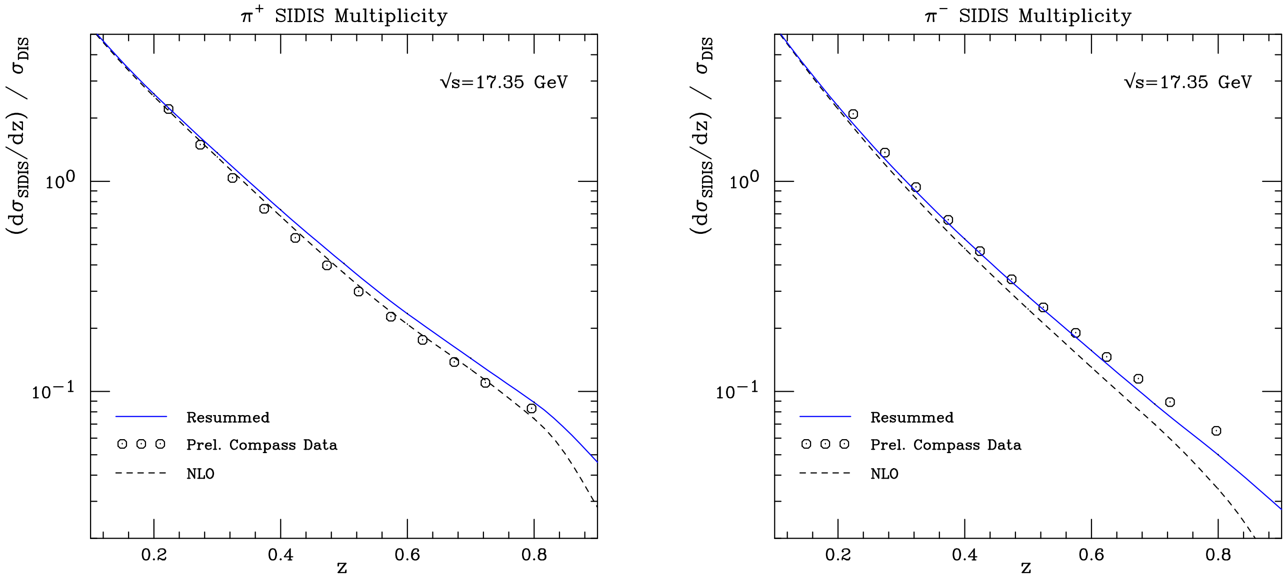

Figure 2.5: NLO and NLL resummed SIDIS multiplicities for π^+ (left) and π^- (right). The results are compared to the preliminary COMPASS data [92]. The uncertainties of the data are smaller than the symbol size used in the plot.

leads to modest but significant enhancements of the multiplicities. The recent preliminary SIDIS data turn out to be overall better described when resummation effects are included in the calculation, at least for the DSS set of fragmentation functions that we have used. However, we do not ascribe much significance to this point as the fragmentation functions are still rather poorly constrained so that a new NLO fit to the new data would likely also work well [88]. Our main point is that, given the good accuracy of the new preliminary SIDIS and BELLE data, it will be crucial to include resummation effects for both processes in the next generation of analyses of fragmentation functions. In fact, because of the enhancements from threshold resummation, the extracted fragmentation functions would be expected to be softer or smaller at high z than functions extracted purely on the basis of an NLO framework. This may well have important ramifications for the QCD predictions obtained for other processes sensitive to fragmentation functions. For instance, it has recently been observed [88, 116] that the ALICE data [117] for neutral-pion production at 7 TeV are well below the theoretical NLO expectations. One may speculate if this is due in part to fragmentation functions that are too large at high z.

We note that at very high z or x_E, besides the logarithmic perturbative corrections also nonperturbative power corrections will ultimately become relevant and will need to be analyzed theoretically. Resummation offers ways to address these contributions (see, for example [93, 118], and references therein). Based on the ideas presented there, we do not think that power corrections play an overwhelming role in the presently accessible kinematic regime in SIDIS. As we saw in Eq. (3.15), the logarithmic contributions to SIDIS come from the region $k_\perp \gtrsim Q/\sqrt{\bar{N}\bar{M}}$. In x-z-space this scale roughly corresponds to $Q\sqrt{(1-z)(1-x)}$. We have checked that for COMPASS kinematics even at $z = 0.9$ the average value of this scale is significantly larger than 1 GeV, implying that perturbation theory should still provide a reliable answer here. This issue obviously deserves a more detailed inves-

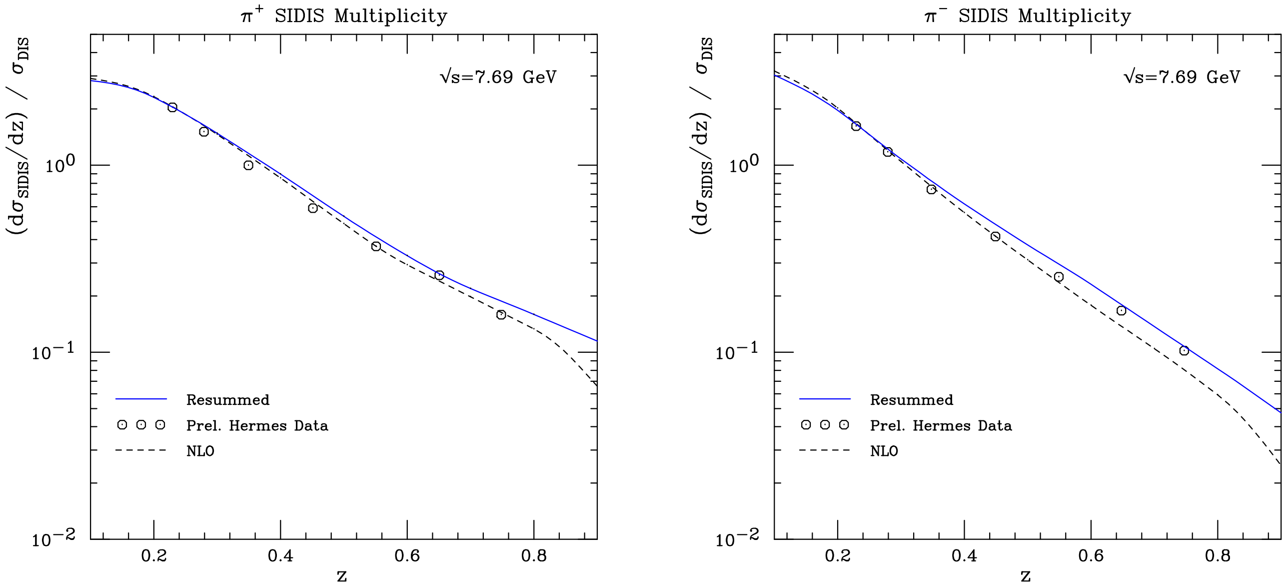

Figure 2.6: Same as Fig. 2.5, but for HERMES kinematics. The preliminary data are from [91]. The uncertainties of the data are smaller than the symbol size used in the plot.

tigation in the future, in particular also for the case of e^+e^- annihilation.

We stress that our study may be extended in several ways. First, as mentioned in the Introduction, resummation for $e^+e^- \to hX$ could be carried out at next-to-next-to-leading logarithm and even beyond, thanks to [100, 101]. The high precision of the BELLE data may well warrant a future study along these lines. Resummation for SIDIS could probably also be extended to next-to-next-to-leading logarithmic accuracy with some moderate further developments. This may become a very worthwhile task in the future when high-precision SIDIS data will become available from measurements at the Jefferson Laboratory after the CEBAF upgrade to 12 GeV beam energy [119]. Finally, one may readily adapt the resummation framework to the case of polarized SIDIS, which serves as an important probe of the spin structure of the nucleon. Present polarized-SIDIS measurements have the same kinematics as those considered in this chapter.

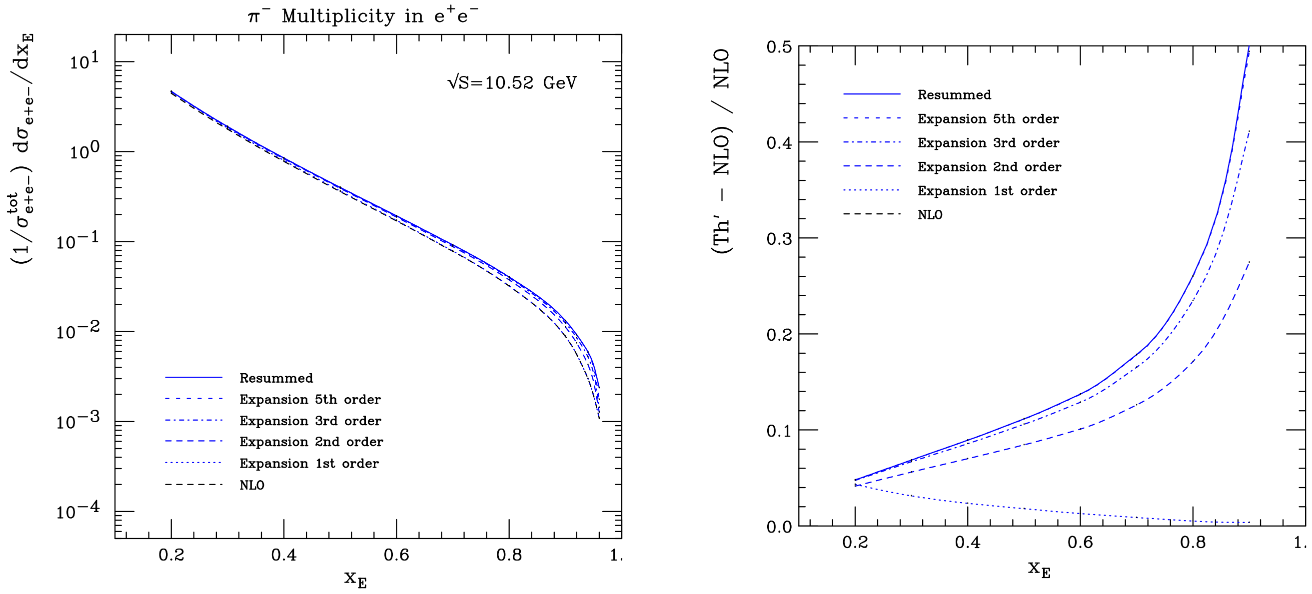

Figure 2.7: On the left: π^- multiplicity in electron-positron annihilation at $\sqrt{s} = 10.52$ GeV. The two lowest lines show the NLO result and the (unmatched) first-order expansion of the resummed one, which are practically indistinguishable. The other lines show matched higher-order expansions of the resummed multiplicity, and the resummed result itself (solid line). On the right: Ratios $(\mathrm{Th}' - \mathrm{NLO})/\mathrm{NLO}$ corresponding to the various curves shown on the right.

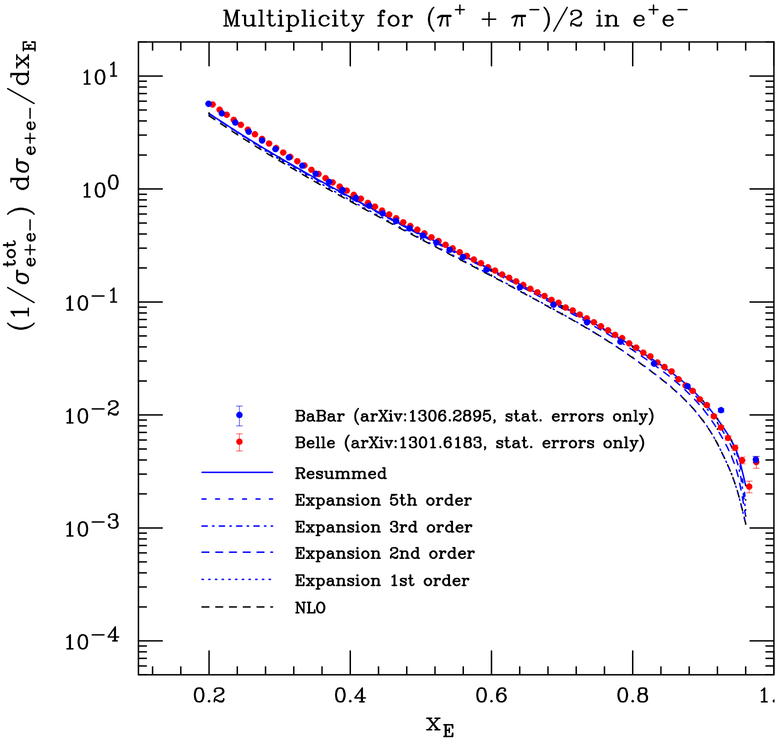

Figure 2.8: $(\pi^+ + \pi^-)/2$ multiplicity in e^+e^- annihilation computed at $\sqrt{s} = 10.52$ GeV. The data are from Belle [10] and BaBar [11] ("conventional" data set, $z \geq 0.2$, $\sqrt{s} = 10.54$ GeV).

CHAPTER 3

THRESHOLD RESUMMATION FOR POLARIZED (SEMI-)INCLUSIVE DEEP INELASTIC SCATTERING

We explore the effects of the resummation of large logarithmic perturbative corrections to double-longitudinal spin asymmetries for inclusive and semi-inclusive deep inelastic scattering in fixed-target experiments. We find that the asymmetries are overall rather robust with respect to the inclusion of the resummed higher-order terms. Significant effects are observed at fairly high values of x, where resummation tends to decrease the spin asymmetries. This effect turns out to be more pronounced for semi-inclusive scattering. We also investigate the potential impact of resummation on the extraction of polarized valence quark distributions in dedicated high-x experiments. This Chapter is based on publication [ii].

3.1 Introduction

Longitudinal double-spin asymmetries in inclusive and semi-inclusive deep inelastic scattering have been prime sources of information on the nucleon's spin structure for several decades. They may be used to extract the helicity parton distributions of the nucleon,

$$\Delta f(x,Q^2) \equiv f^+(x,Q^2) - f^-(x,Q^2) \ , \tag{3.1}$$

where f^+ and f^- are the distributions of parton $f = q, \bar{q}, g$ with positive and negative helicity, respectively, when the parent nucleon has positive helicity. x denotes the momentum fraction of the parton and Q the hard scale at which the distribution is probed. Inclusive polarized DIS, $\vec{\ell}\vec{p} \to \ell X$, offers access to the combined quark and antiquark distributions for a given flavor, $\Delta q + \Delta\bar{q}$, whereas in SIDIS, $\vec{\ell}\vec{p} \to \ell h X$, one exploits the fact that a produced hadron h (like a π^+) may for instance have a quark of a certain flavor as a valence quark, but not the corresponding antiquark [120]. In this way, it becomes possible to separate quark and antiquark distributions in the nucleon from one another, as well as to better determine the distributions for the various flavors. HERMES [121] and recent COMPASS [122] measurements have marked significant progress concerning the accuracy and kinematic coverage of polarized SIDIS measurements. The inclusive measurements have improved vastly as well [89, 123–127]. Some modern analyses of spin-dependent parton distributions include both inclusive and semi-inclusive data [128–131]. In addition, high-precision data for polarized SIDIS will become available from experiments to be carried out at the Jefferson Lab after the CEBAF upgrade to a 12 GeV beam [119]. Here the focus will be on the large-x regime.

A good understanding of the theoretical framework for the description of spin asymmetries in lepton scattering is vital for a reliable extraction of polarized parton distributions. In Chapter 2, we have investigated the effects of QCD threshold resummation on hadron multiplicities in SIDIS in the HERMES and COMPASS kinematic regimes. SIDIS is characterized by two scaling variables, Bjorken-x and a variable z given by the energy of the produced hadron over the energy of the virtual photon in the target rest frame. Large logarithmic corrections to the SIDIS cross section arise when the corresponding partonic variables become large, corresponding to scattering near a phase space boundary, where real-gluon emission is suppressed. This is typically the case for the presently relevant fixed-target kinematics. Threshold resummation addresses these logarithms to all orders in the strong coupling. In [63] we found fairly significant resummation effects on the spin-averaged multiplicities. Since the spin-dependent cross section is subject to similar logarithmic corrections as the unpolarized one, it is worthwhile to explore the effects of resummation on the spin asymmetries. This is the goal of the present Chapter. Our calculations will be carried out both for inclusive DIS and for SIDIS. We note that previous work [112, 132] has addressed the large-x resummation for the inclusive spin-dependent structure function g_1, with a focus on the moments of g_1 and their Q^2-dependence. In this Chapter, we are primarily concerned with spin asymmetries and with semi-inclusive scattering.

Our work will use the framework developed in [63]. In Section 3.2, we briefly review the basic terms and definitions relevant for longitudinal spin asymmetries, and we describe the extension of threshold resummation to the polarized case. In Section 3.3 our phenomenological results are presented. We compare our resummed inclusive and semi-inclusive spin asymmetries with available HERMES, COMPASS and Jefferson Lab data. We also discuss the relevance of resummation for the extraction of $\Delta u/u$ and $\Delta d/d$ at large values of x.

3.2 Resummation for Longitudinal Spin Asymmetries in DIS and SIDIS

3.2.1 Leading and next-to-leading order expressions

We first consider the polarized SIDIS process $\vec{\ell}(k)\vec{p}(P) \to \ell(k')h(P_h)X$ with longitudinally polarized beam and target and with an unpolarized hadron in the final state. The corresponding double-spin asymmetry is given by a ratio of structure functions [121]:

$$A_1^h(x,z,Q^2) \approx \frac{g_1^h(x,z,Q^2)}{F_1^h(x,z,Q^2)} \;, \tag{3.2}$$

where $Q^2 = -q^2$ with q the momentum of the virtual photon, $x = Q^2/(2P\cdot q)$ is the usual Bjorken variable, and $z \equiv P\cdot P_h/P\cdot q$ the corresponding hadronic scaling variable associated with the fragmentation process.

Using factorization, the polarized structure function g_1^h, which appears in the numerator of Eq. (3.2), can be written as

$$2g_1^h(x,z,Q^2) \;=\; \sum_{f,f'=q,\bar{q},g} \int_x^1 \frac{d\hat{x}}{\hat{x}} \int_z^1 \frac{d\hat{z}}{\hat{z}}\, \Delta f\left(\frac{x}{\hat{x}},\mu^2\right) \times D_{f'}^h\left(\frac{z}{\hat{z}},\mu^2\right) \Delta\mathcal{C}_{f'f}\left(\hat{x},\hat{z},\frac{Q^2}{\mu^2},\alpha_s(\mu^2)\right), \tag{3.3}$$

where $\Delta f(\xi,\mu^2)$ denotes the polarized distribution function for parton f of Eq. (3.1), whereas $D_{f'}^h\left(\zeta,\mu^2\right)$ is the corresponding fragmentation function for parton f' going to the observed hadron h. The $\Delta\mathcal{C}_{f'f}$ are spin-dependent coefficient functions. We have set all factorization and renormalization scales equal and collectively denoted them by μ. In (3.3) $\hat{x}$ and $\hat{z}$ are the partonic counterparts of the hadronic variables x and z. Setting for simplicity $\mu = Q$, we use the short-hand-notation

$$2g_1^h(x,z,Q^2) \equiv \sum_{f,f'=q,\bar{q},g} \left[\Delta f \otimes \Delta\mathcal{C}_{f'f} \otimes D_{f'}^h\right](x,z,Q^2) \tag{3.4}$$

for the convolutions in (3.3). A corresponding expression for the "transverse" unpolarized structure function $2F_1^h$ can be written by replacing the polarized parton distributions with the unpolarized ones, and using unpolarized coefficient functions which we denote here by $\mathcal{C}_{f'f}$.

The spin-dependent hard-scattering coefficient functions $\Delta\mathcal{C}_{f'f}$ in (3.3) can be computed in perturbation theory:

$$\Delta\mathcal{C}_{f'f} \;=\; \Delta\mathcal{C}_{f'f}^{(0)} + \frac{\alpha_s(\mu^2)}{2\pi}\Delta\mathcal{C}_{f'f}^{(1)} + \mathcal{O}(\alpha_s^2)\,. \tag{3.5}$$

At leading order, we have

$$\Delta\mathcal{C}_{qq}(\hat{x},\hat{z}) \;=\; \Delta\mathcal{C}_{\bar{q}\bar{q}}(\hat{x},\hat{z}) \;=\; e_q^2\,\delta(1-\hat{x})\delta(1-\hat{z})\,, \tag{3.6}$$

with the quark's fractional charge e_q. All other coefficient functions vanish. The same result holds for the LO coefficient function for the spin-averaged structure function $2F_1^h$. Hence the asymmetry in Eq. (3.2) reduces to

$$A_1^h = \frac{\sum\limits_q e_q^2\left[\Delta q(x,Q^2)D_q^h(z,Q^2) + \Delta\bar{q}(x,Q^2)D_{\bar{q}}^h(z,Q^2)\right]}{\sum\limits_q e_q^2\left[q(x,Q^2)D_q^h(z,Q^2) + \bar{q}(x,Q^2)D_{\bar{q}}^h(z,Q^2)\right]}\,. \tag{3.7}$$

At next-to-leading order, Eq. (3.3) becomes

$$\begin{aligned}2g_1^h(x,z,Q^2) &= \sum_q e_q^2 \Big\{ \Delta q(x,Q^2) D_q^h(z,Q^2) + \bar{q}(x,Q^2) D_{\bar{q}}^h(z,Q^2) \\ &+ \frac{\alpha_s(Q^2)}{2\pi} \Big[\Big(\Delta q \otimes D_q^h + \Delta\bar{q} \otimes D_{\bar{q}}^h \Big) \otimes \Delta C_{qq}^{(1)} + (\Delta q + \Delta\bar{q}) \otimes \Delta C_{gq}^{(1)} \otimes D_g^h \\ &+ \Delta g \otimes \Delta C_{qg}^{(1)} \otimes (D_q^h + D_{\bar{q}}^h) \Big] (x,z,Q^2) \Big\}, \end{aligned} \tag{3.8}$$

where the symbol $\otimes$ denotes the convolution defined in Eqs. (3.3),(3.4). The explicit expressions for the spin-dependent NLO coefficients $\Delta C_{f'f}^{(1)}$ have been derived in [108, 109]. Graudenz:1994dq The corresponding spin-averaged NLO coefficient functions $C_{f'f}^{(1)}$ may be found in the Appendix C or in [51, 63, 105–109].

In the case of *inclusive* polarized DIS, the longitudinal spin asymmetry A_1 is given in analogy with (3.2) by

$$A_1(x,Q^2) \approx \frac{g_1(x,Q^2)}{F_1(x,Q^2)} \, . \tag{3.9}$$

The inclusive structure functions g_1 and F_1 have expressions analogous to their SIDIS counterparts, except for the fact that they do not contain any fragmentation functions, of course. The unpolarized and polarized NLO coefficient functions for inclusive DIS may be found at many places; see, for example [51, 133].

3.2.2 Threshold resummation

As was discussed in [63], the higher-order terms in the spin-averaged SIDIS coefficient function $\mathcal{C}_{qq}$ introduce large terms near the "partonic threshold" $\hat{x} \to 1$, $\hat{z} \to 1$. The same is true for the spin-dependent $\Delta\mathcal{C}_{qq}$. At NLO, choosing again for simplicity the scale $\mu = Q$, one has

$$\begin{aligned}\Delta C_{qq}^{(1)}(\hat{x},\hat{z}) &\sim e_q^2 C_F \Bigg[2\delta(1-\hat{x}) \left(\frac{\ln(1-\hat{z})}{1-\hat{z}} \right)_+ + 2\delta(1-\hat{z}) \left(\frac{\ln(1-\hat{x})}{1-\hat{x}} \right)_+ \\ &+ \frac{2}{(1-\hat{x})_+ (1-\hat{z})_+} - 8\delta(1-\hat{x})\delta(1-\hat{z}) \Bigg], \end{aligned} \tag{3.10}$$

where the "+"-distribution is defined as usual. The expression on the right-hand side is in fact identical to the one for the unpolarized coefficient function near threshold [63]. At the kth order of perturbation theory, the coefficient function contains terms of the form $\alpha_s^k \delta(1-\hat{x}) \left(\frac{\ln^{2k-1}(1-\hat{z})}{1-\hat{z}} \right)_+$, $\alpha_s^k \delta(1-\hat{z}) \left(\frac{\ln^{2k-1}(1-\hat{x})}{1-\hat{x}} \right)_+$, or "mixed" distributions $\alpha_s^k \left(\frac{\ln^m(1-\hat{x})}{1-\hat{x}} \right)_+ \left(\frac{\ln^n(1-\hat{z})}{1-\hat{z}} \right)_+$ with $m+n = 2k-2$, plus terms less singular by one or more logarithms. Again, each of these terms will appear equally in the unpolarized and in the polarized coefficient function. The reason for this is that the terms are associated with emission of soft gluons [63], which does not care about spin. Threshold resummation addresses the large logarithmic terms to all orders in the strong coupling. The resummation for the case of SIDIS was carried out in [63]. Given these results and the equality of the spin-averaged and spin-dependent coefficient functions near threshold, it is relatively straightforward to perform the resummation for the polarized case. Having the resummation for both g_1^h and F_1^h, we obtain resummed predictions for the experimentally relevant spin asymmetry A_1^h.

In [63, 93, 99] threshold resummation for SIDIS was derived using an eikonal approach, for which exponentiation of the threshold logarithms is achieved in Mellin space. One takes Mellin moments of g_1^h separately in the two independent variables x and z [105, 110]:

$$\tilde{g}_1^h(N, M, Q^2) \equiv \int_0^1 dx\, x^{N-1} \int_0^1 dz\, z^{M-1}\, g_1^h(x, z, Q^2). \tag{3.11}$$

With this definition, Eq. (3.4) takes the form (again at scale $\mu = Q$)

$$2\tilde{g}_1^h(N, M, Q^2) \;=\; \sum_{f,f'=q,\bar{q},g} \Delta\tilde{f}^N(Q^2) \times \Delta\tilde{\mathcal{C}}_{f'f}(N, M, \alpha_s(Q^2))\tilde{D}_{f'}^{h,M}(Q^2)\,, \tag{3.12}$$

where the moments of the polarized parton distributions and the fragmentation functions are defined as

$$\begin{aligned} \Delta\tilde{f}^N(Q^2) \;&\equiv\; \int_0^1 dx\, x^{N-1}\Delta f(x, Q^2), \\ \tilde{D}_{f'}^{h,M}(Q^2) \;&\equiv\; \int_0^1 dz\, z^{M-1} D_{f'}^h(z, Q^2), \end{aligned} \tag{3.13}$$

and the double Mellin moments of the polarized coefficient functions are

$$\Delta\tilde{\mathcal{C}}_{f'f}\left(N, M, \alpha_s(Q^2)\right) \;\equiv\; \int_0^1 d\hat{x}\, \hat{x}^{N-1} \int_0^1 d\hat{z}\, \hat{z}^{M-1} \times \Delta\mathcal{C}_{f'f}\left(\hat{x}, \hat{z}, 1, \alpha_s(Q^2)\right)\,. \tag{3.14}$$

Large $\hat{x}$ and $\hat{z}$ in $\Delta\mathcal{C}_{f'f}$ correspond to large N and M in $\Delta\tilde{\mathcal{C}}_{f'f}$, respectively.

The resummed spin-dependent coefficient function is identical to the spin-averaged one of [63] and reads to next-to-leading logarithmic accuracy in the $\overline{\text{MS}}$-scheme:

$$\Delta\tilde{\mathcal{C}}_{qq}^{\text{res}}(N, M, \alpha_s(Q^2)) = e_q^2 H_{qq}\left(\alpha_s(Q^2)\right) \times \exp\left[2\int_{\frac{Q^2}{\bar{N}\bar{M}}}^{Q^2} \frac{dk_\perp^2}{k_\perp^2} A_q\left(\alpha_s(k_\perp^2)\right) \ln\left(\frac{k_\perp}{Q}\sqrt{\bar{N}\bar{M}}\right)\right], \tag{3.15}$$

where $\bar{N} \equiv N e^{\gamma_E}$, $\bar{M} \equiv M e^{\gamma_E}$, with γ_E the Euler constant, and

$$A_q(\alpha_s) = \frac{\alpha_s}{\pi} A_q^{(1)} + \left(\frac{\alpha_s}{\pi}\right)^2 A_q^{(2)} + \ldots \tag{3.16}$$

is a perturbative function. The coefficients required to NLL read

$$A_q^{(1)} = C_F, \quad A_q^{(2)} = \frac{1}{2} C_F \left[C_A \left(\frac{67}{18} - \frac{\pi^2}{6} \right) - \frac{5}{9} N_f \right], \tag{3.17}$$

where $C_F = 4/3$, $C_A = 3$ and N_f is the number of active flavors. Furthermore,

$$H_{qq}(\alpha_s) = 1 + \frac{\alpha_s}{2\pi} C_F \left(-8 + \frac{\pi^2}{3} \right) + \mathcal{O}(\alpha_s^2) \, . \tag{3.18}$$

The explicit NLL expansion of the exponent in (3.15) can be found in Chapter 2.

The polarized moment-space structure function $\tilde{g}_1^{h,\mathrm{res}}$ resummed to NLL is obtained by inserting the resummed coefficient function into in Eq. (3.12). To get the physical hadronic structure function $g_1^{h,\mathrm{res}}$ one needs to take the Mellin inverse of the moment-space expression. As in [63], we choose the required integration contours in complex N, M-space according to the *minimal prescription* of [64], in order to properly deal with the singularities arising from the Landau pole due to the divergence of the perturbative running strong coupling constant α_s at scale Λ_{QCD}. Moreover, we match the resummed $g_1^{h,\mathrm{res}}$ to its NLO value, *i.e.* we subtract the $\mathcal{O}(\alpha_s)$ expansion from the resummed expression and add the full NLO result:

$$g_1^{h,\mathrm{match}} \equiv g_1^{h,\mathrm{res}} - g_1^{h,\mathrm{res}} \Big|_{\mathcal{O}(\alpha_s)} + g_1^{h,\mathrm{NLO}} \, . \tag{3.19}$$

The final resummed and matched expression for the spin asymmetry A_1^h is then given by

$$A_1^{h,\mathrm{res}}(x, z, Q^2) \equiv \frac{g_1^{h,\mathrm{match}}(x, z, Q^2)}{F_1^{h,\mathrm{match}}(x, z, Q^2)} \, . \tag{3.20}$$

Similar considerations can be made for inclusive DIS, where again the resummation for g_1 proceeds identically to that of F_1 in moment space. Only single Mellin moments of the structure function have to be taken:

$$\tilde{g}_1(N, Q^2) \equiv \int_0^1 dx \, x^{N-1} \, g_1(x, Q^2). \tag{3.21}$$

The threshold resummed coefficient function is the same as in the spin-averaged case and is discussed for example in [63]. We note that the outgoing quark in the process $\gamma^* q \to q$ remains “unobserved” in inclusive DIS. At higher orders this is known to generate Sudakov *suppression* effects [134] that counteract the Sudakov enhancement associated with soft-gluon radiation from the initial quark. This is in contrast to SIDIS, where the outgoing quark fragments and hence is “observed”, so that both the initial and the final quark contribute to Sudakov enhancement. As a result, resummation effects are generally larger in SIDIS than in DIS, for given kinematics.

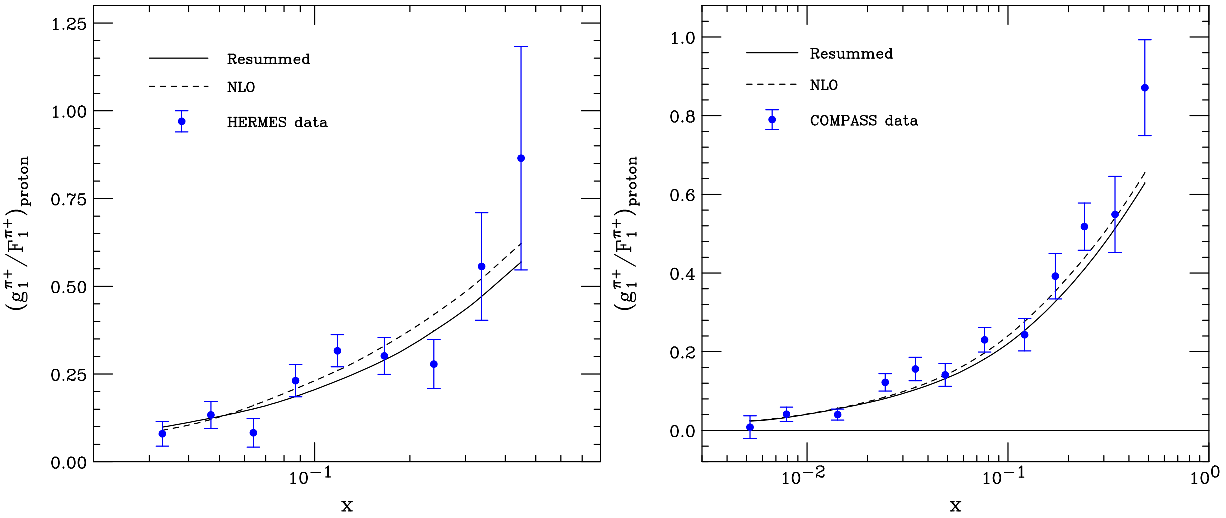

Figure 3.1: On the left side: Spin asymmetry for semi-inclusive π^+ production off a proton target. The data points are from [121] and show statistical errors only. The $\langle x \rangle$ and $\langle Q^2 \rangle$ values were taken accordingly to the HERMES measurements. On the right side: Same but comparing to the COMPASS measurements [122].

3.3 Phenomenological results

We now analyze numerically the impact of threshold resummation on the semi-inclusive and inclusive DIS asymmetries A_1^h and A_1. Given that the resummed exponents are identical for the spin-averaged and spin-dependent structure functions, we expect the resummation effects to be generally very modest. On the other hand, it is also clear that the effects will not cancel identically in the spin asymmetries: Even though the resummed exponents for g_1 and F_1 are identical in Mellin-moment space, they are convoluted with different parton distributions and hence no longer give identical results after Mellin inversion. Moreover, the matching procedure also introduces differences since the NLO coefficient functions are somewhat different for g_1 and F_1. It is therefore still relevant to investigate the impact of resummation on the spin asymmetries. We will compare our results to data sets from HERMES [121] and COMPASS [122, 124]. In addition, we present some results relevant for measurements at the Jefferson Laboratory [125–127], in particular those to be carried out in the near future after the CEBAF upgrade to 12 GeV [119].

For our calculations we use the NLO polarized parton distribution functions of [128, 129] and the unpolarized ones of [135]. Our choice of the latter is motivated by the fact that this set was also adopted as the baseline unpolarized set in [128, 129], so that the two sets are consistent in the sense that the same strong coupling constant is used. Additionally, in the case of SIDIS we choose the "de Florian-Sassot-Stratmann" [71] NLO set of fragmentation functions. In this work, we choose to focus only on pions in the final state. Resummation effects for other hadrons will be very similar. The factorization and renormalization scales are set to Q.

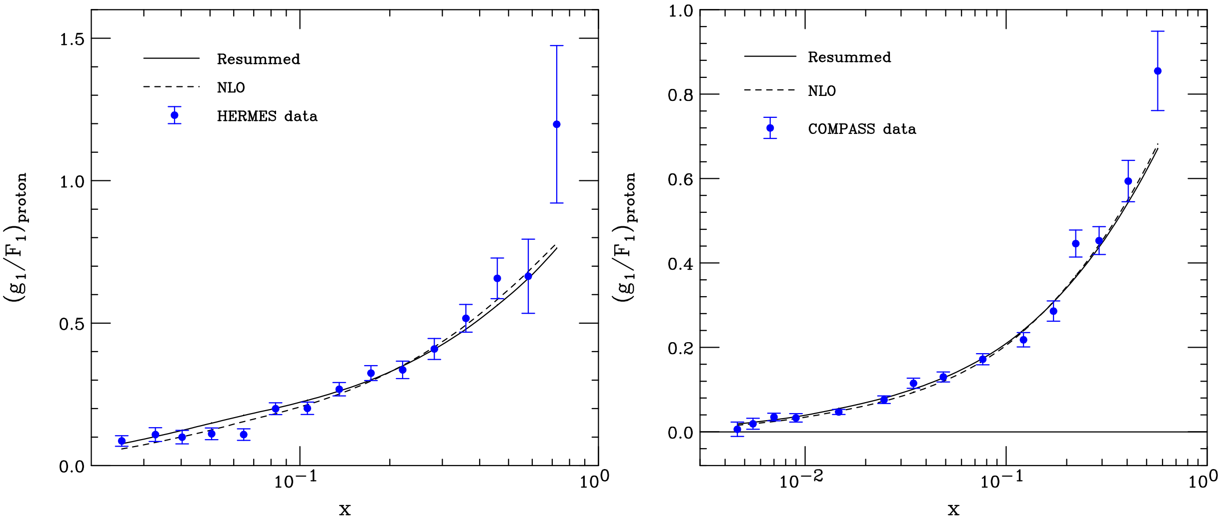

Figure 3.2: On the left side: Spin asymmetry for inclusive polarized DIS off a proton target. The data points are from [123] and show statistical errors only. The $\langle x\rangle$ and $\langle Q^2\rangle$ values were taken accordingly to the HERMES measurements. On the right side: but comparing to the COMPASS measurements [124].

On the left sides of Figures 3.1 and 3.2, we present comparisons of our resummed calculations with HERMES data [121] for semi-inclusive (π^+) and inclusive DIS, respectively, both off a proton target at $\sqrt{s} \approx 7.25$ GeV. The error bars show the statistical uncertainties only. For the SIDIS asymmetry, we integrate the numerator and the denominator of Eq. (3.2) separately over a region of $0.2 < z < 0.8$. We plot the theoretical results at the average values of x and Q^2 of each data point and connect the points by a line. The figures show the NLO (dashed lines) and the resummed-matched (solid lines) results. As one can see, the higher-order effects generated by resummation are indeed fairly small, although not negligible. They are overall more significant for SIDIS, which is expected due to the additional threshold logarithms in SIDIS (see discussion at the end of Sec. 3.2.2). We expect the resummed results to be most reliable at rather high values of $x \gtrsim 0.2$ or so [63]. In this regime, there is a clear pattern that resummation tends to decrease the spin asymmetries compared to NLO, more pronounced so for SIDIS. In other words, higher-order corrections enhance the spin-averaged cross section somewhat more strongly than the polarized one.

On the right sides of Figures 3.1 and 3.2, we show similar comparisons to the SIDIS and DIS asymmetries measured by COMPASS [122, 124] with a polarized muon beam at $\sqrt{s}$ ≈17.4 GeV. For COMPASS kinematics Alekseev:2010hcthe effects of threshold resummation are overall somewhat smaller due to the fact that one is further away from partonic threshold because of the higher center-of-mass energy. However, the results remain qualitatively similar to what we observed for HERMES kinematics.

The inclusive *neutron* spin asymmetry is particularly interesting from the point of view of resummation, since it is known [125, 126] to exhibit a sign change at fairly large values of x. Near a zero of the

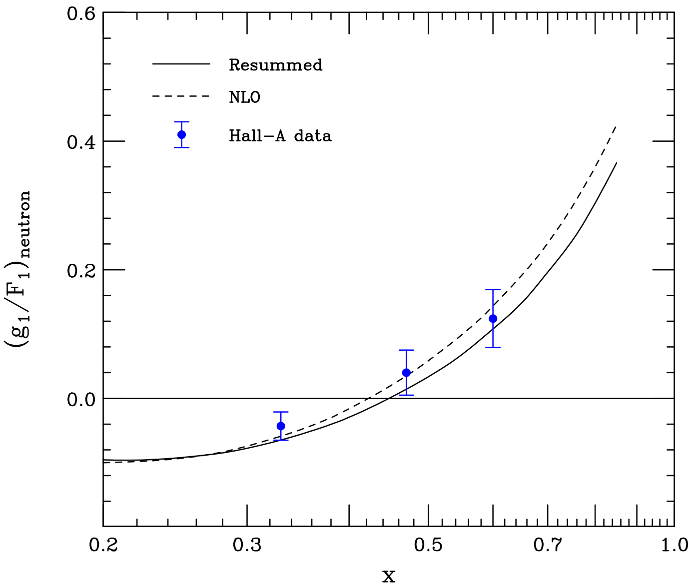

Figure 3.3: Spin asymmetry for inclusive polarized DIS off a neutron target. The data points are from [125, 126] and show statistical errors only. The Q^2 values in the theoretical calculation were chosen as $Q^2 = x \times 8$ GeV^2.

polarized cross section resummation effects are expected to be particularly relevant. Figure 3.3 shows the asymmetry at NLO and for the NLL resummed case. For illustration, we show the presently most precise data available, which are from the Hall-A Collaboration [125, 126] at the Jefferson Laboratory. In order to mimic the correlation of x and Q^2 for the present Jefferson Lab kinematics, we choose $Q^2 = x \times 8$ GeV^2 in the theoretical calculation. As one can see, the effects of resummation are indeed more pronounced than for the inclusive proton structure functions considered in Fig. 3.2. Evidently the zero of the asymmetry shifts slightly due to resummation. On the other hand, the asymmetry is overall still quite stable with respect to the resummed higher order corrections. The latter observation is quite relevant for the extraction of polarized large-x parton distributions from data for proton and neutron spin asymmetries in lepton scattering. For instance, to good approximation [125, 126] one may use the inclusive structure functions to directly determine the combinations $(\Delta u + \Delta \bar{u})/(u + \bar{u})$ and $(\Delta d + \Delta \bar{d})/(d + \bar{d})$. At lowest order, and neglecting the contributions from strange and heavier quarks and antiquarks, one has

$$\begin{aligned} R_u &\equiv \frac{\Delta u + \Delta \bar{u}}{u + \bar{u}}(x, Q^2) = \frac{4g_{1,\mathrm{p}} - g_{1,\mathrm{n}}}{4F_{1,\mathrm{p}} - F_{1,\mathrm{n}}}(x, Q^2)\,, \\ R_d &\equiv \frac{\Delta d + \Delta \bar{d}}{d + \bar{d}}(x, Q^2) = \frac{4g_{1,\mathrm{n}} - g_{1,\mathrm{p}}}{4F_{1,\mathrm{n}} - F_{1,\mathrm{p}}}(x, Q^2)\,, \end{aligned} \tag{3.22}$$

where the subscripts p,n denote a proton or neutron target, respectively. One may therefore determine $(\Delta u + \Delta \bar{u})/(u + \bar{u})$ and $(\Delta d + \Delta \bar{d})/(d + \bar{d})$ directly from experiment by using measured structure func-

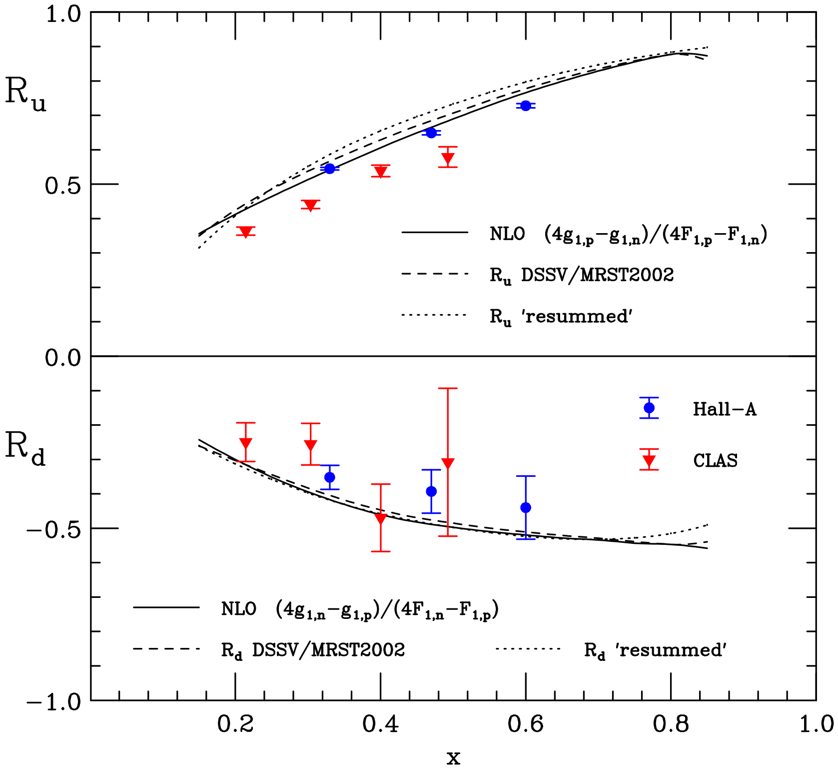

Figure 3.4: High-x up and down polarizations $(\Delta u + \Delta\bar{u})/(u+\bar{u})$ and $(\Delta d + \Delta\bar{d})/(d+\bar{d})$. The solid lines show the ratios of structure functions on the right-hand sides of Eq. (3.22), while the dashed lines show the actual parton distribution ratios as represented by the NLO sets of [128, 129] and [135]. The dotted lines show the expected shift of the distributions when resummation effects are included in their extraction, using Eq. (3.23). The Q^2 values in the theoretical calculation were chosen as $Q^2 = x \times 8$ GeV^2. We also show the present Hall-A [125, 126] and CLAS [127] data obtained from inclusive DIS measurements. Their error bars are statistical only.

tions $g_{1,\mathrm{p}}, g_{1,\mathrm{n}}, F_{1,\mathrm{p}}, F_{1,\mathrm{n}}$ in (3.22). Up to certain refinements required by the fact that measurements of the ratios $g_{1,\mathrm{p}}/F_{1,\mathrm{p}}$ and $g_{1,\mathrm{n}}/F_{1,\mathrm{n}}$ are more readily available than those of the individual structure functions, this is essentially the approach used by the Hall-A Collaboration (alternatively, one may also use the corresponding spin asymmetry for the deuteron instead of the neutron one [127]). In the following we explore the typical size of the corrections to the ratios due to higher orders. Figure 3.4 shows first of all the structure function ratios on the right-hand side of (3.22), computed at NLO using as before the polarized and unpolarized parton distribution functions of [128, 129] and [135], respectively (solid lines). We have again chosen $Q^2 = x \times 8\ \mathrm{GeV}^2$. Using (3.22), these ratios would correspond to the "direct experimental determinations" of R_u and R_d. The dashed lines in the figure show the actual ratios $(\Delta u + \Delta\bar{u})/(u + \bar{u})$ and $(\Delta d + \Delta\bar{d})/(d + \bar{d})$ as given by the sets of parton distribution functions that we use. Any difference between the solid and dashed lines is, therefore, a measure of the significance of effects related to strange quarks and antiquarks, and to NLO corrections. As one can see, these have relatively modest size. Finally, we estimate the potential effect of resummation on R_u, R_d: Following [60, 136], we define 'resummed' quark (and antiquark) distributions by demanding that their contributions to the structure functions g_1, F_1 match those of the corresponding NLO distributions, which is ensured by setting

$$\tilde{q}^{N,\mathrm{res}}(Q^2) \equiv \frac{\tilde{\mathcal{C}}_q^{\mathrm{NLO}}(N, \alpha_s(Q^2))}{\tilde{\mathcal{C}}_q^{\mathrm{res}}(N, \alpha_s(Q^2))} \tilde{q}^{N,\mathrm{NLO}}(Q^2) \tag{3.23}$$

in Mellin-moment space. Here, $\tilde{\mathcal{C}}_q^{\mathrm{NLO}}$ and $\tilde{\mathcal{C}}_q^{\mathrm{res}}$ are the NLO and resummed quark coefficient functions for the inclusive structure function F_1, respectively. We match the resummed coefficient function to the NLO one by subtracting out its NLO contribution and adding the full NLO one, in analogy with (3.19). Equation (3.23) can be straightforwardly extended to the spin-dependent case. The ratios R_u, R_d for these 'resummed' parton distributions are shown by the dotted lines in Fig. 3.4. As one can see, they are quite close to the other results, indicating that resummation is not likely to induce very large changes in the parton polarizations extracted from future high-precision data. For illustration, we also show the Hall-A [125, 126] and CLAS [127] data in the figure, which have been obtained using parton-model relations for the inclusive structure functions, similar to (3.22). One can see that the error bars of the data are presently still larger than the differences between our various theoretical results. This situation is expected to be improved with the advent of the Jefferson Lab 12-GeV upgrade [119] or an Electron Ion Collider [137]. As is well-known, SIDIS measurements provide additional information on R_u, R_d, albeit so far primarily at lower x [121].

3.4 Conclusions

We have investigated the size of threshold resummation effects on double-longitudinal spin asymmetries for inclusive and semi-inclusive deep inelastic scattering in fixed-target experiments. Overall, the asymmetries are rather stable with respect to resummation, in particular for the inclusive case. Towards large values of x, resummation tends to cause a decrease of the spin asymmetries, which is more pronounced in the semi-inclusive case and for asymmetries measured off neutron targets.

The relative robustness of the spin asymmetries bodes well for the extraction of high-x parton polarizations $(\Delta u + \Delta \bar{u})/(u + \bar{u})$ and $(\Delta d + \Delta \bar{d})/(d + \bar{d})$, which are consequently also rather robust. Nevertheless, knowledge of the predicted higher-order corrections should be quite relevant when future high-statistics large-x data become available. On the theoretical side, it will be interesting to study the interplay of our perturbative corrections with power corrections that are ultimately also expected to become important at high-x [112, 132, 138–142], although it appears likely that present data are in a window where the perturbative corrections clearly dominate. Finally, we note that related large-x logarithmic effects have also been investigated for the nucleon's light cone wave function [143], where they turn out to enhance components of the wave function with non-zero orbital angular momentum, impacting the large-x behavior of parton distributions. It will be very worthwhile to explore the possible connections between the logarithmic corrections discussed here and in [143].

CHAPTER 4

INTERPLAY OF THRESHOLD RESUMMATION AND HADRON MASS CORRECTIONS IN DEEP INELASTIC PROCESSES

We discuss hadron mass corrections and threshold resummation for deep-inelastic scattering $\ell N \to \ell' X$ and semi-inclusive annihilation $e^+e^- \to hX$ processes, and provide a prescription how to consistently combine these two corrections respecting all kinematic thresholds. We find an interesting interplay between threshold resummation and target mass corrections for deep-inelastic scattering at large values of Bjorken x_B. In semi-inclusive annihilation, on the contrary, the two considered corrections are relevant in different kinematic regions and do not affect each other. A detailed analysis is nonetheless of interest in the light of recent high precision data from BaBar and BELLE on pion and kaon production, with which we compare our calculations. For both deep inelastic scattering and single inclusive annihilation, the size of the combined corrections compared to the precision of world data is shown to be large. Therefore, we conclude that these theoretical corrections are relevant for global QCD fits in order to extract precise parton distributions at large Bjorken x_B, and fragmentation functions over the whole kinematic range. This Chapter is based on publication [iii].

4.1 Introduction

Predictions from QCD rely on perturbative calculations of parton-level hard scattering processes as well as on non-perturbative input in the form of parton distribution functions and fragmentation functions. On the one hand, PDFs contain information about the distributions of quarks and gluons in hadrons, which is relevant for processes with initial-state hadrons. On the other hand, FFs describe the fragmentation of an outgoing parton into the observed hadron and, to some extent, may be viewed as the final-state analogue of PDFs. The applicability of this framework within perturbative QCD was established in factorization theorems [5] allowing one to absorb long-distance dynamics into these two universal non-perturbative objects. Therefore, the predictive power of QCD relies crucially on the precise knowledge of PDFs and FFs, that are nowadays extracted from a global analysis of a wide set of experimental data, see Refs. [144–146] for recent reviews.

Modern PDF fits [115, 147–149] are available within a next-to-leading order framework and most of them also at (partial) next-to-next-to-leading order. Key data sets for the extraction of PDFs are provided by measurements of inclusive deep-inelastic scattering $\ell N \to \ell' X$, which is one of the two processes that we are considering in this work. Despite a lot of progress in the past years, large uncertainties are still present for large values of the parton momentum fraction x [150]. As it turns out, it is precisely this region that is particularly relevant at the LHC, when trying to find signals of new physics in, for example, (di-)jet measurements [151, 152]. Furthermore, the large-x region is also interesting as it can provide a window into the non-perturbative dynamics of the color confinement mechanism holding quarks and gluons inside hadrons [153, 154].

On the experimental side, improvements for the gluon PDF at large-x can be obtained from jet data taken at the Tevatron and the LHC, direct photon production in fixed target experiments, and from longitudinal DIS structure functions. Concerning quark PDFs, the present focus is mostly on low-energy experiments carried out for example at JLab [155], with important information coming from directly reconstructed W charge asymmetries at the Tevatron [150]. On the theoretical side a number of corrections to the pQCD calculations of these events are needed in order to harvest fully the available and upcoming experimental data, and extract precise large-x quark and gluon PDFs from global QCD fits. These corrections include, in particular, resummation of threshold logarithms, Target Mass Corrections (TMCs), higher-twist diagrams, and nuclear corrections when nuclear targets are considered. The last three have been included consistently, for example, in the CTEQ-JLab collaboration PDF fits [147] and the fits by Alekhin and collaborators [156], allowing one to substantially extend the range in x of the fitted DIS data (see also [157] for the interplay of TMC, higher-twists and higher order perturbative corrections). Threshold resummation, however, has been considered so far only to estimate the theoretical errors of PDFs or used in fits of only a subset of the data [136, 158–160], but has not yet been fully included for all relevant data sets in a global QCD fit.

In the first part of this work, we consider the interplay between two major corrections to the standard NLO formalism for DIS both of which have their greatest impact at large-x, namely TMCs and higher order contributions derived from threshold resummation. Here we choose the collinear factorization TMC framework of Accardi and Qiu [47], that contrary to most other approaches [161, 162] respects the kinematic $x_B \leq 1$ bound on the Bjorken variable. Threshold resummation for QCD processes was derived in [6, 8, 94, 95] and recently revisited in [63, 163, 164]. Large logarithms that need to be resummed to all orders arise near the phase space boundary where gluon radiation is limited. We perform the resummation at the level of next-to-leading logarithmic accuracy. In particular, we derive a resummation procedure that also respects the Bjorken x_B bound when a non-zero target mass is considered, and can therefore be consistently combined with the TMC calculation. We discuss the interplay of both kinds of corrections, and assess their relevance for PDF global fits by comparing them to a selection of world data on DIS scattering.

Unlike for PDFs, global fits of FFs [71–76] are less constrained by presently existing data sets. One of the main sources of constraints on FFs is semi-inclusive annihilation (SIA) $e^+e^- \to hX$ which we are going to consider in this work. Recently, very precise data sets from BELLE [10] and BaBar [11] became available, where the statistical accuracy is partially in the sub one percent level. In addition, a very fine binning was applied over a wide range of the fragmentation variable $x_E = 2E^h/\sqrt{s}$ reaching up to ≈ 0.95. Here, E^h is the energy of the observed hadron in the center-of-mass system (c.m.s.) and $\sqrt{s} = 10.5$ GeV is the energy for collisions at both experiments. This offers a new possibility for studying effects that go beyond the standard NLO framework and for learning more about QCD dynamics in fragmentation processes. On the theory side, the present day state of the art is NLO in QCD. Several additional effects, including small-x resummation, threshold resummation and hadron mass effects have been studied in [73, 165].

In the second part of this Chapter we revisit calculations of hadron mass corrections (HMCs) and threshold resummation in analogy to our DIS analysis. We present for the first time (to our knowledge) a resummed calculation for kaon SIA events, and compare our kaon and pion production cross section to the recent BELLE and BaBar data. In contrast to the Operator Product Expansion based formalism for mass corrections, the approach in [47] may be generalized to other processes, such as semi-inclusive deep-inelastic scattering [141]. Here we extend this framework to SIA in electron-positron scattering, we perform a detailed analysis of the effects of the produced hadron mass on the parton-level kinematics, and evaluate their numerical consequences. We note that previous studies of HMCs were carried out in [73, 165], showing in particular that inclusion of these HMCs in global FF fits results in better χ^2 values. We then consider the combination with threshold resummation [99] in the framework of the so-called "crossed resummation" [93], that exploits similarities between various color-singlet QCD processes such as DIS, SIA, Drell-Yan, and semi-inclusive deep-inelastic scattering. We will again also build upon the recent threshold resummation studies in [63, 163, 164]. Contrary to DIS, we find that HMCs are dominant at low x_E, whereas threshold resummation is again most relevant for large x_E. We analyze the crosstalk of these effects and evaluate their relevance to global FF fits by comparing these to the new data sets from BELLE and BaBar.

This Chapter is organized as follows. In Sec. 4.2, we discuss TMCs and threshold resummation in DIS before we derive our prescription to combine both. In order for this Chapter to be self-contained, we briefly review the TMC derivation of [47], and provide some basic formulas concerning threshold resummation in order to establish our notation. Then, we analyze the numerical relevance of the corrections, and compare these to a selection of world DIS data. In Sec. 4.3, we discuss SIA following the same steps as for the DIS case before, and compare our numerical results to the recent BELLE and BaBar data on pion and kaon production. Finally, we draw our conclusions in Sec. 9.5.

4.2 Target Mass Corrections and Resummation for DIS

4.2.1 Target Mass Corrections

In DIS, a parton of momentum k belonging to a nucleon of momentum p is struck by a virtual photon of momentum q. This generates in the final state a target jet with momentum p_Y and a current jet with momentum p_j, see Fig. 4.3. We work in a "collinear" frame where the spacial components of p and

q are parallel and directed along the longitudinal axis, and we parametrize the involved the momenta p, q, k following [47]:

$$\begin{aligned} p^\mu &= p^+\bar{n}^\mu + \frac{m_N^2}{2p^+}n^\mu\,, \\ q^\mu &= -\xi p^+\bar{n}^\mu + \frac{Q^2}{2\xi p^+}n^\mu\,, \\ k^\mu &= xp^+\bar{n}^\mu + \frac{k^2+k_T^2}{2xp^+}n^\mu + \boldsymbol{k}_T^\mu\,, \end{aligned} \tag{4.1}$$

In this expression p^+ can be regarded as a parameter for boosts along the longitudinal axis. The light-cone vectors n^μ and $\bar{n}^\mu$ satisfy

$$n^2 = \bar{n}^2 = 0 \quad n\cdot\bar{n} = 1\,, \tag{4.2}$$

and the plus- and minus- components of a general 4-vector a are given by

$$a^+ = a\cdot n \quad a^- = a\cdot\bar{n}. \tag{4.3}$$

The momenta are parametrized in terms of the external (*i.e.*, experimentally measurable) variables

$$x_B = \frac{-q^2}{2p\cdot q}, \quad Q^2 = -q^2, \quad p^2 = m_N^2\,, \tag{4.4}$$

where m_N is the target mass and Q^2 the photon virtuality. The parton fractional light-cone momentum with respect to the nucleon is a kinematic internal (*i.e.*, non measurable) variable and is defined by

$$x = \frac{k^+}{p^+}. \tag{4.5}$$

In an analogous way we can define the virtual boson fractional momentum as

$$\xi = -\frac{q^+}{p^+} = \frac{2x_B}{1+\sqrt{1+4x_B^2m_N^2/Q^2}}, \tag{4.6}$$

which is an external kinematic variable and coincides with the Nachtmann variable [166]. The target's mass can be neglected in the Bjorken limit $Q^2 \gg m_N^2$ at fixed x_B, and in many analysis is omitted from the outset. (This is fine for unpolarized scattering but poses problems for the definition of the nucleon's spin in the case of polarized scattering.) In this Chapter we explicitly work at finite Q^2 and verify that our result correctly reproduces the "massless target" formulas in the Bjorken limit, where $\xi \to x_B$.

In order to perform collinear factorization of the DIS structure functions, one expands the momentum k of the struck parton around its positive light-cone component $xp^+\bar{n}^\mu$, and neglects in the kinematics the transverse components, as well as (for light quarks) the negative light-cone component.

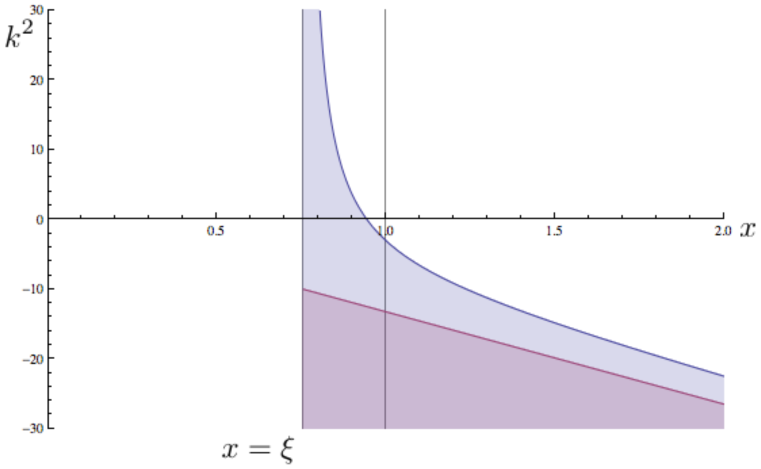

Figure 4.1: $k^2 - x$ plot for DIS based on Eqs. (4.8) and (4.12). The allowed values for k^2 are shown in light blue.

This is equivalent to kinematically treating the parton as massless and collinear to the parent nucleon from the very beginning, and setting $k^2 = 0$ and ${\boldsymbol{k}_T}^\mu = 0$ in Eq. (4.1) from the beginning. However, for now we choose to leave $k^2 \neq 0$ in order to better contrast the situation for DIS to SIA in Section 4.3.

The parton's momentum fraction x then appears as an integration variable in the structure functions, that are given by a convolution integral of perturbatively calculable coefficient functions and non-perturbative PDFs [5, 167]. Following [47], we may derive limits on the dx integration by examining both the external and internal kinematics of the diagram shown in Fig. 4.3, and apply four momentum and net baryon number conservation. This latter, in particular requires that at least one baryon of mass larger than m_N be present in the final state. This can appear in either the target jet (lower right part in Fig. 4.3) or the current jet (upper right part in Fig. 4.3). Unless the rapidity difference between the current jet and the target jet is too small [168, 169], the baryon mass appears in the latter [47], so that $p_Y^2 \geq m_N^2$ and $p_j^2 \geq 0$. Next, considering four-momentum conservation the hard-scattering vertex we find

$$0 \leq p_j^2 = (q+k)^2 = \left(1 - \frac{\xi}{x}\right)\left(k^2 + \frac{Q^2 x}{\xi}\right) , \tag{4.7}$$

where we used the momenta defined in Eq. (4.1). Hence, we find the inequalities for x and k^2

$$\begin{aligned} x &\geq \xi \\ k^2 &\geq -\frac{Q^2 x}{\xi} . \end{aligned} \tag{4.8}$$

In order to obtain another constraint on the dx integration, it is not sufficient to analyze the other vertex. Instead, we have to consider the invariant momentum squared of the whole process:

$$(q+p)^2 = (p_j + p_Y)^2 \geq (q+k)^2 + m_N^2 . \tag{4.9}$$

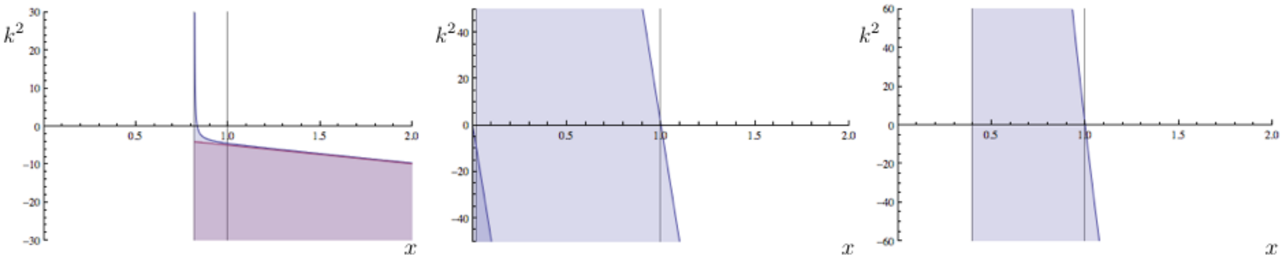

Figure 4.2: Allowed range for x and k^2 in DIS. The situation for $x_B \to 1$ (left), $x_B \to 0$ (middle) and $Q^2 \to \infty$ (right) is shown.

where we used $p_Y^2 \geq m_N$, as previously discussed, as well as $2p_j \cdot p_Y \geq 0$ since both final state jets consist of on-shell particles. Evaluating $(q+k)^2$ as before in Eq. (4.7) we finally obtain

$$1 - \frac{1}{x_B} \leq \left(1 - \frac{x}{\xi}\right)\left(1 + \frac{\xi}{x}\frac{k^2}{Q^2}\right) . \tag{4.10}$$

As a cross-check, we immediately find the result from [47] by setting $k^2 = 0$. The parton's fractional momentum x is kinematically bound by

$$\xi \leq x \leq \xi / x_B . \tag{4.11}$$

Now, leaving the virtuality $k^2 \neq 0$, we may deduce the allowed range for k^2 and x as follows. We choose to plot k^2 as a function of x by solving the inequality in Eq. (4.10) for k^2 as a function of x. We end up with

$$k^2 \leq -Q^2 \frac{x}{\xi}\left(\frac{x - \xi/x_B}{x - \xi}\right) , \tag{4.12}$$

which has a pole for $x = \xi$ corresponding to the lower limit on x. In addition, we find $k^2 \leq 0$ for $x = \xi/x_B$. The corresponding $k^2 - x$ plot is shown in Fig. 4.1. We choose the values $m_N^2 = 1\,\mathrm{GeV}^2$, $Q^2 = 10\,\mathrm{GeV}^2$, $x_B = 0.8$ in order to illustrate the most characteristic features. Additionally, we are obviously required to choose $x < 1$. Let us consider the limits of large and small x_B, *i.e.* $x_B \to 1, 0$. For large x_B, we find an upper k_+^2 and lower k_-^2 limit for k^2 which is

$$k_+^2 = k_-^2 = -\frac{Q^2 x}{\xi_{\mathrm{th}}} . \tag{4.13}$$

In other words, we find that the upper limit k_+^2 converges against the lower limit k_-^2. For small x_B, we find

$$\begin{aligned} k_+^2 &= -\frac{Q^2 x}{x_B} , \\ k_-^2 &= -\frac{Q^2}{x_B}(x-1) . \end{aligned} \tag{4.14}$$

Hence, they only differ by a shift in $x \to x - 1$. These two situations are illustrated in Fig. 4.2. In general, we find that the choice of the parton's virtuality $k^2 = 0$ is always allowed. However, there

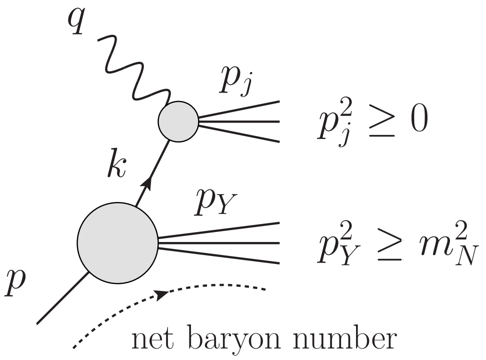

Figure 4.3: Diagram for DIS specifying all momenta. The net baryon number is shown to flow into the target jet. Figure taken from [47].

is no particular choice for k^2 that appears as the "natural" choice. This situation is very different to what we will find for SIA in Section 4.3.

The structure functions including the finite target mass kinematics we have discussed can be written in collinear factorization at leading twist as [47, 142]

$$\begin{aligned}
\mathcal{F}_1^{\mathrm{TMC}}(x_B, Q^2) &\equiv 2F_1^{\mathrm{TMC}}(x_B, Q^2) = \mathcal{F}_1(\xi, Q^2)\,, \\
\mathcal{F}_2^{\mathrm{TMC}}(x_B, Q^2) &\equiv \frac{1}{x_B}F_2^{\mathrm{TMC}}(x_B, Q^2) = \frac{1}{\rho^2}\mathcal{F}_2(\xi, Q^2)\,, \\
\mathcal{F}_L^{\mathrm{TMC}}(x_B, Q^2) &\equiv \frac{1}{x_B}F_L^{\mathrm{TMC}}(x_B, Q^2) = \mathcal{F}_L(\xi, Q^2)\,,
\end{aligned} \tag{4.15}$$

where for convenience we defined

$$\rho^2 = 1 + \frac{4x_B^2 m_N^2}{Q^2}\ . \tag{4.16}$$

Note that we adopted the convention of Ref. [63, 109] for the $\mathcal{F}_i^{\mathrm{TMC}}$ structure functions in terms of the customary ones appearing in the Lorentz decomposition of the hadronic tensor satisfying $\mathcal{F}_L^{\mathrm{TMC}}(x_B, Q^2) = \rho^2\mathcal{F}_2^{\mathrm{TMC}}(x_B, Q^2) - \mathcal{F}_1^{\mathrm{TMC}}(x_B, Q^2)$. On the right hand side of Eq. (4.15), convolution integrals appear

$$\mathcal{F}_i(\xi, Q^2) = \sum_f \int_{\xi}^{\xi/x_B} \frac{dx}{x} f(x, \mu^2)\, \mathcal{C}_f^i\left(\frac{\xi}{x}, \frac{Q^2}{\mu^2}, \alpha_s(\mu^2)\right)\ , \tag{4.17}$$

where the integration over dx ranges only over the region allowed by the limits in Eq. (4.11). The notation we use implies that whenever the lower limit exceeds the upper limit the integral is zero, so that the structure functions are indeed zero in the kinematically forbidden region $x_B > 1$. The functions $f(x, \mu^2)$ denote the distribution of a parton of flavor f in the target nucleon and the sum runs over $f = q, \bar{q}, g$, with q a shorthand for all active quark flavors. We choose $\mu_R = \mu_F = \mu$. The hard-scattering coefficient functions $\mathcal{C}_f^i$ encode the short-distance hard scattering of the virtual photons with partons from the nucleon target, and are independent of the mass of the latter. They can be calculated in perturbative QCD order-by-order in powers of the strong coupling constant,

$$\mathcal{C}_f^i = C_f^{i,(0)} + \frac{\alpha_s(\mu^2)}{2\pi} C_f^{i,(1)} + \mathcal{O}(\alpha_s^2)\,, \tag{4.18}$$

which are related by $\mathcal{C}_f^L = \mathcal{C}_f^2 - \mathcal{C}_f^1$ for massless partons. For example, at leading-order (LO) we have

$$\begin{aligned} &C_{q,\bar{q}}^{2,(0)}(\hat{x}) = e_q^2 \delta(1-\hat{x}),\ C_g^{2,(0)}(\hat{x}) = 0\,, \\ &C_{q,\bar{q},g}^{L,(0)}(\hat{x}) = 0\,, \end{aligned} \tag{4.19}$$

with $\hat{x} = \xi/x$. F_2^{TMC} reduces to the target mass corrected version of the parton model [170, 171] except for a step function imposing the proper kinematic bounds:

$$F_2^{\mathrm{TMC}}(x_B, Q^2) = \frac{x_B}{\rho^2} \sum_{f=q,\bar{q}} e_f^2 f(\xi, Q^2) \theta(1-x_B)\,. \tag{4.20}$$

For completeness, we list all the relevant coefficient functions $\mathcal{C}_f^i$ up to NLO in Appendix C.

Note that in the large Q^2 limit (in which $M^2/Q^2 \to 0$), as well as in the small Bjorken-x limit $x_B \to 0$, the Nachtmann variable $\xi \to x_B$ and $\rho \to 1$, so that

$$\mathcal{F}_i^{\mathrm{TMC}}(x_B, Q^2) \to \mathcal{F}_i(x_B, Q^2) \tag{4.21}$$

and the usual massless target formulas are recovered. Conversely, in the $x_B \to 1$ limit, the Nachtmann variable $\xi \to \xi_{\mathrm{th}}$, where

$$\xi_{\mathrm{th}} = \frac{2}{1 + \sqrt{1 + 4m_N^2/Q^2}}\,, \tag{4.22}$$

and ξ differs maximally from x_B (see Fig. 4.4). Therefore, in this limit, TMC effects are the largest. Since the integral over dx is limited to the region defined by the kinematic bounds in Eq. (4.11), the structure functions $\mathcal{F}_i^{\mathrm{TMC}}$ have support only over the physical region at $x_B \leq 1$. This is the defining characteristics of the treatment of TMCs proposed in Ref. [47] and sets this apart from most other TMC prescriptions, that in fact violate that bound and allow for non-zero structure functions also at $x_B > 1$. When combining TMCs with threshold resummation in Section 4.2.3, we will pay special attention to preserve this feature of our TMC treatment and not introduce a spurious violation of the Bjorken-x bound.

4.2.2 Threshold Resummation for DIS

The DIS coefficient functions $\mathcal{C}_f^i$ contain singular distributions. Near threshold they can get large and weaken or even violate the convergence of the perturbative expansion in the strong coupling constant. Therefore, they have to be taken into account to all orders via threshold resummation. At NLO, singular distributions only appear in the structure function $\mathcal{F}_1$ (or equivalently $\mathcal{F}_2$) but not in $\mathcal{F}_L$. In

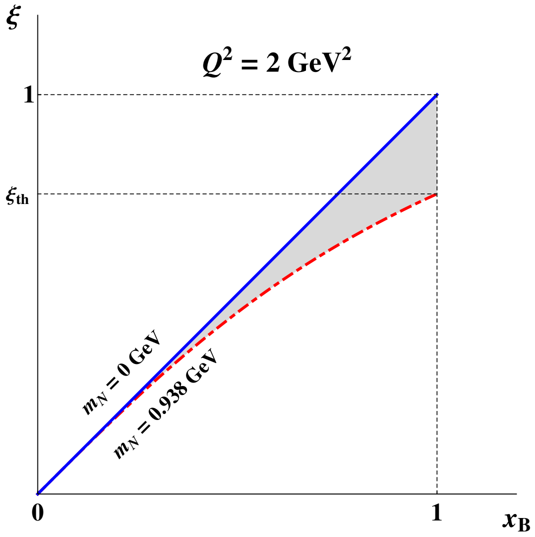

Figure 4.4: The Nachtmann variable ξ as a function of x_B with $m_N = 0$ GeV (solid blue line) and $m_N = 0.938$ GeV (dash-dotted red line) at $Q^2 = 2\ \text{GeV}^2$.

the $\overline{\text{MS}}$ scheme, they read

$$C^{1,(1)}_{q,\text{th}}(x) \quad = \quad C_F \left[(1+x^2) \left(\frac{\ln(1-x)}{1-x} \right)_+ - \frac{3}{2} \frac{1}{(1-x)_+} - \left(\frac{9}{2} + \frac{\pi^2}{3} \right) \delta(1-x) \right] , \tag{4.23}$$

where the plus-distribution is defined as

$$\int_0^1 dx\, f(x) [g(x)]_+ \equiv \int_0^1 dx\, (f(x) - f(1))\, g(x) \tag{4.24}$$

In general, at a given order k in the perturbative expansion, the coefficient function contains logarithms of the form

$$\alpha_s^k \left(\frac{\ln^n(1-x)}{1-x} \right)_+ , \quad \text{with } n \leq 2k-1 \,. \tag{4.25}$$

Performing the resummation at NLL, we fully take into account contributions down to $n = 2k-3$ at all orders. In other words, resummation at NLL accuracy sums up correctly the three most dominant towers of threshold logarithms. Results at next-to-next-to leading logarithmic accuracy were derived in [100, 101], where the next two subleading towers of threshold logarithms are also correctly taken into account. However, the main phenomenological effects are already captured at the level of NLL. In addition, the proposed prescription for combining TMC and resummation, as discussed in the next subsection, is independent of the accuracy of resummation that we are considering.

In the massless limit, $m_N^2/Q^2 \to 0$, resummation may be performed by introducing Mellin moments in x_B of the massless structure functions:

$$\begin{aligned}\mathcal{F}_1^N(Q^2) &= \int dx_B\, x_B^{N-1}\, \mathcal{F}_1(x_B, Q^2) \\ &= \mathcal{C}_f^{1,N}\left(Q^2/\mu^2, \alpha_s(\mu^2)\right) \cdot f^N(\mu^2)\,, \end{aligned} \tag{4.26}$$

where

$$\mathcal{C}_f^{1,N} = \left(\int_0^1 dx\, x^{N-1} \mathcal{C}_f^1\left(x, Q^2/\mu^2, \alpha_s(\mu^2)\right)\right) \tag{4.27}$$

$$f^N = \left(\int_0^1 dy\, y^{N-1} f(y, \mu^2)\right) \tag{4.28}$$

and the superscript N denotes the dependence on the complex Mellin variable N. The Mellin space expression of the NLO coefficient function up to terms that are suppressed as $\mathcal{O}(1/N)$ and choosing $\mu^2 = Q^2$ is given by

$$C_q^{1,(1),N} = C_F \left[\ln^2 \bar{N} + \frac{3}{2} \ln \bar{N} - \frac{9}{2} - \frac{\pi^2}{6}\right]\,, \tag{4.29}$$

where large logarithms in $\bar{N} = N e^{\gamma_E}$ correspond to large logarithms in $1 - x$ in Eq. (4.23). The resummed DIS coefficient function for the structure function $\mathcal{F}_1$ reads to NLL [8, 63, 93, 99]:

$$\mathcal{C}_{q,\mathrm{res}}^{1,N}(Q^2/\mu^2, \alpha_s(\mu^2)) \;=\; e_q^2 H_q\left(Q^2/\mu^2, \alpha_s(\mu^2)\right) \times \Delta_q^N(Q^2/\mu^2, \alpha_s(\mu^2))\, J_q^N(Q^2/\mu^2, \alpha_s(\mu^2))\,. \tag{4.30}$$

The radiative factor Δ_q^N describes gluon radiation from the initial quark that is both soft *and* collinear. The function J_q^N takes into account collinear (*i.e.* soft and hard) emissions from the unobserved parton in the final state. See Chapter 2 for further details concerning the functions Δ_q^N, J_q^N and H_q.

In the end, we go back to x-space by numerically performing the Mellin inverse, which is given by

$$\mathcal{F}_{1,\mathrm{res}}(x_B, Q^2) = \int_{\mathcal{C}_N} \frac{dN}{2\pi i}\, x_B^{-N} \times \mathcal{C}_{q,\mathrm{res}}^{1,N}(Q^2/\mu^2, \alpha_s(\mu^2))\, f^N(\mu^2)\,. \tag{4.31}$$

The contour $\mathcal{C}_N$ is taken to run between the rightmost pole of the moments of the PDFs and the Landau pole following the minimal prescription of [64]. After the Mellin inverse is taken, we match to the full NLO which is still a good approximation away from threshold. We avoid double counting of threshold distributions at NLO by considering the matched combination

$$\mathcal{F}_{\mathrm{match}} = \mathcal{F}_{\mathrm{res}} - \mathcal{F}_{\mathrm{res}}\big|_{\mathcal{O}(\alpha_s)} + \mathcal{F}_{\mathrm{NLO}}\,. \tag{4.32}$$

4.2.3 Combining TMC and Threshold Resummation

After target mass corrections, the integration over the parton's momentum fraction in the collinear factorization formula (4.17) ranges from ξ to ξ/x_B. As a consequence, the Mellin moments of the structure function are no longer the product of the moments of the coefficient function $\mathcal{C}_1$ and the

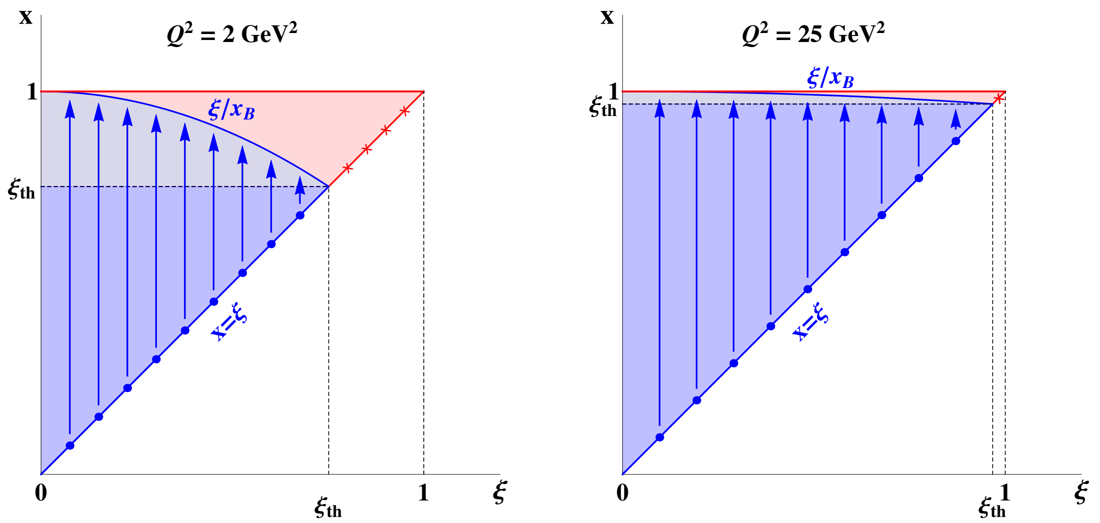

Figure 4.5: On the left (right) hand side the integration regions for $Q^2 = 2$ GeV^2 ($Q^2 = 25$ GeV^2) concerning Eq. (4.34) are shown. The blue dots denote the boundary where the threshold singularities arise and the arrows indicate the direction of integration.

parton distribution f. One therefore may be tempted to express the structure function (4.17) as

$$\mathcal{F}_1^{\text{TMC}} = \int_{\xi}^{1} \frac{dx}{x} \mathcal{C}_f^1\left(\frac{\xi}{x}\right) f(x) - \int_{\xi/x_B}^{1} \frac{dx}{x} \mathcal{C}_f^1\left(\frac{\xi}{x}\right) f(x)\,, \tag{4.33}$$

where for ease of notation we omitted any dependence of the coefficient functions and the PDFs on the scale Q^2/μ^2 and on $\alpha_s(\mu^2)$. The advantage of this reformulation is that the first term is integrated up to 1 (and differs from the Bjorken limit approximation only by a $x_B \to \xi$ replacement), so that its Mellin transform would indeed be given by the product of moments of the coefficient and parton distribution functions. However, written in this way, $\mathcal{F}_1^{\text{TMC}}$ acquires support also in the unphysical region $x_B > 1$, where it actually becomes negative after crossing 0 at $x_B = 1$.

A better way to manipulate the structure function convolution in Eq. (4.17) in order to obtain a product of moments after performing its Mellin transformation, is to write

$$\mathcal{F}_1^{\text{TMC}} = \int_{\xi}^{\xi_{\text{th}}} \frac{dx}{x} \mathcal{C}_f^1\left(\frac{\xi}{x}\right) f(x) + \int_{\xi_{\text{th}}}^{\xi/x_B} \frac{dx}{x} \mathcal{C}_f^1\left(\frac{\xi}{x}\right) f(x)\,. \tag{4.34}$$

In the small x_B limit only the first term on the right hand side survives, and the massless limit is recovered, as it should be. In the $x_B \to 1$ limit, each term separately tends to zero and remain zero for larger values of x_B. Therefore, the structure function as well remains zero in the unphysical region $x_B > 1$, as it happens with the original Eq. (4.17). This is then a good starting point for performing the resummation of threshold distributions in a way that respects the partonic and hadronic kinematics discussed in Section 4.2.1.

In order to get a deeper insight into the effects of TMCs on resummation, we can more closely analyze

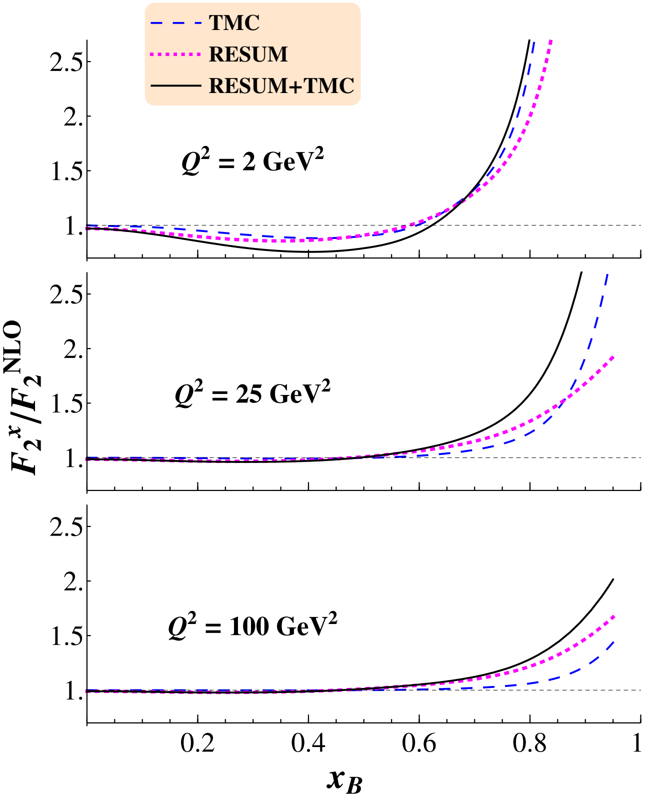

Figure 4.6: We show the effects of TMC (dashed blue), threshold resummation (dotted magenta) and the combination of both (solid black) normalized to NLO for the DIS structure function F_2 for different values of $Q^2 = 2,\ 25,\ 100\ \mathrm{GeV}^2$. The PDF set of [115] is used.

the integration region, that we depict in Fig. 4.5 for a small and a large value of Q^2. The partonic threshold for resummation is set by $x = \xi$, as indicated by the blue dots. Hence, we may view the effect of TMCs as cutting out the singularities lying at $x > \xi_{\mathrm{th}}$. As Q^2 increases, the amount of excluded singularities decreases, as can be seen from the diagram on the right. In the Bjorken limit ($Q^2 \to \infty$), ξ_{th} tends to 1, the integration region spans the whole triangle, and no singularity is excluded. Since the threshold for gluon radiation is set for $x \to \xi$ the threshold singularities appear only at the lower integration boundary of the first term, which is therefore the only one where large logarithms appear and need resummation. This can then be achieved without introducing a non-zero result for the resummed structure function in the unphysical region of $x_B > 1$ because the first term in Eq. (4.34) is zero at $x_B \geq 1$. In the second term, that also tends to zero as $x_B \to 1$, the threshold limit is not reached so that there is no need to regularize any of the terms in the coefficient function and we can treat this as part of the matching procedure to the full NLO calculation, see Eq. (4.32).

As in the massless target approximation, we derive threshold resummation in Mellin space but taking special care of the fact that at finite Q^2 the first term in Eq. (4.34) does not have the standard convolution structure as for the massless approximation of the structure functions. Taking Mellin moments with respect to ξ of the first term in Eq. (4.34) only, we obtain

$$\begin{aligned}
\mathcal{F}_1^{\mathrm{TMC},N} &= \int_0^1 d\xi\, \xi^{N-1} \int_\xi^{\xi_{\mathrm{th}}} \frac{dx}{x} \mathcal{C}_f^1\left(\frac{\xi}{x}\right) f(x) \\
&= \int_0^1 d\xi\, \xi^{N-1} \int_0^1 dy \int_0^{\xi_{\mathrm{th}}} dx\, \mathcal{C}_f^1(y)\, f(x)\, \delta(xy-\xi) \\
&= \left(\int_0^1 dy\, y^{N-1} \mathcal{C}_f^1(y)\right)\left(\int_0^{\xi_{\mathrm{th}}} dx\, x^{N-1} f(x)\right) \\
&= \mathcal{C}_f^{1,N}\, f_{\xi_{\mathrm{th}}}^N\,, \qquad (4.35)
\end{aligned}$$

where we denoted by $f_X^N = \int_0^X dx\, x^{N-1} f(x)$ the N-th truncated moment of a function f. Hence, In Mellin space, the TMC corrected structure function $\mathcal{F}_1^{\mathrm{TMC}}$ factorizes into a product of the moments of the coefficient function $\mathcal{C}_f^{1,N}$, exactly as in the massless approximation, and of the truncated moments of parton distributions. The appearance of the latter reflects the reduced support for integration over x in Eq. (4.17) (as illustrated in Fig. 4.5). The truncation of the PDF moments increases in magnitude with the increase of x_B and the decrease of Q^2.

Using the resummed coefficient function $\mathcal{C}_{q,\mathrm{res}}^{1,N}$ in Eq. (4.30), we may perform the inverse transformation,

$$\mathcal{F}_{1,\mathrm{res}}^{\mathrm{TMC}}(x_B, Q^2) = \int_{\mathcal{C}_N} \frac{dN}{2\pi i}\, \xi^{-N}\, \mathcal{C}_{q,\mathrm{res}}^{1,N}\, f_{\xi_{\mathrm{th}}}^N\,, \qquad (4.36)$$

using the same contour as in the massless target case, see e.g. [63]. Note that this corresponds only to resummation of the first term in Eq. (4.34). We always have to calculate the second term separately and add it to the resummed result. Other than that, the matching procedure required to include the full NLO calculation is the same as that without TMCs, see Eq. (4.32).

4.2.4 Phenomenological Results

We now investigate the numerical effects of TMC and threshold resummation as well as their combination. Throughout this work we only consider a proton target. We make use of both the NLO "Martin–Stirling–Thorne–Watt" (MSTW 2008) set of parton distribution functions [115] as well as the NLO CJ12 PDF set of [147] . As shown in Eq. (4.35), in order to perform numerical calculations for threshold resummation, we have to compute Mellin moments of the PDFs. Since these are provided in x space, we first fit suitable functions to the PDFs using the following parametrization

$$a_0\, x^{a_1}\, (1-x)^{a_2} \left(\sum_{j=3}^{n} a_j x^{b_j}\right), \qquad (4.37)$$

where a_i are free parameters and b_j are some chosen fixed values in the range of 0 to 3. We take into account the Q^2 evolution of the PDFs by allowing a Q^2 dependence in the parameters a_i of the form

$$a_i = a_{i1} + a_{i2} \log(\log(Q^2/Q_0^2))\,. \qquad (4.38)$$

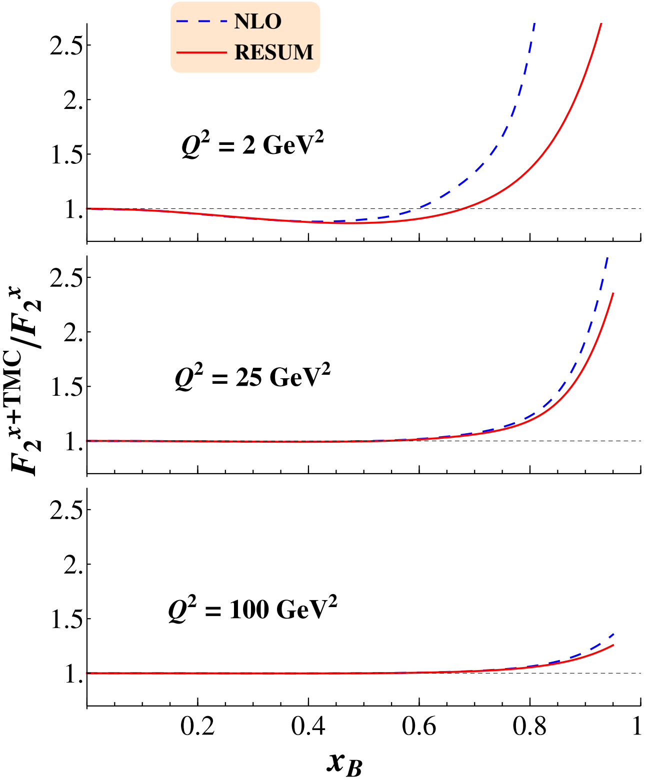

Figure 4.7: The effect of TMC is shown for the structure function F_2 on top of a NLO and a resummed calculation. We show TMC normalized to NLO (dashed blue) as well as TMC and resummation combined normalized to the resummed result (solid red). Again, we choose three representative values of $Q^2 = 2,\, 25,\, 100\ \mathrm{GeV}^2$. The PDF set of [115] is used.

The parameters $a_{i1,i2}$ are free parameters to be fitted for each different PDF and Q_0^2 is a chosen fixed scale. The truncated Mellin moments of the fitted PDFs are then taken analytically. With TMCs, we obtain a sum of incomplete Beta functions of the type

$$B_{\xi_{\mathrm{th}}}(N + a_1 + b_j, a_2 + 1). \tag{4.39}$$

The index ξ_{th} corresponds to the upper integration limit in the definition of the incomplete Beta function. (Without TMCs, or rather in the large Q^2 limit, where $\xi_{\mathrm{th}} = 1$, we obtain a sum regular Beta functions, B_1.)

In our code, we implement the incomplete Beta functions by making use of the identity

$$B_{\xi_{\mathrm{th}}}(N + a_1 + b_j, a_2 + 1) = \frac{\xi_{\mathrm{th}}^{N+a_1+b_j}}{N + a_1 + b_j}\ {}_2F_1(N + a_1 + b_j, -a_2, 1 + N + a_1 + b_j, \xi_{\mathrm{th}})\,, \tag{4.40}$$

and for the complex hypergeometric function ${}_2F_1$ we use the routine provided in [172]. In order to rule out uncertainties introduced in our calculation when using the fitted functions for the Mellin inversion,

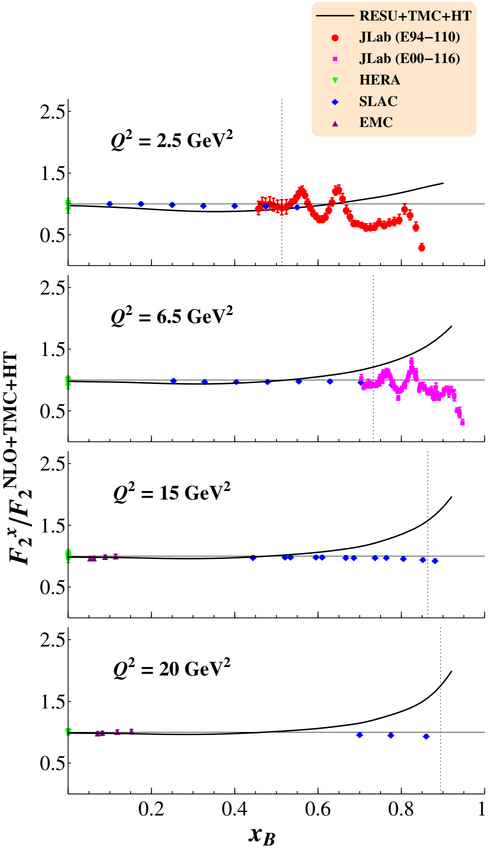

Figure 4.8: We plot ratios of data/theory for DIS structure function F_2 at several Q^2. Here "theory" denotes the NLO results with TMC and higher twist contributions based on the CJ PDF set of [147]. The data is taken from [173–177]. Due to our choice of a linear scale for the horizontal axis, the HERA data appears clustered at the vertical axis, i.e. at very small x_B. In addition, using the same normalization, we plot the theoretical prediction when resummation is included as well. The dotted line corresponds to $W^2 = 3.25\,\mathrm{GeV}^2$.

we checked the accuracy of the fits by comparing results at NLO obtained from the convolution code in x-space and the Mellin inverse. Indeed, we find very good agreement even for very large values of x_B.

The reason behind the numerical stability of our result is the following. When performing the Mellin inverse, we obtain an exponential suppression for large negative real values of N due to the factor ξ^{-N} in Eq. (4.36). When TMCs are included, this suppression is softened by the factor ξ_{th}^N in Eq. (4.40). These two exponential factors originate from two different parts of the calculation: the first comes from the definition of the inverse Mellin transform, whereas the second is due to the incomplete beta function. We need to combine the two factors into one single exponential, $\exp[-N\ln(\xi/\xi_{\mathrm{th}})]$, where the cancellations between the two is made explicit and makes the numerical integration over dN well-behaved even for very large values of x_B.

In Fig. 4.6, we present our numerical results for the DIS structure function F_2 using the PDF set of [115]. All results are normalized to the massless NLO calculation. We choose to plot our results only up to $x_B = 0.95$ as non-perturbative effects are expected to set in for too large values of x_B, which is beyond the scope of this work. The two effects under consideration are shown separately in dashed blue (TMCs) and in dotted magenta (threshold resummation) for three representative values of $Q^2 = 2$, 25, 100 GeV^2. Both TMC and resummation effects become increasingly large as x_B tends to 1, as it is clear from the kinematic analysis presented in Sec. 4.2. Both vanish at small x_B, the former because the Nachtmann variable ξ and the kinematic factor ρ tend to their massless value of x_B and 1, respectively, and the latter because the integrals are evaluated more and more far from the resummation threshold. Concerning the Q^2 dependence of the two corrections under discussion, both effects taken separately are large at small values of squared momentum transfer, and decrease with increasing Q^2. However, TMCs exhibit a power law suppression in Q^2, while resummation corrections decrease much less rapidly and become dominant, and non-negligible, at $Q^2 \gtrsim 25$ GeV. The results we find for TMCs are in agreement with numerical results in previous work such as [142] and [47] up to some prefactor conventions. Concerning the validity of our results on DIS threshold resummation one may compare to Ref. [63, 136].

We can now turn to the combination of TMC and threshold resummation, shown by the solid black line in Fig. 4.6. We notice that the strength of the two effects does not add in a simple way. In order to understand the interplay of TMCs and threshold resummation, we analyze the plots in Fig. 4.7. Again, we use the PDF set of [115]. There, we compare the ratio of the target mass corrected F_2 structure function to the massless calculation without resummation (Dashed blue line), and the ratio of the structure function with both TMC and resummation, but normalized to the resummed result (solid red line). This way, we can see how the TMC contribution acts on top of a purely NLO calculation compared to being added to a resummed calculation. Firstly, we note that the effects remain decoupled for small values of x_B, where both ratios lie exactly on top of each other. This decoupled region extends to larger values of x_B as Q^2 increases. However, at large enough values of x_B the two functions deviate and TMC acts differently for NLO than for the resummed result.

As discussed in [150, 178], such a variation in the calculation of the F_2 structure function can lead to considerable difference in the value of the d-quark parton distribution extracted in a global fit. The theoretical description of the data crucially depends on whether resummation is included or not. In order to gauge the relevance of TMCs and resummation for the extraction of PDFs, but leaving a detailed QCD fit for future work, we present in Fig. 4.8 a comparison of our calculations to a variety of electron-proton scattering data from JLab (E94-110) [173], JLab (E00-116) [174], HERA [175], SLAC [176], and EMC [177]. Here we use the CJ12 PDF set of [147]. The data was bin-centered in Q^2 for the analysis of Nachtmann moments of the DIS longitudinal structure function in [179] allowing a direct comparison of different experimental results [180]. The data was normalized to a calculation including TMCs only; but in order to do so we also need to add the "residual" power corrections in $1/Q^2$ not taken care of by target mass corrections. These were included in the CJ12 QCD fit [147] via a multiplicative factor $1 + C(x_B)/Q^2$, with C a parametrized function of Bjorken x_B with parameters fitted to a variety of DIS data. We include the same multiplicative factor in our NLO calculation, and use the parameters obtained in the CJ12 fit. The vertical dotted line in Fig. 4.8 corresponds to a value of $W^2 = (P_h + q)^2 = m_N^2 + Q^2(1 - x_B)/x_B = 3.25\,\mathrm{GeV}^2$, which is generally regarded as the end of the DIS regime and the beginning of the resonance region where fluctuations of the data around the DIS calculation are generally understood in terms of quark-hadron duality [181].

Finally, in order to gauge the relevance of resummation corrections to a global fit of parton distributions, we also plot in Fig. 4.8 the structure function F_2 with resummation, TMCs and higher twist contributions, normalized by the pure NLO calculation including TMCs and higher twists which was also used to normalize the data. Comparing the obtained deviation of this curve from one with the experimental uncertainties, we find a very significant effect which is getting larger for increasing Q^2, while at low Q^2, TMCs already capture the main effects. In fact, threshold resummation also decreases with increasing Q^2, as can be seen from both Figs. 4.6 and 4.7 above. However, as already remarked, TMCs die off rather quickly, whereas resummation remains clearly non-negligible in both the DIS and the resonance regions. Hence, resummation is likely to affect the extraction of large-x partons (quarks directly, and gluons indirectly through QCD evolution in DIS) in global PDF fits. In this respect, it is important to remark that the non power law dependence of the resummation corrections cannot be effectively included in a phenomenological higher-twist term, and needs to be instead explicitly calculated in order to obtain the correct behavior of the quark PDFs at large values of the parton momentum fraction x. In particular it would be interesting to see how the effect is on the $u-$ and d-quark PDFs, and how much the extrapolation of the d/u quark ratio to $x \to 1$ obtained in Ref. [147] would be affected.
Finally, see also the work of [182, 183] concerning TMC effects for (polarized) structure functions.

4.3 Hadron Mass Corrections and Resummation for SIA

4.3.1 Hadron Mass Corrections

Hadron level and parton level kinematics

We study the kinematics for Single Inclusive electron-positron Annihilation hadron in the $\gamma - h$ frame, where both the photon γ and the observed hadron h have no transverse momentum component. We start by parametrizing the momenta of the virtual photon q, the observed hadron in the final state P_h and the momentum of the fragmenting parton k. All momenta are also shown in Fig. 4.9. We find,

$$\begin{aligned} q^\mu &= q^+ \bar{n}^\mu + \frac{Q^2}{2q^+} n^\mu \,, \\ P_h^\mu &= \xi_E q^+ \bar{n}^\mu + \frac{m_h^2}{2\xi_E q^+} n^\mu \,, \\ k^\mu &= \frac{\xi_E}{z} q^+ \bar{n}^\mu + \frac{(k^2 + \boldsymbol{k}_T^2) z}{2\xi_E q^+} n^\mu + \boldsymbol{k}_T \,, \end{aligned} \tag{4.41}$$

where $Q^2 = q^\mu q_\mu$ denotes the virtuality of the photon, m_h is the mass of the observed hadron h, and $\xi_E = P_h^+/q^+$ its light cone momentum fraction; analogously, $z = P_h^+/k^+$ is the light-cone fractional momentum of the hadron relative to the parton that it is fragmenting from. The external Lorenz invariants are

$$Q^2 = q^2 = s, \quad x_E = \frac{2q \cdot P_h}{q^2}, \quad P_h^2 = m_h^2 \,, \tag{4.42}$$

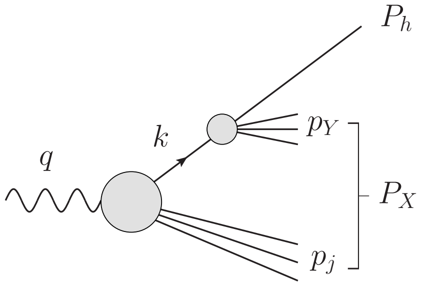

Figure 4.9: Diagram for SIA $e^+e^- \to hX$ where all momenta are specified.

where s is the center of mass energy of the process. Solving for the virtual boson fractional momentum, we obtain

$$\xi_E = \frac{P_h^+}{q^+} = \frac{1}{2} x_E \left(1 + \sqrt{1 - \frac{4}{x_E^2} \frac{m_h^2}{Q^2}} \right) , \tag{4.43}$$

which is a "Nachtmann-type" fragmentation variable, *cf.* Eq. (4.6). Note that the radicand is always positive due to energy conservation at the hadron level, as we derive below. Inverting Eq. (4.43) we obtain

$$x_E = \xi_E \left(1 + \frac{m_h^2}{\xi_E^2 Q^2} \right) . \tag{4.44}$$

Concerning the unobserved parton's (internal) kinematics, we work in collinear factorization but refrain from fixing the value of the parton virtuality k^2 until we analyze the effects of non-zero hadron masses on the partonic kinematic bounds. Therefore, for the time being, we only set

$$\boldsymbol{k}_T = 0 . \tag{4.45}$$

Finally, we define the partonic fragmentation invariant $\hat{x}_E$ by

$$\hat{x}_E = \frac{2k \cdot q}{q^2} = \frac{\xi_E}{z} + \frac{z k^2}{\xi_E Q^2} , \tag{4.46}$$

where the parton virtuality k^2 appears explicitly for the time being.

Four momentum conservation and kinematic bounds

We consider now the kinematics at the hadron level, and derive the kinematic limits for x_E and ξ_E due to four momentum conservation. Firstly, we find a lower bound for x_E which ensures that ξ_E in Eq. (4.43) is well defined. Calculating in the e^+e^- c.m. frame with $q^+ = q^- = Q/\sqrt{2}$, we find

$$\begin{aligned} x_E &= \frac{2P_h \cdot q}{Q} = \frac{\sqrt{2}}{Q}(P_h^+ + P_h^-) = \frac{2E_h}{Q} \\ &\geq \frac{2m_h}{Q} \equiv x_E^{\min} . \end{aligned} \tag{4.47}$$

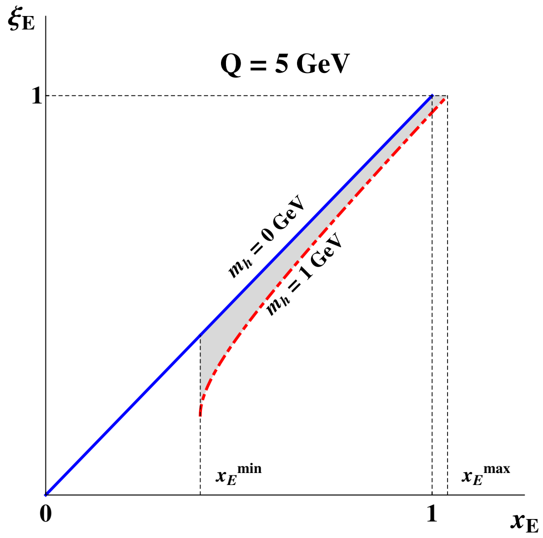

Figure 4.10: The fragmentation "Nachtmann-type" fragmentation variable ξ_E as a function of x_E at fixed $Q = 5$ GeV. For illustration purposes, we choose a fictional mass of $m_h = 1$ GeV (dash-dotted red) and compare it with a massless hadron, $m_h = 0$ GeV (solid blue line).

As a next step, we may derive an upper bound by considering the overall momentum conservation at the hadron level, $q = P_h + P_X$. We find

$$0 \leq P_X^2 = (P_h - q)^2 = m_h^2 - x_E Q^2 + Q^2\,. \tag{4.48}$$

Hence,

$$x_E \leq 1 + m_h^2/Q^2 \equiv x_E^{\rm max}\,, \tag{4.49}$$

which implies that x_E can become slightly larger than one. This is due to the neglect of hadron mass effects in the unobserved hadron jet shown at the bottom of Fig. 4.9, and is analogous to the neglect of pion production in the target jet in deriving the DIS kinematics. Relaxing these assumptions goes beyond the scope of this Chapter, which deals with the interplay of TMCs and threshold resummation, and is left for future work. Using these two relations, we may determine the minimal and maximal values for ξ_E, which are

$$\begin{aligned} \xi_E^{\rm min} &= \frac{x_E^{\rm min}}{2} = \frac{m_h}{Q} \\ \xi_E^{\rm max} &= 1\,. \end{aligned} \tag{4.50}$$

With these limits at hand, we may plot ξ_E as a function of x_E, see Fig. 4.10. Here, the effects of hadron mass corrections are large when the invariant x_E is small, contrary to the case of DIS, where target mass corrections are most relevant at large values of x_B. This can be understood as a consequence of crossing symmetry on the kinematics of the process, where now the virtual photon is time-like.

In a second step, again analogously to the procedure for DIS, we analyze the kinematics at the parton level. Firstly, we consider the hard-scattering vertex which corresponds to the lower grey circle in Fig. 4.9. Using momentum conservation at the vertex $q = k + p_j$ and neglecting any non-zero lower bound for the mass of the recoiling jet, we obtain the following constraint

$$0 \leq p_j^2 = (q-k)^2 = Q^2 \left(1 - \frac{z}{\xi_E}\frac{k^2}{Q^2}\right)\frac{z-\xi_E}{z}\,. \tag{4.51}$$

Secondly, we consider the hadronization vertex which corresponds to the upper right grey circle in Fig. 4.9, and we apply again four-momentum conservation. We obtain

$$0 \leq p_Y^2 = (k-P_h)^2 = \left(zk^2 - m_h^2\right)\frac{1-z}{z}\,. \tag{4.52}$$

It is important to notice that while the parton virtuality k^2 in the first of these inequalities is parametrically suppressed at large Q^2, no hard scale suppresses this nor the hadron mass m_h in the second inequality. Therefore, it is not possible to define a “massless hadron limit” as was done for the DIS case, where the nucleon mass, m_N, always appears divided by Q. The physical solutions of Eqs. (4.51)-(4.52) are:

$$\xi_E \leq z \leq 1 \tag{4.53}$$

$$m_h^2 \leq zk^2 \leq \xi_E Q^2\;. \tag{4.54}$$

In particular, the quark virtuality must always be larger than m_h^2 because this value corresponds to the minimum invariant mass of the parton fragmentation products when a hadron of flavor h is detected. Following our philosophy, we should then perform the collinear expansion around an on-shell massive quark rather than around $k^2 = 0$. However, dealing with the subtleties involved in proving the factorization theorem at NLO for this case goes beyond the scope of this Chapter and is left for future work [184]. From the next (Sub-) Section on, we only use the well known collinear factorization theorem for massless, $k^2 = 0$, fragmenting partons as in [73, 165] and we continue to explore the interplay of hadron mass corrections and threshold resummation. However, for completeness, we briefly comment here on the situation with $k^2 \neq 0$. Solving this system of inequalities in Eqs. (4.53)-(4.54), we will plot the allowed solutions for k^2 as a function of z. First of all, we find the minimally and maximally allowed values for z and k^2 which are given by

$$\begin{array}{ccc} \xi_E \leq & z & \leq 1 \\ m_h^2 \leq & k^2 & \leq Q^2\,. \end{array} \tag{4.55}$$

In addition, from the Eqs. (4.51)-(4.52), we find the constraint

$$z \leq \frac{Q^2\xi_E}{k^2} \;\Leftrightarrow\; k^2 \leq \frac{Q^2\xi_E}{z}\,, \tag{4.56}$$

and similarly

$$\frac{m_h^2}{k^2} \leq z \;\Leftrightarrow\; k^2 \geq \frac{m_h^2}{z}\,. \tag{4.57}$$

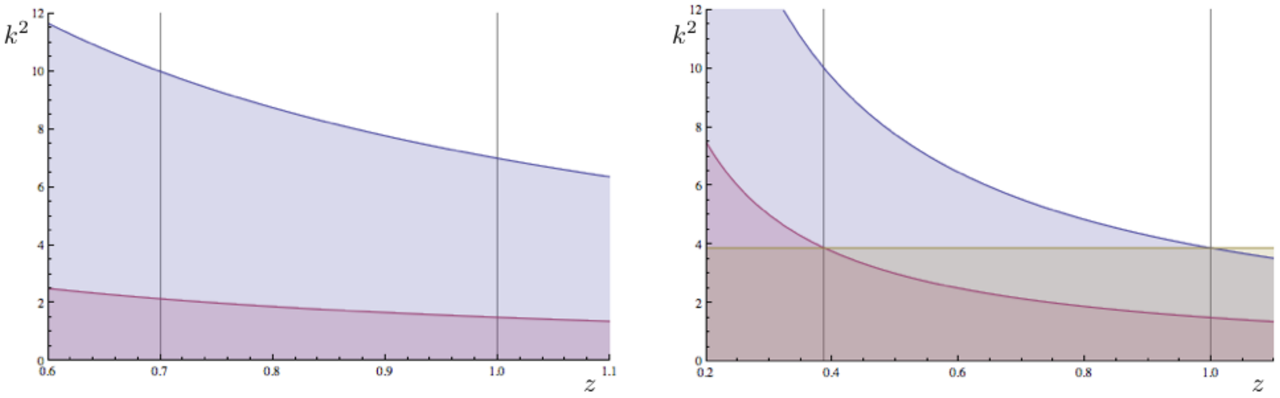

a)

b)

Figure 4.11: a) $k^2 - z$ Plot solving the inequalities in Eqs. Eqs. (4.51)-(4.52), where the inner area displays the allowed range for k^2 and z. b) Situation for $\xi_E = \xi_E^{\min}$ where in addition, the value for $k^2 = m_h Q$ is plotted.

All these results are summarized and plotted on the left hand side of Fig. 4.11 which is showing the allowed range for z and k^2. For illustration purposes, we chose the values $Q^2 = 10\,\mathrm{GeV}^2$, $m_h^2 = 1.5\,\mathrm{GeV}^2$, $\xi_E = 0.7$ for the plot. The four corners/ intersections of this figure are obtained as

$$\begin{aligned} z = \xi_E \quad &\Rightarrow \quad k^2 \leq Q^2, \;\; k \geq \frac{m_h^2}{\xi_E} \\ z = 1 \quad &\Rightarrow \quad k^2 \leq Q^2 \xi_E, \;\; k \geq m_h^2 \,. \end{aligned} \tag{4.58}$$

Firstly, we note that choosing $k^2 = 0$ is apparently not allowed by the kinematics as long as $m_h^2 \neq 0$ which is in clear contrast to DIS in Section 4.2. Secondly, one might be tempted to choose the minimally required virtuality for the fragmenting parton which is given by $k^2 = m_h^2/z$. However, we would run into various problems with that choice. It is important to choose a value for k^2 that is independent of z and ξ, otherwise the convolution structure of the cross section is lost. See for example, Eq. (4.46) where $\hat{x}_E$ is always written as a function of the combination ξ_E/z. A much more natural choice is obtained by considering the kinematical limits of x_E or equivalently ξ_E which leads to a z and ξ_E independent choice for k^2.

From Eqs. (4.56) and (4.57), we find that for this kinematical limit $\xi_E = \xi_E^{\min}$, there is only one z and ξ_E independent value for the parton's virtuality which is given by

$$k^2 = m_h Q \,. \tag{4.59}$$

For the minimal value of ξ_E, the lower left and the upper right corners of the diagram in Fig. 4.11 are on the same height, which is given by $k^2 = m_h Q$. Moving away from this limit, we find that there is always a wider range allowed. This situation is illustrated on the right side of Fig. 4.11, where in addition, we plotted the line $k^2 = m_h Q$. Hence, this choice for the virtuality of the fragmenting parton is the only possibility of choosing a value that is independent of z and ξ_E and which always allowed in the sense that it is independent of the kinematical situation.

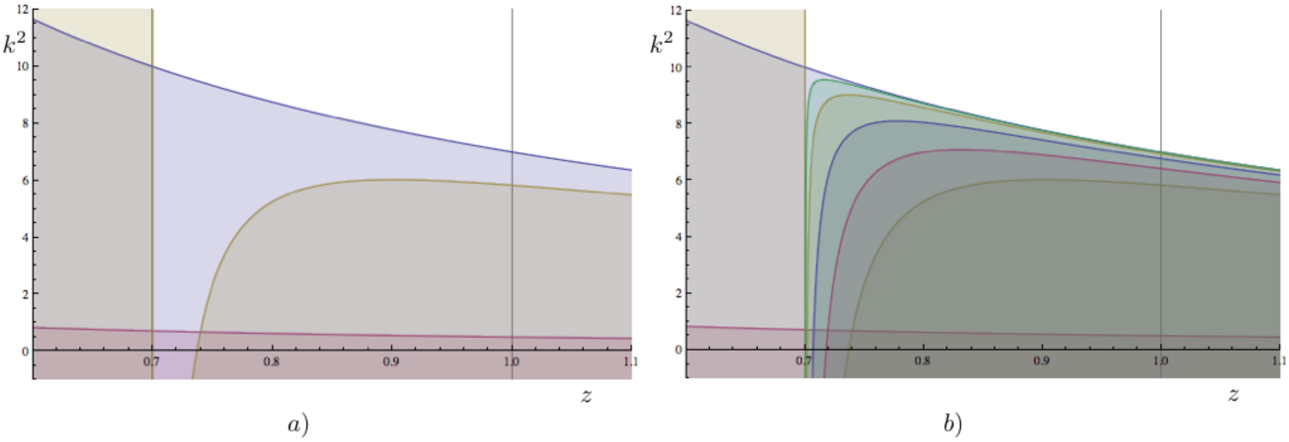

Figure 4.12: a) $k^2 - z$ Plot showing the allowed range for k^2 and z, see text. We also show the old boundaries for $P_X^2 \geq 0$. b) Stepwise relaxation of the requirement $P_X^2 \geq m_h^2$ until the old one $P_X^2 \geq 0$ is recovered.

In principle, one should also introduce a mass for the recoiling jet, *i.e.* $P_X^2 \geq m_h^2$. This additional requirement is necessary in order to cure the "threshold problem" in Eq. (4.49), where x_E can get slightly larger than one. Without going into further detail, we only sketch the situation for the allowed values for k^2 and z in Fig. 4.12 (on the left side). The upper and left boundaries now merge into one as it is shown by the new additional line in comparison to Fig. 4.11. On the right hand side of Fig. 4.12, we show how this constraint $P_X^2 \geq m_h^2$ is released until the old one one $P_X^2 \geq 0$ is recovered. All these issues and their numerical impact will be addressed in more detail in future work [184].

Cross section at NLO

Introducing $k^2 = 0$ for now, we may start writing down a cross section with HMCs. In order to compare our results to the SIA measurements from BELLE and BaBar, we need to compute hadron multiplicities in $e^+e^- \to hX$ which are defined as

$$R^h_{e^+e^-} \equiv \frac{1}{\sigma^{\text{tot}}} \frac{d^2\sigma^h}{dx_E d\cos\theta} \,. \tag{4.60}$$

Here the hadron h is produced at an angle θ relative to the initial positron. σ^{tot} denotes the totally inclusive cross section for $e^+e^- \to X$. At NLO, this is given by

$$\sigma^{\text{tot}} = \frac{4\pi\alpha^2}{3Q^2} N_c \sum_q e_q^2 \left(1 + \frac{\alpha_s}{\pi}\right) \,, \tag{4.61}$$

where $N_c = 3$ is the number of colors and α is the electromagnetic fine structure constant. As mentioned before, we may write the differential cross section $d^2\sigma^h/dx_E d\cos\theta$ in terms of two structure functions which we denote as $\hat{\mathcal{F}}_i^h$ (i=1,L), cf. [51, 106, 164]. Including HMC, we find

$$\begin{aligned}
\frac{d^2\sigma^h}{dx_E d\cos\theta} &= \frac{\pi\alpha^2}{Q^2} N_c \frac{1}{1-\frac{m_h^2}{\xi_E^2 Q^2}} \left[\frac{1+\cos^2\theta}{2}\hat{\mathcal{F}}_1^h(x_E,Q^2) + \sin^2\theta\,\hat{\mathcal{F}}_L^h(x_E,Q^2)\right] \\
&= \frac{1}{1-\frac{m_h^2}{\xi_E^2 Q^2}} \left.\frac{d^2\sigma^h}{d\xi_E d\cos\theta}\right|_{x_E=\xi_E} ,
\end{aligned} \tag{4.62}$$

where the Jacobian factor of $1/(1-m_h^2/\xi_E^2 Q^2)$ is included in order to obtain a cross section differential in x_E instead of ξ_E [73, 165]. The structure functions $\hat{\mathcal{F}}_i^h$ with HMCs take into account the kinematic bounds on z from Eq. (4.53) and read

$$\hat{\mathcal{F}}_i^h(x_E,Q^2) = \sum_f \int_{\xi_E}^1 \frac{dz}{z} D_f^h\left(z,\mu^2\right) \hat{\mathcal{C}}_f^i\left(\frac{\xi_E}{z},\frac{Q^2}{\mu^2},\alpha_s(\mu^2)\right) , \tag{4.63}$$

where $D_f^h(z,\mu^2)$ denotes the fragmentation function for an observed hadron h in the final state resulting from a parent parton f. The $\hat{\mathcal{C}}_f^i$ are the corresponding coefficient functions which we list in Appendix C for completeness up to NLO. The cross section without HMCs is obtained by replacing ξ_E with x_E in Eq. (4.63) and by setting $m_h = 0$ in Eq. (4.62). Having chosen to factorize the cross section around a parton virtuality $k^2 = 0$ this massless hadron limit can also be achieved in the $Q^2 \to \infty$ limit.

4.3.2 Combining HMC and Threshold Resummation

In the spirit of "crossed resummation" [93], we note that the only difference concerning the resummation in SIA in comparison to DIS is that we have to adjust one term in the matching coefficient H_q in Eq. (2.37) $-\pi^2/6 \to 5\pi^2/6$, see also Capter 2 and [63, 99]. This similarity may be understood in the sense that both processes have one "observed" and one "unobserved" parton. Hence, the threshold resummed expression may again be written as a product of the form $H_q' \, \Delta_q^N \, J_q^N$. HMC and resummation are combined by simply replacing $x_E \to \xi_E$ in the resummed formula. There are no issues with ξ_{th} as it was the case for DIS, since the upper integration limit for z in Eqs. (4.53), (4.63) is left unchanged compared to the massless hadron calculation. Since resummation effects increase with x_E and HMC effects become large at small values of x_E, we do not expect a significant interplay of the two, contrary to the DIS case in which both effects increase at large x_B. We can numerically assess the interplay of HMC and threshold resummation similarly to what we did for DIS. In Fig. 4.13, we plot the cross section including the effect of HMCs on top of an NLO (dashed-dotted blue line) and a resummed (solid red line) calculation. These are normalized to the corresponding massless hadron calculation to highlight HMC effects. We find that both ratios match completely. Hence, there is no crosstalk between the two effects.

4.3.3 Phenomenological Results

Given the actuality of the recent BELLE [10] and BaBar [11] results, we choose to present our numerical results for HMC and threshold resummation directly in comparison to data. The BELLE experiment

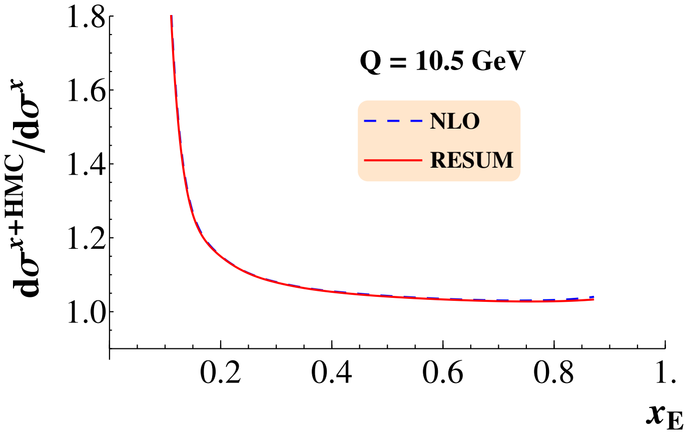

Figure 4.13: Comparison of the effect of HMC on top of NLO (dashed blue) and the resummed result (solid red) for $Q = \sqrt{s} = 10.5$ GeV and the kaon mass $m_{K^0} = 497.6$ MeV.

is operating at a c.m.s. energy of $\sqrt{s} = 10.52$ GeV and similarly BaBar at $\sqrt{s} = 10.54$ GeV, just below the lower end of the energy range of experiments typically included in FF fits, see for example Refs. [71, 73]. This way, we maximize the effect of HMC and resummation of threshold logarithms and we may directly evaluate the significance of the two corrections compared to statistical and systematic uncertainties of the data.

For the plots we discuss in this section, as well as for that in Fig. 4.13, we used the “de Florian-Sassot-Stratmann” [71] set of fragmentation functions at NLO, where the new data from BELLE and BaBar is not yet included. The goal is to show the phenomenological importance of threshold resummation and HMCs, and to qualitatively assess their relevance in global FF fits, rather than obtain a perfect description of the data. Comparing the size of HMC and threshold resummation to statistical and systematical errors, we will conclude that a fit including the two effects may yield rather different results for the extracted FFs. Whether indeed a better χ^2 can be obtained given all the other data sets used in a global fit, as the study presented in [73] indicates, will be left for future work.

Both BELLE and BaBar have an angular coverage of $-1 < \cos\theta < 1$. Hence, we integrate over the full range of $\cos\theta$ and obtain a cross section differential only in x_E. An important difference between the two data sets is that BELLE data is presented as a function of the Lorentz invariant energy fraction x_E, whereas BaBar is using the momentum fraction variable

$$x_p = \frac{2|\boldsymbol{p}_h|}{\sqrt{s}}\,. \tag{4.64}$$

Only for massless calculations are these equivalent, however, and in particular for kaons at present energies the difference between x_E and x_p is quite significant. When comparing our results to data, we multiply the BaBar data set by $J = dx_p/dx_E$ to obtain a cross section differential in x_E and compare this to measurements at BELLE.

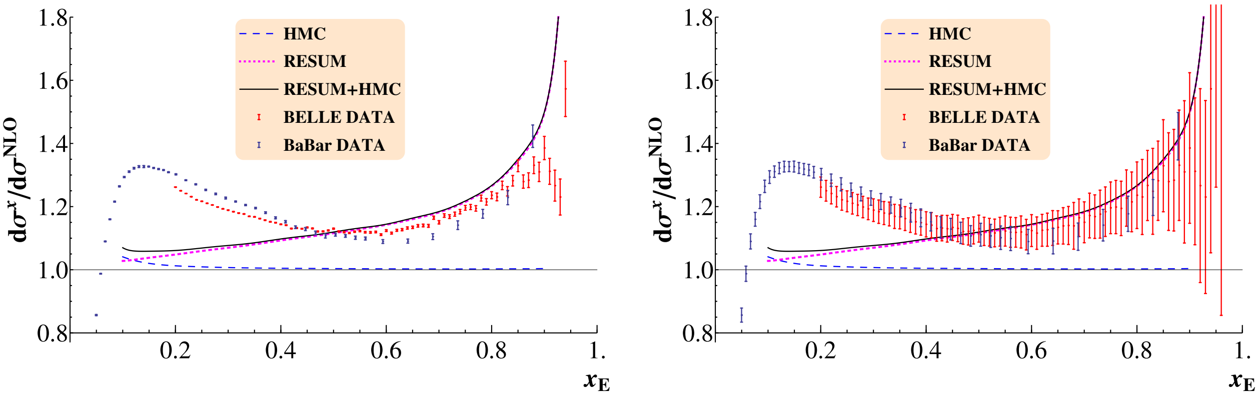

Figure 4.14: Both theory and data $1/\sigma_{\text{tot}}\, d\sigma/dx_E$ are normalized to NLO for charge integrated pions at $\sqrt{s} = 10.5$ GeV. The dashed blue lines shows the HMC corrected multiplicities, magenta dotted the resummed calculation and solid black the combination of both. BELLE data (red) and BaBar data (blue) is shown along with statistical (left) and systematical uncertainties (right). The FFs of [71] are used.

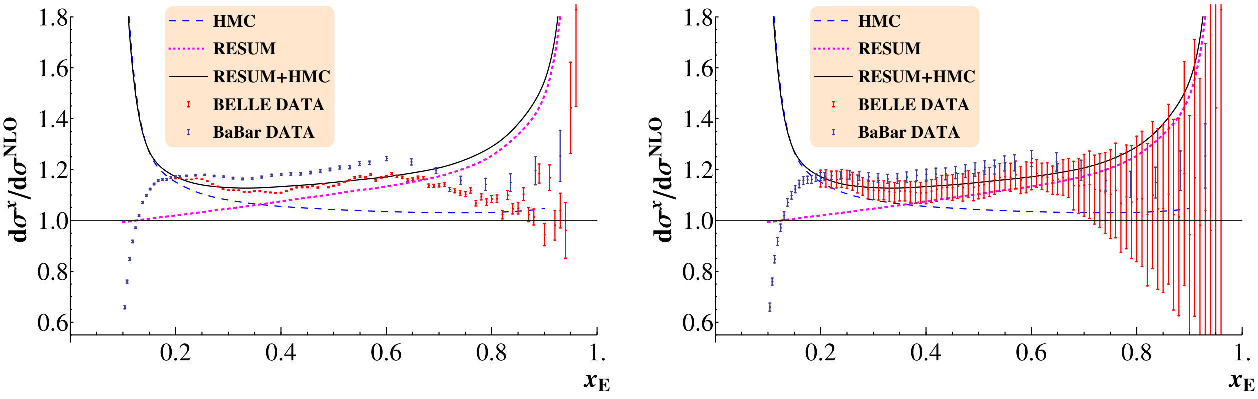

Figure 4.15: Same as Fig. 4.14 but for observed kaons.

We start by analyzing our calculations for (charge integrated) pion production, plotted in Fig. 4.14. All multiplicities $1/\sigma_{\text{tot}}\, d\sigma/dx_E$ presented here are normalized to the calculation at NLO without hadron mass corrections. Our results for HMC (dashed blue line), threshold resummation (dotted magenta line) and the combination of both (solid black line) is shown. On the left (right) panels of Fig. 4.14, we show BELLE and BaBar data with statistical (systematic) uncertainties. As expected, the effects of threshold resummation are quite significant and most relevant at large x_E, whereas HMCs affect the calculation at small x_E, and in the measured range are not large, due to the smallness of the pion mass, $m_{\pi^0} = 135$ MeV. Nonetheless, given the statistical precision of this data, it seems important to account for HMCs in a global fit. Much of discrepancy between NLO calculations and pion data can be resolved by including the new data in a global FF fit, as it was very recently shown in Ref. [72]. Finally, we note that below $x_E = 0.1$, small-x logarithms start to become relevant and would also need to be resummed [165], which however is beyond the scope of this work.

For kaons, with mass $m_{K^0} = 497.6$ MeV, HMCs are much larger than for pions, as shown in Fig. 4.15. The combination of HMC and resummation leads to a significant increase of the cross section compared to a massless hadron NLO calculation for all values of x_E, and their inclusion in global FF fits is even more important than in the pion case. The steep rise of the HMC corrected result over the NLO calculation at small x_E is mostly due to the kinematic limit $x_E > 2m_{K^0}/Q \approx 0.1$ derived in Eq. (4.47), and in its vicinity the validity of our treatment of HMCs may come into question. This is also the region where resummation of small-x logarithms becomes important, and a proper treatment of these is likely to require a careful consideration of the interplay with HMCs. It would then be very interesting to explore the similarities and differences of this with the interplay of threshold logarithms and target mass corrections in large-x_B DIS events we have discussed in Section 4.2, but we defer this analysis to a future effort.

4.4 Conclusions

We have investigated two phenomenologically important effects for the analysis of data in inclusive DIS and single-inclusive electron-positron annihilation, namely the corrections to NLO calculations due to a non-zero mass of the nucleon target in DIS, and of the detected hadron in SIA, as well as the resummation of threshold logarithms arising in the perturbative expansion of the hard scattering coefficients. In both cases, these lead to a non-negligible enhancement in the calculated observable compared to the precision of the currently available experimental data. Therefore, both effects are significant for precise QCD fits of PDFs as well as FFs.

In DIS, target mass corrections and threshold resummation are both most relevant at large values of x_B. In particular, we have derived a way to perform resummation respecting the parton level kinematic constraints arising from consideration of the non-zero target mass. The resulting structure functions can then be consistently combined with TMC calculations such that they remain zero in the unphysical region $x_B \geq 1$. We find that two effects are coupled especially for small values of Q^2. At large x_B, the size of the combined TMC and resummation corrections is considerably larger than the accuracy of the existing DIS data over an extended Q^2 range. Therefore, it should be taken into account for a precise extraction of large-x PDFs in global fits.

In SIA processes, hadron mass corrections are relevant at small x_E while threshold resummation is important at large x_E, and we find no interplay of the two effects. We have included both in our calculations of cross sections for pion and kaon production, and compared these to recent data from the BELLE and BaBar collaborations. The effects are again large, and non-negligible for the extraction of FFs, given the precision of the new data sets. This is particularly true for kaons due to their bigger mass compared to observed pions. Given this large effect for kaon SIA, it becomes a topic of practical as well as theoretical interest to determine what the interplay is between the finite mass kinematics and the resummation of small-x logarithms. We leave this for future efforts.

Finally, we remark that we have performed calculations in collinear factorization around massless, on-shell partons. For SIA, we have found that this choice, however commonly made, actually violates parton-level four momentum conservation. A detailed analysis of collinear factorization with non-zero virtuality partons is in preparation.

In the future, it would be very interesting to look at power corrections derived from resummation for e^+e^- annihilation and DIS, cf. [185]. In addition, an NNLO fit for e^+e^- alone would be important. Both topics will be addressed in the future.

CHAPTER 5

TOWARD NNLL THRESHOLD RESUMMATION FOR HADRON PAIR PRODUCTION IN HADRONIC COLLISIONS

We investigate QCD threshold resummation effects beyond the next-to-leading logarithmic order for the process $H_1 H_2 \to h_1 h_2 X$ at high invariant mass of the produced hadron pair. We take into account the color structure of the underlying partonic hard-scattering cross sections and determine the relevant hard and soft matrices in color space that contribute to the resummed cross section at next-to-next-to-leading logarithmic accuracy. We present numerical results for fixed-target and collider regimes. We find a significant improvement compared to previous results at NLL accuracy. In particular, the scale dependence of the resummed cross section is greatly reduced. Use of the most recent set of fragmentation functions also helps in improving the comparison with the experimental data. Our calculation provides a step towards a systematic NNLL extension of threshold resummation also for other hadronic processes, in particular for jet production. This Chapter is based on publication [iv].

5.1 Introduction

The resummation of threshold logarithms in partonic hard-scattering cross sections contributing to hadronic scattering has received an ever-growing attention in recent years. On the one hand, resummation is phenomenologically relevant in many kinematical situations, ranging from fixed-target energies all the way to the LHC. At the same time, it offers insights into the structure of perturbative corrections at higher orders, which among other things may provide benchmarks for explicit full fixed-order calculations in QCD.

Threshold logarithms typically arise when the initial partons have just enough energy to produce the observed final state. In this case, the phase space available for gluon bremsstrahlung vanishes, resulting in large logarithmic corrections. Taking the hadron-pair production cross section to be discussed in this Chapter as an example, the partonic threshold is reached when $\hat{s} = \hat{m}^2$, that is, $\hat{\tau} \equiv \hat{m}^2/\hat{s} = 1$, where $\sqrt{\hat{s}}$ is the partonic center-of-mass system (c.m.s.) energy and $\hat{m}$ the pair mass of two outgoing produced partons that eventually fragment into the observed hadron pair. The leading large contributions near threshold arise as $\alpha_s^k \left[\ln^{2k-1}(1-\hat{\tau})/(1-\hat{\tau})\right]_+$ at the kth order in perturbation theory, where α_s is the strong coupling and the "plus" distribution will be defined below. There is a double-logarithmic structure, with two powers of the logarithm arising for every new order in the coupling. Subleading terms have fewer logarithms, so that the threshold logarithms in the perturbative series take the general form

$$\sum_{k=0}^{\infty} \sum_{\ell=1}^{2k} \alpha_s^k \, \mathcal{A}_{k,\ell} \left(\frac{\ln^{2k-\ell}(1-\hat{\tau})}{1-\hat{\tau}} \right)_+ , \tag{5.1}$$

with perturbative coefficients $\mathcal{A}_{k,\ell}$. One often refers to the all-order set of logarithms with a fixed ℓ as the ℓth *tower* of logarithms. As has been established in the literature [7, 8, 78, 79], threshold logarithms exponentiate after taking an integral transform conjugate to the relevant kinematical variable ($\hat{\tau}$ in the above example). Under this transform the threshold logarithms translate into logarithms of the transform variable N. The exponent may itself be written as a perturbative series and is only *single-logarithmic* in the transform variable. Ignoring for the moment the color structure of the underlying partonic cross section, the structure of the resummed cross section becomes in transform space

$$\Big(1 + \alpha_s C^{(1)} + \alpha_s^2 C^{(2)} + \ldots\Big) \exp\left[\sum_{k=1}^{\infty} \sum_{\ell=1}^{k+1} \mathcal{B}_{k,\ell} \alpha_s^k \, \ln^{\ell}(N) \right] , \tag{5.2}$$

again with coefficients $\mathcal{B}_{k,\ell}$ and with "matching coefficients" $C^{(k)}$ that ensure that at every fixed order the resummed cross section agrees with the exact fixed-order one, up to corrections suppressed at threshold. They contain the full virtual corrections at order α_s^k, corresponding to contributions $\propto \delta(1-\hat{\tau})$ in the partonic cross section, and may be compared by comparison to a full fixed-order calculation performed near threshold. Thanks to the exponentiated single-logarithmic structure of the exponent, knowledge of the two leading towers $\alpha_s^k \ln^{k+1}(N)$ and $\alpha_s^k \ln^k(N)$, along with the coefficient $C^{(1)}$, is sufficient to predict the *three* leading towers in the perturbative series (5.1) for the cross section in $\hat{\tau}$-space. This is termed "next-to-leading logarithmic" resummation. At full next-to-next-to-leading logarithmic accuracy, one needs three towers in the exponent and the two-loop coefficient $C^{(2)}$, providing control of already five towers in the partonic cross section.

While NLL resummation was the state of the art for many years, much progress has been made recently on extending the framework to NNLL accuracy, or even beyond. The most advanced results have been obtained for color-singlet processes such as Higgs production, where NNLL [186, 187] and, most recently, even studies up to the N^{3}LL level [188, 189] have been obtained, in which seven towers of logarithms are fully taken into account to all orders. This became possible when all threshold distributions at three-loop order were computed [190]. For processes that are not characterized by a color-singlet lowest-order hard scattering reaction, progress beyond NLL has also been made. For such processes, the resummation framework becomes more complex because the interference between soft emissions by the various external partons in the hard scattering process becomes sensitive to the color structure of the hard scattering itself. This requires a color basis for the partonic scattering process which, as will be reviewed below, leads to a matrix structure of the soft emission [78–82]. This ultimately turns the exponential in (5.2) into a sum of exponentials, each with its own set of matching coefficients $C^{(k)}$. An extensive list of color-non-singlet reactions of this type along with corresponding references to NLL studies may be found in [87]. Resummation studies beyond NLL have been presented in the context of top quark pair production [191, 192], for single-inclusive hadron production [87], and for squark and gluino production [193]. At present, full NNLL resummation in the sense described above is not yet possible for most processes, since the required two-loop matching coefficients are usually not yet available (see, however, the recent calculation [194] for massless scattering). Nonetheless, already with knowledge of the one-loop matching coefficients an improvement of the resummation framework becomes possible, providing control of four (instead of five at full NNLL) towers in the partonic cross sections. A prerequisite for this is that the appropriate color structure be taken into account for all ingredients in the resummed expression.

In the present Chapter, we will develop such a partial NNLL resummation for the process of di-hadron production in hadronic collisions, collecting all necessary ingredients. Previously, Ref. [83] presented a NLL study for this process which forms the basis for this Chapter. Kinematically, hadron pair production shares many features with the much simpler color-singlet Drell-Yan process, if one confronts the produced partonic pair mass $\hat{m}$ with the invariant mass of the lepton pair. The interesting aspect of di-hadron production is that it possesses all the color complexity of the underlying $2 \to 2$ QCD hard scattering. As such, the process becomes an ideal test for the study of QCD resummation beyond NLL and can serve as a template for reactions of more significant phenomenological interest, especially single or two-jet production in hadronic collisions. That said, di-hadron production is phenomenologically relevant in its own right as experimental data as a function of the pair's mass are available from various fixed-target experiments [195–198], as well as from the ISR [199]. In addition, di-hadron cross sections are also accessible at the Relativistic Heavy Ion Collider.

This Chapter is structured as follows. In Sec. 5.2 we recall the basic formulas for the di-hadron cross section as a function of pair mass at fixed order in perturbation theory, and display the role of the threshold region. In order for this Chapter to be self-contained, we recall a number of results from [83]. Section 5.3 presents details of the NNLL threshold resummation for the cross section. In particular, we derive the various hard and soft matrices in color space that are needed for the analysis. Here, we make use of one-loop results available in the literature [200–202] and compare to related work [203]. In Sec. 5.4 we give phenomenological results, comparing the threshold resummed calculations at NLL and NNLL to some of the available experimental data. Finally, we summarize our results in Sec. 5.5.

5.2 Hadron pair production near partonic threshold

5.2.1 Perturbative cross section

As in [83], we consider the process $H_1(P_a) + H_2(P_b) \to h_1(P_c) + h_2(P_d) + X$ at measured pair invariant mass squared,

$$M^2 \equiv (P_c + P_d)^2 \,, \tag{5.3}$$

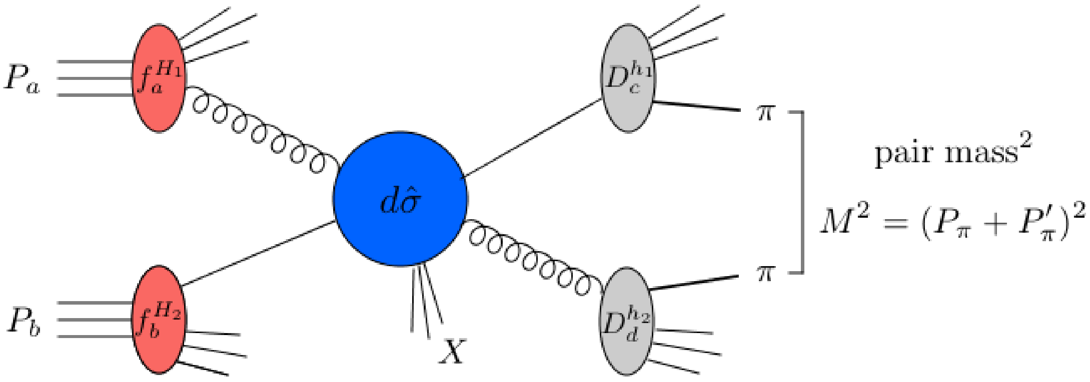

Figure 5.1: Diagrammatic illustration of Di-Hadron production in hadronic collisions.

and at c.m.s. rapidities η_1, η_2 of the two produced hadrons. See Fig. 5.1 for a sketch of the corresponding diagram.

It is convenient to introduce

$$\begin{aligned} \Delta\eta &= \frac{1}{2}(\eta_1 - \eta_2) \, , \\ \bar{\eta} &= \frac{1}{2}(\eta_1 + \eta_2) \, . \end{aligned} \tag{5.4}$$

For sufficiently large M^2, the cross section for the process can be written in the factorized form

$$\begin{aligned} M^4 \frac{d\sigma^{H_1 H_2 \to h_1 h_2 X}}{dM^2 d\Delta\eta d\bar{\eta}} &= \sum_{abcd} \int_0^1 dx_a dx_b dz_c dz_d \, f_a^{H_1}(x_a, \mu_F^2) f_b^{H_2}(x_b, \mu_F^2) \, z_c D_c^{h_1}(z_c, \mu_F^2) z_d D_d^{h_2}(z_d, \mu_F^2) \\ &\quad \times \omega_{ab \to cd}\left(\hat{\tau}, \Delta\eta, \hat{\eta}, \alpha_s(\mu_R^2), \frac{\mu_R^2}{\hat{m}^2}, \frac{\mu_F^2}{\hat{m}^2}\right) \, , \end{aligned} \tag{5.5}$$

where $\hat{\eta}$ is the average rapidity in the partonic c.m.s., which is related to $\bar{\eta}$ by

$$\hat{\eta} = \bar{\eta} - \frac{1}{2} \ln\left(\frac{x_a}{x_b}\right) \, . \tag{5.6}$$

The quantity $\Delta\eta$ is a difference of rapidities and hence boost invariant. The average and relative rapidities for the hadrons and their parent partons are the same, since all particles are taken to be massless. The functions $f_{a,b}^{H_{1,2}}$ in Eq. (5.5) are the parton distribution functions for partons a, b in hadrons $H_{1,2}$ and $D_{c,d}^{h_{1,2}}$ the fragmentation functions for partons c, d fragmenting into the observed hadrons $h_{1,2}$. The distribution functions are evaluated at a factorization scale μ_F that we choose to be the same for the initial and the final state. μ_R denotes the renormalization scale, which may differ from μ_F. The partonic momenta are given in terms of the hadronic ones by $p_a = x_a P_a$, $p_b = x_b P_b$,

$p_c = P_c/z_c$, $p_d = P_d/z_d$. We introduce

$$\begin{aligned}
S &= (P_a + P_b)^2 \; , \\
\tau &\equiv \frac{M^2}{S} \; , \\
\hat{s} &\equiv (x_a P_a + x_b P_a)^2 = x_a x_b S \; , \\
\hat{m}^2 &\equiv \left(\frac{P_c}{z_c} + \frac{P_d}{z_d}\right)^2 = \frac{M^2}{z_c z_d} \; , \\
\hat{\tau} &\equiv \frac{\hat{m}^2}{\hat{s}} = \frac{M^2}{x_a x_b z_c z_d S} = \frac{\tau}{x_a x_b z_c z_d} \; . \qquad (5.7)
\end{aligned}$$

The $\omega_{ab\to cd}$ in Eq. (5.5) are the hard-scattering functions for the contributing partonic processes $ab \to cdX'$, where X' denotes some additional unobserved partonic final state. Since the cross section in Eq. (5.5) has been written in a dimensionless form, the $\omega_{ab\to cd}$ can be chosen to be functions of $\hat{m}^2/\hat{s} = \hat{\tau}$ and the ratios of $\hat{m}$ to the factorization and renormalization scales, as well as the rapidities and the strong coupling. They may be computed in QCD perturbation theory, where they are expanded as

$$\omega_{ab\to cd} = \left(\frac{\alpha_s}{\pi}\right)^2 \left[\omega^{\mathrm{LO}}_{ab\to cd} + \frac{\alpha_s}{\pi}\,\omega^{\mathrm{NLO}}_{ab\to cd} + \left(\frac{\alpha_s}{\pi}\right)^2 \omega^{\mathrm{NNLO}}_{ab\to cd} + \ldots\right] \; . \qquad (5.8)$$

Here we have separated the overall power of $\mathcal{O}(\alpha_s^2)$, which arises because the leading order partonic hard-scattering processes are the ordinary 2 → 2 QCD scatterings.

5.2.2 Threshold limit

The limit $\hat{\tau} \to 1$ corresponds to the partonic threshold, where the hard-scattering uses all available energy to produce the pair. This is kinematically similar to the Drell-Yan process, if one thinks of the hadron pair replaced by a lepton pair. The presence of fragmentation of course complicates the analysis somewhat, because only a fraction $z_c z_d$ of $\hat{m}^2$ is used for the invariant mass of the observed hadron pair. As shown in [83], it is useful to introduce the variable

$$\tau' \equiv \frac{\hat{m}^2}{S} = \frac{M^2}{z_c z_d S} \; , \qquad (5.9)$$

which may be viewed as the "τ-variable" at the level of produced partons when fragmentation has not yet been taken into account, akin to the variable $\tau = Q^2/S$ in Drell-Yan.

At LO, one has $\hat{\tau} = 1$ and also $\hat{\eta} = 0$. One can therefore write the LO term as

$$\omega^{\mathrm{LO}}_{ab\to cd}\left(\hat{\tau}, \Delta\eta, \hat{\eta}\right) = \delta\left(1 - \hat{\tau}\right)\,\delta\left(\hat{\eta}\right)\,\omega^{(0)}_{ab\to cd}(\Delta\eta) \; , \qquad (5.10)$$

where $\omega^{(0)}_{ab\to cd}$ is a function of $\Delta\eta$ only. According to (5.6), the second delta-function implies that $\bar{\eta} = \frac{1}{2}\ln(x_a/x_b)$. At next-to-leading order, or overall $\mathcal{O}(\alpha_s^3)$, one can have $\hat{\tau} \neq 1$ and $\hat{\eta} \neq 0$. In general, as discussed in [83], near partonic threshold the kinematics becomes “LO like”. One has:

$$\begin{aligned}\omega_{ab\to cd}\left(\hat{\tau},\Delta\eta,\hat{\eta},\alpha_s(\mu_R^2),\frac{\mu_R^2}{\hat{m}^2},\frac{\mu_F^2}{\hat{m}^2}\right) &= \delta\left(\hat{\eta}\right)\,\omega^{\mathrm{sing}}_{ab\to cd}\left(\hat{\tau},\Delta\eta,\alpha_s(\mu_R^2),\frac{\mu_R^2}{\hat{m}^2},\frac{\mu_F^2}{\hat{m}^2}\right)\\ &+\ \omega^{\mathrm{reg}}_{ab\to cd}\left(\hat{\tau},\Delta\eta,\hat{\eta},\alpha_s(\mu_R^2),\frac{\mu_R^2}{\hat{m}^2},\frac{\mu_F^2}{\hat{m}^2}\right)\ ,\end{aligned} \tag{5.11}$$

where all singular behavior near threshold is contained in the functions $\omega^{\mathrm{sing}}_{ab\to cd}$. Threshold resummation addresses this singular part to all orders in the strong coupling. All remaining contributions, which are subleading near threshold, are collected in the “regular” functions $\omega^{\mathrm{reg}}_{ab\to cd}$. Specifically, for the NLO corrections, one finds the following structure:

$$\begin{aligned}\omega^{\mathrm{NLO}}_{ab\to cd}\left(\hat{\tau},\Delta\eta,\hat{\eta},\frac{\mu_R^2}{\hat{m}^2},\frac{\mu_F^2}{\hat{m}^2}\right) &= \delta\left(\hat{\eta}\right)\left[\omega^{(1,0)}_{ab\to cd}\left(\Delta\eta,\frac{\mu_R^2}{\hat{m}^2},\frac{\mu_F^2}{\hat{m}^2}\right)\delta(1-\hat{\tau})\right.\\ &\left.+\,\omega^{(1,1)}_{ab\to cd}\left(\Delta\eta,\frac{\mu_F^2}{\hat{m}^2}\right)\left(\frac{1}{1-\hat{\tau}}\right)_+ +\,\omega^{(1,2)}_{ab\to cd}(\Delta\eta)\left(\frac{\log(1-\hat{\tau})}{1-\hat{\tau}}\right)_+\right]\\ &+\,\omega^{\mathrm{reg,NLO}}_{ab\to cd}\left(\hat{\tau},\Delta\eta,\hat{\eta},\frac{\mu_R^2}{\hat{m}^2},\frac{\mu_F^2}{\hat{m}^2}\right)\ ,\end{aligned} \tag{5.12}$$

where the singular part near threshold is represented by the functions $\omega^{(1,0)}_{ab\to cd}, \omega^{(1,1)}_{ab\to cd}, \omega^{(1,2)}_{ab\to cd}$, which are again functions of only $\Delta\eta$, up to scale dependence. The “plus”-distributions are defined by

$$\int_{x_0}^1 f(x)\left(g(x)\right)_+ dx \equiv \int_{x_0}^1 \left(f(x)-f(1)\right)\,g(x)dx - f(1)\int_0^{x_0} g(x)dx\ . \tag{5.13}$$

The functions $\omega^{(1,0)}_{ab\to cd}, \omega^{(1,1)}_{ab\to cd}, \omega^{(1,2)}_{ab\to cd}$ were derived in [83] from an explicit NLO calculation near threshold. We will use these results below as a useful check on the resummed formula and on the matching coefficients.

5.2.3 Mellin and Fourier transforms

In order to prepare the resummation of threshold logarithms, we take integral transforms of the cross section. Following [83], we first write the hadronic cross section in Eq. (5.5) as

$$M^4\frac{d\sigma^{H_1H_2\to h_1h_2X}}{dM^2d\Delta\eta d\bar{\eta}} = \sum_{cd}\int_0^1 dz_c\,dz_d\,z_c\,D_c^{h_1}(z_c,\mu_F^2)\,z_d\,D_d^{h_2}(z_d,\mu_F^2)\,\Omega_{H_1H_2\to cd}\left(\tau',\Delta\eta,\bar{\eta},\alpha_s(\mu_R^2),\frac{\mu_R^2}{\hat{m}^2},\frac{\mu_F^2}{\hat{m}^2}\right)\ , \tag{5.14}$$

where $\tau' = \hat{m}^2/S = \hat{\tau} x_a x_b$ and

$$\Omega_{H_1 H_2 \to cd}\left(\tau', \Delta\eta, \bar{\eta}, \alpha_s(\mu_R^2), \frac{\mu_R^2}{\hat{m}^2}, \frac{\mu_F^2}{\hat{m}^2}\right) \equiv \sum_{ab} \int_0^1 dx_a\, dx_b\, f_a^{H_1}\left(x_a, \mu_F^2\right)\, f_b^{H_2}\left(x_b, \mu_F^2\right) \times\, \omega_{ab\to cd}\left(\hat{\tau}, \Delta\eta, \hat{\eta}, \alpha_s(\mu_R^2), \frac{\mu_R^2}{\hat{m}^2}, \frac{\mu_F^2}{\hat{m}^2}\right) . \quad (5.15)$$

Taking Mellin moments of this function with respect to τ' and a Fourier transform in $\bar{\eta}$, we obtain

$$\int_{-\infty}^{\infty} d\bar{\eta}\, \mathrm{e}^{i\nu\bar{\eta}} \int_0^1 d\tau' \left(\tau'\right)^{N-1} \Omega_{H_1 H_2 \to cd}\left(\tau', \Delta\eta, \bar{\eta}, \alpha_s(\mu_R^2), \frac{\mu_R^2}{\hat{m}^2}, \frac{\mu_F^2}{\hat{m}^2}\right)$$
$$= \sum_{ab} \tilde{f}_a^{H_1}(N+1+i\nu/2, \mu_F^2) \tilde{f}_b^{H_2}(N+1-i\nu/2, \mu_F^2)\, \tilde{\omega}_{ab\to cd}\left(N, \nu, \Delta\eta, \alpha_s(\mu_R^2), \frac{\mu_R^2}{\hat{m}^2}, \frac{\mu_F^2}{\hat{m}^2}\right), \quad (5.16)$$

where $\tilde{f}_a^H(N, \mu_F^2) \equiv \int_0^1 x^{N-1} f_a^H(x, \mu_F^2) dx$, and

$$\tilde{\omega}_{ab\to cd}\left(N, \nu, \Delta\eta, \alpha_s(\mu_R^2), \frac{\mu_R^2}{\hat{m}^2}, \frac{\mu_F^2}{\hat{m}^2}\right) \equiv \int_{-\infty}^{\infty} d\hat{\eta}\, \mathrm{e}^{i\nu\hat{\eta}} \int_0^1 d\hat{\tau}\, \hat{\tau}^{N-1}\, \omega_{ab\to cd}\left(\hat{\tau}, \Delta\eta, \hat{\eta}, \alpha_s(\mu_R^2), \frac{\mu_R^2}{\hat{m}^2}, \frac{\mu_F^2}{\hat{m}^2}\right) . \quad (5.17)$$

Near threshold, keeping only the singular terms in (5.11), the right-hand-side of this reduces to

$$\int_0^1 d\hat{\tau}\, \hat{\tau}^{N-1}\, \omega_{ab\to cd}^{\mathrm{sing}}\left(\hat{\tau}, \Delta\eta, \alpha_s(\mu_R^2), \frac{\mu_R^2}{\hat{m}^2}, \frac{\mu_F^2}{\hat{m}^2}\right) \equiv \tilde{\omega}_{ab\to cd}^{\mathrm{resum}}\left(N, \Delta\eta, \alpha_s(\mu_R^2), \frac{\mu_R^2}{\hat{m}^2}, \frac{\mu_F^2}{\hat{m}^2}\right) . \quad (5.18)$$

We have labeled the new function on the right by the superscript "resum" as it is this quantity that contains all threshold logarithms and that threshold resummation addresses. As discussed in [83], it is important here that we consider fixed $\hat{m}$ and fixed renormalization/factorization scales, which is achieved by isolating the fragmentation functions as in Eq. (5.14). Note that $\tilde{\omega}_{ab\to cd}^{\mathrm{resum}}$ depends on the Mellin variable N only. All dependence on the Fourier variable ν resides in the moments of the parton distribution functions.

5.3 Threshold resummation for hadron-pair production

In this section we present the framework for threshold resummation for di-hadron production at NNLL. We start by giving the main result and discussing its structure. Subsequently, we will describe the various new ingredients in more detail.

5.3.1 Resummation formula at next-to-next-to-leading logarithm

For di-hadron production near threshold, all gluon radiation is soft. Since all four external partons in the hard scattering are "observed" in the sense that they are either incoming or fragmenting partons, each of them makes the same type of (double-logarithmic) contribution to the resummed cross section in moment space, given by a "jet" function Δ_i^N $(i = a, b, c, d)$ that takes into account soft and collinear gluon radiation off an external parton [83, 93, 99]. In addition, large-angle soft emission is sensitive to the color state of the hard scattering, giving rise to a trace structure in color space [78, 80, 81]. The resumBonciani:2003ntmed partonic cross section in moment space then takes the following form [78–83]:

$$\begin{aligned}
\tilde{\omega}^{\rm resum}_{ab\to cd}\left(N,\Delta\eta,\alpha_s(\mu_R^2),\frac{\mu_R^2}{\hat{m}^2},\frac{\mu_F^2}{\hat{m}^2}\right) &= \Delta_a^{N+1}\left(\alpha_s(\mu_R^2),\frac{\mu_R^2}{\hat{m}^2},\frac{\mu_F^2}{\hat{m}^2}\right)\Delta_b^{N+1}\left(\alpha_s(\mu_R^2),\frac{\mu_R^2}{\hat{m}^2},\frac{\mu_F^2}{\hat{m}^2}\right)\\
&\times \Delta_c^{N+2}\left(\alpha_s(\mu_R^2),\frac{\mu_R^2}{\hat{m}^2},\frac{\mu_F^2}{\hat{m}^2}\right)\Delta_d^{N+2}\left(\alpha_s(\mu_R^2),\frac{\mu_R^2}{\hat{m}^2},\frac{\mu_F^2}{\hat{m}^2}\right)\\
&\times \mathrm{Tr}\left\{H\left(\Delta\eta,\alpha_s(\mu_R^2)\right)\mathcal{S}_N^\dagger\left(\Delta\eta,\alpha_s(\mu_R^2),\frac{\mu_R^2}{\hat{m}^2}\right)\right.\\
&\qquad \left. S\left(\alpha_s(\hat{m}^2/\bar{N}^2),\Delta\eta\right)\mathcal{S}_N\left(\Delta\eta,\alpha_s(\mu_R^2),\frac{\mu_R^2}{\hat{m}^2}\right)\right\}_{ab\to cd}\\
&\times \xi_R\left(\alpha_s(\mu_R^2),\frac{\mu_R^2}{\hat{m}^2}\right)\xi_F^{abcd}\left(\alpha_s(\mu_R^2),\frac{\mu_F^2}{\hat{m}^2}\right)\ . \qquad (5.19)
\end{aligned}$$

This form is valid to all logarithmic order, up to corrections that are suppressed by powers of $1/N$, or $1-\hat{\tau}$. The additional functions $\xi_{R,F}$ do not contain threshold logarithms but are N-independent. They serve to improve the dependence of the resummed cross section on the scales μ_R and μ_F. We will now discuss the various functions in Eq. (7.7) and their NNLL expansions.

Jet functions

The radiative functions Δ_i^N are familiar from threshold resummation for the Drell-Yan process. They exponentiate logarithms that arise due to soft-collinear gluon emission by the initial and final-state partons. In the $\overline{\rm MS}$ scheme, they are given by [7, 8, 58, 186]

$$\begin{aligned}
\Delta_i^N\left(\alpha_s(\mu_R^2),\frac{\mu_R^2}{\hat{m}^2},\frac{\mu_F^2}{\hat{m}^2}\right) &= R_i(\alpha_s(\mu_R^2))\exp\left\{\int_0^1 dz\frac{z^{N-1}-1}{1-z}\right.\\
&\times\left.\left[\int_{\mu_F^2}^{(1-z)^2\hat{m}^2}\frac{d\mu^2}{\mu^2}A_i(\alpha_s(\mu^2))+D_i(\alpha_s((1-z)^2\hat{m}^2))\right]\right\}. \qquad (5.20)
\end{aligned}$$

The functions A_i and D_i may be calculated perturbatively as series in α_s,

$$\begin{aligned}
A_i(\alpha_s) &= \frac{\alpha_s}{\pi}A_i^{(1)}+\left(\frac{\alpha_s}{\pi}\right)^2A_i^{(2)}+\left(\frac{\alpha_s}{\pi}\right)^3A_i^{(3)}+\mathcal{O}(\alpha_s^4)\\
D_i(\alpha_s) &= \left(\frac{\alpha_s}{\pi}\right)^2D_i^{(2)}+\mathcal{O}(\alpha_s^3)\ , \qquad (5.21)
\end{aligned}$$

where, up to NNLL, one needs the coefficients [52, 204–209]

$$\begin{aligned}
A_i^{(1)} &= C_i \,, \qquad A_i^{(2)} = \frac{1}{2}\, C_i \left[C_A \left(\frac{67}{18} - \frac{\pi^2}{6} \right) - \frac{5}{9} N_f \right] \,, \\
A_i^{(3)} &= \frac{1}{4} C_i \left[C_A^2 \left(\frac{245}{24} - \frac{67}{9}\zeta(2) + \frac{11}{6}\zeta(3) + \frac{11}{5}\zeta(2)^2 \right) + C_F N_f \left(-\frac{55}{24} + 2\zeta(3) \right) \right. \\
&\qquad \left. + C_A N_f \left(-\frac{209}{108} + \frac{10}{9}\zeta(2) - \frac{7}{3}\zeta(3) \right) - \frac{1}{27} N_f^2 \right] \,, \\
D_i^{(2)} &= C_i \left[C_A \left(-\frac{101}{27} + \frac{11}{3}\zeta(2) + \frac{7}{2}\zeta(3) \right) + N_f \left(\frac{14}{27} - \frac{2}{3}\zeta(2) \right) \right] \,,
\end{aligned} \tag{5.22}$$

with N_f the number of flavors and

$$C_q = C_F = \frac{N_c^2 - 1}{2N_c} = \frac{4}{3} \,, \quad C_g = C_A = N_c = 3 \,. \tag{5.23}$$

The D_i term in the radiative factor Δ_i^N first appears at NNLL accuracy [7, 8, 58, 186]. It takes into account logarithms that arise from soft gluons that are emitted at large angles. Incoming and outgoing external lines of a given parton type carry the same D_i term, as discussed in the Appendix.

Finally, the coefficient R_i in Eq. (6.7) ensures that our soft functions for this process are defined relative to that for the Drell-Yan process; again see the Appendix for details. To the order we consider, we have

$$R_i(\alpha_s) \;=\; 1 - \frac{3\alpha_s}{4\pi}\, A_i^{(1)}\, \zeta(2) + \mathcal{O}(\alpha_s^2) \,. \tag{5.24}$$

Evaluating the integrals in Eq. (6.7), one obtains an explicit expression for the NNLL expansion of the function Δ_i^N:

$$\begin{aligned}
\Delta_i^N \left(\alpha_s(\mu_R^2), \frac{\mu_R^2}{\hat{m}^2}, \frac{\mu_F^2}{\hat{m}^2} \right) \;&=\; \tilde{R}_i(\alpha_s(\mu_R^2)) \exp \left\{ h_i^{(1)}(\lambda) \ln \bar{N} + h_i^{(2)} \left(\lambda, \frac{\mu_R^2}{\hat{m}^2}, \frac{\mu_F^2}{\hat{m}^2} \right) \right. \\
&\qquad \left. + \; \alpha_s(\mu_R^2)\, h_i^{(3)} \left(\lambda, \frac{\mu_R^2}{\hat{m}^2}, \frac{\mu_F^2}{\hat{m}^2} \right) \right\} \,.
\end{aligned} \tag{5.25}$$

Here $\tilde{R}_i$ is a combination of R_i in Eq. (5.24) and a π^2-term arising in the NNLL expansion [186]:

$$\tilde{R}_i(\alpha_s) \;=\; 1 + \frac{\alpha_s}{4\pi}\, A_i^{(1)}\, \zeta(2) + \mathcal{O}(\alpha_s^2) \,. \tag{5.26}$$

In (5.25) we have furthermore defined $\lambda = b_0 \alpha_s(\mu_R^2) \ln(N e^{\gamma_E})$ with γ_E the Euler constant. In the following we denote $N e^{\gamma_E} \equiv \bar{N}$. The functions $h_i^{(1)}, h_i^{(2)}, h_i^{(3)}$ read

$$
\begin{aligned}
h_i^{(1)}(\lambda) &= \frac{A_i^{(1)}}{2\pi b_0 \lambda}\left(2\lambda + (1-2\lambda)\ln(1-2\lambda)\right) \,, && (5.27)\\
h_i^{(2)}\left(\lambda, \frac{\mu_R^2}{\hat{m}^2}, \frac{\mu_F^2}{\hat{m}^2}\right) &= -\frac{A_i^{(2)}}{2\pi^2 b_0^2}\left[2\lambda + \ln(1-2\lambda)\right] \\
&+ \frac{A_i^{(1)} b_1}{2\pi b_0^3}\left[2\lambda + \ln(1-2\lambda) + \frac{1}{2}\ln^2(1-2\lambda)\right] \\
&- \frac{A_i^{(1)}}{2\pi b_0}\left[2\lambda + \ln(1-2\lambda)\right]\ln\frac{\mu_R^2}{\hat{m}^2} + \frac{A_i^{(1)}}{\pi b_0}\lambda \ln\frac{\mu_F^2}{\hat{m}^2} \,, && (5.28)
\end{aligned}
$$

and [58]

$$
\begin{aligned}
h_i^{(3)}\left(\lambda, \frac{\mu_R^2}{\hat{m}^2}, \frac{\mu_F^2}{\hat{m}^2}\right) &= \frac{2A_i^{(1)}}{\pi}\zeta(2)\frac{\lambda}{1-2\lambda} - \frac{A_i^{(2)} b_1}{2\pi^2 b_0^3}\frac{1}{1-2\lambda}\left[2\lambda + \ln(1-2\lambda) + 2\lambda^2\right] \\
&+ \frac{A_i^{(1)} b_1^2}{2\pi b_0^4 (1-2\lambda)}\left[2\lambda^2 + 2\lambda\ln(1-2\lambda) + \frac{1}{2}\ln^2(1-2\lambda)\right] \\
&+ \frac{A_i^{(1)} b_2}{2\pi b_0^3}\left[2\lambda + \ln(1-2\lambda) + \frac{2\lambda^2}{1-2\lambda}\right] + \frac{A_i^{(3)}}{\pi^3 b_0^2}\frac{\lambda^2}{1-2\lambda} \\
&+ \frac{A_i^{(2)}}{\pi^2 b_0}\lambda\ln\frac{\mu_F^2}{\hat{m}^2} - \frac{A_i^{(1)}}{2\pi}\lambda\ln^2\frac{\mu_F^2}{\hat{m}^2} + \frac{A_i^{(1)}}{\pi}\lambda\ln\frac{\mu_R^2}{\hat{m}^2}\ln\frac{\mu_F^2}{\hat{m}^2} \\
&- \frac{1}{1-2\lambda}\left(\frac{A_i^{(1)} b_1}{2\pi b_0^2}\left[2\lambda + \ln(1-2\lambda)\right] - \frac{2A_i^{(2)}}{\pi^2 b_0}\lambda^2\right)\ln\frac{\mu_R^2}{\hat{m}^2} \\
&+ \frac{A_i^{(1)}}{\pi}\frac{\lambda^2}{1-2\lambda}\ln^2\frac{\mu_R^2}{\hat{m}^2} - \frac{D_i^{(2)}}{2\pi^2 b_0}\frac{\lambda}{1-2\lambda} \,. && (5.29)
\end{aligned}
$$

Here b_0, b_1, b_2 are the first three coefficients of the QCD beta function which are given in Eq. (1.12).

Color trace contribution

Next we discuss the trace $\mathrm{Tr}\{H\mathcal{S}_N^\dagger S\mathcal{S}_N\}$ in color space in Eq. (7.7). We note that this is the only contribution to the resummed cross section that depends on the difference of the rapidities $\Delta\eta$. Each of the functions $H_{ab\to cd}$, $\mathcal{S}_{N,ab\to cd}$, $S_{ab\to cd}$ is a matrix in the space of color exchange operators [78, 80, 81]. The $H_{ab\to cd}$ are the hard-scattering functions. They are perturbative and have the expansions

$$
H_{ab\to cd}\left(\Delta\eta, \alpha_s\right) = \left(\frac{\alpha_s}{\pi}\right)^2 \left[H_{ab\to cd}^{(0)}\left(\Delta\eta\right) + \frac{\alpha_s}{\pi} H_{ab\to cd}^{(1)}\left(\Delta\eta\right) + \mathcal{O}(\alpha_s^2)\right] \,. \qquad (5.30)
$$

The LO (i.e. $\mathcal{O}(\alpha_s^2)$) contributions $H^{(0)}_{ab\to cd}$ may be found in [78, 80–82]. For resummation beyond NLL accuracy, one needs all entries of the NLO hard-scattering matrices $H^{(1)}_{ab\to cd}$. These matrices may be extracted from a color decomposed one-loop calculation [83, 203]. We will outline the derivation of the first-order corrections $H^{(1)}_{ab\to cd}$ in Section 5.3.2. We note that they depend in principle also on the renormalization scale μ_R, in the form of a term $\propto \ln(\mu_R^2/\hat{m}^2)H^{(0)}_{ab\to cd}$. This dependence, however, has been absorbed into the contribution involving the function ξ_R in (7.7); see below.

The $S_{ab\to cd}$ are known as soft functions. In general, they depend on the rapidity difference $\Delta\eta$ and on the strong coupling whose argument is to be set to $\hat{m}/\bar{N}$ [78, 80, 81, 191]. This dependence on $\hat{m}/\bar{N}$ and hence on N occurs first at NNLL. The soft functions have the expansion

$$S_{ab\to cd}\left(\alpha_s(\hat{m}/\bar{N}),\Delta\eta\right) = S^{(0)}_{ab\to cd} + \frac{\alpha_s(\hat{m}^2/\bar{N}^2)}{\pi} S^{(1)}_{ab\to cd}\left(\Delta\eta\right) + \mathcal{O}(\alpha_s^2)\ . \tag{5.31}$$

Relating the coupling at scale $\hat{m}/\bar{N}$ to that at scale μ_R, one can construct the explicit N-dependence of the soft matrix at NLO. To the accuracy of resummation that we are considering in this work, it is sufficient to use

$$\alpha_s(\hat{m}^2/\bar{N}^2) = \frac{\alpha_s(\mu_R^2)}{1-2\lambda}\ . \tag{5.32}$$

The LO expressions $S^{(0)}_{ab\to cd}$, which are independent of $\Delta\eta$, may also be found in [78, 80–82]. Like the hard-scattering matrices $H^{(1)}_{ab\to cd}$, at NNLL accuracy, we need the explicit expressions for the full NLO soft-matrices $S^{(1)}_{ab\to cd}$. These may be extracted by performing a color-decomposed calculation of the 2 → 3 contributions to the partonic cross sections in the eikonal approximation, as will be described in Section 5.3.3.

The resummation of wide-angle soft gluons is contained in $\mathcal{S}_{ab\to cd}$. The two exponentials $\mathcal{S}_N^\dagger$ and $\mathcal{S}_N$ that enclose the soft function $S_{ab\to cd}$ within the trace structure appear when solving the renormalization group equation for the soft function [78, 80–82]. The exponentials are given in terms of soft anomalous dimensions $\Gamma_{ab\to cd}$:

$$\mathcal{S}_{N,ab\to cd}\left(\Delta\eta,\alpha_s(\mu_R^2),\frac{\mu_R^2}{\hat{m}^2}\right) \;=\; \mathcal{P}\exp\left[\frac{1}{2}\int_{\hat{m}^2}^{\hat{m}^2/\bar{N}^2}\frac{d\mu^2}{\mu^2}\Gamma_{ab\to cd}\left(\Delta\eta,\alpha_s(\mu^2)\right)\right]\ , \tag{5.33}$$

where $\mathcal{P}$ denotes path ordering. The soft anomalous dimension matrices start at $\mathcal{O}(\alpha_s)$,

$$\Gamma_{ab\to cd}\left(\alpha_s,\Delta\eta\right) = \frac{\alpha_s}{\pi}\,\Gamma^{(1)}_{ab\to cd}\left(\Delta\eta\right) + \left(\frac{\alpha_s}{\pi}\right)^2\Gamma^{(2)}_{ab\to cd}(\Delta\eta) + \mathcal{O}(\alpha_s^3)\ . \tag{5.34}$$

Their first-order terms are presented in [78, 80–82, 210]. We will discuss the $\Gamma_{ab\to cd}$ matrices in more detail in Section 5.3.3. For NNLL resummation, we also need to take into account the second-order contributions $\Gamma^{(2)}_{ab\to cd}$ which were derived in [211–214] and are determined by the one-loop terms:

$$\Gamma^{(2)}_{ab\to cd}(\Delta\eta) = \frac{K}{2}\Gamma^{(1)}_{ab\to cd}(\Delta\eta)\ , \tag{5.35}$$

where $K = C_A(67/18 - \pi^2/6) - 5N_f/9$. We also give here our result for the NNLL expansion of the integral in Eq. (5.33):

$$\ln \mathcal{S}_{N,ab\to cd}\left(\Delta\eta, \alpha_s(\mu_R^2), \frac{\mu_R^2}{\hat{m}^2}\right) = \Gamma^{(1)}_{ab\to cd}(\Delta\eta)\left[\frac{\ln(1-2\lambda)}{2\pi b_0} + \frac{\alpha_s}{\pi}\frac{1}{2b_0^2\pi(1-2\lambda)} \times \left(b_1\pi(2\lambda+\ln(1-2\lambda)) - b_0\lambda\left(K + 2\pi b_0 \ln\frac{\mu_R^2}{\hat{m}^2}\right)\right)\right] . \tag{5.36}$$

We note that in our phenomenological applications we follow [83] and perform the exponentiation of the matrices numerically by iterating the exponential series to an adequately high order.
In order to gauge the roles of the various matrices appearing in the color trace, it is instructive to analyze the structure of the resummed cross section (7.7) in Mellin space after expansion to NLO:

$$\begin{aligned}\tilde{\omega}^{\text{resum}}_{ab\to cd}\left(N, \Delta\eta, \alpha_s(\mu_R^2), \frac{\mu_R^2}{\hat{m}^2}, \frac{\mu_F^2}{\hat{m}^2}\right) &= \left(\frac{\alpha_s(\mu_R^2)}{\pi}\right)^2 \left[\text{Tr}\{H^{(0)}S^{(0)}\}_{ab\to cd}\left\{1 + 2b_0\alpha_s(\mu_R)\ln\frac{\mu_R^2}{\hat{m}^2}\right.\right.\\ &+ \left.\frac{\alpha_s(\mu_R^2)}{\pi}\sum_{i=a,b,c,d}\left(A_i^{(1)}\ln^2\bar{N} + \frac{1}{4}A_i^{(1)}\zeta(2) + \left(A_i^{(1)}\ln\bar{N} + \frac{1}{2}B_i^{(1)}\right)\ln\frac{\mu_F^2}{\hat{m}^2}\right)\right\}\\ &+ \left.\frac{\alpha_s(\mu_R^2)}{\pi}\text{Tr}\Big\{ - \left[H^{(0)}(\Gamma^{(1)})^{\dagger}S^{(0)} + H^{(0)}S^{(0)}\Gamma^{(1)}\right]\ln\bar{N} + H^{(1)}S^{(0)} + H^{(0)}S^{(1)}\Big\}_{ab\to cd}\right] + \mathcal{O}(\alpha_s^4) .\end{aligned} \tag{5.37}$$

Here the term $\propto \zeta(2)$ arises from the coefficient $\tilde{R}_i$ in (5.26). We have anticipated the contributions by the functions ξ_R and ξ_F in (7.7) that will be specified in the next subsection. ξ_R yields the term involving the renormalization scale, and ξ_F contributes the ones $\propto B_i^{(1)}$, with

$$B_q^{(1)} = -\frac{3}{2}C_F , \qquad B_g^{(1)} = -2\pi b_0 . \tag{5.38}$$

The term $\text{Tr}\{H^{(0)}S^{(0)}\}_{ab\to cd}$ in (5.37) is proportional to the LO function $\omega^{(0)}_{ab\to cd}(\Delta\eta)$ introduced in Eq. (5.10). In [83] (as in many previous studies of threshold resummation for hadronic hard-scattering), the combination $\text{Tr}[H^{(1)}S^{(0)} + H^{(0)}S^{(1)}]$, which carries no dependence on N, was extracted as a whole by matching the expression in Eq. (5.37) to the NLO calculation at threshold. Of course, this is not sufficient for determining the full first-order matrices $H^{(1)}$ and $S^{(1)}$. However, it is a valid approach at NLL accuracy, where the three most dominant towers of logarithms are taken into account. For a given fixed-order expansion to $\mathcal{O}(\alpha_s^k)$, the following terms are under control:

$$\alpha_s^k \left\{\ln^{2k}\bar{N},\ \ln^{2k-1}\bar{N},\ \ln^{2k-2}\bar{N}\right\} . \tag{5.39}$$

It is straightforward to see that the hard and soft matrices will contribute to the third tower of threshold logarithms always in the combination $\text{Tr}\{H^{(1)}S^{(0)} + H^{(0)}S^{(1)}\}_{ab\to cd}$ in the following way:

$$\left(\frac{\alpha_s}{\pi}\right)^k \frac{\sum_i A_i^{(1)}}{(k-1)!}\,\text{Tr}\left\{H^{(1)}S^{(0)} + H^{(0)}S^{(1)}\right\}_{ab\to cd}\ln^{2k-2}\bar{N} . \tag{5.40}$$

Hence, to NLL, it is sufficient to know the combined expression of $H^{(1)}$ and $S^{(1)}$ instead of having to compute the full matrices separately. It is then legitimate to that order to approximate the trace term in the resummed formula by

$$\mathrm{Tr}\left\{H\mathcal{S}_N^{\dagger}S\mathcal{S}_N\right\}_{ab\to cd,\,\mathrm{NLL}} = \left(1+\frac{\alpha_s}{\pi}\,C^{(1),\,\mathrm{NLL}}_{ab\to cd}\right)\,\mathrm{Tr}\left\{H^{(0)}\mathcal{S}_N^{\dagger}S^{(0)}\mathcal{S}_N\right\}_{ab\to cd}\,, \tag{5.41}$$

where

$$C^{(1),\,\mathrm{NLL}}_{ab\to cd}\,(\Delta\eta) \equiv \frac{\mathrm{Tr}\left\{H^{(1)}S^{(0)}+H^{(0)}S^{(1)}\right\}_{ab\to cd}}{\mathrm{Tr}\left\{H^{(0)}S^{(0)}\right\}_{ab\to cd}}\,. \tag{5.42}$$

This was the approach adopted in [83] and also, for example, in studies on single-inclusive hadron [215] or jet production [216].

On the other hand, in order to control the fourth tower of logarithms, $\alpha_s^k\,\ln^{2k-3}\bar{N}$, one needs to know $H^{(1)}$ and $S^{(1)}$ explicitly as they also appear separately in various combinations with the anomalous dimension matrices. Computation of the full matrices is therefore a necessary ingredient for NNLL resummation. Clearly, having the matrices at hand, one can compute also the known combination $\mathrm{Tr}\{H^{(1)}S^{(0)}+H^{(0)}S^{(1)}\}_{ab\to cd}$, which provides an important cross-check on them. We stress further that, in order to fully take into account also the fifth tower $\alpha_s^k\,\ln^{2k-4}\bar{N}$ at NNLL, one would need to know the full matrices $H^{(2)}$ and $S^{(2)}$ and perform a matching to NNLO. Although $H^{(2)}$ became available very recently [194], this is beyond the scope of the present work.

We finally note that a new feature which first appears at NNLL is that the hard-scattering matrix H obtains an imaginary part. This is due to the fact that H is constructed from virtual corrections to partonic $2\to 2$ scattering, which contain logarithms of ratios of space- and timelike invariants. We write

$$H = H_R + iH_I \tag{5.43}$$

with H_R and H_I real. It turns out that H_R is a symmetric matrix, whereas H_I is antisymmetric; see Section 5.3.2. Hence, the hard-scattering matrix H as a whole is hermitian, as it should be. The imaginary part H_I contributes to the resummed cross section due to the fact that the remaining terms inside the color trace in the resummed cross section (7.7), $M \equiv \mathrm{e}^{\Gamma^{\dagger}}S\mathrm{e}^{\Gamma}$, also develop an imaginary part since the anomalous dimension matrices are complex-valued [78, 80, 81]. M is also hermitian as the soft matrix S is symmetric, and therefore we may also decompose $M = M_R + iM_I$ with M_R symmetric and M_I antisymmetric. The trace $\mathrm{Tr}\left\{HM\right\}$ is then real, as it must be, but both the real and imaginary parts of H, M contribute:

$$\mathrm{Tr}\left\{HM\right\} = \mathrm{Tr}\left\{H_R M_R\right\} - \mathrm{Tr}\left\{H_I M_I\right\}\,. \tag{5.44}$$

Note that the contribution by the imaginary part of H drops out from $\mathrm{Tr}[H^{(1)}S^{(0)}+H^{(0)}S^{(1)}]$, so that it is not present at NLL. Performing an analytical fixed-order expansion of our NNLL resummed result, we find that the imaginary parts of H and M first start to play a role at N^{3}LO, where they contribute to the fifth tower, $\alpha_s^3\,\ln^2\bar{N}$. We note, however, that the imaginary parts of $\Gamma_{ab\to cd}$ also contribute to the real part of M, since $M = \mathrm{e}^{\Gamma^{\dagger}}S\mathrm{e}^{\Gamma}$. It turns out that they already appear in the *fourth* tower of logarithms. In this way we see that the imaginary parts of the various contributions are important ingredients of the NNLL resummed cross section.

Functions ξ_R and ξ_F

The N-independent function ξ_F^{abcd} in Eq. (7.7) addresses the factorization scale dependence of the cross section [78, 80–82, 97]:

$$\ln \xi_F^{abcd}\left(\alpha_s(\mu_R^2), \frac{\mu_F^2}{\hat{m}^2}\right) = -\frac{1}{2}\sum_{i=a,b,c,d}\int_{\mu_F^2}^{\hat{m}^2}\frac{d\mu^2}{\mu^2}\frac{\alpha_s(\mu^2)}{\pi}B_i^{(1)}\,, \tag{5.45}$$

where we are summing over all four external partons. The coefficients $B_i^{(1)}$, which have been given in Eq. (5.38), correspond to the δ-function contributions to the corresponding LO diagonal parton-to-parton splitting functions and thus depend on whether the considered parton i is a quark or a gluon. As follows from [217], the function ξ_F^{abcd} takes into account all N-independent pieces corresponding to the evolution of parton distributions and fragmentation functions between scales μ_F and $\hat{m}$. Again its first-order contribution would explicitly appear in $H^{(1)}_{ab\to cd}$, from where it has been absorbed. It is straightforward to expand (5.45) to the desired NNLL accuracy.

ξ_R governs the renormalization scale dependence of the resummed cross section. This function was also introduced in [82]. ξ_R essentially serves to set the scale in the strong coupling constant in the overall factor α_s^2 (see Eq. (5.8)) of the cross section to $\hat{m}$:

$$\ln \xi_R\left(\alpha_s(\mu_R^2), \frac{\mu_R^2}{\hat{m}^2}\right) = 2\int_{\mu_R^2}^{\hat{m}^2}\frac{d\mu^2}{\mu^2}\beta(\alpha_s(\mu^2))\,. \tag{5.46}$$

Evaluating the integral while keeping only the first two terms in the QCD β-function,

$$\beta(\alpha_s) \equiv \frac{1}{\alpha_s}\frac{d\alpha_s}{d\log(\mu^2)} = -b_0\alpha_s - b_1\alpha_s^2 + \mathcal{O}(\alpha_s^3)\,, \tag{5.47}$$

and expanding the result up to second order in α_s, we find

$$\ln \xi_R\left(\alpha_s(\mu_R^2), \frac{\mu_R^2}{\hat{m}^2}\right) = 2b_0\alpha_s\ln\frac{\mu_R^2}{\hat{m}^2} + \alpha_s^2\left(2b_1\ln\frac{\mu_R^2}{\hat{m}^2} + b_0^2\ln^2\frac{\mu_R^2}{\hat{m}^2}\right)\,. \tag{5.48}$$

Here b_0, b_1 are as given in (1.12). The first term on the right reproduces the explicit μ_R-dependence of the first-order hard-scattering function that we have chosen to pull out of $H^{(1)}_{ab\to cd}$. The additional terms generated by this expression produce higher-order scale-dependent contributions that will occur in the perturbative series. When combined with resummation at NNLL level, they necessarily help to stabilize the cross section with respect to changes in μ_R, as we shall discuss in more detail now.

Following [218] and suppressing all arguments except for the renormalization scale, we write the perturbative expansion of a generic partonic cross section ω as

$$\omega = \sum_{k=0}^{\infty}\alpha_s^{k+2}(\mu_R^2)\,\omega^{(k)}(\mu_R)\,. \tag{5.49}$$

The LO coefficient $\omega^{(0)}$ is independent of μ_R; all higher-order terms depend on μ_R through the logarithm $L \equiv \ln(\mu_R^2/\hat{m}^2)$. Truncating the series at some fixed $k = n$, the uncertainty introduced by the renormalization scale dependence is of the order of $\mathcal{O}(\alpha_s(\mu_R^2)^{n+3})$. In the following we consider as an example the renormalization scale dependence after truncation to next-to-next-to-leading order (NNLO), which is given by

$$\begin{aligned}
\omega|_{\mathrm{NNLO}} &= \alpha_s^2(\mu_R^2)\,\omega^{(0)} + \alpha_s^3(\mu_R^2)\,\omega^{(1)}(\mu_R) + \alpha_s^4(\mu_R^2)\,\omega^{(2)}(\mu_R) \\
&= \alpha_s^2(\mu_R^2)\,\omega^{(0)} + \alpha_s^3(\mu_R^2)\,\left(\omega'^{\,(1)} + 2b_0\,L\,\omega^{(0)}\right) \\
&+ \alpha_s^4(\mu_R^2)\,\left(\omega'^{\,(2)} + 3b_0\,L\,\omega'^{\,(1)} + (3b_0^2\,L^2 + 2b_1\,L)\,\omega^{(0)}\right)\,, \qquad (5.50)
\end{aligned}$$

where the coefficients $\omega'^{\,(k)}$ denote the terms in $\omega^{(k)}$ that do not carry any dependence on μ_R. As is well-known, the μ_R-dependence of the NNLO cross section is entirely determined by the NLO terms in the perturbative expansion.

We may now compare the general expression in Eq. (5.50) to an NNLO expansion of the resummed cross section $\tilde{\omega}^{\mathrm{resum}}$ at either NLL or NNLL. First of all, we find that the NLO scale dependence and the contribution $(3b_0^2\,L^2+2b_1\,L)\,\omega^{(0)}$ at NNLO are entirely reproduced by the exponential ξ_R in Eqs. (5.46) and (5.48). The interesting term at NNLO is now the term $3b_0\,L\,\omega'^{\,(1)}$ in the last line. Out of the five towers of threshold logarithms that appear at NNLO, the renormalization scale dependence resides only in the lowest three. Indeed, as can be seen from the explicit NLO expansion given in Eq. (5.37), the coefficient $\omega'^{\,(1)}$ contains terms proportional to $\ln^2\bar{N}$, $\ln\bar{N}$, 1 which, at NNLO, correspond to the 3rd, 4th and 5th towers. If we now compare to the NNLO expansion of the *NLL*-resummed cross section, we find that only the scale dependence of the 3rd tower is correctly reproduced. For the 4th and 5th tower, that are not fully taken into account at NLL, we find a factor of $2b_0\,L$ instead of $3b_0\,L$ multiplying the corresponding part of the coefficient $\omega'^{\,(1)}$. If instead resummation is performed at NNLL, the scale dependence in the 4th tower is correctly reproduced as well, whereas in the 5th tower the incorrect factor $2b_0\,L$ remains. (In addition, of course, the scale-independent coefficient $\omega'^{\,(2)}$ also changes). As it turns out, going from NLL to NNLL leads to a dramatic reduction of the renormalization scale uncertainty of the resummed cross section, as will be seen in our numerical studies in Sec. 5.4.

5.3.2 Hard-scattering function

In this Section we present our derivation of the matrices $H^{(1)}_{ab\to cd}$. We note that these were also determined in [203]; the results of our independent computation are in agreement with that reference. As the resulting expressions become rather lengthy in general, we present explicit results only for the simplest partonic channel, $qq'\to qq'$. For ease of notation, we will usually drop the ubiquitous subscript "$qq'\to qq'$" of the matrices. We also refer the reader to Ref. [82], where many details of the relevant color bases have been collected. In fact, for each partonic channel we adopt the corresponding color basis from that reference. We note that our choice differs from the one in [203], where an overcomplete basis was chosen for the $gg\to gg$ channel.

Color basis and lowest-order contribution

We consider the partonic process

$$q(p_1,a)q'(p_2,b) \to q(p_3,c)q'(p_4,d)\ , \tag{5.51}$$

where the p_i are the momenta of the incoming and outgoing quarks, and the indices a, b, c, d denote their color. Given the fact that the leading-order process has only a t-channel contribution, it is convenient to choose the t-channel octet-singlet color basis which leads to a simple form for the lowest-order hard-scattering matrix $H^{(0)}$. The contributing color tensors in this basis are given by (1=octet, 2=singlet)

$$\begin{aligned} \mathcal{C}_1 &\equiv T^g_{ca}T^g_{db} = \frac{1}{2}\left(\delta_{ad}\,\delta_{bc} - \frac{1}{N_c}\,\delta_{ac}\,\delta_{bd}\right)\ , \\ \mathcal{C}_2 &\equiv \delta_{ac}\delta_{bd}\ , \end{aligned} \tag{5.52}$$

where T^g is the generator in the fundamental representation and the indices a, b, c, d will be kept implicit throughout most of our discussion. The soft and hard functions become matrices in this basis, whose entries are determined as the coefficients multiplying the respective tensor structures. The elements of the leading-order contribution to the soft function $S^{(0)}$ in Eq. (5.31) are given by $(I, J = 1, 2)$

$$(S^{(0)})_{JI} \equiv \mathrm{Tr}[\mathcal{C}_J^\dagger \mathcal{C}_I] \equiv \sum_{a,b,c,d=1}^{N_c} \mathcal{C}_J^* \mathcal{C}_I\ . \tag{5.53}$$

In our basis one finds

$$S^{(0)} = \begin{pmatrix} \frac{N_c^2-1}{4} & 0 \\ 0 & N_c^2 \end{pmatrix}\ . \tag{5.54}$$

We next color-decompose the Born amplitude for the process as

$$M^{(0)} = \sum_I h_I^{(0)} \mathcal{C}_I\ . \tag{5.55}$$

Squaring the amplitude and summing (averaging) over external colors and helicities, we find

$$\frac{1}{4N_c^2} \sum_{a,b,c,d=1}^{N_c} |M^{(0)}|^2 = \frac{1}{4N_c^2} \sum_{a,b,c,d=1}^{N_c} \sum_{IJ} h_I^{(0)} h_J^{(0)*} \mathcal{C}_J^* \mathcal{C}_I = \frac{1}{4N_c^2} \sum_{IJ} h_I^{(0)} h_J^{(0)*} S_{JI}^{(0)} \equiv \mathrm{Tr}[H^{(0)} S^{(0)}]\ , \tag{5.56}$$

where

$$(H^{(0)})_{IJ} \equiv \frac{1}{4N_c^2}\, h_I^{(0)} h_J^{(0)*}\ . \tag{5.57}$$

While the matrix $H^{(0)}$ follows from a simple direct calculation, we extract it from the results of [200], since we can then follow the same strategy for the one-loop results given there. The color-decomposed tree-level four-point helicity amplitudes for $qq' \to qq'$ are given in [200] as

$$\begin{aligned}\mathcal{A}^{\lambda\lambda'}_{\text{tree}} &= \left(\delta_{ad}\,\delta_{bc} - \frac{1}{N_c}\,\delta_{ac}\,\delta_{bd}\right) a^{\lambda\lambda'}_{4;0} \\ &\equiv \mathcal{C}_1 \times \left(2a^{\lambda\lambda'}_{4;0}\right) + \mathcal{C}_2 \times 0\,, \end{aligned} \tag{5.58}$$

where $\lambda\lambda'$ denotes the helicity configuration of the initial partons. For a given pair of helicity settings we have $h^{(0)}_{I=1} = 2a_{4;0}$, $h^{(0)}_{I=2} = 0$. The squares of the two helicity amplitudes are

$$\begin{aligned}|a^{--}_{4;0}|^2 &= \frac{s^2}{t^2}\,, \\ |a^{-+}_{4;0}|^2 &= \frac{u^2}{t^2}\,, \end{aligned} \tag{5.59}$$

with the Mandelstam variables

$$\begin{aligned}s &= (p_1+p_2)^2 = \hat{m}^2\,, \\ t &= (p_1-p_3)^2 = -\hat{m}^2\frac{e^{-\Delta\eta}}{e^{\Delta\eta}+e^{-\Delta\eta}}\,, \\ u &= (p_1-p_4)^2 = -\hat{m}^2\frac{e^{\Delta\eta}}{e^{\Delta\eta}+e^{-\Delta\eta}}\,. \end{aligned} \tag{5.60}$$

Averaging over external colors and helicities appropriately, following Eq. (5.56), we obtain the lowest-order hard-scattering matrix as

$$H^{(0)} = \begin{pmatrix} \frac{2}{N_c^2}\frac{s^2+u^2}{t^2} & 0 \\ 0 & 0 \end{pmatrix} \equiv \begin{pmatrix} h_0 & 0 \\ 0 & 0 \end{pmatrix}\,, \tag{5.61}$$

in agreement with [82]. As expected, its only entry is in the "octet-octet" corner, thanks to our choice of color basis.

Hard part at one loop

The hard-scattering matrix $H_{ab\to cd}$ is a perturbative function that contains all contributions associated with momenta of the order of the hard scale $\hat{m}$. Since in the threshold regime there is no phase space for hard on-shell radiation, only purely virtual contributions contribute to $H_{ab\to cd}$. Writing the virtual one-loop amplitude as (again we suppress the indices for the external particles)

$$M^{(1),\text{virt}} = \sum_I \tilde{h}^{(1)}_I \mathcal{C}_I\,, \tag{5.62}$$

and considering the interference with the Born amplitude, the elements of the first-order contribution $H^{(1)}_{ab\to cd}$ are obtained from the finite part of

$$(\tilde{H}^{(1)})_{IJ} \equiv \frac{1}{4N_c^2} \left(\tilde{h}_I^{(1)} h_J^{(0)*} + h_I^{(0)} \tilde{h}_J^{(1)*} \right) . \tag{5.63}$$

Most of the one-loop amplitudes that we need are given in [200]. For the gluonic channel $gg \to gg$, we additionally use the results of [201, 202]. For the process $qq' \to qq'$, the one-loop four-point helicity amplitudes are given in [200] as

$$\begin{aligned} \mathcal{A}^{\lambda\lambda'}_{\text{1loop}} &= \left(\delta_{ad}\, \delta_{bc} - \frac{1}{N_c}\, \delta_{ac}\, \delta_{bd} \right) a^{\lambda\lambda'}_{4;1} + \delta_{ad}\, \delta_{bc}\, a^{\lambda\lambda'}_{4;2} \\ &= \mathcal{C}_1 \times 2 \left(a^{\lambda\lambda'}_{4;1} + a^{\lambda\lambda'}_{4;2} \right) + \mathcal{C}_2 \times \frac{1}{N_c} a^{\lambda\lambda'}_{4;2} \, . \end{aligned} \tag{5.64}$$

From this we can determine the $\tilde{h}_I^{(1)}$. Keeping in mind that we have pulled out an overall factor α_s/π in our definition of the hard-scattering matrix $H^{(1)}$, cf. Eq. (5.30), we have $\tilde{h}^{(1)}_{I=1} = 2(a^{\lambda\lambda'}_{4;1} + a^{\lambda\lambda'}_{4;2})$ and $\tilde{h}^{(1)}_{I=2} = a^{\lambda\lambda'}_{4;2}/N_c$. As shown in [200], the $a^{\lambda\lambda'}_{4;1}$, $a^{\lambda\lambda'}_{4;2}$ are proportional to the tree-level $a^{\lambda\lambda'}_{4;0}$ in (5.58) for each helicity configuration:

$$\begin{aligned} a^{\lambda\lambda'}_{4;1} &= C_\Gamma\, F^{\lambda\lambda'}_{4;1}\, a^{\lambda\lambda'}_{4;0} \, , \\ a^{\lambda\lambda'}_{4;2} &= C_\Gamma\, F^{\lambda\lambda'}_{4;2}\, a^{\lambda\lambda'}_{4;0} \, , \end{aligned} \tag{5.65}$$

where in our normalization

$$C_\Gamma = \frac{e^{\gamma_E \varepsilon}}{4} \, \frac{\Gamma^2(1-\varepsilon)\, \Gamma(1+\varepsilon)}{\Gamma(1-2\varepsilon)} \, . \tag{5.66}$$

Here dimensional regularization with $D = 4 - 2\varepsilon$ dimensions is used. The $F^{\lambda\lambda'}_{4;1}$, $F^{\lambda\lambda'}_{4;2}$ are functions of the Mandelstam variables. Using the shorthand notation

$$L(t) = \log \frac{-t}{s} \, , \;\; L(u) = \log \frac{-u}{s} \, , \;\; L(s) = -i\pi \, , \tag{5.67}$$

we have from [200]:

$$
\begin{aligned}
F_{4;1}^{--} \;=\;& N_c\left[-\frac{2}{\varepsilon^2}-\frac{3}{\varepsilon}+2\frac{L(s)}{\varepsilon}+L^2(t)-\frac{2}{3}L(t)\left(1+3L(s)\right)+\frac{13}{9}+\pi^2\right]+N_f\left[\frac{2}{3}L(t)-\frac{10}{9}\right]\\
&-\frac{1}{N_c}\left[-\frac{2}{\varepsilon^2}-\frac{3}{\varepsilon}-\frac{2}{\varepsilon}(L(s)-L(t)-L(u))-8-L^2(t)+\frac{u^2-s^2}{2s^2}\left((L(t)-L(u))^2+\pi^2\right)\right.\\
&\left.+2L(t)(1+L(s)-L(u))-\frac{1}{s}(uL(t)+tL(u))\right]+4\pi b_0\log\left(\frac{\mu_R^2}{\hat{m}^2}\right)\,,\\
F_{4;1}^{-+} \;=\;& N_c\left[-\frac{2}{\varepsilon^2}-\frac{3}{\varepsilon}+2\frac{L(s)}{\varepsilon}+L^2(t)-\frac{2}{3}L(t)\left(1+3L(s)\right)+\frac{13}{9}+\pi^2\right]+N_f\left[\frac{2}{3}L(t)-\frac{10}{9}\right]\\
&-\frac{1}{N_c}\left[-\frac{2}{\varepsilon}-\frac{3}{\varepsilon}-\frac{2}{\varepsilon}(L(s)-L(t)-L(u))-8-L^2(t)+L(t)(3+2L(s)-2L(u))\right]\\
&+\left(N_c+\frac{1}{N_c}\right)\left[\frac{s^2-u^2}{2u^2}(L^2(t)-2L(s)L(t))+\frac{t}{u}(L(t)-L(s))\right]+4\pi b_0\log\left(\frac{\mu_R^2}{\hat{m}^2}\right)\,,\\
F_{4;2}^{--} \;=\;& 2C_F\left[\frac{2}{\varepsilon}(L(u)-L(s))+\frac{u^2-s^2}{2s^2}\left(L^2(t)+L^2(u)+\pi^2\right)+\frac{t}{s}(L(t)-L(u))+2L(s)L(t)\right.\\
&\left.\qquad-\frac{u^2+s^2}{s^2}L(t)L(u)\right]\,,\\
F_{4;2}^{-+} \;=\;& 2C_F\left[\frac{2}{\varepsilon}(L(u)-L(s))-\frac{s^2-u^2}{2u^2}L^2(t)-\frac{t}{u}(L(t)-L(s))-2L(t)L(u)+\frac{s^2+u^2}{u^2}L(t)L(s)\right]\,.
\end{aligned}
\tag{5.68}
$$

Note that the loop corrections have imaginary parts arising from the analytic continuation of Mandelstam variables into the physical region $s > 0;\ t, u < 0$. They appear in the finite part as well as in the pole contributions.

From this we can construct the matrix $\tilde{H}^{(1)}$ defined in Eq. (5.63) as

$$
\tilde{H}^{(1)}=\frac{C_\Gamma}{4N_c^2}\begin{pmatrix} 16\left(\mathcal{R}e\left(F_{4;2}^{--}+F_{4;1}^{--}\right)\frac{s^2}{t^2}+\mathcal{R}e\left(F_{4;2}^{-+}+F_{4;1}^{-+}\right)\frac{u^2}{t^2}\right) & \frac{4}{N_c}\left(F_{4;2}^{--\,*}\frac{s^2}{t^2}+F_{4;2}^{-+\,*}\frac{u^2}{t^2}\right)\\ \frac{4}{N_c}\left(F_{4;2}^{--}\frac{s^2}{t^2}+F_{4;2}^{-+}\frac{u^2}{t^2}\right) & 0\end{pmatrix}.
\tag{5.69}
$$

The full expression for this matrix is rather lengthy. It has the following explicit structure:

$$
\begin{aligned}
\tilde{H}^{(1)} \;=\;& \frac{1}{2}\left[\left(-\frac{4C_F}{\varepsilon^2}-\frac{6C_F}{\varepsilon}\right)H^{(0)}-\frac{L(s)}{\varepsilon}\frac{C_F}{N_c}\begin{pmatrix}0 & -1\\ 1 & 0\end{pmatrix}-\frac{2}{\varepsilon}L(t)\frac{h_0}{N_c}\begin{pmatrix}1 & 0\\ 0 & 0\end{pmatrix}\right.\\
&\left.+\;\frac{1}{\varepsilon}L(u)\frac{h_0}{N_c}\begin{pmatrix}2(N_c^2-2) & C_F\\ C_F & 0\end{pmatrix}+4\pi b_0\log\left(\frac{\mu_R^2}{\hat{m}^2}\right)H^{(0)}\right]+H^{(1)}\,,
\end{aligned}
\tag{5.70}
$$

where h_0 and $H^{(0)}$ have been given in (5.61). Following [219], we have identified the finite part in the last line with the first-order correction to the hard-scattering matrix. This finite part is a function of the Mandelstam variables only. As one can see, the explicit dependence on the renormalization scale μ_R has been separated from $H^{(1)}$. It is proportional to $H^{(0)}$ and therefore fully taken into account by the exponential ξ_R in Eq. (5.46), as discussed in Sec. 5.3.1.

To present our final results for $H^{(1)}$, we adopt the notation of Ref. [203], where the matrix was derived in the context of the soft-collinear effective theory. We find full agreement with the result in their Eq. (39):

$$\begin{aligned}
\left(H^{(1)}\right)_{11} &= \mathcal{R}e\left\{\frac{1}{2N_c^2}\left[\frac{s^2+u^2}{t^2}\left(-4C_F L(t)^2 + 2X_1(s,t,u)L(t) + 2Y\right)\right.\right.\\
&\qquad\left.\left. +\frac{s^2}{t^2}(C_A-4C_F)Z(s,t,u) - \frac{u^2}{t^2}(2C_A-4C_F)Z(u,t,s)\right]\right\},\\
\left(H^{(1)}\right)_{21} &= \frac{1}{2N_c^2}\left[\frac{s^2+u^2}{t^2}X_2(s,t,u)L(t) - \frac{s^2}{t^2}\frac{C_F}{2C_A}Z(s,t,u) + \frac{u^2}{t^2}\frac{C_F}{2C_A}Z(u,t,s)\right],\\
\left(H^{(1)}\right)_{12} &= \left(H^{(1)}\right)^*_{21},\\
\left(H^{(1)}\right)_{22} &= 0,
\end{aligned} \tag{5.71}$$

with [203]

$$\begin{aligned}
X_1(s,t,u) &= 6C_F - 4\pi b_0 + 8C_F[L(s)-L(u)] - 2C_A[2L(s)-L(t)-L(u)],\\
X_2(s,t,u) &= \frac{2C_F}{C_A}[L(s)-L(u)],\\
Y &= C_A\left(\frac{10}{3}+\pi^2\right) + C_F\left(\frac{\pi^2}{3}-16\right) + \frac{5}{3}4\pi b_0,\\
Z(s,t,u) &= \frac{t}{s}\left(\frac{t+2u}{s}[L(u)-L(t)]^2 + 2[L(u)-L(t)] + \pi^2\frac{t+2u}{s}\right).
\end{aligned} \tag{5.72}$$

There are several ways of checking the validity of the results. The simplest one is to compute

$$\mathrm{Tr}\left[\tilde{H}^{(1)}\,S^{(0)}\right], \tag{5.73}$$

which should reproduce the known one-loop virtual correction to $qq' \to qq'$ scattering given in [200]. This indeed turns out to be the case. Since $S^{(0)}$ is diagonal in our basis, this provides a check on the diagonal elements of $H^{(1)}$.

We also note that the pole terms of the NLO virtual amplitudes $M^{(1),\mathrm{virt}}$ in (5.62), including their imaginary parts, have been predicted in [219, 220] to be given by

$$\tilde{h}_I^{(1)}|_{\substack{\text{pole}\\ \text{terms}}} = \frac{1}{2}\left[-C_F\left(\frac{2}{\varepsilon^2}+\frac{3}{\varepsilon}\right)\mathbb{1}+\frac{1}{\varepsilon}\Gamma^{(1)}_{qq'\to qq'}\right]_{IJ} h_J^{(0)}\,, \tag{5.74}$$

where $\mathbb{1}$ denotes the 2×2 unit matrix and $\Gamma^{(1)}_{qq'\to qq'}$ is the soft anomalous dimension matrix introduced in (5.33) which possesses imaginary parts, see also Eq. (5.76) below. We have verified that this correctly reproduces the pole terms in the $\tilde{h}_I^{(1)}$. In the color generator form, the matrices at the one-loop level are given by [211–214]

$$\Gamma^{(1)}_{ab\to cd} = \frac{1}{2}\sum_{i\in f}\sum_{j\neq i}\boldsymbol{T}_i\cdot\boldsymbol{T}_j\ln\left(\frac{\mu^2}{-s_{ij}}\right)\,, \tag{5.75}$$

with $s_{ij}=(p_i+p_j)^2$ with all momenta flowing in (or out) of the amplitude and some scale μ^2. Hence, the s_{ij} still need to be crossed to the physical Mandelstam variables s,t,u. The $\boldsymbol{T}_i$ are the color generators for parton i up to a factor of ±1, cf. [211–214]. In order to obtain the matrix structure, we have to choose a color basis for a given process. Since the color decomposition is almost analogous to the one presented below in Section 5.3.3 for the matrix $S^{(1)}$, we limit ourselves here to present only the results. For the qq' process, choosing the t-channel color octet-singlet basis cf. [82], we obtain

$$\Gamma^{(1)}_{qq'\to qq'} = \begin{pmatrix} \frac{1}{N_c}(2S-T-U)+2C_FU & 2(U-S) \\ \frac{C_F}{N_c}(U-S) & 2C_FT \end{pmatrix}\,, \tag{5.76}$$

with

$$S=\ln\left(\frac{-s_{12}}{\mu^2}\right),\quad T=\ln\left(\frac{-s_{14}}{\mu^2}\right),\quad U=\ln\left(\frac{-s_{13}}{\mu^2}\right)\,. \tag{5.77}$$

Crossing the s_{ij} to the physical variables $s>0$ and $t,u<0$ via [200]

$$\ln\left(\frac{-s_{ij}}{\mu^2}\right)\to\ln\left|\frac{s_{ij}}{\mu^2}\right|-i\pi\,\theta\left(\frac{s_{ij}}{\mu^2}\right) \tag{5.78}$$

and choosing the scale $\mu^2=s$, we obtain

$$S=-i\pi,\quad T=\ln\left(\frac{-t}{s}\right),\quad U=\ln\left(\frac{-u}{s}\right)\,. \tag{5.79}$$

which matches with the logarithms in Eq. (8.40). As we are particularly interested in the complex part of the Γ matrices and of $H^{(1)}$, we briefly comment on the relation to the $\Gamma^{(1)}_{ab\to cd}$ matrices reported here and the ones in [82]. We find that the $\Gamma^{(1)}_{ab\to cd}$ in [82] are reproduced from our matrix in Eq. (5.76) by choosing S,T,U as

$$S=0,\quad T=\ln\left(\frac{-t}{s}\right)+i\pi,\quad U=\ln\left(\frac{-u}{s}\right)+i\pi \tag{5.80}$$

instead of the choice given in Eq. (5.79) which results in a different imaginary part for $\Gamma^{(1)}_{ab\to cd}$. However, only the combination $e^{\Gamma^\dagger}Se^{\Gamma}$ contributes to the resummed cross section. We note that the the off-diagonal entries of $\Gamma^{(1)}_{qq'\to qq'}$ are a function of the combination $U-S$ which is independent of the choice for S,T,U in Eqs. (5.79), (5.80). We find that the difference between the two choices is always proportional to the unit matrix which commutes and hence drops out in the combination $e^{\Gamma^\dagger}Se^{\Gamma}$. Having checked all processes explicitly, we find that this holds true in general. For example, for the qq' process, we find that this difference is given by the $i\pi\cdot 2C_F\mathbb{1}_{2\times 2}$. In summary, we note that there is some ambiguity for defining the $\Gamma^{(1)}_{ab\to cd}$ matrices which cancels in the physical cross section.

In the way described in this subsection we have determined the one-loop hard-scattering matrix for each partonic channel contributing to di-hadron production. As one can see in Eqs. (5.70), (5.71), for $qq'\to qq'$ the final expression always contains the squares of the tree-level helicity amplitudes $a_{4;0}$. This becomes different for partonic channels involving both external quarks and gluons.

5.3.3 Soft function

We now turn to the computation of the first-order correction $S^{(1)}_{ab\to cd}$ to the soft function in Eq. (5.31). Again we present explicit results only for the qq' channel, although we have of course considered all partonic channels. In fact, in the course of the study of qq' scattering we find a general construction rule for the soft matrix $S^{(1)}_{ab\to cd}$ that turns out to be applicable to all partonic channels.

Color structure of diagrams in the eikonal approximation

In order to to compute the soft matrix at NLO for qq' scattering, we need to consider the process $q(p_1)+q'(p_2)\to q(p_3)+q'(p_4)+g(k)$, where g denotes a radiated gluon with soft momentum k. The diagrams are treated in the eikonal approximation, decomposed according to our color basis. They are shown in Fig. 5.2. The blobs on either side of the cut denote a Born hard part that can be a color-octet or a singlet. There are six diagrams labeled “34” or “12” for example, depending on the external legs between which the additional gluon is exchanged. Eventually, all contributions must be summed. Using the notation of the previous subsection, each of the diagrams in Fig. 5.2 has the structure

$$\sum_{IJ} h_I^{(0)} h_J^{(0)*}\,(\mathcal{R}_{ij})_{JI}\,I_{ij}\;, \tag{5.81}$$

where ij labels the diagram, I_{ij} is an integral over the eikonal factor corresponding to the diagram that we will specify below, and the $(\mathcal{R}_{ij})_{JI}$ form a 2×2 matrix with entries labeled by JI =octet-octet, singlet-octet, etc. For example, for the “octet-octet” entry of $\mathcal{R}_{34}$ we have

$$\begin{aligned}(\mathcal{R}_{34})_{\substack{J=\text{octet}\\ I=\text{octet}}} &= \sum_{\substack{a,b,c,d,c',d'\\ g,g_1,g_2}} T^{g_2}_{bd'}T^{g_2}_{ac'}\,T^{g}_{d'd}T^{g}_{c'c}\,T^{g_1}_{db}T^{g_1}_{ca}\\ &= \sum_{g,g_1,g_2}\mathrm{Tr}[T^{g_2}T^{g}T^{g_1}]\,\mathrm{Tr}[T^{g_2}T^{g}T^{g_1}]\\ &= -\frac{N_c^2-1}{4N_c} = -\frac{C_F}{2}\;. \end{aligned}\tag{5.82}$$

Here g corresponds to the color of the gluon exchanged between the external legs, while g_1 and g_2 are those for the gluons in the amplitudes on the two sides of the cut. Computing in this way the matrices $\mathcal{R}_{ij}$ for all diagrams, we find:

$$\begin{aligned}
\mathcal{R}_{12} &= \mathcal{R}_{34} = \frac{C_F}{2}\begin{pmatrix} -1 & N_c \\ N_c & 0 \end{pmatrix} , \\
\mathcal{R}_{13} &= \mathcal{R}_{24} = \frac{C_F}{2}\begin{pmatrix} -\frac{1}{2} & 0 \\ 0 & 2N_c^2 \end{pmatrix} , \\
\mathcal{R}_{14} &= \mathcal{R}_{23} = \frac{C_F}{2}\begin{pmatrix} \frac{1}{2}(N_c^2-2) & N_c \\ N_c & 0 \end{pmatrix} .
\end{aligned} \tag{5.83}$$

For the sum of all diagrams we thus have

$$\sum_{ij} \mathcal{R}_{ij}\, I_{ij} = \frac{C_F}{2}\begin{pmatrix} \frac{1}{2}(I_{13}+I_{24}) - I_{12} - I_{34} - \frac{N_c^2-2}{2}(I_{14}+I_{23}) & N_c(I_{12}+I_{34}-I_{14}-I_{23}) \\ N_c(I_{12}+I_{34}-I_{14}-I_{23}) & -2N_c^2(I_{13}+I_{24}) \end{pmatrix} . \tag{5.84}$$

We note that the eikonal factor for the interference between initial- and final-state emission has an extra minus sign which we included here.

Integrals I_{ij}

Next, we need to specify and compute the I_{ij}. They are essentially given by eikonal factors integrated over the gluon phase space. They are normalized relative to the Born cross section. Adopting the three-particle phase space in $d = 4 - 2\varepsilon$ dimensions from [83] (see also [191]), one has

$$I_{ij} = -\frac{\alpha_s}{\pi}\frac{s}{4\pi} e^{\varepsilon\gamma_E} \frac{\Gamma(1-\varepsilon)}{\Gamma(1-2\varepsilon)} \int_0^1 d\hat{\tau}\, \hat{\tau}^{-\varepsilon}(1-\hat{\tau})^{1-2\varepsilon} \int d\Omega\, \frac{p_i \cdot p_j}{(p_i \cdot k)(p_j \cdot k)} , \tag{5.85}$$

where

$$\int d\Omega = \int_0^\pi d\psi \sin^{1-2\varepsilon}\psi \int_0^\pi d\theta\, \sin^{-2\varepsilon}\theta\, . \tag{5.86}$$

For completeness, we also give the explicit expressions for the corresponding three-particle Φ_3 and two-particle Φ_2 phase space. From [83], we have the three-particle phase space which is given by

$$\Phi_3 = \frac{s}{(4\pi)^4\Gamma(1-2\varepsilon)}\left(\frac{4\pi}{s}\right)^{2\varepsilon} \int_0^1 d\hat{\tau}\, \hat{\tau}^{-\varepsilon}(1-\hat{\tau})^{1-2\varepsilon} \int_0^\infty d\rho\, \rho^{-\varepsilon}(1+\rho)^{-2+2\varepsilon} \int d\Omega\, , \tag{5.87}$$

where $\rho = t/u = e^{-\Delta\eta}$. Φ_2 that is needed for the normalization in (5.85) and it is given by [45]

$$\Phi_2 = \frac{1}{8\pi\Gamma(1-\varepsilon)}\left(\frac{4\pi}{s}\right)^{\varepsilon} \int_0^1 d\hat{\tau}\, \delta(1-\hat{\tau}) \int_0^\infty d\rho\, \rho^{-\varepsilon}(1+\rho)^{-2+2\varepsilon}\, . \tag{5.88}$$

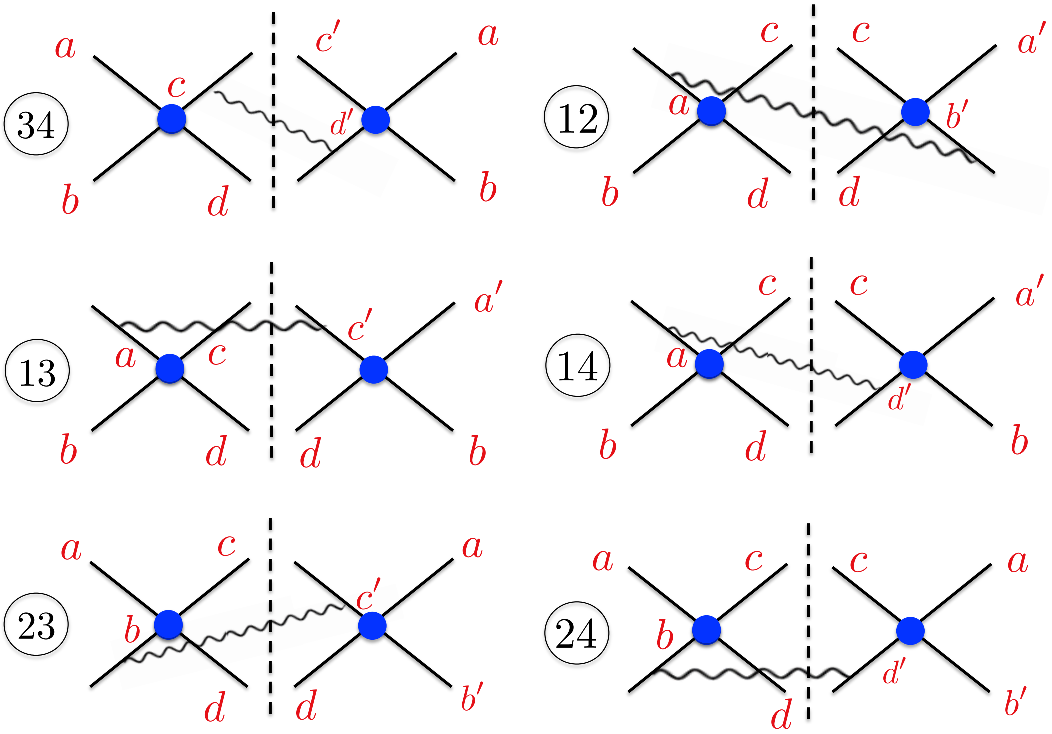

Figure 5.2: Diagrams relevant for the calculation of the NLO soft matrix $S^{(1)}$. The blobs represent a Born amplitude and the letters are color indices.

We work in the c.m.s. of the incoming partons; ψ and θ are the gluon's polar and azimuthal angles relative to the plane defined by the directions of incoming and outgoing hard partons. The relevant angular integrals are well-known [221]:

$$\int d\Omega \, \frac{1}{(1-\cos\psi)^j(1-\cos\psi\cos\chi-\sin\psi\cos\theta\sin\chi)^k}$$
$$= 2\pi\frac{\Gamma(1-2\varepsilon)}{\Gamma(1-\varepsilon)^2}\, 2^{-j-k}\, B(1-\varepsilon-j, 1-\varepsilon-k)\, {}_2F_1\left(j,k,1-\varepsilon,\cos^2\frac{\chi}{2}\right) \ , \qquad (5.89)$$

with the Hypergeometric function ${}_2F_1$. Performing the integrations over $d\Omega$, but leaving the integration over $\hat{\tau}$ (or, equivalently, gluon energy) aside for the moment, we find near threshold

$$\begin{aligned}
\frac{dI_{12}}{d\hat{\tau}} &= \frac{dI_{34}}{d\hat{\tau}} = -\frac{\alpha_s}{\pi}\left[\left(\frac{1}{\varepsilon^2}-\frac{\pi^2}{4}\right)\delta(1-\hat{\tau}) - \frac{2}{\varepsilon}\,\frac{1}{(1-\hat{\tau})_+} + 4\left(\frac{\ln(1-\hat{\tau})}{1-\hat{\tau}}\right)_+\right]\,,\\
\frac{dI_{13}}{d\hat{\tau}} &= \frac{dI_{24}}{d\hat{\tau}} = -\frac{\alpha_s}{\pi}\left[\left(\frac{1}{\varepsilon^2}-\frac{\pi^2}{4}-\frac{1}{\varepsilon}\ln\left(-\frac{t}{s}\right)-\mathrm{Li}_2\left(-\frac{u}{t}\right)\right)\delta(1-\hat{\tau})\right.\\
&\qquad\qquad\left. +2\left(-\frac{1}{\varepsilon}+\ln\left(-\frac{t}{s}\right)\right)\frac{1}{(1-\hat{\tau})_+} + 4\left(\frac{\ln(1-\hat{\tau})}{1-\hat{\tau}}\right)_+\right]\,,\\
\frac{dI_{23}}{d\hat{\tau}} &= \frac{dI_{14}}{d\hat{\tau}} = \left.\frac{dI_{13}}{d\hat{\tau}}\right|_{t\leftrightarrow u}\,,
\end{aligned} \tag{5.90}$$

where Li_2 denotes the Dilogarithm function.

Extraction of $S^{(1)}$

Combining Eqs. (5.84) and (5.90), we obtain

$$\begin{aligned}
&\sum_{ij}\mathcal{R}_{ij}\,\frac{dI_{ij}}{d\hat{\tau}}\\
&= C_F\frac{\alpha_s}{\pi}\left[\left\{\delta(1-\hat{\tau})\left(\frac{1}{2\varepsilon^2}-\frac{\pi^2}{8}\right)-\frac{1}{\varepsilon}\,\frac{1}{(1-\hat{\tau})_+}+2\left(\frac{\ln(1-\hat{\tau})}{1-\hat{\tau}}\right)_+\right\}\begin{pmatrix} N_c^2-1 & 0\\ 0 & 4N_c^2\end{pmatrix}\right.\\
&\quad+\left\{\delta(1-\hat{\tau})\,\frac{1}{2\varepsilon}-\frac{1}{(1-\hat{\tau})_+}\right\}\begin{pmatrix}\ln\left(-\frac{t}{s}\right)+(2-N_c^2)\ln\left(-\frac{u}{s}\right) & -2N_c\ln\left(-\frac{u}{s}\right)\\ -2N_c\ln\left(-\frac{u}{s}\right) & -4N_c^2\ln\left(-\frac{t}{s}\right)\end{pmatrix}\\
&\quad\left.+\,\delta(1-\hat{\tau})\,\frac{1}{2}\begin{pmatrix}\mathrm{Li}_2\left(-\frac{u}{t}\right)+(2-N_c^2)\,\mathrm{Li}_2\left(-\frac{t}{u}\right) & -2N_c\,\mathrm{Li}_2\left(-\frac{t}{u}\right)\\ -2N_c\,\mathrm{Li}_2\left(-\frac{t}{u}\right) & -4N_c^2\,\mathrm{Li}_2\left(-\frac{u}{t}\right)\end{pmatrix}\right].
\end{aligned} \tag{5.91}$$

In the first term we recognize the lowest-order soft matrix of Eq. (5.54). The matrix in the second term has a direct relation to the one-loop soft anomalous dimension matrix $\Gamma^{(1)}_{qq'\to qq'}$ introduced in (5.33), (5.34) and which is given explicitly in Eq. (5.76) for the $qq'\to qq'$ channel.

One easily checks that the matrix in the second line of (5.91) is given by $-[(\Gamma^{(1)})^\dagger S^{(0)} + S^{(0)}\Gamma^{(1)}]/C_F$.

Hence, we have after some reordering of terms:

$$\begin{aligned}\sum_{ij} \mathcal{R}_{ij}\,\frac{dI_{ij}}{d\hat{\tau}} \;=\;& \frac{\alpha_s}{\pi}\Bigg[\delta(1-\hat{\tau})\left\{\frac{2C_F}{\varepsilon^2}S^{(0)}-\frac{1}{2\varepsilon}\left[(\Gamma^{(1)})^\dagger S^{(0)}+S^{(0)}\Gamma^{(1)}\right]\right\}\\ & -\frac{4C_F}{\varepsilon}\,\frac{1}{(1-\hat{\tau})_+}S^{(0)}+8C_F\left(\frac{\ln(1-\hat{\tau})}{1-\hat{\tau}}\right)_+S^{(0)}+\frac{1}{(1-\hat{\tau})_+}\left[(\Gamma^{(1)})^\dagger S^{(0)}+S^{(0)}\Gamma^{(1)}\right]\\ & +\frac{C_F}{2}\delta(1-\hat{\tau})\left\{\begin{pmatrix}\mathrm{Li}_2\left(-\frac{u}{t}\right)+(2-N_c^2)\,\mathrm{Li}_2\left(-\frac{t}{u}\right) & -2N_c\,\mathrm{Li}_2\left(-\frac{t}{u}\right)\\ -2N_c\,\mathrm{Li}_2\left(-\frac{t}{u}\right) & -4N_c^2\,\mathrm{Li}_2\left(-\frac{u}{t}\right)\end{pmatrix}-\pi^2S^{(0)}\right\}\Bigg]\,.\end{aligned} \tag{5.92}$$

Each of the terms in this equation has a transparent interpretation. The pole terms $\propto \delta(1-\hat{\tau})$ in the first line will be canceled by corresponding terms in the virtual correction; see Eq. (5.74). The single pole term $\propto 1/(1-\hat{\tau})_+$ will be canceled by collinear factorization in the eikonal approximation, as described in the Appendix. The next two terms precisely match the threshold logarithms at NLO, as becomes evident by going to Mellin-moment space and comparing to (5.37). The remaining term involves the one-loop soft matrix we are interested in. More precisely, since $S^{(1)}$ appears in the Mellin-space expression for the resummed cross section, and since the moments of $(\ln(1-\hat{\tau})/(1-\hat{\tau}))_+$ are given by $\frac{1}{2}(\ln^2\bar{N}+\pi^2/6)$ (up to corrections suppressed as $1/N$), all terms $\propto \pi^2$ match when comparing to (5.37), and we are just left with

$$S^{(1)} \;=\; \frac{C_F}{2}\begin{pmatrix}\mathrm{Li}_2\left(-\frac{u}{t}\right)+(2-N_c^2)\,\mathrm{Li}_2\left(-\frac{t}{u}\right) & -2N_c\,\mathrm{Li}_2\left(-\frac{t}{u}\right)\\ -2N_c\,\mathrm{Li}_2\left(-\frac{t}{u}\right) & -4N_c^2\,\mathrm{Li}_2\left(-\frac{u}{t}\right)\end{pmatrix}\,. \tag{5.93}$$

This is our final result for the one-loop soft matrix for this process. A powerful check on the result comes from comparison with the full cross section at NLO: Inserting our $S^{(1)}$ along with $H^{(1)}$ from Eq. (5.71) into (5.37), we verify that the resulting expression correctly reproduces all threshold logarithms *and all constant terms* in the NLO partonic cross section.

As it turns out, we can give a very simple rule for obtaining $S^{(1)}$ directly from $S^{(0)}$ and the anomalous dimension matrix $\Gamma^{(1)}$. This becomes already evident from comparison of the two matrices in the second and third lines of (5.91): They have identical structure, except that each logarithm has to be replaced by a dilogarithm with suitably modified argument,

$$\begin{aligned}\ln\left(-\frac{t}{s}\right) &\;\to\; \mathrm{Li}_2\left(-\frac{u}{t}\right)\,,\\ \ln\left(-\frac{u}{s}\right) &\;\to\; \mathrm{Li}_2\left(-\frac{t}{u}\right)\,.\end{aligned} \tag{5.94}$$

The deeper reason for this is of course that already in the integrals (5.90) the logarithm and the dilogarithm always appear in the same ratio in the term $\propto \delta(1-\hat{\tau})$. Since we know how the matrix in the second line is expressed in terms of $S^{(0)}$ and $\Gamma^{(1)}$, we also know how to construct $S^{(1)}$: Compute the combination $-1/2\left((\Gamma^{(1)})^\dagger S^{(0)}+S^{(0)}\Gamma^{(1)}\right)$ and substitute each logarithm according to (5.94). As the integrals I_{ij} are the same no matter which process we are considering, this simple construction rule works for all partonic channels. All necessary ingredients, the $\Gamma^{(1)}_{ab\to cd}$ and the $S^{(0)}_{ab\to cd}$, may be found in the Appendix of Ref. [82]; we therefore do not present the explicit expressions for the resulting $S^{(1)}_{ab\to cd}$ for all the other channels, which become rather lengthy. It is likely that the simple rule we find is a special property of the pair mass kinematics we are considering here.

5.3.4 Inverse Mellin and Fourier transforms and matching procedure

In order to produce phenomenological results for the resummed case, we need to perform inverse Mellin transform and Fourier transforms. The Mellin inverse requires a prescription for dealing with the singularity in the perturbative strong coupling constant in the NNLL expansions of the resummed exponents. As in [83] we will use the *Minimal Prescription* developed in [64], which relies on use of the NNLL expanded forms given in Sec. 5.3.1 and on choosing a Mellin contour in complex-N space that lies to the *left* of the poles at $\lambda = 1/2$ and $\lambda = 1$ in the Mellin integrand. The function $\Omega_{H_1H_2\to cd}$ in (5.15) is obtained as [83]

$$\Omega^{\mathrm{resum}}_{H_1H_2\to cd}\left(\tau', \Delta\eta, \bar{\eta}, \alpha_s(\mu_R^2), \frac{\mu_R^2}{\hat{m}^2}, \frac{\mu_F^2}{\hat{m}^2}\right) = \frac{1}{2\pi}\int_{-\infty}^{\infty} d\nu\, \mathrm{e}^{-i\nu\bar{\eta}} \int_{C_{MP}-i\infty}^{C_{MP}+i\infty} \frac{dN}{2\pi i}\, \left(\tau'\right)^{-N}$$

$$\times \sum_{ab} \tilde{f}_a^{H_1}(N+1+i\nu/2, \mu_F^2)\tilde{f}_b^{H_2}(N+1-i\nu/2, \mu_F^2)\, \tilde{\omega}^{\mathrm{resum}}_{ab\to cd}\left(N, \nu, \Delta\eta, \alpha_s(\mu_R^2), \frac{\mu_R^2}{\hat{m}^2}, \frac{\mu_F^2}{\hat{m}^2}\right), \quad (5.95)$$

with a suitable Mellin contour consistent with the minmal prescription. As shown in [83], it is straightforward to perform the convolution of the inverted resummed $\Omega^{\mathrm{resum}}_{H_1H_2\to cd}$ with the fragmentation functions, as given by (5.14).

As in [83], we match the resummed cross section to the full NLO one, by expanding the resummed cross section to $\mathcal{O}(\alpha_s^3)$, subtracting the expanded result from the resummed one, and adding the full NLO cross section:

$$d\sigma^{\mathrm{match}} = \left(d\sigma^{\mathrm{resum}} - d\sigma^{\mathrm{resum}}\Big|_{\mathcal{O}(\alpha_s^3)} \right) + d\sigma^{\mathrm{NLO}}\ . \quad (5.96)$$

For the NLO cross section we use the results of [222]. In this way, NLO is taken into account in full, and the soft-gluon contributions beyond NLO are resummed in the way described above. Of course, for a full NNLL resummed cross section one would prefer to match to an NNLO calculation, which however is not available for this observable yet.

5.4 Phenomenological results

We now examine the numerical effects of our approximate NNLL resummation in comparison to the NLL and NLO results shown in [83]. Since the NNLL effects are generally rather similar for the experimental situations considered in [83], we show only two representative examples here. We will also make predictions for the di-hadron cross section at RHIC, where one would expect the effects of resummation to be smaller.

Our examples from [83] concern the NA24 [195] and the CCOR [199] $pp \to \pi^0\pi^0$ scattering experiments. The fixed-target experiment NA24 recorded data at a beam energy of $E_p = 300$ GeV, while CCOR operated at the ISR collider at $\sqrt{S} = 62.4$ GeV. Both experiments employed the cuts $p_T^{\mathrm{pair}} < 1$ GeV, $|Y| < 0.35$, and $|\cos\theta^*| < 0.4$. Here, p_T^{pair} and Y are the transverse momentum and rapidity of the pion pair, respectively, which are given in terms of the individual pion transverse momenta $p_{T,i}$ and of $\Delta\eta, \bar{\eta}$ in (5.4) by

$$\begin{aligned} p_T^{\mathrm{pair}} &= |p_{T,1} - p_{T,2}| \, , \\ Y &= \bar{\eta} - \frac{1}{2} \ln\left(\frac{p_{T,1}\,\mathrm{e}^{-\Delta\eta} + p_{T,2}\,\mathrm{e}^{\Delta\eta}}{p_{T,1}\,\mathrm{e}^{\Delta\eta} + p_{T,2}\,\mathrm{e}^{-\Delta\eta}} \right) \, , \end{aligned} \tag{5.97}$$

where LO kinematics have been assumed as appropriate in the threshold regime. Furthermore, $\cos\theta^*$ is the cosine of the scattering angle in the partonic c.m.s. and is for LO kinematics given by

$$\cos\theta^* = \frac{1}{2} \left(\frac{p_{T,1}}{p_{T,2} + p_{T,1}\cosh(2\Delta\eta)} + \frac{p_{T,2}}{p_{T,1} + p_{T,2}\cosh(2\Delta\eta)} \right) \sinh(2\Delta\eta) \, . \tag{5.98}$$

For details on the kinematical variables, see [83]. Thanks to our way of organizing the threshold resummed cross section, inclusion of cuts on any of these variables is straightforward.

In all our calculations, we use the CTEQ6M5 set of parton distribution functions [223], along with its associated value of the strong coupling constant. As compared to our results in [83], we update to the latest "de Florian-Sassot-Stratmann" (DSS) set of fragmentation functions [72]. We note that one might object that the use of NLO parton distribution functions and fragmentation functions is not completely justified for obtaining NNLL resummed predictions. However, since anyway fragmentation functions evolved at NNLO are not available yet, we have decided to stick to NLO functions throughout. As in [83], we choose the renormalization and factorization scales to be equal, $\mu_R = \mu_F \equiv \mu$, and we give them the values M and $2M$, in order to investigate the scale dependence of the results.

Figure 5.3 shows the comparison to the NA24 [195] data. As known from [83], the full NLO cross section and the first-order expansion of the resummed expression, that is, the last two terms in Eq. (5.96), agree to a remarkable degree. Their difference actually never exceeds 1% for the kinematics relevant for NA24. We recall these results by the dashed lines and the crosses in the figure. They provide confidence that the soft-gluon terms constitute the dominant part of the cross section, so that their resummation is sensible. The dot-dashed lines in the figure present the NLL results, computed by dropping all NNLL terms and matching to NLO via Eqs. (5.41),(5.42), as in [83]. As found there, resummation leads to a significant enhancement of the theoretical prediction and provides a much better description of the NA24 data [195] than for the NLO calculation. Finally, the two solid lines show our NNLL resummed results. The key observations are that the two NNLL results for scales $2M$ and M are very close together and both roughly fall within the "band" spanned by the two NLL results for the two scales. One also notices that the NNLL curves have a slope somewhat less steep than the NLL ones. Given the relatively large uncertainties of the data, it is fair to say that the main effects are already taken into account at NLL. However, the precision of the NNLL calculation, in particular the strong reduction of the scale dependence, still provides a significant theoretical and phenomenological improvement.

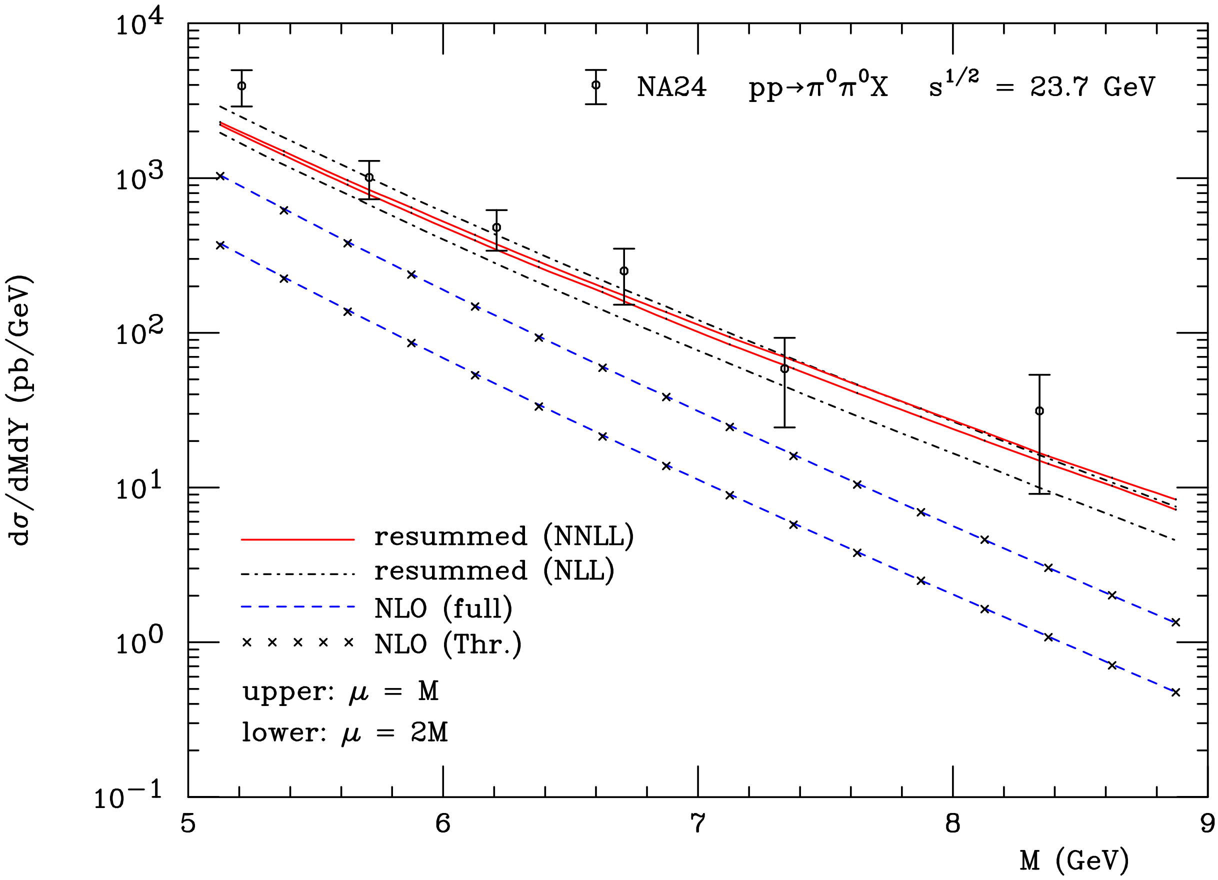

Figure 5.3: Comparison of NLO (dashed), NLL resummed (dot-dashed) and NNLL resummed (solid) calculations of the cross section for $pp \to \pi^0\pi^0 X$ to the NA24 data [195], for two different choices of the renormalization and factorization scales, $\mu_R = \mu_F = M$ (upper lines) and $\mu_R = \mu_F = 2M$ (lower lines). The crosses display the NLO $\mathcal{O}(\alpha_s)$ expansion of the resummed cross section.

In order to assess the improvement in scale dependence in a more detailed way, we show in Fig. 5.4 results for the predicted cross section as a function of μ/M (where again $\mu_R = \mu_F \equiv \mu$), using a fixed pair invariant mass $M = 5.125$ GeV, which corresponds to the left-most point in Fig. 5.3. The dot-dashed line corresponds to the variation of the NLL resummed cross section, where for ξ_R in Eq. (5.48) we include only the first term in the exponent, i.e. $2b_0\alpha_s \ln(\mu_R^2/\hat{m}^2)$. This is the only term justified for a cross section resummed to this accuracy. We note that keeping this term in the exponent or expanding the exponential to first order (as done in [83]) makes only a modest numerical difference. At NNLL, we include the full exponent ξ_R in Eq. (5.48), keeping in mind the discussion following Eq. (5.50). Our result for the scale variation of the NNLL resummed cross section is shown as a solid line in Fig. 5.4. One observes a very strong improvement when going from NLL to NNLL, with the NNLL resummed cross section rather flat even out to scales as large as $\mu = 10M$.

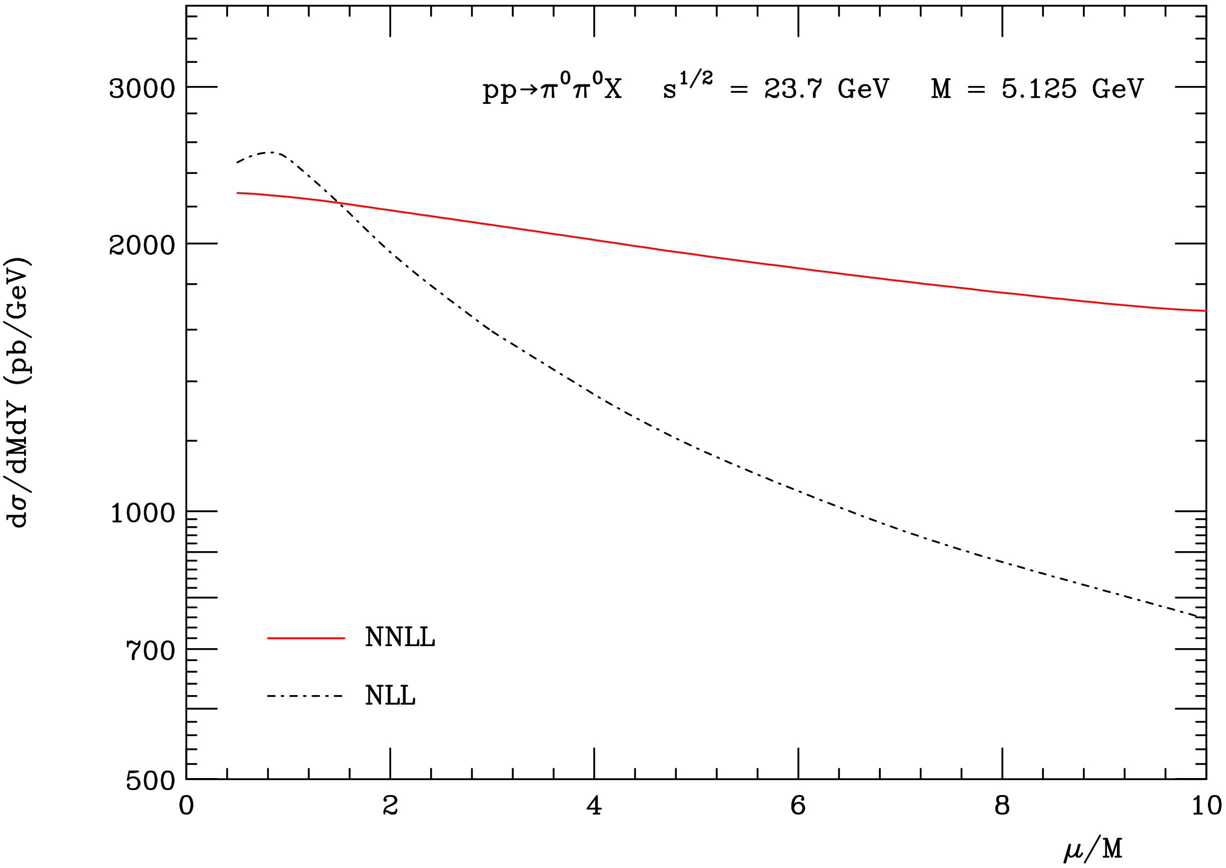

Figure 5.4: Comparison of the scale dependence of the NLL resummed (dot-dashed) and the NNLL resummed (solid) cross sections for NA24 kinematics. We choose a pion pair invariant mass of $M = 5.125$ GeV and show the variation of the cross sections as a function of μ/M, where $\mu_R = \mu_F = \mu$.

Figure 5.5 shows the comparison of our results to the CCOR data [199]. The main features of the results are very similar to those in Fig. 5.3. Again the scale dependence is strongly reduced at NNLL. As a side remark we note that the new fragmentation functions of [72] also help to achieve a much better description of the data than we found in our previous study [83].

Finally, we consider di-hadron production in pp collisions at RHIC with a c.m.s. energy of $\sqrt{S} = 200$ GeV. For simplicity, we use the same cuts as for the NA24 experiment. In Fig. 5.6, we show our results for an invariant mass range of $M = 10 - 75$ GeV. We find that at this energy the full NLO (dashed) and the NLO expansion of the resummed result (crosses) do not match quite as well as observed for fixed target scattering in Fig. 5.3, although the agreement is usually at the 10% level or better. Threshold resummation again yields a sizable enhancement over NLO, but the effects are somewhat smaller than in the fixed-target regime, since at RHIC's higher energy one is typically further away from threshold. Also here, the NNLL-resummed result is nearly within the NLL scale uncertainty

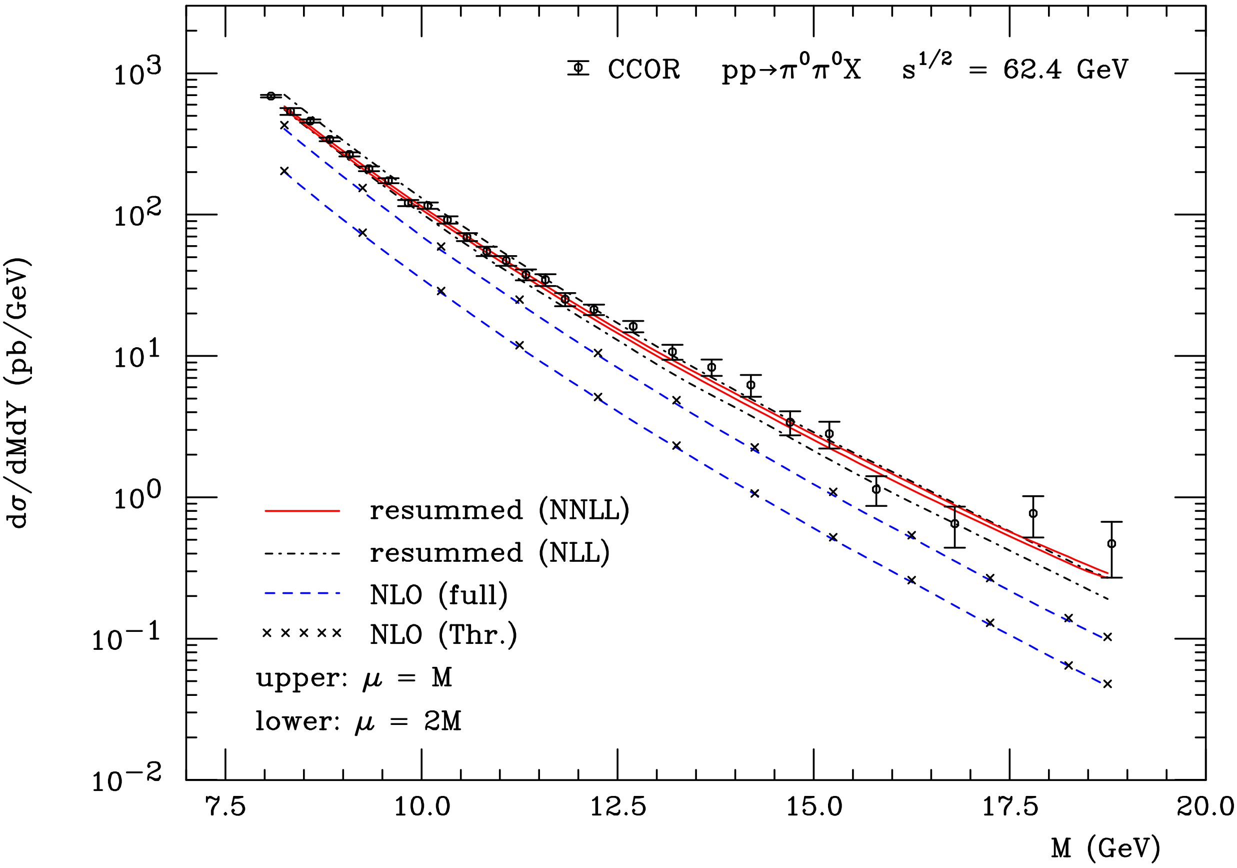

Figure 5.5: Same as Fig. 5.3, but for pp-collisions at $\sqrt{S} = 62.4$ GeV. The data are from CCOR [199].

band and shows a reduced scale dependence.

5.5 Conclusions

We have extended the threshold resummation framework for di-hadron production in hadronic collisions, $H_1H_2 \to h_1h_2X$, beyond the next-to-leading logarithmic level. To achieve this, we have determined the first-order corrections to the hard-scattering function H and the soft function S, which both are matrices in color space. With these, it becomes possible to resum four towers of threshold logarithms in the perturbative series. In our numerical studies, we have found that the NNLL resummed results fall within the scale uncertainty band of the NLL resummed calculation. They also show a much reduced scale dependence.

There are important further applications of our work. Of particular interest are di-jet, single-inclusive jet and single-inclusive hadron cross sections, all of which have much phenomenological relevance at present-day collider experiments. Given the promising results we have obtained for di-hadron

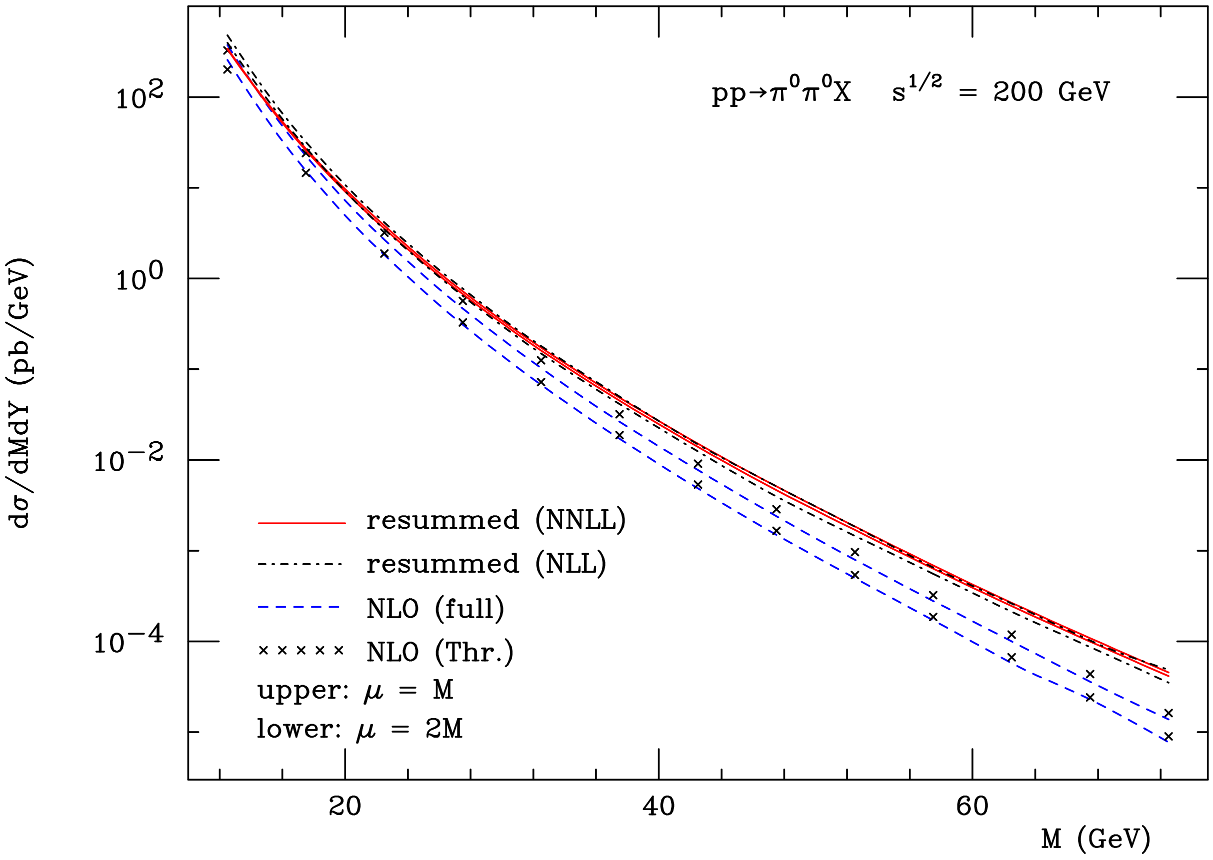

Figure 5.6: Di-hadron production at RHIC at a center-of-mass energy of $\sqrt{S} = 200$ GeV. The full NLO result (dashed) is shown in comparison to the NLO expansion of the resummed result (crosses). The solid line shows the NNLL resummed cross section. As before, we use the scales $\mu_R = \mu_F = M$ and $\mu_R = \mu_F = 2M$.

production, we may expect that a similar resummation at NNLL for these reactions would also improve the theoretical QCD prediction.

CHAPTER 6

TOWARD NNLL THRESHOLD RESUMMATION FOR SINGLE-INCLUSIVE HADRON PRODUCTION

We consider the cross section for single-inclusive hadron production in hadronic collisions $H_1 H_2 \to hX$ where the observed final state hadron has a large transverse momentum. We discuss resummation of threshold logarithms that appear in the partonic cross section. We provide all necessary ingredients for the extension of threshold resummation beyond next-to-leading logarithmic accuracy. This Chapter is based on publication [v].

6.1 Introduction

Single-inclusive hadron production in hadronic collisions $H_1 H_2 \to hX$ plays an important role in QCD studies. At large transverse momentum of the observed hadron the cross section may be calculated within perturbative QCD. Following the factorization theorems developed in [5], the partonic hard scattering part may be calculated as a power series in the strong coupling constant whereas long-distance dynamics are captured in PDFs and FFs for initial and final state particles respectively. On the one hand, this process provides an important test ground for the framework of factorization. On the other hand, single-inclusive hadron production offers an excellent opportunity to extract information on fragmentation functions. Within a global analysis this process is particularly relevant for constraints on the gluon fragmentation function.

On the experimental side, there are various data sets available nowadays from both fixed target and collider experiments. It was found in [215, 224, 225] that in particular at fixed target energies the NLO falls short of the data. This is due to missing higher order corrections. In particular threshold logarithms turn out to be important which appear at every order in perturbation theory and need to be resummed to all orders. Threshold resummation for single-inclusive hadron production was developed in [84, 87, 215]. In this work we extend the resummation framework toward NNLL following the techniques developed in Chapter 5. The process that we are considering here is closely related to dihadron production and single-inclusive jet production discussed in Chapters 5 and 7 respectively. The same partonic channels contribute where at LO four colored partons are taking part in the scattering. Hence, for all three processes the nontrivial underlying color structure needs to be properly taken in account when the resummation is performed.

In [215], threshold resummation for single-inclusive hadron production was performed at the level of NLL accuracy for the rapidity integrated cross section. The methods developed in [77] will allow us to consider a cross section differential in both the transverse momentum p_T and the rapidity η of the observed hadron. We derive all ingredients relevant for the resummation beyond NLL. However, we leave detailed phenomenological studies for future work. In addition, this framework is also applicable to spin-dependent observables [226].

We denote the momenta of the involved particles as $H_1(P_a)H_2(P_b) \to h(P_c)X$, where one hadron is observed in the final state and we are summing over any additional final state X. We write the partonic momenta as

$$p_{a,b} = x_{a,b}P_{a,b}\,, \qquad p_c = \frac{P_c}{z_c}\,. \tag{6.1}$$

We introduce the usual kinematical variables for single-inclusive cross sections

$$V = 1 + \frac{T}{S}\,, \quad W = \frac{-U}{S+T}\,, \tag{6.2}$$

where S, T, U are the usual Mandelstam variables. Analogous relations hold at the partonic level for the variables v, w, see also Chapter 9. We can write the double differential cross section involving two PDFs $f_{a,b}^{H_{1,2}}$, a fragmentation function D_c^h and the partonic cross section $d\hat{\sigma}^{ab\to cd}$ as

$$\begin{aligned}\frac{p_T^2\, d^2\sigma^{H_1H_2\to hX}}{dp_T^2 d\eta} &= \sum_{abcd}\int_{1-V+VW}^{1} dz_c \int_{VW/z_c}^{1-(1-V)/z_c} dv \int_{VW/(vz_c)}^{1} dw\, x_a f_a^{H_1}(x_a,\mu_F^2)\, x_b f_b^{H_2}(x_b,\mu_F^2) \\ &\times\; D_c^h(z_c,\mu_F^2)\,\frac{d^2\hat{\sigma}^{ab\to cd}}{dvdw}\left(v, w, \frac{\mu_F^2}{s}, \frac{\mu_R^2}{s}, \alpha_s(\mu_R^2)\right)\,,\end{aligned} \tag{6.3}$$

where

$$x_a = \frac{VW}{vwz_c}\,, \qquad x_b = \frac{1-V}{(1-v)z_c}\,. \tag{6.4}$$

The integration limits in Eq. (6.3) follow from $x_{a,b} < 1$ and from the requirement that for each integral, the lower limit has to be smaller than the upper one. Threshold distributions that will be addressed in the next Section to all orders appear in the perturbative expansion of the partonic cross section $d\hat{\sigma}^{ab\to cd}$ as

$$\alpha_s^k \left(\frac{\ln^n(1-w)}{1-w}\right)_+\,, \qquad \text{with } n \le 2k-1\,, \tag{6.5}$$

where the partonic threshold is set for $w \to 1$.

6.2 Resummed Cross Section

Taking moments with Mellin variable N, the resummation of threshold logarithms may be achieved [7, 8, 84], see also Chapter 1 for further details. See [77, 111] for further details concerning resummation for a double differential cross section. In Mellin space, the threshold logarithms in Eq. (6.5) get transformed into $\alpha_s^k \ln^n \bar{N}$ with $n \leq 2k$. The resummed result for single-inclusive hadron production in Mellin space is given by [77–82, 84, 87]

$$\begin{aligned}\tilde{\Omega}^{\text{res}}_{abcd}\left(v, N, \alpha_s(\mu_R^2), \frac{\mu_R^2}{s}, \frac{\mu_F^2}{s}\right) &= \xi_R\left(\alpha_s(\mu_R^2), \frac{\mu_R^2}{s}\right) \xi_F^{abc}\left(\alpha_s(\mu_R^2), \frac{\mu_R^2}{s}, \frac{\mu_F^2}{s}\right) \\ &\times \Delta_a^{N_a}\left(\alpha_s(\mu_R^2), \frac{\mu_R^2}{s}, \frac{\mu_F^2}{s}\right) \Delta_b^{N_b}\left(\alpha_s(\mu_R^2), \frac{\mu_R^2}{s}, \frac{\mu_F^2}{s}\right) \Delta_c^{N}\left(\alpha_s(\mu_R^2), \frac{\mu_R^2}{s}, \frac{\mu_F^2}{s}\right) J_d^N\left(\alpha_s(\mu_R^2), \frac{\mu_R^2}{s}\right) \\ &\times \operatorname{Tr}\left\{H\left(v, \alpha_s(\mu_R^2)\right) \mathcal{S}_N^\dagger\left(v, \alpha_s(\mu_R^2), \frac{\mu_R^2}{s}\right) S\left(\alpha_s(s/\bar{N}^2), v\right) \mathcal{S}_N\left(v, \alpha_s(\mu_R^2), \frac{\mu_R^2}{s}\right)\right\}_{ab\to cd}\end{aligned} \tag{6.6}$$

with $N_a = vN$ and $N_b = (1-v)N$. The function $\mathcal{S}_N$ was defined in Chapter 1 and evaluated up to NNLL in the context of di-hadron production in Chapter 5. As can be seen this is very similar to single-inclusive jet production discussed in Chapter 7. The main difference is that, we would have to replace the radiative factor for the observed parton $\Delta_c^N \leftrightarrow J_c^{\text{jet}}$. In addition, even though they are closely related, one has to use different expressions for the hard-scattering matrices, the soft matrices and ξ_F and we need to include a non-global contribution in the case of jet production.

Jet functions

The radiative factors in the $\overline{\text{MS}}$ scheme are given by [7, 8, 58, 186]

$$\begin{aligned}\Delta_i^{N_a}\left(\alpha_s(\mu_R^2), \frac{\mu_R^2}{s}, \frac{\mu_F^2}{s}\right) &= R_i(\alpha_s(\mu_R^2)) \exp\left\{\int_0^1 dz \frac{z^{N_a-1}-1}{1-z}\right. \\ &\times \left.\left[\int_{\mu_F^2}^{(1-z)^2 s} \frac{d\mu^2}{\mu^2} A_i(\alpha_s(\mu^2)) + D_i(\alpha_s((1-z)^2 s))\right]\right\} \\ J_i^N\left(\alpha_s(\mu_R^2), \frac{\mu_R^2}{s}\right) &= P_i(\alpha_s(\mu_R^2)) \exp\left\{\int_0^1 dz \frac{z^{N-1}-1}{1-z}\right. \\ &\times \left.\left[\int_{(1-z)^2 s}^{(1-z)s} \frac{d\mu^2}{\mu^2} A_i(\alpha_s(\mu^2)) + \frac{1}{2} B_i(\alpha_s((1-z)s))\right]\right\}.\end{aligned} \tag{6.7}$$

The coefficients R_i and P_i [227] ensure that the soft function for this process is defined relative to that for the Drell-Yan process (initial state jet functions) and single-inclusive $e^+e^- \to hX$ (final state jet functions). Therefore, we only include a D_i term

$$D_i^{(2)} = C_i \left[C_A \left(-\frac{101}{27} + \frac{11}{3}\zeta(2) + \frac{7}{2}\zeta(3) \right) + N_f \left(\frac{14}{27} - \frac{2}{3}\zeta(2) \right) \right] \tag{6.8}$$

for two out of the three Δ^N in Eq. (6.6) [228].The correct normalization is obtained by using the coefficients

$$\begin{aligned} R_i(\alpha_s(\mu_R^2)) &= 1 - \frac{\alpha_s}{2\pi} A_i^{(1)} \frac{3}{2}\zeta(2) + \mathcal{O}(\alpha_s^2)\,, \\ P_q(\alpha_s(\mu_R^2)) &= 1 + \frac{\alpha_s}{2\pi} C_F \left(\frac{7}{2} - \frac{3}{2}\zeta(2) \right) + \mathcal{O}(\alpha_s^2)\,, \\ P_g(\alpha_s(\mu_R^2)) &= 1 + \frac{\alpha_s}{2\pi} \left(C_A \left(\frac{67}{18} - \frac{3}{2}\zeta(2) \right) - \frac{5}{9} N_f \right) + \mathcal{O}(\alpha_s^2)\,, \end{aligned} \tag{6.9}$$

see below in Section 6.3. We now present more details about how to calculate the radiative factors Δ^N and J^N up to NNLL. Firstly, we consider the function Δ^N. The D-term for Δ^N may be evaluated in a straightforward way. Focusing only on the A_i contribution, we obtain

$$\begin{aligned} &\int_0^1 dz \frac{z^{N-1} - 1}{1-z} \int_{\mu_F^2}^{(1-z)^2 s} \frac{d\mu^2}{\mu^2} A_i(\alpha_s(\mu^2)) \\ = &\; -\tilde{\Gamma}\left(1 - \frac{\partial}{\partial \ln \bar{N}} \right) \int_0^{1-1/\bar{N}} dz \frac{1}{1-z} \int_{\mu_F^2}^{(1-z)^2 s} \frac{d\mu^2}{\mu^2} A_i(\alpha_s(\mu^2))\,, \end{aligned} \tag{6.10}$$

where we made use of the relation [186]

$$z^{N-1} - 1 = -\tilde{\Gamma}\left(1 - \frac{\partial}{\partial \ln \bar{N}} \right) \Theta(1 - z - 1/\bar{N}) + \mathcal{O}(1/\bar{N})\,, \tag{6.11}$$

with

$$\begin{aligned} \tilde{\Gamma}\left(1 - \frac{\partial}{\partial \ln \bar{N}} \right) &= \exp\left\{ \sum_{n=2}^{\infty} (-)^n \frac{\zeta(n)}{n} \left(-\frac{\partial}{\partial \ln \bar{N}} \right)^n \right\} \\ &= 1 + \frac{\zeta(2)}{2} \left(\frac{\partial}{\partial \ln \bar{N}} \right)^2 + \ldots\,, \end{aligned} \tag{6.12}$$

where in the second line, we expanded the result up to NNLL accuracy. In a second step, we change the order of the dz and $d\mu^2$ integration in Eq. (6.10) and we directly perform the dz integration. We end up with

$$-\tilde{\Gamma}\left(1 - \frac{\partial}{\partial \ln \bar{N}} \right) \left[\frac{1}{2} \int_s^{s/\bar{N}^2} \frac{d\mu^2}{\mu^2} A_i(\alpha_s(\mu^2)) \ln\left(\frac{\bar{N}^2 \mu^2}{s} \right) + \int_{\mu_F^2}^{s} \frac{d\mu^2}{\mu^2} A_i(\alpha_s(\mu^2)) \ln \bar{N} \right]\,. \tag{6.13}$$

The remaining $d\mu^2$ integration over powers of the strong coupling constant may then be performed with MATHEMATICA for example. Note that the second term in Eq. (6.13) is constructed such that it vanishes when choosing $\mu_F^2 = s$. Finally, we note that the operator $\Gamma(1 - \partial/\partial \ln \bar{N})$ expanded up to NNLL in Eq. (6.12) yields an additional term proportional $\zeta(2)/(1-2\lambda)$ in the exponent which does not vanish for $\lambda \to 0$, where $\lambda = \alpha_s b_0 \ln \bar{N}$. Therefore, we rewrite it as

$$\frac{\zeta(2)}{1-2\lambda} = \zeta(2)\left(\frac{2\lambda}{1-2\lambda} + 1\right) . \tag{6.14}$$

The first term remains in the exponent, whereas the second term is will be part of the "C-coefficient" as it does not depend on $\ln \bar{N}$. Here it will be absorbed in the coefficient $R_i \to \tilde{R}_i$, see below.

The function J^N may be evaluated analogously. The B-term may be integrated directly and for the A-term, we proceed as follows. We split the $d\mu^2$ integration at s and we directly follow the same steps as described above for the two terms. We obtain the following result

$$\tilde{\Gamma}\left(1 - \frac{\partial}{\partial \ln \bar{N}}\right)\left[\frac{1}{2}\int_s^{s/\bar{N}^2} \frac{d\mu^2}{\mu^2} A_i(\alpha_s(\mu^2)) \ln\left(\frac{\bar{N}^2\mu^2}{s}\right) - \int_s^{s/\bar{N}} \frac{d\mu^2}{\mu^2} A_i(\alpha_s(\mu^2)) \ln\left(\frac{\bar{N}\mu^2}{s}\right)\right] . \tag{6.15}$$

In this case, we rewrite the $\zeta(2)$ term due to the operator $\Gamma(1 - \partial/\partial \ln \bar{N})$ as

$$-\frac{\zeta(2)}{2(1-\lambda)(1-2\lambda)} = -\frac{\zeta(2)}{2}\left(\frac{\lambda(3-2\lambda)}{(1-\lambda)(1-2\lambda)} + 1\right) \tag{6.16}$$

where again the first term remains in the exponent, whereas the second one will be absorbed in the following redefinition $P_i \to \tilde{P}_i$. Note the different overall sign in Eq. (6.16) in comparison to Eq. (6.14).

We now summarize the results for the functions Δ^{N_a} and J^N expanded up to NNLL accuracy. Firstly, for Δ^{N_a}, we obtain

$$\begin{aligned}\Delta_i^{N_a}\left(\alpha_s(\mu_R^2), \frac{\mu_R^2}{s}, \frac{\mu_F^2}{s}\right) &= \tilde{R}_i(\alpha_s(\mu_R^2)) \exp\Big\{h_i^{(1)}(\lambda_a) \ln \bar{N}_a \\ &\quad + h_i^{(2)}\left(\lambda_a, \frac{\mu_R^2}{s}, \frac{\mu_F^2}{s}\right) + \alpha_s(\mu_R^2)\, h_i^{(3)}\left(\lambda_a, \frac{\mu_R^2}{s}, \frac{\mu_F^2}{s}\right)\Big\} ,\end{aligned} \tag{6.17}$$

where the functions h_i can be found in Chapter 5 and everything is straightforwardly evaluated for $N \to N_a$ and $\lambda \to \lambda_a = \lambda + \alpha_s b_0 \ln v$. Note that this leads to the exponentiation of terms such as $\ln^2 v$ which have no dependence on $\ln \bar{N}$. However, this approach is very similar to terms with γ_E which are also naturally kept in the exponent. For the factor $\tilde{R}_i(\alpha_s(\mu_R^2))$, we obtain

$$\tilde{R}_i(\alpha_s(\mu_R^2)) = 1 + \frac{\alpha_s}{\pi} A_i^{(1)} \frac{\zeta(2)}{4} + \mathcal{O}(\alpha_s^2) . \tag{6.18}$$

Secondly, we expand J^N as

$$J_i^N\left(\alpha_s(\mu_R^2), \frac{\mu_R^2}{s}\right) = \tilde{P}_i(\alpha_s(\mu_R^2)) \exp\left\{f_i^{(1)}(\lambda) \ln \bar{N} + f_i^{(2)}\left(\lambda, \frac{\mu_R^2}{s}\right) + \alpha_s(\mu_R^2)\, f_i^{(3)}\left(\lambda, \frac{\mu_R^2}{s}\right)\right\} . \tag{6.19}$$

Written in terms of the results of [227] in Chapter 5, we obtain [228]

$$\begin{aligned}
f_i^{(1)}(\lambda) &= h_i^{(1)}\left(\frac{\lambda}{2}\right) - h_i^{(1)}(\lambda)\,,\\
f_i^{(2)}\left(\lambda,\frac{\mu_R^2}{s}\right) &= 2h_i^{(2)}\left(\frac{\lambda}{2},\frac{\mu_R^2}{s},1\right) - h_i^{(2)}\left(\lambda,\frac{\mu_R^2}{s},1\right) + \frac{B_i^{(1)}}{2\pi b_0}\ln(1-\lambda)\,,\\
f_i^{(3)}\left(\lambda,\frac{\mu_R^2}{s}\right) &= 2h_i^{(3)}\left(\frac{\lambda}{2},\frac{\mu_R^2}{s},1\right) - h_i^{(3)}\left(\lambda,\frac{\mu_R^2}{s},1\right) - \frac{3A_i^{(1)}}{2\pi}\zeta(2)\frac{\lambda}{1-\lambda} + \frac{B_i^{(1)}b_1}{2\pi b_0^2}\frac{\lambda+\ln(1-\lambda)}{1-\lambda}\\
&\quad -\frac{B_i^{(2)}}{2\pi^2 b_0}\frac{\lambda}{1-\lambda} - \frac{B_i^{(1)}}{2\pi}\frac{\lambda}{1-\lambda}\ln\left(\frac{\mu_R^2}{s}\right)\,. \qquad (6.20)
\end{aligned}$$

The factor $\tilde{P}_i(\alpha_s(\mu_R^2))$ in Eq. (6.19) is given by

$$\begin{aligned}
\tilde{P}_q(\alpha_s(\mu_R^2)) &= 1 + \frac{\alpha_s}{2\pi}C_F\left(\frac{7}{2} - \frac{5}{2}\zeta(2)\right) + \mathcal{O}(\alpha_s^2)\,,\\
\tilde{P}_g(\alpha_s(\mu_R^2)) &= 1 + \frac{\alpha_s}{2\pi}\left(C_A\left(\frac{67}{18} - \frac{5}{2}\zeta(2)\right) - \frac{5}{9}N_f\right) + \mathcal{O}(\alpha_s^2)\,, \qquad (6.21)
\end{aligned}$$

for the unobserved parton being a quark or gluon respectively, see the discussion below in Section 6.3. The coefficients B_i are given by

$$\begin{aligned}
B_q^{(1)} &= -\frac{3}{2}C_F\,, \quad B_g^{(1)} = -2b_0\pi\\
B_q^{(2)} &= C_F^2\left[-\frac{3}{16} + \frac{3}{2}\zeta(2) - 3\zeta(3)\right] + C_F C_A\left[-\frac{3155}{432} + \frac{11}{6}\zeta(2) + 5\zeta(3)\right]\\
&\quad + C_F N_f\left[\frac{247}{216} - \frac{1}{3}\zeta(2)\right]\,,\\
B_g^{(2)} &= C_A^2\left[-\frac{611}{72} + \frac{11}{3}\zeta(2) + 2\zeta(3)\right] + C_A N_f\left[\frac{107}{54} - \frac{2}{3}\zeta(2)\right] + \frac{1}{4}C_F N_f - \frac{5}{54}N_f^2\,. \qquad (6.22)
\end{aligned}$$

The Functions ξ_R and ξ_F

ξ_R is exactly the same as for di-hadron production in Chapter 5. However, ξ_F^{abc} is different in the sense that we do not have a contribution for the unobserved parton d. In addition, we expand the parton's anomalous dimension up to NLO

$$\gamma_i = \left(\frac{\alpha_s}{\pi}\right)\gamma_i^{(1)} + \left(\frac{\alpha_s}{\pi}\right)^2 + \gamma_i^{(2)} \qquad (6.23)$$

with [229]

$$\begin{aligned}
\gamma_q^{(1)} &= \frac{3}{4}C_F\,, \quad \gamma_g^{(1)} = b_0\pi \\
\gamma_q^{(2)} &= C_F^2\left(\frac{3}{32}-\frac{3}{4}\zeta(2)+\frac{3}{2}\zeta(3)\right)+C_AC_F\left(\frac{17}{96}+\frac{11}{12}\zeta(2)-\frac{3}{4}\zeta(3)\right)+C_FN_f\left(-\frac{1}{48}-\frac{1}{6}\zeta(2)\right) \\
\gamma_g^{(2)} &= C_A^2\left(\frac{2}{3}+\frac{3}{4}\zeta(3)\right)-N_f\left(\frac{C_F}{8}+\frac{C_A}{6}\right)\,. \qquad (6.24)
\end{aligned}$$

which also introduces an explicit dependence on the scale μ_R. We have [78, 80–82, 97]

$$\ln\xi_F^{abc}\left(\alpha_s(\mu_R^2),\frac{\mu_R^2}{s},\frac{\mu_F^2}{s}\right)=\sum_{i=a,b,c}\int_{\mu_F^2}^{\hat{m}^2}\frac{d\mu^2}{\mu^2}\frac{\alpha_s(\mu^2)}{\pi}\gamma_i(\alpha_s(\mu^2))\,, \qquad (6.25)$$

Note that at LO, we have $\gamma_i^{(1)}=-2B_i^{(1)}$. Performing the integration in Eq. (6.25), we obtain

$$\begin{aligned}
\ln\xi_F^{abc}\left(\alpha_s(\mu_R^2),\frac{\mu_R^2}{s},\frac{\mu_F^2}{s}\right) &= \sum_{i=a,b,c}\Bigg[-\frac{\alpha_s}{\pi}\gamma_i^{(1)}\ln\frac{\mu_F^2}{s} \\
&\quad+\left(\frac{\alpha_s}{\pi}\right)^2\left(-\gamma_i^{(2)}+\frac{b_0\pi}{2}\gamma_i^{(1)}\ln\frac{\mu_F^2}{s}-b_0\pi\gamma_i^{(1)}\ln\frac{\mu_R^2}{s}\right)\ln\frac{\mu_F^2}{s}\Bigg]\,. \qquad (6.26)
\end{aligned}$$

6.3 Soft Function

Throughout this Chapter, we work in the ’t Hooft-Veltman scheme (HV scheme) [230]. See [30, 200] for transition rules to the conventional dimensional regularization scheme (CDR scheme). Firstly, we consider to the two color singlet processes Drell-Yan and $e^+e^-\to hX$ which we use to normalize the soft function for single-inclusive hadron production. Secondly, we consider the $2\to 3$ processes $q(p_1)q'(p_2)\to q(p_3)q'(p_4)g(k)$ and $q(p_1)\bar{q}(p_2)\to g(p_3)g(p_4)g(k)$. We note that our labeling of the momenta for the three final state particles is consistent with Chapter 5 but differs from the standard notation used for single-inclusive kinematics, e.g. [231, 232], where $k_{1,2,3}$ is used instead. We note that the hard-scattering matrix $H^{(1)}$ is exactly the same as the one derived in Chapter 5.

6.3.1 Comparison to Drell-Yan and $e^+e^-\to hX$

In the di-hadron case our strategy was to fix the incoming jets by requiring them to reproduce (eikonal) Drell-Yan exactly, see Appendix D. This led to the resummed Δ_i^N in Eq. (6.7); see also Chapter 5. After expansion to NLO one has

$$\Delta_i^N = 1+\frac{\alpha_s}{2\pi}A_i^{(1)}\left[2\ln^2\bar{N}+\frac{1}{2}\zeta(2)\right]\,. \qquad (6.27)$$

The finite part of the first-order virtual correction for Drell-Yan is known to give rise to the hard factor [45]

$$H_{q\bar{q}} = 1+\frac{\alpha_s}{2\pi}C_F\left(-8+7\zeta(2)\right)\,, \qquad (6.28)$$

relative to Born. We have dropped any scale dependence. We then have

$$\Delta_q^N\,\Delta_{\bar q}^N\,H_{q\bar q}\;=\;1+\frac{\alpha_s}{2\pi}C_F\left(4\ln^2\bar N-8+\frac{4}{3}\pi^2\right)\,. \tag{6.29}$$

This is exactly the known [45] NLO correction factor near threshold. In other words, the choice (6.7) makes sure that our "Δ^N's", along with the hard part, reproduce Drell-Yan without need for any additional soft function.

We can now do a similar analysis for the process $e^+e^-\to qX$ in order to fix the final state jet functions for single-inclusive hadron production. For the observed quark and unobserved anti-quark, we use the functions Δ_q^N and $J_{\bar q}^N$ respectively as defined in Eq. (6.7). For consistency, we check that the prefactors R_q and P_q in (6.9) are chosen correctly such that we can directly reproduce the NLO result for $e^+e^-\to qX$ near threshold without any additional soft function. To check this, we have to first order

$$\begin{aligned}\Delta_q^N\;&=\;1+\frac{\alpha_s}{2\pi}C_F\left[2\ln^2\bar N+\frac{1}{2}\zeta(2)\right]\,,\\ J_{\bar q}^N\;&=\;1+\frac{\alpha_s}{2\pi}C_F\left[-\ln^2\bar N+\frac{3}{2}\ln\bar N+\frac{7}{2}-\frac{5\pi^2}{12}\right]\,.\end{aligned} \tag{6.30}$$

The hard virtual correction is identical to that for Drell-Yan. Combining all factors, we obtain

$$\Delta_q^N\,H_{q\bar q}\,J_{\bar q}^N\;=\;1+\frac{\alpha_s}{2\pi}C_F\left(\ln^2\bar N+\frac{3}{2}\ln\bar N-\frac{9}{2}+\frac{5}{6}\pi^2\right)\,, \tag{6.31}$$

which is in agreement with [99] for example; see also Chapters 2 and 4.

6.3.2 Eikonal Calculation for $qq'\to qq'$: Real Emission

Color Structure $\mathcal{R}_{ij}$

In order to compute $S^{(1)}$ for single-inclusive hadron production, we need to consider the diagrams shown in Fig. 5.2 in Chapter 5. The blue circle on either side of the cut denotes a Born hard part that can be either a color octet or singlet. Each of the diagrams in Fig. 5.2 has the structure

$$\sum_{IL} h_I^{(0)}h_L^{(0)*}\,(\mathcal{R}_{ij})_{LI}\,I_{ij}\,. \tag{6.32}$$

where ij labels the diagram. The I_{ij} are integrals over the eikonal factor corresponding to the diagram. $(\mathcal{R}_{ij})_{LI}$ is a matrix in color space with entries LI =octet-octet, singlet-octet, etc. Calculating the matrices $\mathcal{R}_{ij}$ we find the same matrices as in Chapter 5, see Eq. (5.83). Summing over all diagrams we thus find

$$\sum_{ij}\mathcal{R}_{ij}\,I_{ij}\;=\;\frac{C_F}{2}\begin{pmatrix}\frac{1}{2}(I_{13}+I_{24})-I_{12}-I_{34}-\frac{N_c^2-2}{2}(I_{14}+I_{23}) & N_c(I_{12}+I_{34}-I_{14}-I_{23})\\ N_c(I_{12}+I_{34}-I_{14}-I_{23}) & -2N_c^2(I_{13}+I_{24})\end{pmatrix}. \tag{6.33}$$

Here we included a minus sign whenever the eikonal factor is due to an interference between an initial- and final-state emission. This statement also holds true for the channels qq, qg and gg. Whenever anti-quarks are taking part in the scattering process, the extra minus signs needs to be adjusted differently, cf. [212] for example.

Integrals I_{ij}

Now we specify the integrals I_{ij} for single-inclusive hadron production. They are given by eikonal factors integrated over the gluon phase space. Starting with the the three-particle phase space for single-inclusive kinematics following [231, 232], we have

$$\Phi_3 = \frac{s}{(4\pi)^4\Gamma(1-2\varepsilon)}\left(\frac{4\pi}{s}\right)^{2\varepsilon}\int_0^1 dv\, v^{1-2\varepsilon}(1-v)^{-\varepsilon}\int_0^1 dw\,(w(1-w))^{-\varepsilon}\int d\Omega \tag{6.34}$$

where, using the standard notation for the Mandelstam variables [231, 232], we have

$$t_1 = (p_1-p_3)^2 = -s(1-v), \quad s_{23} = (p_4+k)^2 = sv(1-w) \tag{6.35}$$

and

$$\int d\Omega = \int_0^\pi d\theta_1 \int_0^\pi d\theta_2\, \sin^{1-2\varepsilon}\theta_1\, \sin^{-2\varepsilon}\theta_2\,. \tag{6.36}$$

The relevant angular integrals are given by [221]

$$\begin{aligned}&\int d\Omega\, \frac{1}{(1-\cos\theta_1)^j(1-\cos\theta_1\cos\chi-\sin\theta_1\cos\theta_2\sin\chi)^k}\\ =\;& 2\pi\frac{\Gamma(1-2\varepsilon)}{\Gamma(1-\varepsilon)^2}\,2^{-j-k}\,B(1-\varepsilon-j,1-\varepsilon-k)\,{}_2F_1\left(j,k,1-\varepsilon,\cos^2\frac{\chi}{2}\right)\,.\end{aligned} \tag{6.37}$$

In order to obtain the integrals I_{ij}, we need to factorize out the Born cross section. Therefore, we have to normalize to the leading-order phase space Φ_2 which is given by [45]

$$\Phi_2 = \frac{1}{8\pi\Gamma(1-\varepsilon)}\left(\frac{4\pi}{s}\right)^{\varepsilon}\int_0^1 dv\,(v(1-v))^{-\varepsilon}\int_0^1 dw\,\delta(1-w) \tag{6.38}$$

Summarizing everything, we end up with the definition of the terms I'_{ij}

$$I'_{ij} = -\frac{\alpha_s}{\pi}\frac{s}{4\pi}e^{\varepsilon\gamma_E}\frac{\Gamma(1-\varepsilon)}{\Gamma(1-2\varepsilon)}\int_0^1 dw\, v^{1-\varepsilon}w^{-\varepsilon}(1-w)^{-\varepsilon}\int d\Omega\,\frac{p_i\cdot p_j}{(p_i\cdot k)(p_j\cdot k)}\,. \tag{6.39}$$

We note that the minus sign is due to the eikonal factors that are being integrated. It turns out that the structure of the soft matrix will be more clear using the variables (v,z) instead of the standard ones (v,w). The variable z is defined as $z\equiv v(1-w)$ analogous to the variable used in Chapter 7. This choice turns out to be more convenient as z is invariant under the crossing $p_1 \leftrightarrow p_2$ or equivalently $v\to 1-vw$ and $w\to(1-v)/(1-vw)$. Instead of Eq. (6.39) we may directly write the integrals I'_{ij}

in terms of the variables (v,z) as

$$I_{ij}=-\frac{\alpha_s}{\pi}\frac{s}{4\pi}e^{\varepsilon\gamma_E}\frac{\Gamma(1-\varepsilon)}{\Gamma(1-2\varepsilon)}\int_0^1 dz\,(1-z/v)^{-\varepsilon}z^{-\varepsilon}\int d\Omega\,\frac{p_i\cdot p_j}{(p_i\cdot k)(p_j\cdot k)}\,. \tag{6.40}$$

Note, that we may also neglect the factors $w^{-\varepsilon}$ in Eq. (6.39) and $(1-z/v)^{-\varepsilon}$ in Eq. (6.40) as we are only interested in the singular distributions at threshold. In this case, the only dependence of I_{ij} on the variable v is introduced by the eikonal factors integrated over $d\Omega$.

Without carrying out the dz integration, we obtain the following results for the three integrals that do not involve the radiation of a gluon from the unobserved parton four

$$\begin{aligned}
\frac{dI_{12}}{dz} &= -\frac{\alpha_s}{\pi}\left[\left(\frac{1}{\varepsilon^2}-\frac{\zeta(2)}{2}+\frac{1}{\varepsilon}\log(v(1-v))+\frac{1}{2}\log^2(v(1-v))\right)\delta(z)\right.\\
&\qquad\left.+\left(-\frac{2}{\varepsilon}-2\log(v(1-v))\right)\left(\frac{1}{z}\right)_+ +4\left(\frac{\ln(z)}{z}\right)_+\right]\\
\frac{dI_{13}}{dz} &= -\frac{\alpha_s}{\pi}\left[\left(\frac{1}{\varepsilon^2}-\frac{\zeta(2)}{2}-\frac{1}{\varepsilon}\log\left(\frac{1-v}{v}\right)+\frac{1}{2}\log^2\left(\frac{1-v}{v}\right)\right)\delta(z)\right.\\
&\qquad\left.+\left(-\frac{2}{\varepsilon}+2\log\left(\frac{1-v}{v}\right)\right)\left(\frac{1}{z}\right)_+ +4\left(\frac{\ln(z)}{z}\right)_+\right]\\
\frac{dI_{23}}{dz} &= \left.\frac{dI_{13}}{dz}\right|_{v\leftrightarrow(1-v)}
\end{aligned} \tag{6.41}$$

Where the interchange $v\leftrightarrow(1-v)$ corresponds to a $t\leftrightarrow u$ crossing. Next, we consider the integrals I_{i4}, where $i=1,2,3$. Integrating the corresponding eikonal factors, we find that all three yield the same result

$$\frac{dI_{i4}}{dz}=-\frac{\alpha_s}{\pi}\left[\left(\frac{1}{\varepsilon^2}+\frac{1}{\varepsilon}+2-\frac{3}{2}\zeta(2)\right)\delta(z)-\left(\frac{1}{\varepsilon}+1\right)\left(\frac{1}{z}\right)_+ +\left(\frac{\ln(z)}{z}\right)_+\right]\,. \tag{6.42}$$

For all I_{ij} we have left the dz integral aside for now. The dz integration is trivial in the sense that all plus-distributions vanish. However, we still need to keep the full result in order to extract the soft matrix in Mellin moment space, as it is there, where threshold resummation is derived. In addition, it will turn out to be very useful to analyze the structure of the sum in Eq. (5.2) using the results for I_{ij} before the integration is performed.

Jet Functions and Extraction of $S^{(1)}$

According to the definition of the soft function, see Appendix D, we need to normalize by the four jet functions associated with the four partons taking part in the scattering at LO. We want our incoming jets to be defined as in Drell-Yan, except for the shifts $N\to N_a=Nv$ and $N\to N_b=N(1-v)$. From Drell-Yan (or from the di-hadron calculation in Chapter 5) we know that the real-emission part of the jet functions is given by

$$\tilde{\jmath}_{\rm in} \equiv 1+\frac{\alpha_s}{2\pi}C_F\left[\frac{1}{\varepsilon^2}+\frac{2}{\varepsilon}\ln\bar{N}+2\ln^2\bar{N}+\frac{1}{2}\zeta(2)\right]\,. \tag{6.43}$$

We therefore have the incoming jets as

$$\begin{aligned}\tilde{\jmath}_{{\rm in},a} &= 1+\frac{\alpha_s}{2\pi}C_F\left[\frac{1}{\varepsilon^2}+\frac{2}{\varepsilon}\ln\bar{N}_a+2\ln^2\bar{N}_a+\frac{1}{2}\zeta(2)\right]\,,\\ \tilde{\jmath}_{{\rm in},b} &= 1+\frac{\alpha_s}{2\pi}C_F\left[\frac{1}{\varepsilon^2}+\frac{2}{\varepsilon}\ln\bar{N}_b+2\ln^2\bar{N}_b+\frac{1}{2}\zeta(2)\right]\,.\end{aligned} \tag{6.44}$$

Note that this is consistent with the integral I_{12} for which we had

$$\int_0^1 dz\, z^{N-1}\frac{dI_{12}}{dz} = -\frac{\alpha_s}{\pi}\left[\frac{1}{\varepsilon^2}+\frac{1}{\varepsilon}(\ln\bar{N}_a+\ln\bar{N}_b)+\ln^2\bar{N}_a+\ln^2\bar{N}_b+\frac{3}{2}\zeta(2)-\frac{1}{2}\ln^2\left(\frac{1-v}{v}\right)\right]\,, \tag{6.45}$$

the difference only residing in the N-independent pieces. (One needs a factor $(-C_F)$ to get the right normalization). Now we need to consider the final-state jets. Again, following the di-hadrons, we want the "observed" (fragmenting) one to be defined as that for an incoming parton. We therefore have for its real-emission contribution

$$\tilde{\jmath}_{{\rm out},c} = 1+\frac{\alpha_s}{2\pi}C_F\left[\frac{1}{\varepsilon^2}+\frac{2}{\varepsilon}\ln\bar{N}+2\ln^2\bar{N}+\frac{1}{2}\zeta(2)\right]\,. \tag{6.46}$$

The only remaining issue is to find the jet function $\tilde{\jmath}_{{\rm out},d}$ for the recoil parton. We may construct it by demanding that the product $\tilde{\jmath}_{{\rm out},c}\tilde{\jmath}_{{\rm out},d}$ has to reproduce the integral I_{34}. The latter is given by

$$\int_0^1 dz\, z^{N-1}\frac{dI_{34}}{dz} = -\frac{\alpha_s}{\pi}\left[\frac{1}{\varepsilon^2}+\frac{1}{\varepsilon}+\left(\frac{1}{\varepsilon}+1\right)\ln\bar{N}+\frac{1}{2}\ln^2\bar{N}+2-\zeta(2)\right]\,, \tag{6.47}$$

(again we need $(-C_F)$ for normalization). From this, and using $\tilde{\jmath}_{{\rm out},c}$ above, we conclude that

$$\tilde{\jmath}_{{\rm out},d} = 1+\frac{\alpha_s}{2\pi}C_F\left[\frac{1}{\varepsilon^2}+\frac{2}{\varepsilon}-\ln^2\bar{N}+2\ln\bar{N}+4-\frac{5}{2}\zeta(2)\right]\,. \tag{6.48}$$

To summarize, we have for the real-emission parts of the jet functions

$$\begin{aligned}
\tilde{j}_{\text{in},a} &= 1+\frac{\alpha_s}{2\pi}C_F\left[\frac{1}{\varepsilon^2}+\frac{2}{\varepsilon}\ln\bar{N}_a+2\ln^2\bar{N}_a+\frac{1}{2}\zeta(2)\right]\,,\\
\tilde{j}_{\text{in},b} &= 1+\frac{\alpha_s}{2\pi}C_F\left[\frac{1}{\varepsilon^2}+\frac{2}{\varepsilon}\ln\bar{N}_b+2\ln^2\bar{N}_b+\frac{1}{2}\zeta(2)\right]\,,\\
\tilde{j}_{\text{out},c} &= 1+\frac{\alpha_s}{2\pi}C_F\left[\frac{1}{\varepsilon^2}+\frac{2}{\varepsilon}\ln\bar{N}+2\ln^2\bar{N}+\frac{1}{2}\zeta(2)\right]\,,\\
\tilde{j}_{\text{out},d} &= 1+\frac{\alpha_s}{2\pi}C_F\left[\frac{1}{\varepsilon^2}+\frac{2}{\varepsilon}-\ln^2\bar{N}+2\ln\bar{N}+4-\frac{5}{2}\zeta(2)\right]\,.
\end{aligned}\tag{6.49}$$

Equipped with these, we now go back to the color-decomposed calculation for the real-emission diagrams near threshold:

$$\begin{aligned}
\int_0^1 dz\, z^{N-1}\sum_{ij}\mathcal{R}_{ij}\,I_{ij} \;=\; &\frac{\alpha_s}{\pi}\left[\frac{2C_F}{\varepsilon^2}S^{(0)}-\frac{1}{2\varepsilon}[(\Gamma^{(1)})^\dagger S^{(0)}+S^{(0)}\Gamma^{(1)}]+\frac{C_F}{\varepsilon}\left(\ln\bar{N}_a+\ln\bar{N}_b+\ln\bar{N}\right)S^{(0)}\right.\\
&+C_F\left[\ln^2\bar{N}_a+\ln^2\bar{N}_b+\ln^2\bar{N}-\frac{1}{2}\ln^2\bar{N}\right]S^{(0)}-\ln\bar{N}\left((\Gamma^{(1)})^\dagger S^{(0)}+S^{(0)}\Gamma^{(1)}\right)\\
&+\left\{\ln\bar{N}+\left(\frac{1}{\varepsilon}+2\right)\right\}C_F\,S^{(0)}\\
&\left.+\frac{C_F}{2}\left\{\begin{pmatrix}-\frac{N_c^2-1}{4}\log^2\left(v(1-v)\right)+2\log(1-v)\log(v) & -2N_c\log(1-v)\log(v)\\ -2N_c\log(1-v)\log(v) & -N_c^2\log^2\left(v(1-v)\right)\end{pmatrix}+\zeta(2)S^{(0)}\right\}\right]\,.
\end{aligned}\tag{6.50}$$

Now we divide by the product of the jet functions in (6.49) (There is a LO term $S^{(0)}$ to do this, see Appendix D). Many terms cancel; the ones that remain are

$$\begin{aligned}
&\frac{\alpha_s}{\pi}\left[-\left(\frac{1}{2\varepsilon}+\ln\bar{N}\right)[(\Gamma^{(1)})^\dagger S^{(0)}+S^{(0)}\Gamma^{(1)}]\right.\\
&\left.+\frac{C_F}{2}\left\{\begin{pmatrix}-\frac{N_c^2-1}{4}\log^2\left(v(1-v)\right)+2\log(1-v)\log(v) & -2N_c\log(1-v)\log(v)\\ -2N_c\log(1-v)\log(v) & -N_c^2\log^2\left(v(1-v)\right)\end{pmatrix}+2\,\zeta(2)S^{(0)}\right\}\right]\,.
\end{aligned}\tag{6.51}$$

The term in the second line directly gives $S^{(1)}$.

Comparison to NLO

With the matrix $S^{(1)}$ at hand from (6.51), along with $H^{(1)}$ from Chapter 5, we are now able to reproduce NLO including all constant terms. The analytic NLO expressions are available from [42, 233]. We start from the resummation formula and expand everything to first order. (All formulas below make use of the choice $\log(2\nu) = 1$ for the gauge parameters.) First we need the Δ^N and J^N cf. Section 6.2 above:

$$\begin{aligned}
\Delta_a^N &= 1 + \frac{\alpha_s}{2\pi} C_F \left[2\ln^2 \bar{N}_a + \frac{1}{2}\zeta(2) \right] , \\
\Delta_b^N &= 1 + \frac{\alpha_s}{2\pi} C_F \left[2\ln^2 \bar{N}_b + \frac{1}{2}\zeta(2) \right] , \\
\Delta_c^N &= 1 + \frac{\alpha_s}{2\pi} C_F \left[2\ln^2 \bar{N} + \frac{1}{2}\zeta(2) \right] , \\
J_d^N &= 1 + \frac{\alpha_s}{2\pi} C_F \left[-\ln^2 \bar{N} + \frac{3}{2}\ln \bar{N} + \frac{7}{2} - \frac{5}{2}\zeta(2) \right] , \qquad (6.52)
\end{aligned}$$

where we have omitted any scale logarithms for now. Furthermore, for the color trace part in the resummation formula, we have

$$\begin{aligned}
\mathrm{Tr}[H\mathcal{S}^\dagger S\mathcal{S}] &= \mathrm{Tr}[H^{(0)}S^{(0)}] \left\{ 1 + \frac{\alpha_s}{\pi} \ln \bar{N} \left(-4C_F \ln v + \frac{2}{C_A}(\ln v + \ln(1-v)) \right) \right\} \\
&+ \frac{\alpha_s}{\pi} \mathrm{Tr}[H^{(1)}S^{(0)} + H^{(0)}S^{(1)}] . \qquad (6.53)
\end{aligned}$$

Combining (6.52) and (6.53) and comparing to NLO, we find full agreement.

6.3.3 Eikonal Calculation for $q\bar{q} \to gg$: Real Emission

Instead of (6.50) we have here

$$\begin{aligned}
\int_0^1 dz\, z^{N-1} \sum_{ij} \mathcal{R}_{ij}\, I_{ij} &= \frac{\alpha_s}{\pi} \left[\frac{(C_F + C_A)}{\varepsilon^2} S^{(0)} - \frac{1}{2\varepsilon} [(\Gamma^{(1)})^\dagger S^{(0)} + S^{(0)}\Gamma^{(1)}] \right. \\
&+ \frac{1}{\varepsilon} (C_F \ln \bar{N}_a + C_F \ln \bar{N}_b + C_A \ln \bar{N}) S^{(0)} \\
&+ \left[C_F \ln^2 \bar{N}_a + C_F \ln^2 \bar{N}_b + C_A \ln^2 \bar{N} - \frac{1}{2} C_A \ln^2 \bar{N} \right] S^{(0)} - \ln \bar{N} \left((\Gamma^{(1)})^\dagger S^{(0)} + S^{(0)}\Gamma^{(1)} \right)
\end{aligned}$$

$$+\left\{\ln\bar{N}+\left(\frac{1}{\varepsilon}+2\right)\right\}C_A\,S^{(0)}$$
$$+\left[-\frac{C_F}{2}\log^2\left(v(1-v)\right)+(2C_F-C_A)\log(1-v)\log(v)+\left(\frac{3}{2}C_F-C_A\right)\zeta(2)\right]S^{(0)}$$
$$+2C_FC_A^3\log(1-v)\log(v)\mathcal{M}\,, \tag{6.54}$$

where $\Gamma^{(1)}$ and $S^{(0)}$ are the known matrices for this process (they are 3 × 3), see [82] for example, and

$$\mathcal{M}=\begin{pmatrix}1&0&0\\0&0&0\\0&0&0\end{pmatrix}. \tag{6.55}$$

As before, we now use the jet functions of Eq. (6.49), but with $C_F \to C_A$ for the final state. Dividing (6.54) by the four jet functions, we obtain

$$\frac{\alpha_s}{\pi}\left[-\left(\frac{1}{2\varepsilon}+\ln\bar{N}\right)[(\Gamma^{(1)})^\dagger S^{(0)}+S^{(0)}\Gamma^{(1)}]\right.$$
$$+\left\{-\frac{C_F}{2}\log^2\left(v(1-v)\right)+(2C_F-C_A)\log(1-v)\log(v)+C_F\zeta(2)\right\}S^{(0)}$$
$$\left.+2C_FC_A^3\log(1-v)\log(v)\mathcal{M}\right], \tag{6.56}$$

which is to be compared with (6.51). As before, the terms in the last two lines directly give $S^{(1)}$.

To do the comparison with NLO, we use

$$\begin{aligned}
\Delta_a^N &= 1+\frac{\alpha_s}{2\pi}C_F\left[2\ln^2\bar{N}_a+\frac{1}{2}\zeta(2)\right],\\
\Delta_b^N &= 1+\frac{\alpha_s}{2\pi}C_F\left[2\ln^2\bar{N}_b+\frac{1}{2}\zeta(2)\right],\\
\Delta_c^N &= 1+\frac{\alpha_s}{2\pi}C_A\left[2\ln^2\bar{N}+\frac{1}{2}\zeta(2)\right],\\
J_d^N &= 1+\frac{\alpha_s}{2\pi}\left[-C_A\ln^2\bar{N}+\frac{\beta_0}{2}\ln\bar{N}+C_A\left(\frac{67}{18}-\frac{5}{2}\zeta(2)\right)-\frac{5}{9}N_f\right],
\end{aligned} \tag{6.57}$$

where

$$\beta_0=\frac{11}{3}C_A-\frac{2}{3}N_f\,. \tag{6.58}$$

In addition, we obtain from the color trace part

$$\begin{aligned}
\mathrm{Tr}[H\mathcal{S}^\dagger S\mathcal{S}] &= \mathrm{Tr}[H^{(0)}S^{(0)}] \\
&+ \frac{\alpha_s}{\pi}\ln\bar{N}\,\frac{2C_F}{C_A}\left(\frac{1-v}{v}+\frac{v}{1-v}\right)\left[\log(v(1-v))(1-v^2C_A^2)-C_A^2\log(v)(1-2v)\right] \\
&+ \frac{\alpha_s}{\pi}\,\mathrm{Tr}[H^{(1)}S^{(0)}+H^{(0)}S^{(1)}]\,. \qquad (6.59)
\end{aligned}$$

Putting everything together and comparing to NLO, we find full agreement. In the Appendix E, we present the explicit results for the NLO soft matrix for all channels.

6.4 Conclusions

We derived all ingredients for the extension of threshold resummation toward NNLL for single-inclusive hadron production in hadronic collisions. In comparison to hadron pair production in Chapter 5, we found several new features. With the help of the methods developed in [77], phenomenological results will become available in the future for cross sections differential in both transverse momentum and rapidity of the observed hadron. Given the availability of various data sets, this will be very interesting for QCD precision phenomenology and for the extraction of fragmentation functions in a global analysis.

CHAPTER 7

APPROXIMATE NNLO AND N^{3}LO CORRECTIONS TO HADRONIC JET PRODUCTION

We determine dominant next-to-next-to-(-next-to)-leading order QCD corrections to single-inclusive jet production at the LHC and Tevatron, using the established threshold resummation framework. In contrast to previous literature on this topic, our study incorporates all of the following features: (1) It properly accounts for the way a jet is defined in experiment and treated in available full next-to-leading order calculations, (2) It includes the three (four) leading classes of logarithmic terms in the perturbative expansion, and (3) It is adapted to the full kinematics in jet transverse momentum and rapidity relevant for experiments. A recent full next-to-next-to-leading order calculation in the purely gluonic channel allows us to assess the region where our approximate corrections provide an accurate description. We expect our results to be important on the way to precision jet phenomenology at the LHC and as benchmark for further full next-to-next-to-leading order calculations. In addition, we extend our results toward next-to-next-to-leading logarithmic accuracy and we directly perform the inversion from Mellin transform space. This Chapter is based on publications [vi] and [vii].

7.1 Introduction

The production of high-transverse-momentum hadron jets plays a fundamental role at the LHC [234] and at Tevatron [235]. Jets are produced very copiously, making them precision probes of the physics of the Standard Model and beyond. Theoretical calculations whose precision matches that achievable in experiment are of critical importance. The efforts made in this context have spanned more than three decades now, culminating so far with the recent calculation of the next-to-next-to-leading order (NNLO) perturbative corrections to jet production in the "gluon-only" channel [236, 237].

As complete NNLO calculations of jet production are probably still a few years away, it is useful to determine approximate NNLO results, at least in certain kinematical regimes. This is possible thanks to the fact that the perturbative series for the partonic cross sections contains classes of logarithmic terms that often dominate. Resummation techniques in QCD [80] allow to determine the all-order structure of these logarithmic terms, and one therefore also obtains the logarithms present at NNLO. Knowledge of approximate NNLO expressions is very useful, since it potentially offers an avenue toward more precise phenomenology than available on the basis of the presently known full next-to-leading order (NLO) corrections. It also serves as benchmark for future full NNLO calculations.

The logarithms just mentioned arise near a threshold from which the production of a jet becomes possible in a partonic collision. They are hence known as "threshold logarithms". The threshold is set by a vanishing invariant mass $\sqrt{s_4}$ of the partonic system that recoils against the observed jet. At the kth order of perturbation theory, one finds threshold corrections to the Born cross section of the form $\alpha_s^k[\log^m(z)/z]_+$, with $0 \leq m \leq 2k-1$, where $z = s_4/s$ with $\sqrt{s}$ the center-of-mass energy of the incoming partons. The systematic resummation of these logarithms to all orders in the strong coupling α_s was derived for the case of jet production in [80], where explicit next-to-leading logarithmic (NLL) results were given that in principle allow to resum the three "towers" of logarithms with $m = 2k-1, 2k-2, 2k-3$.

An important "subtlety" was pointed out in [80] concerning the threshold logarithms in jet production: the structure of the logarithmic corrections depends on whether or not the jet is assumed to be massless at partonic threshold, even at the leading-logarithmic (LL) level. If the jet is taken to be massless at threshold, an approach for which we will use the term "scheme (1)" in the following, leading-logarithmic corrections arise in the resummed perturbative function describing the jet. If, on the other hand, the jet is permitted to have a non-vanishing invariant mass at threshold ("scheme (2)"), the leading logarithms cancel, leaving behind a non-leading logarithm whose coefficient depends on jet "size" parameter R introduced by the jet algorithm. The difference between the two schemes may be understood from the fact that fewer final states contribute in scheme (1) than in scheme (2) [80].

Approximate NNLO corrections for jet production have been derived in [82, 238, 239], adopting scheme (1). As one can see in the very recent study [238], the NLO terms predicted for scheme (1) fail to match a full NLO calculation [240] even in a regime where threshold logs are known to dominate. This becomes particularly evident from the fact that the threshold terms for scheme (1) do not carry any dependence on the jet parameter R, whereas the full NLO results do. These features observed in [238] are in fact not surprising: explicit analytical NLO calculations [40, 43] have shown that jets produced close to partonic threshold do span a range of jet masses. Indeed, for any jet algorithm the jet produced in the perturbative calculation can evidently contain two or more partons and hence have a non-vanishing invariant mass. This is even the case at exact threshold $z = 0$, when for example only a single parton recoils against the entire jet. The maximally allowed jet mass at threshold will depend on the parameter R used in the jet algorithm.

Thus, the assumption of massless jets at threshold that was made in previous studies [82, 238, 239] does not appear to be appropriate. Instead, the resummation ought to be carried out within scheme (2). A resummed study in this scheme was in fact performed in [216], where however only the rapidity-integrated cross section was considered, for which the resummation simplifies considerably. Integration over all rapidity is not quite adequate for comparisons with experimental data. In the present paper we present new predictions for the NNLO threshold terms, using scheme (2) and keeping full dependence on rapidity in the calculation. We will also go beyond the previous studies [82, 238] by determining all three most leading logarithmic contributions $\propto (\log^3(z)/z)_+, (\log^2(z)/z)_+, (\log(z)/z)_+$ at NNLO. The last of these is new; it may be obtained by matching the resummation framework to a full NLO calculation. For the latter we choose that of [40, 43], which provides analytical results for the partonic cross sections. The calculation was performed assuming that the produced jet is rather narrow ("narrow-jet approximation" (NJA)). It has been shown that this approximation is extremely accurate even at relatively large jet sizes of $R \gtrsim 0.7$.

7.2 Theoretical Framework

The factorized cross section for the single-inclusive production of a jet with transverse momentum p_T and pseudorapidity η may be written as

$$\frac{p_T^2 d^2\sigma}{dp_T^2 d\eta} = \sum_{ab} \int_0^{V(1-W)} dz \int_{\frac{VW}{1-z}}^{1-\frac{1-V}{1-z}} dv \, x_a f_a(x_a, \mu_F^2) \, x_b f_b(x_b, \mu_F^2) \frac{d\hat{\sigma}_{ab}}{dvdz}(v, z, p_T, \mu_R^2, \mu_F^2, R), \tag{7.1}$$

where $V = 1 - x_T \mathrm{e}^{-\eta}/2$, $VW = x_T \mathrm{e}^{\eta}/2$, with $x_T = 2p_T/\sqrt{S}$ and the hadronic center-of-mass energy $\sqrt{S}$. The sum runs over all partonic collisions producing the jet; $d\hat{\sigma}_{ab}$ denote the corresponding partonic hard-scattering cross sections and f_a, f_b the parton distribution functions at momentum fractions $x_a = VW/v(1-z)$, $x_b = (1-V)/(1-v)(1-z)$. The partonic cross sections are computed in QCD perturbation theory. As indicated, besides depending on p_T and the usual renormalization and factorization scales μ_R, μ_F, they are functions of the partonic kinematic variables, which we have chosen as

$$v = \frac{u}{t+u}, \qquad z = \frac{s_4}{s}, \tag{7.2}$$

where $s = x_a x_b S$ is the partonic center-of-mass energy squared, $t = (p_a - p_J)^2$, $u = (p_b - p_J)^2$ (with $p_{a,b}$ and p_J the four-momenta of the initial partons and the jet, respectively), and s_4 is the invariant mass squared of the "unobserved" partonic system recoiling against the jet. We stress that the $d\hat{\sigma}_{ab}$ also depend on the algorithm adopted to define the jet, as indicated by the generic jet parameter R in Eq. (7.1). We always assume the jet to be defined by the anti-k_t algorithm [38].

The perturbative series for each of the partonic scattering cross sections may be cast into the form

$$\frac{sd\hat{\sigma}_{ab}}{dvdz} = \left(\frac{\alpha_s}{\pi}\right)^2 \left[\omega_{ab}^{(0)} + \frac{\alpha_s}{\pi}\omega_{ab}^{(1)} + \left(\frac{\alpha_s}{\pi}\right)^2 \omega_{ab}^{(2)} + \mathcal{O}(\alpha_s^3)\right], \tag{7.3}$$

where $\alpha_s \equiv \alpha_s(\mu_R^2)$ is the strong coupling constant, and where each of the $\omega_{ab}^{(k)}$ is a function of v, z and, for $k > 0$, of R and p_T/μ (we choose from now on $\mu_R = \mu_F \equiv \mu$). At lowest order we have

$$\omega_{ab}^{(0)}(v, z) \equiv \tilde{\omega}_{ab}^{(0)}(v)\delta(z), \tag{7.4}$$

since the recoiling system is a single massless parton. Hence $z = 0$ sets a threshold for the process to take place, since the transverse momentum of the observed jet always needs to be balanced. At higher orders in perturbation theory, the hard scattering functions contain logarithmic distributions in z, with increasing powers of logarithms as the perturbative order increases. More precisely, one has near the threshold at $z = 0$:

$$\alpha_s^k \omega_{ab}^{(k)} \sim \alpha_s^k \left(\frac{\log^m(z)}{z} \right)_+ , \quad \text{with } 0 \le m \le 2k-1. \tag{7.5}$$

Here $\int_0^1 dz g(z)[f(z)]_+ \equiv \int_0^1 dz (g(z) - g(0)) f(z)$. As one can see, two additional powers of the logarithm arise for every order of perturbation theory. Due to the integration against the parton distribution functions, which are steeply falling functions of momentum fraction, the threshold region $z \to 0$ typically makes significant contributions to the hadronic cross section. This is particularly the case when the kinematic boundary of the hadronic reaction is approached, that is, when $x_T \cosh \eta \to 1$.

As is well known, the large logarithmic corrections arising in the threshold region are associated with the emission of soft or collinear gluons. It is therefore possible to systematically determine the structure of the corrections to all orders and to resum the "towers" of logarithms with $m = 2k-1, 2k-2, \ldots$. This may be used to derive approximate beyond-NLO corrections for hadronic jet production, by expanding the resummed result appropriately to the desired order [82, 216, 238]. To achieve the all-order resummation, one considers Mellin moments in $(1-z)$ of the partonic cross section:

$$\Omega_{ab}(v, N) \equiv \int_0^1 dz (1-z)^{N-1} \frac{s d\hat{\sigma}_{ab}}{dv dz}. \tag{7.6}$$

In moment space, the resummed hard-scattering function Ω_{ab}^{res} can at large N be written as [80, 87]

$$\begin{aligned} \Omega_{ab}^{\text{res}}(v, N) &= \sum_{c,d} \Delta_a(N_a)\, \Delta_b(N_b)\, J_c^{(\text{jet})}(N, R)\, J_d^{(\text{recoil})}(N) \\ &\times \Delta_{ab \to cd}^{(\text{int})}(N, v)\, \Delta_c^{(\text{ng})}(N), \end{aligned} \tag{7.7}$$

where $N_a = vN$, $N_b = (1-v)N$ and the sum runs over the two final-state partons c, d in an underlying $ab \to cd$ subprocess. Here it is assumed that parton c produces the jet (in a way that we shall clarify below), while the recoiling parton d remains unobserved. Each of the terms is also a function of $\alpha_s(\mu^2)$ and $\log(\mu^2/s)$, which we have not written explicitly. Each of the functions $\Delta_a, \Delta_b, J_c^{(\text{jet})}, J_d^{(\text{recoil})}$ is an exponential. Δ_a, Δ_b resum threshold logarithms arising from soft/collinear radiation off the incoming hard partons. Their expressions are very well known and may be found in the form we need them in, for example, [87]. Likewise, also the expression for gluon radiation off the "unobserved" recoiling parton d is standard and may be found there. Δ_a, Δ_b and $J_d^{(\text{recoil})}$ contain all the leading logarithmic pieces $\propto (\log^3(z)/z)_+, (\log^2(z)/z)_+$ in $\omega_{ab}^{(2)}$.

A crucial point of our study concerns the function $J_c^{(\text{jet})}$ used for the actual jet. As was shown in [80], this function takes different forms depending on whether one assumes the jet to become itself massless at threshold or not. These two forms differ even at *leading* logarithmic level. For scheme (2) introduced earlier, we have to next-to-leading logarithmic accuracy [80]:

$$\log J_c^{(\mathrm{jet})} = \int_s^{s/\bar{N}^2} \frac{dq^2}{q^2}\, \alpha_s\left(q^2\right) \left(-\frac{C_c}{2\pi} \log\left(\frac{p_T^2 R^2}{s}\right)\right), \tag{7.8}$$

where $\bar{N} \equiv N\mathrm{e}^{\gamma_E}$ with the Euler constant γ_E, and where C_c denotes the color charge of parton c, $C_q = C_F$ for a quark and $C_g = C_A$ for a gluon. As expected, $J_c^{(\mathrm{jet})}$ is a function of R in this scheme.

The function $\Delta^{(\mathrm{int})}_{ab\to cd}(N, v)$ is obtained as a trace in color space over hard, soft, and anomalous dimension matrices [80]. All details have been given in [82] and need not be repeated here. The function contributes at NLL level and is the only function in the resummed expression that carries explicit dependence on v.

Finally, $\Delta_c^{(\mathrm{ng})}(N)$ in (7.7) contains the contributions from non-global logarithms. These were shown [241, 242] to arise when an observable is sensitive to radiation in only a part of phase space, as is the case for a jet defined by some jet "size" parameter R. Their resummation is highly non-trivial. Non-global logarithms for jet production first enter as a term $\propto [\log(z)/z]_+$ in $\omega_{ab}^{(2)}$. As discussed in [243], the non-global terms arise independently from the boundary of each individual (narrow) "observed" jet, when jets are assumed to be narrow and well separated. The appropriate second-order coefficient for our case of a single-inclusive jet cross section may therefore be directly obtained from [241–243], adjusting the argument of the logarithm properly. We note that these considerations– and in fact the general structure of our resummed cross section– apply to the anti-k_t algorithm [243] consistent with our choice throughout this paper. We finally also mention that the non-global component makes a rather small contribution (a few per cent) to our numerical NNLO results presented below. All in all, after performing the Mellin-inverse to z-space, the two-loop expansion of the product $\Delta^{(\mathrm{int})}_{ab\to cd}(N, v)\, \Delta_c^{(\mathrm{ng})}(N)$ in Eq. (7.7) takes the form

$$\left(\frac{\alpha_s}{\pi}\right)^2 \left[\tilde{\omega}_{ab}^{(0)}(v) \left(\delta(z) + \frac{1}{2}\left(\frac{\alpha_s}{\pi}\right)^2 \mathcal{C}_c^{(\mathrm{ng})} \left(\frac{\log(z)}{z}\right)_+\right) + \frac{\alpha_s}{\pi}\left(\mathcal{T}_{ab\to cd}(v)\delta(z) + \mathcal{G}^{(1)}_{ab\to cd}(v)\left(\frac{1}{z}\right)_+\right)\right.$$
$$\left. + \left(\frac{\alpha_s}{\pi}\right)^2 \mathcal{G}^{(2)}_{ab\to cd}(v) \left(\frac{\log(z)}{z}\right)_+\right], \tag{7.9}$$

with $\mathcal{C}_c^{(\mathrm{ng})} = -C_A C_c \pi^2/3$ for the coefficient of the non-global term. The coefficients $\mathcal{G}^{(1)}_{ab\to cd}(v)$ are predicted by the resummation formalism. The coefficients $\mathcal{T}_{ab\to cd}(v)$ may be derived by comparison to the explicit NLO results of [43] in the narrow-jet approximation. Along with the known resummation coefficients, knowledge of the $\mathcal{T}_{ab\to cd}(v)$ is sufficient for determining $\mathcal{G}^{(2)}_{ab\to cd}(v)$ [83, 244]. In this way, combining with the contributions from $\Delta_a, \Delta_b, J_c^{(\mathrm{jet})}, J_d^{(\mathrm{recoil})}$, we obtain full control over the terms $\propto (\log^3(z)/z)_+, (\log^2(z)/z)_+, (\log(z)/z)_+$ in $\omega_{ab}^{(2)}$.

7.3 Phenomenological Results - 1

Figure 7.1 shows results for the differential single-inclusive jet cross section at the LHC, at lowest order as well as for the NLO and NNLO threshold terms. Here we use the CTEQ6.6 [245] parton distribution

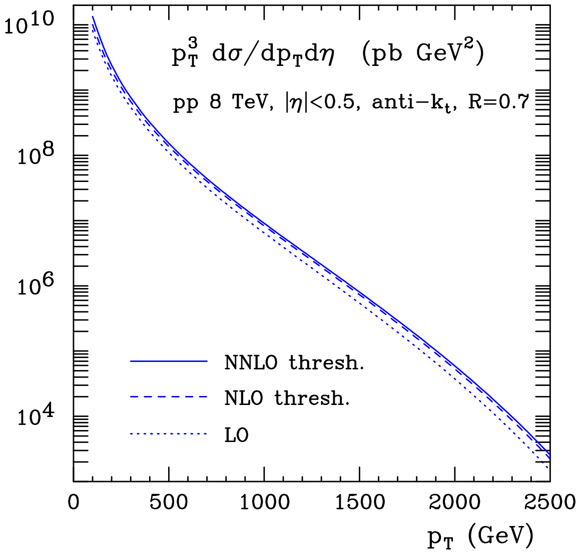

Figure 7.1: Differential cross section for jet production in pp-collisions at the LHC at $\sqrt{S} = 8$ TeV, using the anti-k_t algorithm with $R = 0.7$.

functions and scale $\mu = p_T$. The left part of Figure 7.2 displays the corresponding "K-factors", defined as ratios of higher-order cross sections over the leading-order one, while the right part of the figure is for $p\bar{p}$ collisions at Tevatron at $\sqrt{S} = 1.96$ TeV. Results are presented for various jet parameters R. The dotted lines show the NLO results of [43] which were obtained in the NJA for the anti-k_t algorithm. We note that these agree with the NLO ones by the "FastJet" code [240] (as shown in [238]) to better than 3%, even at $R = 0.7$. The dashed lines present the results for the NLO expansion of the threshold terms. It is evident that the latter provide a very faithful description of the full NLO results for much of the p_T ranges relevant at LHC and Tevatron. This holds true for each value of R, thanks to the fact that the threshold logarithms carry R-dependence in our approach, in contrast to that in [82, 238]. Finally, the solid lines display the approximate NNLO results. These show a striking further increase of the jet cross sections as compared to NLO, particularly so at high p_T where the threshold terms are expected to dominate. There also is an increase toward lower p_T; here, however, the result shows sensitivity to terms non-leading at threshold.

Given the large size of the NNLO corrections observed in Fig. 7.2, it is of course crucial to verify that the predicted enhancements are realistic. Fortunately, as mentioned in the Introduction, recently a full NNLO calculation for jet production in the "gluon-only" channel was presented [236, 237], corresponding to gg scattering and to setting the number of flavors $N_f = 0$ in the partonic matrix elements. It is straightforward to compute our threshold terms in this limit. The comparison is shown in Fig. 7.3. One can see that the large enhancement at high p_T predicted by the NNLO threshold terms is very nicely consistent with the full result. Judging from the comparison, the NNLO threshold terms become accurate at about $p_T = 400$ GeV for the chosen rapidity interval. Additional comparisons with the

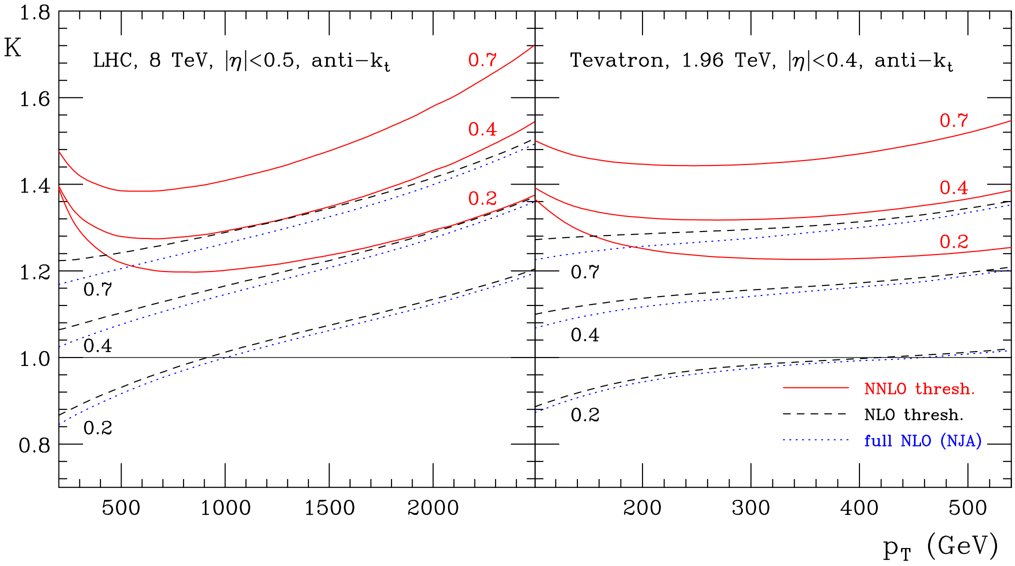

Figure 7.2: Left: K-factors for jet production in pp-collisions at the LHC at $\sqrt{S} = 8$ TeV for $R = 0.2, 0.4, 0.7$, using the anti-k_t algorithm. Right: Same for $p\bar{p}$ collisions at the Tevatron at $\sqrt{S} = 1.96$ TeV.

results of [237] show that this value is representative of rapidity intervals that contain the dominant region $\eta \approx 0$. Detailed comparisons for non-central rapidity regimes will need to be carried out in the future. One also finds that at very forward rapidities, $\eta \sim 4$, our results indicate substantial NNLO K-factors of order 5 or so at $p_T \sim 40$ GeV. In this regime, the coefficients of the threshold logarithms become large, due to “small-x” t-channel gluon exchange contributions. It will be important for future work to address this region in more detail in order to derive reliable predictions for the forward jet cross section at the LHC. Such contributions may also be responsible in part for the rise of the K-factor toward lower p_T seen in Figs. 7.2 and 7.3. This rise is more pronounced for the NNLO threshold terms, implying that subleading contributions become relevant here. Whether these are related to subleading logarithmic terms, or to terms that vanish at partonic threshold $z = 0$, will need to be studied in more detail. In order to shed light on terms of the latter type, the dashed line in Fig. 7.3 shows the NNLO threshold result found when using a different angular variable, $v' \equiv 1 + t/s = z + v(1-z)$, in Eq. (7.1). Clearly, $v' = v + \mathcal{O}(z)$. The difference between the two NNLO threshold results indicates a typical uncertainty of the prediction obtained from threshold resummation. The interplay of exact NNLO calculations with NNLO terms predicted by the threshold expansion will likely prove to be a useful tool: on the one hand, the comparison helps to assess the region where reliable predictions of threshold terms are possible, even beyond NNLO. On the other hand, the threshold terms may constitute a useful benchmark for new full NNLO calculations.

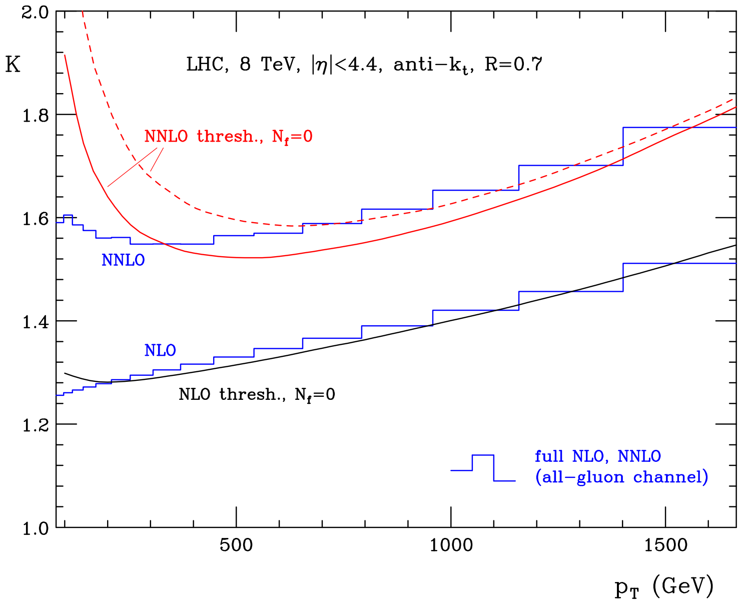

Figure 7.3: K-factors for jet production in pp-collisions at the LHC at $\sqrt{S} = 8$ TeV in the "gluon-only" channel. The anti-k_t algorithm with $R = 0.7$ was used and the NNLO parton distributions of [115]. The histograms show the results of the recent full NNLO calculation [237] and its NLO counterpart, while the lines display the NLO and NNLO threshold terms. Note that the scale choice is different for the results based on threshold resummation ($\mu = p_T$) and the full results ($\mu = p_{T,1}$) as pointed out in [246] and discussed in detail in [247]. Here $p_{T,1}$ corresponds to the transverse momentum of the highest p_T jet for a given event. This has a particularly strong impact for the K-factors at low p_T at NNLO.

7.4 Mellin Space Inversion

There are several ways to extend the results obtained above. An improvement of our results will be particularly relevant at low p_T and when only forward rapidites are considered. We may categorize the full set of distributions at NNLO as follows

$$\left(\frac{\ln^3(z)}{z}\right)_+ , \left(\frac{\ln^2(z)}{z}\right)_+ , \left(\frac{\ln(z)}{z}\right)_+ \Bigg\| \left(\frac{1}{z}\right)_+ , \delta(z) \Bigg\| h(v,z) \,. \tag{7.10}$$

Here $h(v, z)$ denotes all remaining terms that are not singular at threshold. Each of the first five terms is then multiplied by some specific function $g(v)$. The six contributions listed here are of decreasing importance, when going to the right side. So far, at NLL, the three most dominant towers of threshold logarithms are fully taken into account. At NNLO, this corresponds to the first three terms listed above. However, the NLL resummed expression also predicts correctly many terms that appear in the subleading towers even though they are not completely under control. At NNLO-NLL, terms of this type are found in the 4th and 5th tower, which corresponds to the two terms sandwiched between the "double lines" in Eq. (7.10), *i.e.* $(1/z)_+$ and $\delta(z)$.

So far, we made the choice of setting all terms to zero that correspond to towers that are not fully taken into account. In terms of the NNLO set of distributions listed in (7.10), this choice corresponds to a cut after the first three most dominant terms on the left side. In principle, we note that this is a perfectly valid approach at NLL. However, one might view this as not being the "most natural" choice. Instead, one might simply take into account everything that can possibly be derived by resummation for a given fixed order expansion. We are going to adopt this procedure from now on.

In addition, we can extend the accuracy of threshold resummation beyond NLL. Relying on the results obtained for di-hadron production in Chapter 5 and single-inclusive hadron production in Chapter 6, we are able to fully take into account the 4^{th} tower of singular distributions at threshold. At NNLO, this corresponds to the distribution $(1/z)_+$ in (7.10). We will find that this leads to a very important numerical stabilization of our approximate NNLO results.

Finally, threshold resummation is derived in Mellin space. When only the distributions in z-space are extracted from the resummed result, this fact is not correctly taken into account. For the set of terms shown in (7.10), our previous procedure corresponds to setting $h(z) = 0$. In principle, $h(z)$ is subleading at threshold but nevertheless, it turns out to have relevant numerical effects. Therefore, we extend our calculation also in this sense. We perform a numerical Mellin inversion of the resummed result expanded up to NNLO. In addition, we are going to present results for N^{3}LO.

Concerning the Mellin inversion, we proceed as follows. We denote the set of terms obtained by expanding the resummed result in Mellin space by $\tilde{\Omega}(N)$. At NNLO, we have the following structure

$$\begin{aligned}\tilde{\Omega}(N) &= f_{0,0}(v) + \alpha_s \left(f_{1,2}(v)\, L^2 + f_{1,1}(v)\, L + f_{1,0}(v)\right) \\ &+ \alpha_s^2 \left(f_{2,4}(v)\, L^4 + f_{2,3}(v)\, L^3 + f_{2,2}(v)\, L^2 + f_{2,1}(v)\, L + f_{2,0}(v)\right) , \end{aligned} \tag{7.11}$$

where $L^j = \ln^j \bar{N}$. The first index i of the functions $f_{i,j}(v)$ corresponds to the power of α_s^i omitting an overall factor of α_s^2, whereas the second index j denotes the power of the associated logarithm L^j. Note that this structure directly extends to higher orders as well. The goal is to compute the Mellin inverse of $\tilde{\Omega}(N)$ which we denote by $\Omega(z)$. It is possible to directly calculate the full set of distributions in z-space which we denote by $\omega(z)$. Note that $\omega(z)$ are only the distributions in z-space but not the full Mellin inversion which we want to achieve in the end. At NNLO, we have the structure

$$\begin{aligned}\omega(z) &= g_{0,0}(v)\, \delta(z) + \alpha_s \Big(g_{1,2}(v)\, L' + g_{1,1}(v)\, L'^0 + g_{1,0}(v)\, \delta(z)\Big) \\ &+ \alpha_s^2 \Big(g_{2,4}(v)\, L'^3 + g_{2,3}(v)\, L'^2 + g_{2,2}(v)\, L' + g_{2,1}(v)\, L'^0 + g_{2,0}(v)\, \delta(z)\Big) , \end{aligned} \tag{7.12}$$

with some functions $g_{i,j+1}(v)$, where j corresponds to the exponent of the associated logarithm $L'^j = (\ln^j(z)/z)_+$. Note that for $j+1 = 0$, the functions $g_{n,0}(v)$ corresponds to a term involving a $\delta(z)$ instead of a plus distribution. In general, one has $f_{n,2n}(v) = g_{n,2n}(v)$ which implies that the functions multiplying the most important logarithm are the same for any given fixed order. We may now take the exact Mellin moments of $\omega(z)$

$$\tilde{\omega}(N) = \int_0^1 dz\,(1-z)^{N-1}\,\omega(z)\,. \tag{7.13}$$

For example, taking the exact moments leads to expressions such as [248]

$$\int_0^1 dz\,(1-z)^{N-1}\left(\frac{\ln(z)}{z}\right)_+ = \frac{1}{2}\left[(\psi(N)+\gamma_E)^2+\zeta(2)-\psi'(N)\right]\,, \tag{7.14}$$

which generally involve the digamma function $\psi(N)$ and its derivatives. Finally, we can compute the Mellin inverse of $\tilde{\Omega}(N)$ in the following way

$$\Omega(z) = \omega(z) + \frac{1}{2\pi i}\int dN\,(1-z)^{-N}\left(\tilde{\Omega}(N)-\tilde{\omega}(N)\right)\,. \tag{7.15}$$

We can directly see that this is the correct method by taking Mellin moments of the whole expression. In Mellin space, we find that the first and third term cancel out and we are left with $\tilde{\Omega}(N)$. The Mellin inverse integral in (7.15) is constructed such that the combination $\tilde{\Omega}(N)-\tilde{\omega}(N)$ only has terms of the order of $\mathcal{O}(1/N)$ for which we can directly compute the inverse numerically.

7.5 Phenomenological Results - 2

In Chapter 6, we derive the soft and hard matrices for single-inclusive hadron production. Starting from there, one may obtain analogous results for single-inclusive jet production by following the techniques developed in [40, 42, 43]. We present preliminary results for the Tevatron and the LHC. The results presented here are based on the extension toward NNLL and we implement the Mellin inversion as discussed in Section 7.4. Now that full NNLO corrections in the all gluon channel with the scale choice $\mu = p_T$ are available [247], we may directly compare our new results to the kinematics relevant for the Tevatron and the LHC. As expected, the choice $\mu = p_{T,1}$ or $\mu = p_T$ has a significant impact on the calculated K-factors.

In order to estimate the range of validity of our approximate results based on threshold resummation, we compare to the full NNLO results in the all-gluon channel presented in [247] where the PDF set of [249] is used. Firstly, in Fig. 7.4, we consider LHC - ATLAS kinematics at $\sqrt{S} = 7$ TeV in the central rapidity region of $|\eta| < 0.3$ with $R = 0.4$ which corresponds to measurements reported in [250]. The transverse momentum of the observed jets is in the range of $20-1500$ GeV. We consider K-factors with respect to LO. The NLO threshold expansion (dashed blue) matches very well with the full NLO in the NJA (solid blue). Surprisingly, this is the case even for very small values of p_T which is far away from the hadronic threshold. In general, we note that the full NLO in the NJA and the Monte-Carlo based NLO agree to a remarkable degree. One finds that the error introduced by the NJA can be safely neglected given the accuracy of the threshold approximation. Also at NNLO, the threshold approximation (dashed red) and the full result (solid red) agree quite well except for the two lowest bins in p_T. In general, the agreement gets worse when very forward rapidity slices are considered with $|\eta| > 2$. However, in the case that we integrate over the central rapidity region, the agreement is still

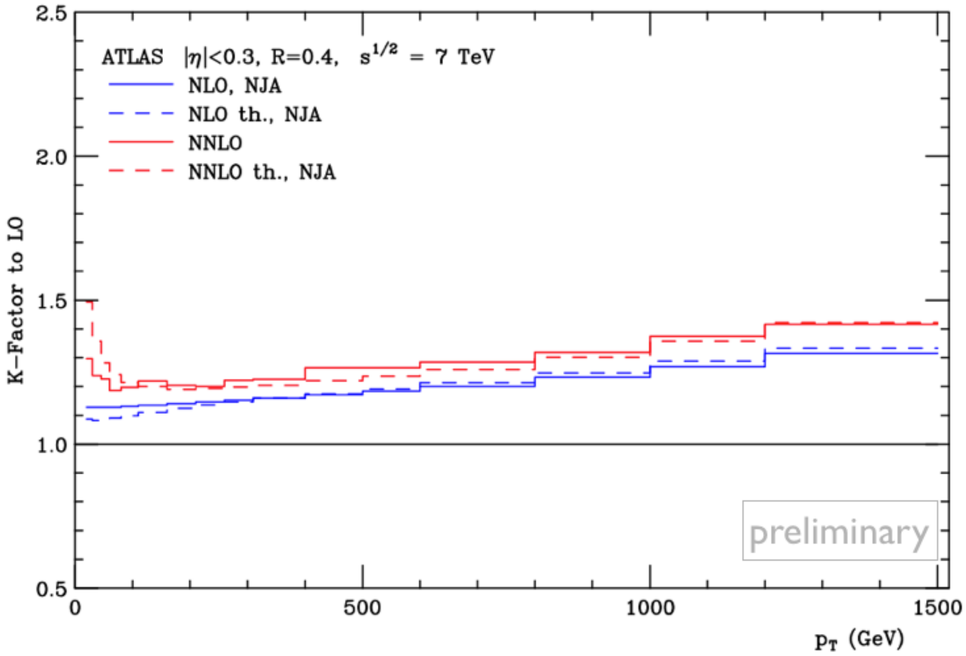

Figure 7.4: K-factors for jet production in pp-collisions at the LHC - ATLAS at $\sqrt{S} = 7$ TeV in the "gluon-only" channel.

very good. The problem at forward rapidities seems to be due to high-energy logarithms of the type $\ln(-t/s)$ with $s \gg |t|$. They also need to be taken into account correctly in order to achieve better approximate results over the full kinematical range.

Secondly, we consider Tevatron - CDF kinematics in Fig. 7.5. We are considering jets in the p_T range of $54 - 700$ GeV with $R = 0.7$, $\sqrt{S} = 1.96$ TeV in the central rapidity region $|\eta| < 0.1$ which corresponds to measurements reported in [251]. We use the same color coding as above. We find that both NLO and NNLO agree very well. With the lessons learnt at NNLO, we also calculated approximate N^{3}LO results (dashed magenta) which are again a sizable contribution. Given the size of the NNLO and N^{3}LO corrections to hadronic jet production, it seems worthwhile to continue exploring even higher order corrections in QCD and eventually perform an all order threshold resummation in the future.

7.6 Beyond the Standard Model

In this Section, we follow roughly the steps outlined in [17]. In the Standard Model, quarks can scatter via gluon exchange as it is shown on the left side of Fig. 7.6. Suppose we have some new physics in the TeV range. For example, quarks might also scatter via the exchange a new object with a mass M in the TeV range, as it is shown on the right hand side of Fig. 7.6. Alternatively, quark substructure could be found in a similar way. We consider the following additional Lagrangian to the SM

$$\Delta\mathcal{L} = \frac{\tilde{g}^2}{M^2}\bar{\psi}\gamma^\mu\psi\,\bar{\psi}\gamma_\mu\psi\,, \tag{7.16}$$

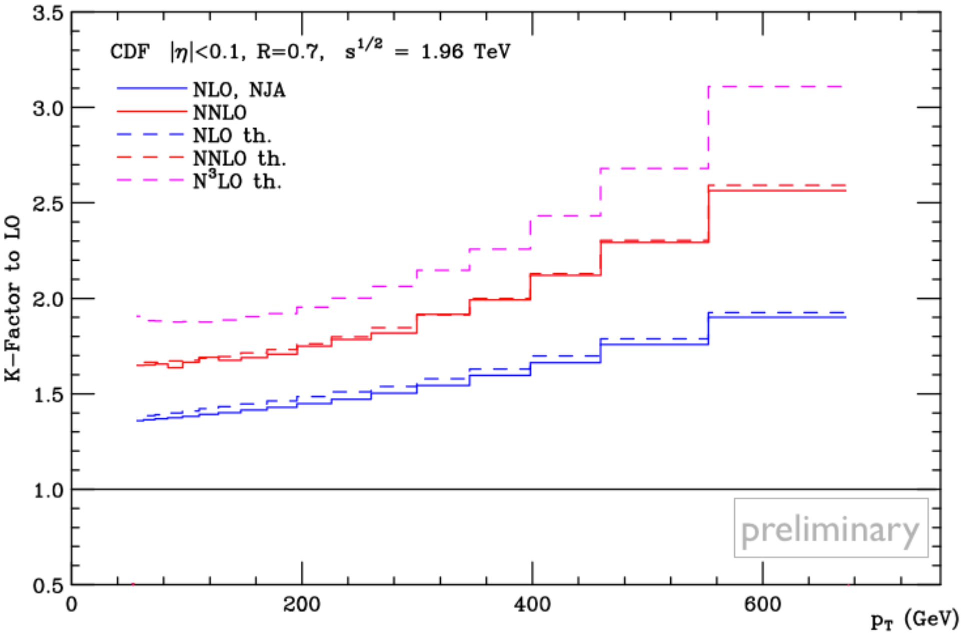

Figure 7.5: K-factors for jet production in pp-collisions at the Tevatron - CDF at $\sqrt{S} = 1.96$ TeV in the "gluon-only" channel.

where $\tilde{g}$ denotes the coupling strength of quarks to the new physics and the factor $1/M^2$ has to be included for dimensional reasons such that we end up with dimension 4 for the Lagrangian.

We consider jet production in pp collisions at the LHC (or equivalently $p\bar{p}$ at the Tevatron). The new term in the Lagrangian $\Delta\mathcal{L}$ should lead to a small enhancement of the observed cross section compared to the prediction of the standard model. Thus, we would expect the following behavior to be observed in experiment

$$\frac{\text{data} - \text{theory}}{\text{theory}} \sim \tilde{g}^2 \frac{E_T^2}{M^2} \,. \tag{7.17}$$

The factors $\tilde{g}^2/M^2$ follow from the additional term in the Lagrangian, see Eq. (7.16). The factor of E_T^2 has to be included because it is the only factor with a mass dimension for this observable rendering the right hand side dimensionless as it should be given the left hand side. Some of the presently publicly available data from the LHC is shown in Fig. 7.7 plotted as ratios data/theory. Overall, the agreement between theory and data is very good. Much of the uncertainty can be traced back to the rather poorly constrained gluon PDF at large x as well as to missing higher order corrections. However, it is precisely this region where BSM physics might show up. Therefore, a solid theoretical understanding of the QCD background is of great importance. See also [252] for example.

Figure 7.6: Gluon exchange (left) and some possible interaction beyond the standard model (right). Figure adapted from [17].

7.7 Conclusions

We have presented approximate higher order predictions for single-inclusive jet production in hadronic collisions. Our results are relevant for the extraction of PDFs and the strong coupling constant α_s. For example, the latest PDF fit from the NNPDF collaboration [149] already included these results in order to determine their NNLO PDF set. In addition, our calculation is a step toward precision phenomenology for the Tevatron and the LHC and eventually for the search of BSM physics.

In future studies, we are going to investigate the relevance of terms of the type $\ln \bar{N}/N$ and how they can be determined. In principle, they are subleading at threshold but for other processes such as deep-inelastic scattering [253], they turned out to be very relevant. In addition, following our numerical studies, high-energy logarithms [254] of the form $\ln(-t/s)$, where $s \gg |t|$, turn out to be very relevant. This is in particular the case for low p_T and forward rapidities $|\eta| > 2$. It would be important to combine results derived from both threshold and high-energy resummation. Finally, non-global logarithms have to be taken into account to a higher accuracy and eventually need to be resummed to all orders. Even when the full NNLO will be available in the future, it can be seen from our numerical studies that also N^{3}LO and even higher corrections are still sizable and need to be taken into account for a precise theoretical description. The availability of full NNLO results for such an involved process as hadronic jet production makes it an ideal test ground to understand the applicability of approximations for higher order corrections.

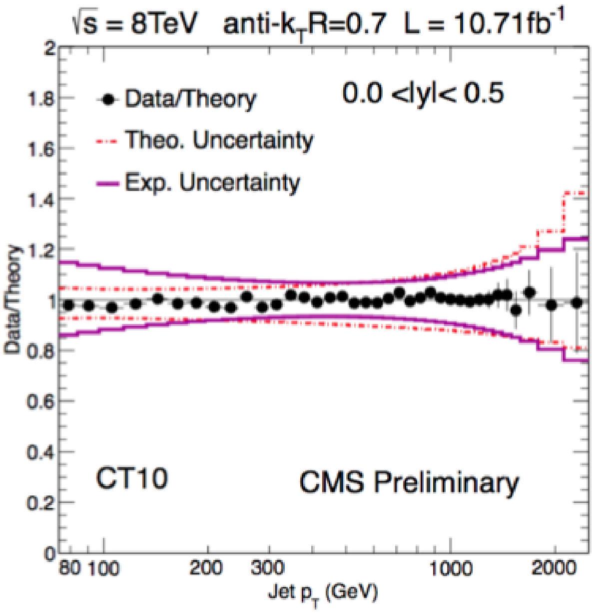

Figure 7.7: Single-inclusive jet production at the LHC plotted as ratios data/theory. Both theoretical and experimental uncertainties are shown. Figure taken from [255].

CHAPTER 8

SINGLE-SPIN ASYMMETRIES IN *W* PRODUCTION AT NLO

We present an analytic next-to-leading order QCD calculation of the partonic cross sections for single-inclusive lepton production in hadronic collisions, when the lepton originates from the decay of an intermediate electroweak boson and is produced at high transverse momentum. In particular, we consider the case of incoming longitudinally polarized protons for which parity-violating single-spin asymmetries arise that are exploited in the W boson program at RHIC to constrain the proton's helicity parton distributions. Our calculation enables a very fast and efficient numerical computation of the relevant spin asymmetries at RHIC, which is an important ingredient for the inclusion of RHIC data in a global analysis of nucleon helicity structure. We confirm the validity of our calculation by comparing with an existing code that treats the next-to-leading order cross sections entirely numerically by Monte-Carlo integration techniques. We also provide new comparisons of the present RHIC data with results for some of the sets of polarized parton distributions available in the literature. This Chapter is based on publication [viii].

8.1 Introduction

The W physics program at RHIC [256] is dedicated to providing new insights into the helicity structure of the proton. It exploits the violation of parity in the weak interactions, which gives rise to *single*-longitudinal spin asymmetries in proton-proton collisions. The main focus is on the production of W bosons, identified by their subsequent decay into a lepton pair. The charged lepton (or antilepton) is observed. From the corresponding cross sections for the various helicity settings $(++), (+-), (-+), (--)$ of the two incoming protons one defines the spin asymmetry

$$A_L^{W^\pm} \equiv \frac{d\sigma^{++} + d\sigma^{+-} - (d\sigma^{-+} + d\sigma^{--})}{d\sigma^{++} + d\sigma^{+-} + d\sigma^{-+} + d\sigma^{--}} \equiv \frac{d\Delta\sigma}{d\sigma} \ . \tag{8.1}$$

As one can see, one takes the difference of cross sections for positive and negative helicities of one proton, while summing over the polarizations of the other. The STAR collaboration at RHIC has published rather extensive and precise data on $A_L^{W^\pm}$ last year [257], and new precise mid-rapidity data from Phenix are forthcoming [258]. Earlier measurements were reported by both Phenix [259] and STAR [260]. Data sets with even higher statistics and kinematic coverage are expected in the near future. Typically, the data are presented at fixed rapidity of the charged lepton, which by convention is counted as positive in the forward direction of the polarized proton.

It has long been recognized [261, 262] that $A_L^{W^\pm}$ offers excellent sensitivity to the individual helicity parton distributions Δu, $\Delta \bar{u}$, Δd, $\Delta \bar{d}$ of the nucleon, where

$$\Delta f(x, Q^2) \equiv f^+(x, Q^2) - f^-(x, Q^2) \; , \tag{8.2}$$

with f^+ (f^-) denoting the distribution of parton f with positive (negative) helicity in a parent proton with positive helicity. The distributions are functions of the longitudinal momentum fraction x of the parton and of a "resolution" scale Q. Information on Δu, $\Delta \bar{u}$, Δd, $\Delta \bar{d}$ is also accessible in (semi-inclusive) deep-inelastic lepton scattering (DIS) [121, 124, 128, 129, 131, 263]. The key advantages of W boson production are that (i) it is characterized by momentum scales of the order of the W mass which are much higher than those presently relevant in DIS and hence deeper in the perturbative domain, (ii) it does not rely on the knowledge of hadronic fragmentation functions, thanks to its clean leptonic final state. In any case, information from the W program at RHIC is complementary to that from DIS.

The main concept behind the RHIC measurements can be easily summarized: For W^- production, taking into consideration only the dominant $\bar{u}d \to W^-$ subprocess, the spin-dependent cross section in the numerator of the asymmetry in Eq. (8.1) is found to be proportional to the combination

$$\Delta \bar{u}(x_1) d(x_2)(1 - \cos\theta)^2 - \Delta d(x_1) \bar{u}(x_2)(1 + \cos\theta)^2 \, , \tag{8.3}$$

where for simplicity we have not written out the straightforward convolutions over the parton momentum fractions. θ is the polar angle of the negatively charged decay lepton in the partonic center-of-mass system, with $\theta > 0$ in the forward direction of the polarized parton. In the backward region of the lepton, one has $x_2 \gg x_1$ and $\theta \gg \pi/2$, so that the first term in Eq. (8.3) strongly dominates. Since the denominator of A_L is proportional to $\bar{u}(x_1) d(x_2)(1 - \cos\theta)^2 + d(x_1)\bar{u}(x_2)(1 + \cos\theta)^2$, the asymmetry then provides a clean probe of $\Delta \bar{u}(x_1)/\bar{u}(x_1)$ at medium values of x_1. By similar reasoning, in the forward lepton region the second term in Eq. (8.3) dominates, giving access to $-\Delta d(x_1)/d(x_1)$ at relatively high x_1.

For W^+ production, within the same approximation, the spin-dependent cross section is proportional to

$$\Delta \bar{d}(x_1) u(x_2)(1 + \cos\theta)^2 - \Delta u(x_1) \bar{d}(x_2)(1 - \cos\theta)^2 \, . \tag{8.4}$$

Here the distinction of the two contributions by considering backward or forward lepton scattering angles is less clear-cut than in the case of W^- because of the reversal of the factors $(1 \pm \cos\theta)^2$ relative to (8.3), which always suppresses the dominant combination of parton distributions. Therefore, both terms in (8.4) will compete. Nonetheless, the W^+ measurements at RHIC are of course of great value in the context of a global analysis of the helicity distributions.

Given the importance of $A_L^{W^\pm}$ for constraining nucleon helicity structure, there has been a lot of activity on the calculation of higher-order QCD corrections to the relevant spin-dependent cross sections. Closed analytic expressions for next-to-leading order (NLO) corrections to polarized W boson production were derived in Refs. [264, 265], with extensions to all-order resummations in [266, 267]. In these papers, direct observation of the W boson and its kinematics was assumed, which simplifies the calculation considerably but is not really applicable to the measurements at RHIC. The proper lepton decay kinematics was taken into account in three further studies [268–270]. The first two of these include the contributions by intermediate Z bosons and photons as well, which may also give rise to charged leptons and provide a background to the lepton signal from W boson decay when the detectors are not hermetic. Reference [268] additionally derives and implements the resummation of large logarithms in the transverse momentum of the intermediate W boson.

In the calculations [268–270] the NLO corrections were obtained numerically in the context of a Monte-Carlo integration routine. The resulting computer codes are very flexible in the sense that kinematic cuts on lepton or recoil jet variables can be easily implemented. Those from Refs. [268] and [269] are known as RHICBOS and CHE, respectively, and have found wide use in comparisons to RHIC data. On the other hand, the Monte-Carlo integration based codes are rather demanding in terms of CPU time. This becomes a significant drawback when one wants to perform a global analysis of the helicity distributions from the RHIC data [128, 129, 263, 271]. Such an analysis typically requires many thousands of computations of the spin asymmetry. Clearly, a fast and stable evaluation at NLO is highly desirable in this context.

In this paper, we derive analytic expressions for the NLO spin-dependent partonic cross sections for electroweak boson production, *including* their leptonic decay. More precisely, we consider the cross sections directly as single-inclusive lepton ones, $\vec{p}p \to \ell^\pm X$, where transverse momentum and rapidity of the charged lepton are observed, precisely as is the case at RHIC. We note that a corresponding calculation in the unpolarized case has been presented a long time ago [272]. We present a new program that produces NLO results for the single-spin asymmetries relevant at RHIC and outruns the Monte-Carlo based codes by about two orders of magnitude in CPU time. We also include the background reactions involving Z bosons and photons. We expect our program to become a useful tool for global analyses of RHIC data based on Mellin-moment [110, 128, 129, 263] or neural-network [271] techniques. We also use our new code to present comparisons of the present RHIC data to NLO predictions for a variety of sets of helicity parton distributions.

In Sec. 8.2 we discuss the technical details of our NLO calculation. Section 8.3 presents our phenomenological results, where we also perform comparisons with the CHE code of [269]. Finally, we conclude in Section 8.4.

8.2 Next-to-Leading Order Calculation

8.2.1 Framework and outline of the NLO calculation

We consider the single-inclusive process $\vec{p}p \to \ell + X$, where ℓ denotes the charged lepton (or antilepton) resulting from production and decay of a W boson. As discussed in the Introduction, charged leptons can of course also be produced by an intermediate photon or Z boson which, subject to the experimental selection criteria, gives rise to a background. We hence perform all our calculations also for γ and Z production and γZ interference. For the sake of simplicity we will, however, present details of our calculation and explicit results only for the most interesting W boson case, and just highlight a few features specifically relevant for intermediate γ and Z.

We denote the momenta of the incoming protons and the produced charged lepton by P_A, P_B, p_ℓ, respectively. Using factorization [5], we write the polarized hadronic cross section $d\Delta\sigma$ which appears in the numerator of Eq. (8.1) in terms of convolution integrals of polarized and unpolarized parton distributions $\Delta f_a(x_a, \mu_F^2)$, $f_b(x_b, \mu_F^2)$ and the perturbative hard-scattering partonic cross sections $d\Delta\hat{\sigma}_{ab}$:

$$d\Delta\sigma \;=\; \sum_{a,b} \int dx_a dx_b \, \Delta f_a(x_a, \mu_F^2) \, f_b(x_b, \mu_F^2) \;\; d\Delta\hat{\sigma}_{ab}(x_a P_A, x_b P_B, p_\ell, \mu_R^2, \mu_F^2) \; , \tag{8.5}$$

where

$$d\Delta\hat{\sigma}_{ab} \equiv \frac{1}{4}\left[d\hat{\sigma}^{++} + d\hat{\sigma}^{+-} - (d\hat{\sigma}^{-+} + d\hat{\sigma}^{--})\right] \; . \tag{8.6}$$

The superscripts on the right refer to parton helicities, so that the helicities of the second parton b are summed over, while he helicity difference is taken for parton a. The sum in Eq. (9.1) runs over quarks, antiquarks and the gluon, and the parton distributions are evaluated at the factorization scale μ_F. The partonic cross sections also depend on a renormalization scale μ_R. The fractions of the parent hadrons' momenta carried by the scattering partons are denoted by x_a and x_b. An analogous expression for the unpolarized cross section $d\sigma$ appearing in the denominator of Eq. (8.1) is obtained by using only unpolarized parton distributions and the corresponding unpolarized partonic cross sections, defined by averaging over the helicities of both incoming partons.

Due to the pure $V - A$ structure of the $Wq\bar{q}'$ vertex, and because of conservation of quark helicity at the vertex, the spin-dependent partonic cross section for an incoming polarized quark is just the negative of the corresponding unpolarized cross section, while for an incoming polarized *anti*-quark it is the same as the unpolarized one:

$$\begin{aligned} d\Delta\hat{\sigma}_{qb} &= -d\hat{\sigma}_{qb} \qquad (b = \bar{q}', g) \, , \\ d\Delta\hat{\sigma}_{\bar{q}b} &= d\hat{\sigma}_{\bar{q}b} \qquad (b = q', g) \, . \end{aligned} \tag{8.7}$$

Note that no such relation occurs for incoming polarized gluons. In case of γ and/or Z exchange, relations (8.7) do not hold.
We now introduce the variables

$$S \equiv (P_A + P_B)^2 \, , \;\; T \equiv (P_A - p_\ell)^2 \, , \;\; U \equiv (P_B - p_\ell)^2 \; , \tag{8.8}$$

and

$$V \equiv 1 + \frac{T}{S}, \;\; W \equiv \frac{-U}{S+T} \,. \tag{8.9}$$

The lepton's transverse momentum p_T and its center-of-mass system rapidity η are related to these variables by

$$V = 1 - \frac{p_T}{\sqrt{S}} \mathrm{e}^{-\eta} \,, \;\; VW = \frac{p_T}{\sqrt{S}} \mathrm{e}^{\eta} \,. \tag{8.10}$$

We furthermore introduce the partonic variables corresponding to Eqs. (8.8), (8.9):

$$\begin{aligned} & s \equiv (p_a + p_b)^2, \;\; t \equiv (p_a - p_\ell)^2, \;\; u \equiv (p_b - p_\ell)^2 \,, \\ & v \equiv 1 + \frac{t}{s}, \;\; w \equiv \frac{-u}{s+t}, \end{aligned} \tag{8.11}$$

so that from $p_a = x_a P_A$, $p_b = x_b P_B$ we have

$$x_a = \frac{VW}{vw} \,, \;\; x_b = \frac{1-V}{1-v} \,. \tag{8.12}$$

Writing out Eq. (9.1) explicitly to $\mathcal{O}(\alpha_s)$ in the strong coupling constant, we now obtain

$$\begin{aligned} \frac{d^2 \Delta\sigma}{dp_T d\eta} \;\; = \;\; & \frac{2}{p_T} \sum_{a,b} \int_{VW}^{V} dv \int_{VW/v}^{1} dw \; x_a \Delta f_a(x_a, \mu_F^2) \, x_b f_b(x_b, \mu_F^2) \\ & \times \left[\frac{d\Delta\hat{\sigma}_{ab}^{(0)}(s,v)}{dv} \delta(1-w) + \frac{\alpha_s(\mu_R^2)}{2\pi} \frac{d\Delta\hat{\sigma}_{ab}^{(1)}(s,v,w,\mu_F^2,\mu_R^2)}{dvdw} \right] \,, \end{aligned} \tag{8.13}$$

where the $d\Delta\hat{\sigma}_{ab}^{(0)}$ represent the leading-order (LO) contributions and the $d\Delta\hat{\sigma}_{ab}^{(1)}$ the NLO ones. The only LO partonic process is $q\bar{q}' \to W \to \ell\nu_\ell$ annihilation, whose Feynman diagram is shown in Fig. 8.1 a). For the NLO correction we have to include the 2 → 3 real-gluon emission diagrams as well as the virtual corrections to the Born cross section. In addition, quark-gluon scattering contributes here as well as a new channel. Some of the relevant NLO Feynman diagrams are shown in Fig. 8.1 (b)-(d).

For our calculations, we work with a general (axial) vector structure for the $Wq\bar{q}'$-vertex of the form

$$V_q^\mu = -i \frac{g_W}{2\sqrt{2}} U_{qq'} \, \gamma^\mu \, (v_q - a_q \, \gamma_5) \,, \tag{8.14}$$

where $U_{qq'}$ is the appropriate CKM matrix element and g_W the fundamental weak charge. Likewise, we use a corresponding expression for the $W\ell\nu_\ell$-vertex, with vector and axial coefficients v_ℓ and a_ℓ (and, of course, with $U_{qq'} = 1$). Using such general vertices will help us to keep better track of the couplings in the NLO calculation and to obtain an understanding of the underlying structure. Also, it allows us to extend our calculation to the case of γ or Z boson exchange (for γZ interference one needs to introduce an even more general vertex structure that allows different couplings in the amplitude and its complex conjugate). The case of a W boson is recovered by setting $v_q = a_q = 1$ and $v_\ell = a_\ell = 1$.

As is very well known, various types of singularities appear at intermediate stages of the NLO calculation. To treat these, we choose dimensional regularization with $d = 4-2\varepsilon$ dimensions. This means that we have to deal with subtleties that occur in Dirac traces involving γ_5 or in the presence of the Levi-Civita tensor $\epsilon^{\mu\nu\rho\sigma}$ when $d \neq 4$. γ_5 appears in the $Wq\bar{q}'$-vertex (see (9.8)) and also acts as projection operator onto definite helicity states of incoming quarks or antiquarks. Likewise, the Levi-Civita tensor projects onto gluon helicity states. We adopt the 't Hooft, Veltman, Breitenlohner, Maison (HVBM) scheme of [273, 274], which basically recognizes the four-dimensional nature of γ_5 and $\epsilon^{\mu\nu\rho\sigma}$, separating the usual four space-time dimensions from the additional $d-4 = -2\varepsilon$ spatial ones. Technically, we compute Dirac traces using the TRACER package of [275]. We also follow Refs. [276, 277] to use a symmetrized version of the W-fermion vertex.

Because of the distinction between four- and $(d-4)$-dimensional subspaces in the HVBM scheme, the squared matrix elements for the partonic processes will contain regular d-dimensional scalar products of the external momenta, but also additionally $(d-4)$-dimensional ones. The latter have to be properly taken into account when the phase space integration is performed. As it turns out, for the unpolarized cross sections all such additional terms are either absent or integrate to zero, *i.e.* are of $\mathcal{O}(\varepsilon)$ after phase space integration. However, in the polarized case, they do contribute, and in fact a finite additional subtraction is required in the procedure of factorization of collinear singularities in order to maintain relations such as (8.7) beyond LO. The deeper reason for this is that the γ_5 and $\epsilon^{\mu\nu\rho\sigma}$ definitions of [273, 274], although algebraically consistent, cause violation of helicity conservation at fermion-boson vertices, which has to be corrected for. Since this is very well established in the literature (see, for example, Refs. [232, 233, 278]) we shall not go into any further detail here but only mention the salient features when they become relevant in the course of the calculation.

8.2.2 Born-level cross section

Thanks to (8.7), we can easily develop the calculations of the unpolarized and polarized cross sections in parallel. Up to the subtleties just mentioned, it is sufficient to present details only for the unpolarized case. The lowest-order contribution to the cross section comes from the $2 \to 2$ scattering process $q\bar{q}' \to \ell\nu_\ell$. The diagram is shown in Fig. 8.1(a). As before, we use "ℓ" for the observed charged lepton, regardless of its charge. We shall see below that it is possible to formulate a partonic cross section in this generic way, despite the fact that the "lepton" can be either a particle or an antiparticle. We also

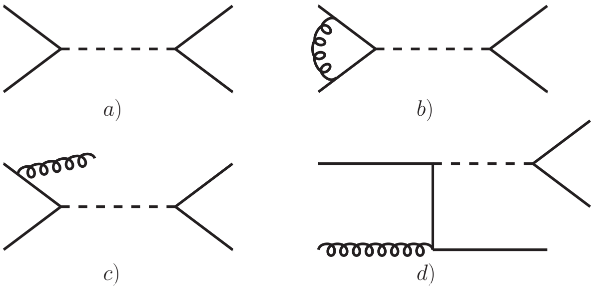

Figure 8.1: Feynman diagrams for heavy gauge boson production: a) leading-order, b) NLO virtual correction, c) NLO real emission, d) NLO qg scattering. Crossed diagrams are not shown.

always refer to the corresponding neutrino or antineutrino as the "neutrino" and denote it by ν_ℓ. Since it remains unobserved, we integrate over its phase space. This leads to an overall factor $\delta(1-w)$ for the Born cross section, so that

$$\frac{d^2\hat{\sigma}^{(0)}_{q\bar{q}'}}{dv\,dw} = \frac{d\hat{\sigma}^{(0)}_{q\bar{q}'}}{dv}\delta(1-w)\ , \tag{8.15}$$

as we have anticipated in (9.5). Using the general vertex structure given in Eq. (9.8), we find that two combinations of the couplings appear in the expression for the cross section, which are given by

$$\begin{aligned} C_1 &= (v_q^2+a_q^2)(a_\ell^2+v_\ell^2) + 4\,a_q a_\ell v_q v_\ell\ , \\ C_2 &= (v_q^2+a_q^2)(a_\ell^2+v_\ell^2) - 4\,a_q a_\ell v_q v_\ell\ . \end{aligned} \tag{8.16}$$

We recall that in case of an exchanged $W^\pm$ boson, we have $v_q = a_q = v_\ell = a_\ell = 1$ and hence always $C_1 = 8$ and $C_2 = 0$. However, it is useful to keep C_2 in the calculation as it allows us to easily switch between W^- and W^+ production. The reason for this becomes clear when we write down the unpolarized Born cross section:

$$\frac{d\hat{\sigma}^{(0)}_{q\bar{q}'}}{dv} = \frac{|U_{qq'}|^2 s}{8\pi N_c}\left(\frac{G_F M_W^2}{\sqrt{2}}\right)^2 \frac{C_1(1-v)^2 + C_2 v^2}{(s-M_W^2)^2+\Gamma_W^2 M_W^2}\ , \tag{8.17}$$

where $N_c = 3$, $G_F = \sqrt{2}g_W^2/(8M_W^2)$ is the Fermi constant, and M_W and Γ_W are the W boson mass and decay width. Let us consider now the partonic channel $u\bar{d} \to e^+\nu_e$. For this indeed Eq. (9.11) provides the correct cross section when $C_1 = 8$ and $C_2 = 0$. In this way the cross section is proportional to $(1-v)^2$, as required by the $V-A$ structure of the interaction and angular momentum conservation. For $d\bar{u} \to e^-\bar{\nu}_e$, on the other hand, the cross section has to be proportional to v^2, rather than $(1-v)^2$. This is immediately realized by interchanging C_1 and C_2 in Eq. (9.11), and subsequently setting again $C_1 = 8$ and $C_2 = 0$. Equivalently, and even more simply, we can just choose in (9.11) $C_1 = 8, C_2 = 0$ for $u\bar{d} \to e^+\nu_e$ and $C_1 = 0, C_2 = 8$ for $d\bar{u} \to e^-\bar{\nu}_e$ to obtain the correct cross sections. We note that the cross sections for the reactions $\bar{d}u \to e^+\nu_e$ and $\bar{u}d \to e^-\bar{\nu}_e$ can be obtained by simple "crossing" $t \leftrightarrow u$, or $v \leftrightarrow 1-v$. Again this may also be achieved by $C_1 \leftrightarrow C_2$. All these considerations also hold at NLO, where the cross section still depends only on the two combinations C_1 and C_2.

The denominator in Eq. (9.11) represents the standard Breit-Wigner form of the propagator. One often also uses the form (see [279])

$$\frac{1}{(s-M_W^2)^2+\Gamma_W^2 s^2/M_W^2}\ , \tag{8.18}$$

which may be obtained from the one given in (9.11) by the simple rescalings $M_W^2 \to M_W^2/(1+\Gamma_W^2/M_W^2)$, $\Gamma_W M_W \to \Gamma_W M_W/(1+\Gamma_W^2/M_W^2)$ and multiplication of the cross section by $1/(1+\Gamma_W^2/M_W^2)$. This also holds at NLO. The numerical difference between these two forms of the propagator is very small and negligible for our purposes.

8.2.3 Real $2 \to 3$ corrections

At NLO, we first consider the $2 \to 3$ real-gluon emission process $q\bar{q}' \to \ell(\nu_\ell g)$, where the gluon and the neutrino remain unobserved. One of the two relevant Feynman diagrams is shown in Fig. 8.1(c). All external particles can be considered as massless, so that the kinematics and the phase space are as usual for single-inclusive calculations. The three-particle phase space in $4 - 2\varepsilon$ dimensions may be written as [232, 233]

$$\begin{aligned}\frac{d^2\Phi_3}{dvdw} &= \frac{s}{(4\pi)^4\Gamma(1-2\varepsilon)}\left(\frac{4\pi}{s}\right)^{2\varepsilon} v^{1-2\varepsilon}(1-v)^{-\varepsilon} w^{-\varepsilon}(1-w)^{-\varepsilon} \\ &\quad \times \int_0^\pi d\theta_1 \int_0^\pi d\theta_2 \sin^{1-2\varepsilon}\theta_1 \sin^{-2\varepsilon}\theta_2 \, \frac{1}{B(1/2,-\varepsilon)} \int_0^1 \frac{dz}{\sqrt{1-z}} z^{-(1+\varepsilon)} \,, \end{aligned} \tag{8.19}$$

where v and w have been defined in Eq. (8.11) and where θ_1 and θ_2 are the polar and azimuthal angles of the neutrino in the rest frame of the neutrino-gluon pair. The integration variable z is specific to the treatment of γ_5 and $\epsilon^{\mu\nu\rho\sigma}$ in the HVBM scheme. It is given by $z \equiv 4\hat{k}^2/(s_{23}\sin^2\theta_1 \sin^2\theta_2)$, where $s_{23} = sv(1-w)$ and $\hat{k}^2$ is the square of the $d-4$-dimensional parts of the neutrino and gluon momenta, which are the same in the adopted frame. It is thus the only $d-4$-dimensional invariant in the calculation [232, 233]. Note that the z-integral cancels against the Beta function in the last line of (8.19) for all terms in the squared matrix element that have no dependence on $\hat{k}^2$.

Since the lepton pair is produced via an intermediate W boson, a propagator with the momentum $p_\ell + p_{\nu_\ell}$ of the W boson appears in the amplitude for the process. As a result, the squared matrix element $|\mathcal{M}|^2$ contains the overall factor

$$\frac{1}{(s_{12} - M_W^2)^2 + \Gamma_W^2 M_W^2} \,, \tag{8.20}$$

with the leptons' pair mass squared:

$$s_{12} \equiv (p_\ell + p_{\nu_\ell})^2 \,. \tag{8.21}$$

s_{12} is a function of the angles θ_1 and θ_2. Since the neutrino is not observed, the propagator will be subject to integration over the phase space. We write it in the following way:

$$\frac{1}{(s_{12} - M_W^2)^2 + g^2} = \frac{1}{2ig}\left(\frac{1}{s_{12} - M_W^2 - ig} - \frac{1}{s_{12} - M_W^2 + ig}\right) , \tag{8.22}$$

where $g \equiv \Gamma_W M_W$. After this partial fractioning, there are only terms in $|\mathcal{M}|^2$ with at most one power of s_{12} in the denominator, either $1/(s_{12} - M_W^2 - ig)$ or $1/(s_{12} - M_W^2 + ig)$. They are usually accompanied by other Mandelstam variables that also depend on θ_1 and θ_2. The ensuing terms may be readily integrated using the integrals

$$I^{(k,n)} = \int_0^\pi d\theta_1 \int_0^\pi d\theta_2 \, \sin^{1-2\varepsilon}\theta_1 \sin^{-2\varepsilon}\theta_2 \, \frac{1}{(a + b\cos\theta_1)^k (A + B\cos\theta_1 + C\sin\theta_1\cos\theta_2)^n} \tag{8.23}$$

tabulated in the Appendix of Ref. [280]. The results contain logarithms of various complex arguments

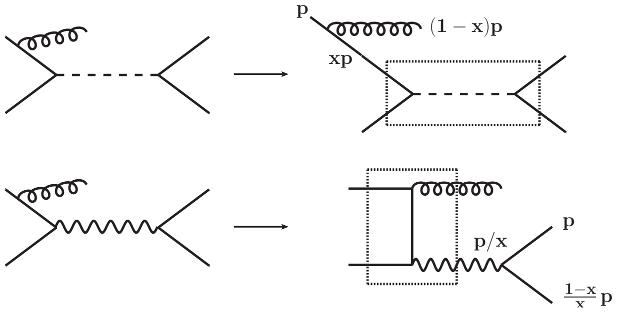

Figure 8.2: Upper row: Representative initial-state collinear contribution for the $q\bar{q}'$ channel. Lower row: Factorization of the final-state collinear singularity which is necessary for the process with an intermediate photon.

which may be combined to produce manifestly real results. This procedure is rather tedious; we have performed numerous numerical checks to ensure its correctness. For terms with dependence on $\hat{k}^2$ the z integration in (8.19) is still trivial. The result may then be further integrated using (8.23). The additional power of $\sin^2\theta_1 \sin^2\theta_2$ arising from the z-integral can be easily accommodated by shifting $\varepsilon \to \varepsilon - 1$ in (8.23).

After integration over phase space the result for the real-gluon emission contribution contains singularities in $1/\varepsilon$. These occur whenever we have a term in $|\mathcal{M}|^2$ with at least a factor of $1/t_3$ or $1/u_3$, where

$$t_3 = (p_q - p_g)^2, \;\; u_3 = (p_{\bar{q}'} - p_g)^2 \,. \tag{8.24}$$

The poles arise when the gluon becomes collinear with the incoming particles, and/or when it becomes soft. The collinear singularities arise directly in the angular integrations. A soft singularity is equivalent to the invariant mass squared of the two unobserved particles becoming small, *i.e.* $s_{23} = sv(1-w) \to 0$, or equivalently $w \to 1$. To make also the soft divergences manifest, we use the standard expansion

$$(1-w)^{-1-\varepsilon} \;\; = \;\; -\frac{1}{\varepsilon}\delta(1-w) + \frac{1}{(1-w)_+} - \varepsilon\left(\frac{\log(1-w)}{1-w}\right)_+ + \mathcal{O}(\varepsilon^2)\,, \tag{8.25}$$

where the “plus” distributions are defined as usual by

$$\int_0^1 dw\, f(w)[g(w)]_+ = \int_0^1 dw\,[f(w) - f(1)]\, g(w)\,. \tag{8.26}$$

The final expression contains quadratic $(1/\varepsilon^2)$ poles as well as single $(1/\varepsilon)$ ones. We note that due to the finite width Γ_W of the W boson, final-state singularities never occur.

The NLO contributions associated with $qg \to \ell\nu q'$ scattering at NLO (Fig. 8.1(d)) can be integrated in the same way as described above. They develop only single poles in $1/\varepsilon$ since soft singularities are absent here.

8.2.4 Virtual correction and factorization of collinear singularities

At NLO, the interference of the virtual diagrams (see for example Fig. 8.1(b)) with the Born diagram contributes. As may be inferred from [45, 276], the first-order virtual corrections only modify the basic $q\bar{q}'W$ vertex by a multiplicative factor of the form $1+\mathcal{O}(\alpha_s)$. Therefore, when computing the interference with the Born diagram, the result will be twice the Born cross section multiplied by this factor. In our notation, we have from [45]:

$$\frac{d\hat{\sigma}^{(1),\mathrm{virt}}_{q\bar{q}'}}{dv dw} = C_F \frac{d\hat{\sigma}^{(0),\varepsilon}_{q\bar{q}'}}{dv} \delta(1-w) \left(-\frac{2}{\varepsilon^2} - \frac{3}{\varepsilon} - 8 + \pi^2\right) \left(\frac{4\pi\mu^2}{s}\right)^{\varepsilon} \frac{\Gamma(1+\varepsilon)\,\Gamma^2(1-\varepsilon)}{\Gamma(1-2\varepsilon)} \, , \tag{8.27}$$

where $C_F = 4/3$. It is important to take into account here that the Born cross section is to be computed in $4-2\varepsilon$ dimensions, where it is given by

$$\frac{d\hat{\sigma}^{(0),\varepsilon}_{q\bar{q}'}}{dv} = \frac{|U_{qq'}|^2 s}{8\pi N_c} \left(\frac{G_F M_W^2}{\sqrt{2}}\right)^2 \left(\frac{4\pi}{s}\right)^{\varepsilon} \frac{(v(1-v))^{-\varepsilon}}{\Gamma(1-\varepsilon)} \frac{C_1(1-v)^2 + C_2 v^2 - C_3\,\varepsilon}{(s-M_W^2)^2 + \Gamma^2 M_W^2} \, . \tag{8.28}$$

Compared to the four-dimensional expression (9.11) a new combination of the vector and axial vertex factors appears:

$$C_3 = (a_\ell - v_\ell)^2 (a_q - v_q)^2 \, . \tag{8.29}$$

As it turns out, this combination appears also in the real-emission contribution and in the factorization subtraction discussed below, in such a way that the final result for the NLO correction only contains the combinations C_1 and C_2 given in (9.10). We furthermore note that the *spin-dependent* Born cross section in $4-2\varepsilon$ dimensions with an incoming polarized quark, $d\Delta\hat{\sigma}^{(0),\varepsilon}_{q\bar{q}'}/dv$, is the negative of $d\Delta\hat{\sigma}^{(0),\varepsilon}_{q\bar{q}'}/dv$ in (8.28), but with $C_3 = 0$. This violation at order $\mathcal{O}(\varepsilon)$ of the relations in (8.7) and hence of helicity conservation is typical of intermediate results in the HVBM scheme [232, 233].

Adding the real and virtual contributions, the double poles in ε cancel. We are left with single poles associated with collinear gluon emission. According to the factorization theorem, these may be absorbed into the parton distribution functions by a suitable subtraction which we perform in the $\overline{\mathrm{MS}}$ scheme. This introduces dependence on a factorization scale μ_F. In the upper row of Fig. 8.2, one of the two initial-state collinear situations for the $2 \to 3$ $q\bar{q}'$ channel is shown. Here, the variable x denotes the momentum fraction of the incoming quark after radiating a gluon. The required subtraction is of the form $\sim \frac{1}{\varepsilon} P_{qq} \otimes d\hat{\sigma}^{(0),\varepsilon}_{q\bar{q}'}$, where P_{qq} is a LO Altarelli-Parisi splitting function [48] and $d\hat{\sigma}^{(0),\varepsilon}_{q\bar{q}'}$ again the Born cross section for the process $q\bar{q}' \to \ell\nu_\ell$ computed in $4-2\varepsilon$ dimensions. More precisely, in case of the contribution shown in the upper part of Fig. 8.2, in the unpolarized case, we have to subtract the term

$$\frac{1}{vs} \frac{d\hat{\sigma}^{(1),\mathrm{fact}}_{q\bar{q}'}}{dv dw} = \int_0^1 dx \, \frac{d\hat{\sigma}^{(0),\varepsilon}_{q\bar{q}'}(xs, xt, u, \varepsilon)}{dv} H_{qq}(x, \mu_F^2) \; \delta(x(s+t)+u) \, , \tag{8.30}$$

where the $\overline{\mathrm{MS}}$ scheme is defined by

$$H_{qq}(x,\mu_F^2) = \left(-\frac{1}{\varepsilon} + \gamma_E - \log 4\pi\right)\left(\frac{\mu_F^2}{s}\right)^{-\varepsilon} P_{qq}(x)\ , \tag{8.31}$$

with γ_E the Euler constant and with

$$P_{qq}(x) = C_F\left[\frac{1+x^2}{(1-x)_+} + \frac{3}{2}\delta(1-x)\right]\ . \tag{8.32}$$

Standard $\overline{\mathrm{MS}}$ factorization requires the splitting function to be computed in four dimensions. After the collinear subtractions have been performed, we end up with the final NLO result in the $\overline{\mathrm{MS}}$ scheme.

If the incoming quark is polarized, the subtraction is similar, but with two crucial differences: First, one needs the spin-dependent Born cross section in $4-2\varepsilon$ dimensions, given as discussed above by the negative of the unpolarized one in (8.28) but with $C_3 = 0$. In addition, as discussed in Refs. [232, 233, 278], in order to correct for violation of helicity conservation in the HVBM scheme, one needs to use the splitting function

$$\Delta P_{qq}(x) = C_F\left[\frac{1+x^2}{(1-x)_+} + \frac{3}{2}\delta(1-x) + 4\varepsilon(1-x)\right] \tag{8.33}$$

in the factorization subtraction. With these differences taken into account, the final spin-dependent NLO partonic cross sections respect the relations in (8.7), as they should.

As already mentioned, in the case of an exchanged W or Z boson one does not encounter any final-state singularities. Effectively, the widths of the bosons act as regulators here. On the other hand, for an intermediate photon – which presents one of the backgrounds – a final-state singularity would occur if the leptons were massless, when the photon goes on its mass shell. Keeping a finite lepton mass is well beyond the scope of this work and is also not necessary since the pure-photon contribution is in any case rather small. Also, because of parity conservation, it is only present in the unpolarized cross section and not in the single-spin one. The artificial singularity that one encounters in this channel for massless leptons may be avoided for instance by imposing a cut on the invariant mass of the outgoing lepton pair [269], or it may be simply subtracted in, say, the $\overline{\mathrm{MS}}$ scheme. Effectively, the latter approach, which we adopt here, introduces a (QED) photon-to-lepton fragmentation function [281]. The diagrammatic situation for the final-state collinear splitting is shown in the lower row of Fig. 8.2. The subtraction to be performed is given by

$$\frac{1}{sv}\frac{d\hat{\sigma}_{q\bar{q}'}^{(1),\text{photon fact}}}{dvdw} = -\int_0^1 dx\, \frac{d\hat{\sigma}^{(0)}_{q\bar{q}\to\gamma g}(s,t/x,u/x,\varepsilon)}{dv}\; H_{\ell\gamma}(x,\mu_F^2)\;\delta\left(s+\frac{t+u}{x}\right), \tag{8.34}$$

where $d\hat{\sigma}_{q\bar{q}\to\gamma g}$ denotes the Born-level cross section for the process $q\bar{q}\to\gamma g$ in $d=4-2\varepsilon$ dimensions, and where

$$H_{\ell\gamma}(x,\mu_F^2) = \left(-\frac{1}{\varepsilon} + \gamma_E - \ln 4\pi\right)\ P_{\ell\gamma}(x)\left(\frac{s}{\mu_F^2}\right)^{\varepsilon}\ , \tag{8.35}$$

with $P_{\ell\gamma}(x)$ the appropriate $\gamma \to \ell$ splitting function. Including the thus defined subtraction renders the full NLO cross section finite. We stress again that the pure-photon contribution is small, except at large lepton rapidities. It can in fact be vetoed experimentally because it is characterized by two charged leptons that almost coalesce. We also note that the γZ interference contribution does not produce any final-state singularities even for massless leptons.

Finally, for qg scattering, there are no virtual corrections at $\mathcal{O}(\alpha_s)$. To obtain the finite cross section for these partonic channels, one therefore only needs the appropriate subtractions for the initial-state collinear singularities.

8.2.5 Final results

Our final analytical NLO expressions for the processes $q\bar{q}' \to \ell X$, $qg \to \ell X$ through W-boson exchange are presented in the Appendix F. We briefly summarize a few features of the result for the $q\bar{q}' \to \ell X$ channel. First of all, it contains the usual distributions in $(1-w)$, which dominate the cross section at $w \to 1$. These multiply the Born cross section:

$$\frac{d^2\hat{\sigma}^{(1)}_{q\bar{q}'}}{dvdw} \overset{w\to 1}{\approx} \frac{d\hat{\sigma}^{(0)}_{q\bar{q}'}}{dv} C_F \left[8 \left(\frac{\log(1-w)}{1-w} \right)_+ - \frac{4\,A(v)}{(1-w)_+} + B(v)\delta(1-w) \right] , \tag{8.36}$$

where the coefficients $A(v), B(v)$ may be found from Eq. (F.4) in the Appendix F. The terms with "plus" distributions represent the well-known threshold logarithms for the process that arise when the incoming partons have just sufficient energy to produce the observed final state, so that any substantial gluon radiation is kinematically inhibited.

The other terms in the NLO result have a more complicated structure. The integration of terms containing (8.20) gives rise to three different types of denominators. We write them by introducing the function

$$P(z) \equiv \frac{zs^2}{(zs - M_W^2)^2 + \Gamma_W^2 M_W^2} . \tag{8.37}$$

We then encounter the terms

$$P_i \equiv P(z_i) \qquad (i = 1, 2, 3) , \tag{8.38}$$

where

$$z_1 = 1 , \quad z_2 = w , \quad z_3 = \frac{1-v}{1-vw} . \tag{8.39}$$

Evidently, P_1 essentially just corresponds to the propagator in the Born cross section. The other two propagators are similar and reduce to P_1 in the limit $w \to 1$.

In addition to the new propagators arising at NLO, we also find several logarithms of the propagator

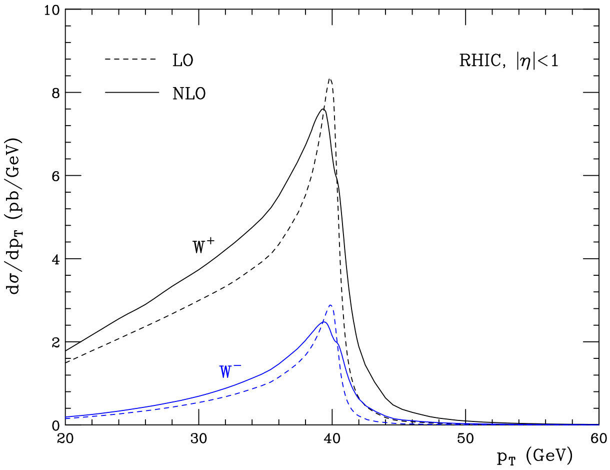

Figure 8.3: LO (dashed) and NLO (solid) cross sections at RHIC ($\sqrt{S} = 510$ GeV) for ℓ^+ and ℓ^--production through $W^\pm$ boson exchange.

terms. The logarithms that occur are

$$\begin{aligned}
&\log\left(\frac{(ws - M_W^2)^2 + \Gamma_W^2 M_W^2}{M_W^4 + \Gamma_W^2 M_W^2}\right) , \\
&\log\left(\frac{(\frac{1-v}{1-vw}s - M_W^2)^2 + \Gamma_W^2 M_W^2}{M_W^4 + \Gamma_W^2 M_W^2}\right) , \\
&\log\left(\frac{((1-v+vw)s - M_W^2)^2 + \Gamma_W^2 M_W^2}{M_W^4 + \Gamma_W^2 M_W^2}\right) . \qquad (8.40)
\end{aligned}$$

As seen in Eq. (F.1), they are accompanied by inverse tangent functions resulting from the imaginary parts of the arguments of the logarithms arising in phase space integration. All these terms are multiplied by simple functions of v and w and by one of the three types of propagators given above. The result for the channel $qg \to \ell X$ does not contain threshold distributions but does have logarithms of the type in Eq. (8.40); see the Appendix F for further details.

8.3 Phenomenological Results

We start with the unpolarized cross section for pp scattering at RHIC at $\sqrt{S} = 510$ GeV. Figure 8.3 shows our LO (dashed) and NLO (solid) results for the cross section $d\sigma/dp_T$ for ℓ^+ and ℓ^- production through intermediate W bosons. We have integrated over $|\eta| \leq 1$ in the charged lepton's rapidity. We have used the NLO parton distributions of [115] and the renormalization and factorization scales $\mu_R = \mu_F = p_T$. Our adopted values for the W mass and width are $M_W = 80.398$ GeV, $\Gamma_W = 2.141$ GeV

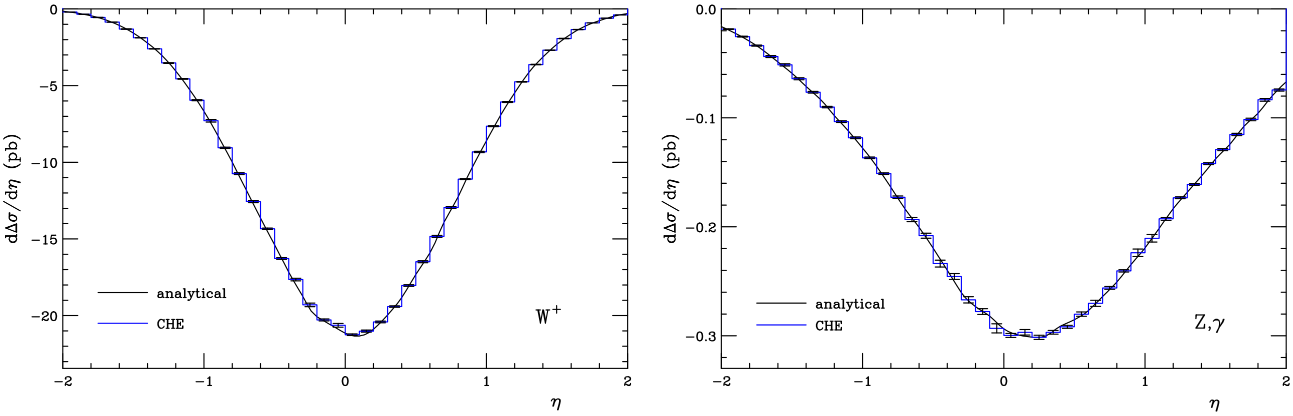

Figure 8.4: Comparison of our analytical results with the corresponding ones from CHE [269] for the polarized cross sections $\Delta\sigma$ for ℓ^+ production through W^+ decay (left) and through intermediate Z or γ. We have considered here pp collisions at $\sqrt{S} = 500$ GeV and have integrated over $20 \leq p_T \leq 60$ GeV. As in [269] the parton distributions have been chosen from Refs. [128, 129, 135].

(later we will also use $M_Z = 91.187$ GeV and $\Gamma_Z = 2.49$ GeV for the Z boson).

Clearly, the NLO corrections are significant everywhere. They have moderate size below and around the Jacobian peak at $p_T \approx M_W/2$ and become very large well above the peak. A close inspection of the results in Fig. 8.3 reveals a hint of a "shoulder" in the NLO cross sections just above $p_T = M_W/2$. This shoulder is a true feature of the NLO results. It comes about in two ways: First, the $q\bar{q}'$ channel itself has non-trivial structure here. Near $p_T = M_W/2$, there is a complicated interplay between positive contributions by terms with distributions in $(1-w)$ ("plus distributions" or δ-function) in Eq. (F.4), and contributions by subleading terms in $(1-w)$, among them the terms involving the functions J and K, which are negative around $p_T \sim M_W/2$ and become positive just below and above the Jacobian peak. This means that the $q\bar{q}'$ channel is sensitive to the exact mix of positive and negative contributions. Secondly, the qg process makes a negative contribution below and around $p_T = M_W/2$ and then becomes positive. This intricate interplay of the various contributions is also the reason why the height of the peak is reduced at NLO as compared to LO. We note that for increasing energy $\sqrt{S}$ the shoulder becomes even more pronounced and in fact quickly turns into a double-peaked structure at NLO; see also [282]. This at first sight surprising feature is a manifestation of the well-established fact [283] that the region around the Jacobian peak cannot be controlled within a fixed-order calculation. Among other things, it is sensitive to small transverse momenta q_T of the intermediate W boson. There are large double-logarithmic corrections to the q_T-distribution of W bosons at low q_T, which need to be taken into account to all orders if one wants to address this region [284]. Such a resummation is incorporated in the RHICBOS code [268]. These issues become relevant for precision determinations of the mass of the W boson from the lepton's p_T spectrum near the Jacobian peak [285]. For RHIC, they are not really relevant since, if one is interested in determining polarized parton distributions, there is no need to focus on the region around the Jacobian peak. Rather, it is advisable to integrate over a sizable range in p_T, so that the Jacobian peak region constitutes only a rather small part of the cross section, and to study the distribution of the charged lepton in rapidity. This is the strategy adopted by the RHIC experiments. We will therefore consider only lepton rapidity distributions in the remainder of this paper. See Chapter 9 for further details.

In order to check the validity of our analytical results and their numerical evaluation, we have performed extensive comparisons to high-statistics runs of the NLO code CHE presented in Ref. [269], both for the unpolarized and for the polarized case. We have found excellent agreement. A representative example is given in Fig. 8.4, where we show the spin-dependent cross sections for ℓ^+ production at RHIC, through W^+ boson exchange (left) and for the background channels, Z-boson exchange and γZ interference (right; the pure-photon channel does not contribute to the spin-dependent cross section). Both our analytical (solid lines) and the CHE results (histograms) are shown. We have followed [269] to use the polarized parton distributions of [128, 129] (referred to as DSSV08) and the unpolarized ones of [135] which were also the baseline set in the DSSV08 global analysis. Furthermore, the figure is for $\sqrt{S} = 500$ GeV, and the transverse momentum of the observed charged lepton has been integrated over the range of $20 < p_T < 60$ GeV. As in [269] we have chosen the renormalization and factorization scales as $\mu_R = \mu_F \equiv \mu = \sqrt{p_T^2 + M_W^2}/2$ and assumed $n_f = 4$ active quark flavors. In Fig. 8.4 the error bars of the results shown for CHE correspond to numerical integration uncertainties. The uncertainties in our new numerical calculation are smaller than the widths of the lines. Since our results are largely analytical whereas the code of [269] is based on a standard Monte-Carlo integration with numerical cancelation of singularities, our new code produces the results shown in about two orders of magnitude less time. Of course, Monte-Carlo based codes are more flexible in general, allowing the implementation of various additional kinematical cuts and observables if necessary.

We now turn to the spin asymmetries A_L which are the quantities of primary interest in RHIC's W physics program. Figure 8.5 shows our NLO results at $\sqrt{S} = 510$ GeV as functions of η. The cross sections have been integrated over $p_T \geq 30$ GeV, as appropriate for comparison to the Phenix data [258, 259]. We have now used the new set of polarized parton distributions of Ref. [263] (referred to as DSSV14). This set primarily contains updated information on the nucleon's spin-dependent gluon distribution, which is less relevant for weak boson production. However, it is also based on new results from inclusive and semi-inclusive lepton scattering [124], so that it offers new information on the quark and antiquark helicity distributions as well. We use the unpolarized parton distributions of [115]. The solid lines in the figure show our results for charged-lepton production via W decay for the scale choice $\mu = M_W/2$, while the dotted and dot-dashed lines correspond to the choices $\mu = p_T$ and $\mu = M_W$, respectively. One can see that the scale dependence of the asymmetries is extremely weak, which is one of the reasons why W boson production at RHIC is an excellent and theoretically well-controlled probe of nucleon spin structure. In Fig. 8.5 we also investigate the impact of the "background" presented by Z and γ exchange. The dashed lines show the NLO results for the scale $\mu = M_W/2$, now including the Z and photon contributions. As is known from previous studies [268, 269], the background channels dilute the spin asymmetries somewhat, which is mostly due to the increase of the unpolarized cross section in the denominator of the asymmetry. We note that the STAR experiment at RHIC is able to identify and subtract this background, using data as well as Monte-Carlo estimates, so that the data can be directly compared to calculations based on only intermediate W bosons. For comparisons to Phenix data, the Z/γ background needs to be included. Figure 8.5 also shows the spin asymmetries for Z and γ exchange alone, in this case integrated over $25 < p_T < 50$ GeV corresponding to conditions

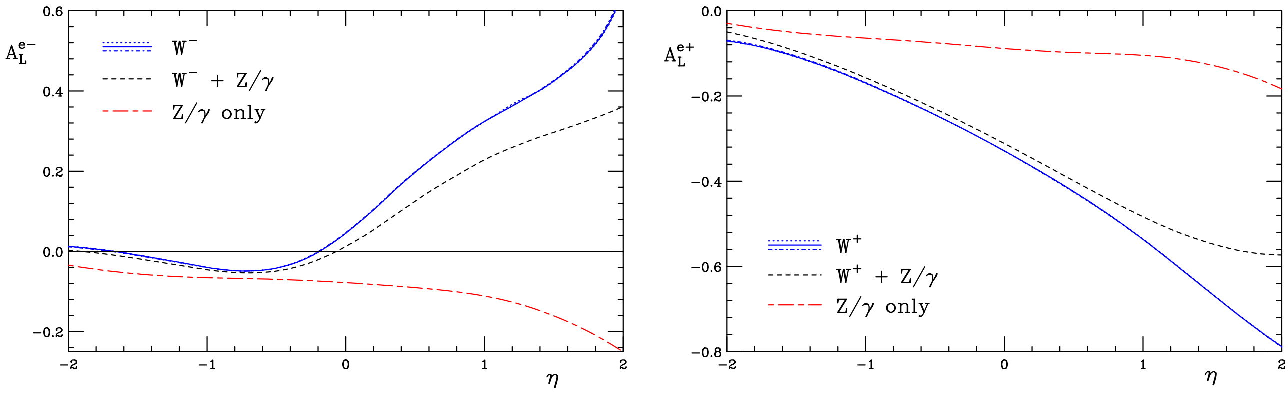

Figure 8.5: Single-spin asymmetries $A_L^{\ell\pm}$ for negatively (left) and positively (right) charged leptons as functions of rapidity at $\sqrt{S} = 510$ GeV. We have integrated over the range $p_T \geq 30$ GeV. The solid lines show the results when the lepton originates exclusively from W bosons, at scale $\mu = M_W/2$. The dotted and dot-dashed lines correspond to the scale choices $\mu = p_T$ and $\mu = M_W$, respectively (note that the lines for the various scales are almost indistinguishable). For the dashed lines the background from exchanged Z bosons and photons has been included, using the scale $\mu = M_W/2$. Finally, the long-dashed lines show the spin asymmetries for Z bosons and photons alone, without the W-boson contributions, this time for $25 < p_T < 50$ GeV. We have used the DSSV14 polarized parton distributions [128, 129] and the unpolarized ones of [115].

in STAR [257].

Using our new NLO code, we finally compare in Fig. 8.6 the results for various sets of spin-dependent parton distributions to the published STAR data [257] for A_L^W taken at $\sqrt{S} = 510$ GeV. The data have been presented for various η, sampled over the range $25 < p_T < 50$ GeV of lepton transverse momenta. In view of the results shown in Fig. 8.5 the scale choice hardly matters; we use $\mu_R = \mu_F = M_W/2$. The sets of spin-dependent parton distributions we use are from [128, 129, 263] (DSSV08 and DSSV14), from [271] (NNPDFpol1.1), as well as the “statistical” parton distributions of [286, 287] and a much earlier set [288] known as the “GRSV valence scenario”. From the figure we draw the following observations:

- all sets describe the W^+ asymmetry data rather well. The main reason for this is that the spin asymmetry is largely driven by the polarized up quark distribution which is relatively well constrained by DIS data and hence similar in all sets.
- among the various sets, NNPDFpol1.1 is the only one for which the STAR data were already included in the analysis, constraining the light sea quark helicity distributions. As a result, the data are quite well described by the set, especially when one includes the corresponding uncertainty estimates [271] that we do not show here. Note, however, that information from semi-inclusive lepton scattering is not included in the NNPDFpol1.1 set.
- at $\eta \leq 0$, the two DSSV sets show W^- asymmetries that are below the data. Since the DSSV14

set contains the latest information available from (semi-inclusive) DIS, this hints at the interesting possibility of a tension between the DIS and RHIC data, the latter favoring a larger $\Delta\bar{u}$ distribution (see also the discussion in [271]). It has to be emphasized, however, that we do not display here any uncertainties for the DSSV set; as shown in [128, 129, 257], the main DSSV08 uncertainty band is such that it just about touches the lower end of the error bars of the data points. In this sense, it is premature to draw any conclusions regarding such a tension. Clearly, it will be interesting to follow up on this issue in the context of a new global analysis, especially when additional experimental information becomes available.

- in the framework of the statistical parton distributions, the helicity distributions are obtained along with the unpolarized ones and depend on only very few parameters to be determined from data. As one can see from Fig. 8.6 (and as discussed in [287]), the model describes the RHIC data quite well.

- the GRSV valence scenario of [288] describes the W^- asymmetry data strikingly well. The main distinctive features for this set are assumptions about the breaking of SU(3) in the relations between nucleon spin structure and hyperon β-decays, and the ansatz [289]

$$\frac{\Delta\bar{d}(x,Q_0^2)}{\Delta\bar{u}(x,Q_0^2)} = \frac{\Delta u(x,Q_0^2)}{\Delta d(x,Q_0^2)} \tag{8.41}$$

  at a low initial scale Q_0. Since Δu and Δd are known to have opposite sign, the latter ansatz forces the ratio $\Delta\bar{d}/\Delta\bar{u}$ to be negative. This requirement, along with the condition $\Delta\bar{u}+\Delta\bar{d}<0$ imposed by the DIS data and the assumptions about SU(3)-breaking, is realized in this model by a fairly large positive $\Delta\bar{u}$ distribution and a negative (and even larger in absolute value) $\Delta\bar{d}$ one. Evidently, the STAR data prefer such a sizable positive $\Delta\bar{u}$. We note that one of the sets of Ref. [290] has a similar $\Delta\bar{u}$ distribution and hence describes the W^- asymmetry data similarly well [269]. It will be interesting to see whether also the large negative $\Delta\bar{d}$ of [288] is realized; unfortunately, the $\Delta\bar{d}$ contribution to the W^+ asymmetry is typically overwhelmed by the Δu one. Note that a negative $\Delta\bar{d}$ pulls the W^+ asymmetry to more negative values (see (8.4) in the introduction), which may explain why the GRSV valence scenario shows the most negative asymmetry of all the sets at $\eta \leq 0$. Needless to say that the GRSV valence scenario has not been confronted with the latest (semi-inclusive) DIS data.

8.4 Conclusions

We have presented a new analytical NLO calculation of the partonic cross sections for single-inclusive lepton production at RHIC, when the lepton originates from the decay of an intermediate electroweak boson, especially a W boson. Our numerical code based on analytical phase space integration is much faster than existing Monte-Carlo integration based codes. In this way, we hope that our code will be a valuable tool for future global analyses of the proton's helicity parton distributions that include the new high-precision data for A_L^W asymmetries obtained at RHIC. Our results may also be useful to obtain insights into the analytical structure of the partonic cross sections, for example in terms of their threshold logarithms or their behavior in the vicinity of the Jacobian peak.

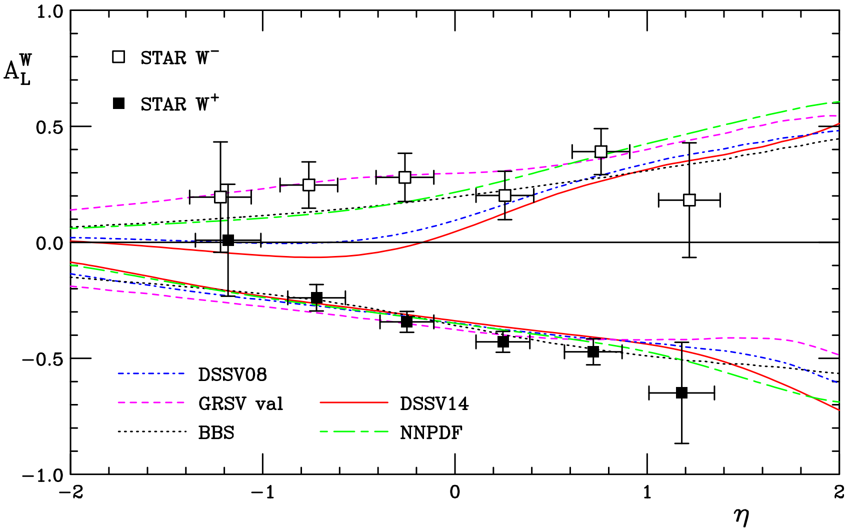

Figure 8.6: Comparisons of NLO results for $A_L^{W^\pm}$ for various sets of helicity parton distributions [128, 129, 263, 271, 286, 288] to the STAR data [257] taken at $\sqrt{S} = 510$ GeV. The cut $25 < p_T < 50$ GeV has been applied on the lepton's transverse momentum. We have chosen the scales $\mu_R = \mu_F = M_W/2$.

We have also presented new comparisons of the latest RHIC data with the NLO predictions for some of the sets of polarized parton distributions available in the literature. In line with observations in the earlier literature we have found that the data prefer a rather sizable positive $\Delta\bar{u}$ helicity distribution in the proton.

CHAPTER 9

HIGHER ORDER QCD EFFECTS FOR HADRONIC *W* PRODUCTION IN THE REGION OF THE JACOBIAN PEAK

We consider the single-inclusive processes $pp \to \ell^{\pm} X$ and $\bar{p}p \to \ell^{\pm} X$ at next-to-leading order in QCD, where the produced charged lepton has a large transverse momentum and results from the decay of a $W^{\pm}$ boson. We continue to analyze the structure of our analytical results presented in Chapter 8. These results shed light on the general role and size of higher-order corrections, especially near the Jacobian peak, where they are relevant for precision determinations of the W boson mass. We find that the next-to-leading order corrections actually produce a double-peak structure in the transverse-momentum spectrum which is usually not resolved in Monte-Carlo treatments of the cross section. This Chapter is based on publication [ix].

9.1 Introduction

The production of W bosons in hadronic collisions plays an important role at past and present-day collider experiments like the Tevatron, RHIC and the LHC, where very high rates of events involving W bosons can be achieved. For example, in pp collisions at RHIC, 1.3×10^6 W bosons are expected to be produced for an integrated luminosity of 800 pb^{-1} and a center-of-mass energy of $\sqrt{S} = 510$ GeV. High precision measurements of the W boson mass M_W and width Γ_W provide a key test of the standard model. The dominant production process in $p\bar{p}$ collisions at $\sqrt{S} = 1.96$ TeV at the Fermilab Tevatron collider is $q\bar{q}' \to W + X$, where X denotes additional unobserved final-state particles that have to be summed over. We consider the channel, where the W boson decays into a charged lepton and a neutrino $W \to \ell\nu_\ell$, where $\ell = e, \mu$.

The invariant mass squared of a W boson cannot be reconstructed directly at hadron colliders because the longitudinal momentum of the decay neutrino remains undetermined. This situation is in contrast to the decay of Z boson, where its mass can be measured directly due to the resonance in the cross section $d\sigma/dM_{\mu^+\mu^-}$. The extraction of M_W is based on the analysis of Jacobian peaks in transverse momentum distributions on the lepton-level. Three different cross sections are used, namely $d\sigma/dp_T^\ell$, $d\sigma/dp_T^\nu$ and $d\sigma/dm_T$. Where p_T^ℓ (p_T^ν) denotes the momentum of the observed charged lepton ℓ (neutrino ν_ℓ) in the plane transverse to the beam axis. The neutrino p_T^ν distribution is determined by measuring the missing transverse momentum $\not{E}_T$ of an event. The third cross section is differential in the transverse mass of the lepton pair which is defined by $m_T \equiv (2p_T^\ell p_T^\nu - 2\vec{p}_T^{\,\ell} \cdot \vec{p}_T^{\,\nu})^{1/2}$. However, in this work we will limit ourselves to the cross section differential in the transverse momentum of the charged lepton p_T^ℓ, which is more sensitive to higher order corrections than the cross section differential in m_T [283].

The standard model predicts a relationship between the W boson mass and the Higgs mass M_H. In combination with several other electroweak parameters like the mass of the top quark m_t constraints on physics beyond the standard model may be obtained. The limiting factor are the uncertainties of the M_W mass. Therefore, it is of great interest for the physics at the LHC to have a solid understanding of higher order effects of perturbative QCD which determine the shape of the Jacobian peak. So far, the current world average is $M_W = 80.385 \pm 0.015$ GeV, see [291, 292].

In this Chapter, we present a calculation at NLO in QCD for the p_T distribution of the detected lepton where we perform the phase space integration analytically. It is well known that large logarithmic contributions appear at higher orders in QCD. Existing purely numerical results at NLO can be found in [268–270]. In addition, the Monte-Carlo package ResBos of [268, 293] takes into accout large logarithms in the transverse momentum q_T of the W boson using the CSS resummation formalism [294]. The leptonic p_T spectrum is deduced afterwards by attaching an appropriate decay channel. Having calculated the leptonic p_T cross section analytically at NLO, we can identify various types of logarithms that are especially important in the peak region. For example, we find the expected threshold logarithms, which become large when the phase space for real-gluon radiation shrinks and all the incoming energy is used to produce the observed charged lepton. However, we find several other types of logarithms as well, which are equally relevant in the peak region. The interplay of all logarithms determines the characteristic shape of the Jacobian peak at NLO, see also [272].

The calculation presented in this Chapter can also be applied to physics at RHIC, where longitudinal single spin asymmetries are measured for W boson production in $p\vec{p}$ collisions. The asymmetry is generated by the parity violating vertex structure of the W. Given the the fact that the detectors are not hermetic, a theoretical calculation of the asymmetries is crucial for the extraction of helicity dependent parton distribution functions.

Section 9.2, presents our calculation at NLO. In section 9.4, we discuss a possible approach in order to resum large logarithmic contributions in the p_T cross section using the narrow width approximation. Our phenomenological results are presented in section 9.3.

9.2 Next-to-leading order calculation

9.2.1 Basics of the NLO calculation

We consider the single-inclusive process $pp \to \ell + X$, where ℓ denotes the charged lepton (or anti-lepton) resulting from W decay. Denoting the momenta of the incoming protons and the produced charged lepton by P_A, P_B, p_ℓ, respectively, we write the hadronic cross section in factorized form:

$$d\sigma = \sum_{a,b} \int dx_a dx_b \, f_a(x_a, \mu_F^2) \, f_b(x_b, \mu_F^2) \, d\hat{\sigma}_{ab}(x_a P_A, x_b P_B, p_\ell, \mu_R^2, \mu_F^2) \; . \tag{9.1}$$

The functions $f(x, \mu_F^2)$ are the parton distributions for the incoming protons, where x is the parton's momentum fraction of the momentum of the parent hadron, and μ_F the factorization scale. The partonic hard-scattering cross sections $d\hat{\sigma}_{ab}$ which also depend on the renormalization scale μ_R, may be calculated in perturbation theory as series in the strong coupling constant α_s. The leading-order (LO) partonic process is $q\bar{q}' \to W$. The corresponding Feynman diagram is shown in Fig. 8.1(a). At NLO, there are $\mathcal{O}(\alpha_s)$ corrections to the Born process as well as the additional $qg \to Wq'$ channel. The relevant diagrams are displayed in Fig. 8.1(b)-(d), where we have omitted crossed diagrams.

We now introduce the variables

$$S \equiv (P_A + P_B)^2 \, , \;\; T \equiv (P_A - p_\ell)^2 \, , \;\; U \equiv (P_B - p_\ell)^2 \; , \tag{9.2}$$

and

$$V \equiv 1 + \frac{T}{S}, \;\; W \equiv \frac{-U}{S+T} \; . \tag{9.3}$$

The lepton's transverse momentum p_T and rapidity η are related to these variables by

$$V = 1 - \frac{p_T}{\sqrt{S}} \mathrm{e}^{-\eta} \, , \;\; VW = \frac{p_T}{\sqrt{S}} \mathrm{e}^{\eta} \; . \tag{9.4}$$

We may now write the differential hadronic cross section explicitly at NLO as

$$\begin{aligned} \frac{d^2\sigma}{dp_T^2 d\eta} \;\; = \;\; & \frac{1}{p_T^2} \sum_{a,b} \int_{VW}^{V} dv \int_{VW/v}^{1} dw \, x_a f_a(x_a, \mu_F^2) \, x_b f_b(x_b, \mu_F^2) \left[\frac{d\hat{\sigma}_{ab}^{(0)}(s,v)}{dv} \delta(1-w) \right. \\ & \left. + \frac{\alpha_s(\mu_R^2)}{2\pi} \frac{d\hat{\sigma}_{ab}^{(1)}(s,v,w,\mu_F^2,\mu_R^2)}{dv dw} \right] , \end{aligned} \tag{9.5}$$

where

$$x_a = \frac{VW}{vw} \, , \;\; x_b = \frac{1-V}{1-v} \, , \tag{9.6}$$

and we have furthermore defined

$$\begin{aligned} & v \equiv 1 + \frac{t}{s} \, , \quad w \equiv \frac{-u}{s+t} \, , \\ & s \equiv (p_a + p_b)^2 = x_a x_b S \, , \quad t \equiv (p_a - p_\ell)^2 = x_a T \, , \quad u \equiv (p_b - p_\ell)^2 = x_b U \; . \end{aligned} \tag{9.7}$$

We have used $p_a = x_a P_A$, $p_b = x_b P_B$ for the partonic momenta.

Throughout this Chapter we work with a general (axial) vector structure for the $Wq\bar{q}'$-vertex of the form

$$V_q^\mu = -i \frac{g_W}{2\sqrt{2}} U_{qq'} \gamma^\mu (v_q - a_q \gamma_5) , \tag{9.8}$$

where $U_{qq'}$ is the appropriate CKM matrix element and g_W the fundamental weak charge. Likewise, we use a similar expression for the $W\ell\nu_\ell$-vertex, with vector and axial coefficients v_ℓ and a_ℓ (and, of course, with $U_{qq'} = 1$). Using such general vertices will help us to keep better track of the couplings in the NLO calculation and to obtain an understanding of the underlying structure.

9.2.2 Born level cross section and the Jacobian peak

The lowest-order contribution to the cross section comes from the $2 \to 2$ scattering process $q\bar{q}' \to \ell\nu_\ell$. The diagram is shown in Fig. 8.1(a). As before, we use "ℓ" for the observed charged lepton, regardless of its charge. We shall see below that it is possible to formulate a partonic cross section in this generic way, despite the fact that the "lepton" can be either a particle or an anti-particle. We also always refer to the corresponding neutrino or anti-neutrino as the "neutrino" and denote it by ν_ℓ. Since it remains unobserved, we integrate over its phase space. This leads to an overall factor $\delta(1-w)$ for the Born cross section, so that

$$\frac{d^2\hat{\sigma}^{(0)}}{dv dw} = \frac{d\hat{\sigma}^{(0)}}{dv} \delta(1-w) , \tag{9.9}$$

as we have anticipated in (9.5). Using the general vertex structure given in Eq. (9.8), we find that two combinations of the couplings appear in the expression for the cross section, which are given by

$$\begin{aligned} C_1 &= (v_q^2 + a_q^2)(a_\ell^2 + v_\ell^2) + 4\, a_q a_\ell v_q v_\ell , \\ C_2 &= (v_q^2 + a_q^2)(a_\ell^2 + v_\ell^2) - 4\, a_q a_\ell v_q v_\ell . \end{aligned} \tag{9.10}$$

We recall that in case of an exchanged $W^\pm$ boson, we have $v_q = a_q = v_\ell = a_\ell = 1$ and hence always $C_1 = 8$ and $C_2 = 0$. However, it is useful to keep C_2 in the calculation as it allows us to easily switch between W^- and W^+ production. The reason for this becomes clear when we write down the Born cross section:

$$\frac{d\hat{\sigma}^{(0)}}{dv} = \frac{|U_{qq'}|^2 s}{8\pi N_c} \left(\frac{G_F M_W^2}{\sqrt{2}} \right)^2 \frac{C_1(1-v)^2 + C_2 v^2}{(s-M_W^2)^2 + \Gamma_W^2 M_W^2} , \tag{9.11}$$

where $N_c = 3$, G_F is the Fermi constant, $G_F = \sqrt{2} g_W^2/(8M_W^2)$, and M_W and Γ_W are the W boson mass and decay width. Let us consider now the partonic channel $u\bar{d} \to e^+\nu_e$. For this indeed Eq. (9.11) provides the correct cross section when $C_1 = 8$ and $C_2 = 0$. In this way the cross section is proportional to $(1-v)^2$, as required by the $V-A$ structure of the interaction and angular momentum conservation. For $d\bar{u} \to e^-\bar{\nu}_e$, on the other hand, the cross section has to be proportional to v^2, rather than $(1-v)^2$. This is immediately realized by interchanging C_1 and C_2 in Eq. (9.11), and subsequently setting again $C_1 = 8$ and $C_2 = 0$. Equivalently, and even more simply, we can just choose in (9.11) $C_1 = 8, C_2 = 0$ for $u\bar{d} \to e^+\nu_e$ and $C_1 = 0, C_2 = 8$ for $d\bar{u} \to e^-\bar{\nu}_e$ to obtain the correct cross sections. We note that the cross sections for the reactions $\bar{d}u \to e^+\nu_e$ and $\bar{u}d \to e^-\bar{\nu}_e$ can be obtained by simple "crossing"

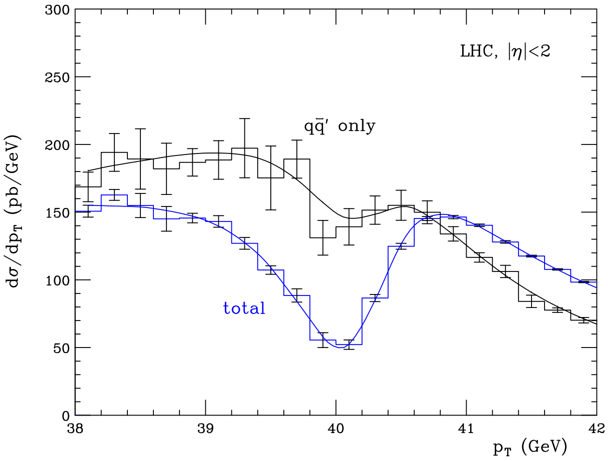

Figure 9.1: Comparison of our NLO analytical results (solid lines) with the results of the Monte-Carlo integration code of [269] (histograms) for ℓ^+ production through an intermediate W^+ boson at the LHC ($\sqrt{S} = 7$ TeV). We have integrated over $|\eta| < 2$. The upper histogram shows the result for the $q\bar{q}'$ channel only, while the lower one shows the full result including the qg contribution. The error bars correspond to this for the code of [269]; the uncertainties in our new numerical calculation are smaller than the width of the lines.

$t \leftrightarrow u$, or $v \leftrightarrow 1 - v$. Again this may also be achieved by $C_1 \leftrightarrow C_2$. All these considerations also hold at NLO, where the cross section still depends only on the two combinations C_1 and C_2.

The NLO cross section in Eq. (9.5) may also be written as

$$\begin{aligned}\frac{d^2\sigma}{dp_T^2 d\eta} &= \frac{1}{p_T^2} \sum_{a,b} \int_{4p_T^2/S}^{1} d\hat{x}_T^2 \int_{\hat{x}_T^2}^{1} \frac{dw}{4w\sqrt{1-\hat{x}_T^2/w}}\, x_a f_a(x_a,\mu_F^2)\, x_b f_b(x_b,\mu_F^2) \left[\frac{d\hat{\sigma}_{ab}^{(0)}}{dv}\delta(1-w)\right.\\ &\left. + \frac{\alpha_s(\mu_R^2)}{2\pi}\frac{d\hat{\sigma}_{ab}^{(1)}}{dv\,dw}\right], \qquad (9.12)\end{aligned}$$

where we have omitted the arguments of the cross section for simplicity, and where we have defined

$$\hat{x}_T^2 \equiv \frac{4p_T^2}{s} = 4vw(1-v)\ . \qquad (9.13)$$

In the form (9.12), the cross section exhibits the well-known *Jacobian peak* in the transverse-momentum distribution. In LO, using the factor $\delta(1-w)$, we obtain

$$\frac{d\hat{\sigma}_{q\bar{q}'}^{(0)}}{dp_T^2} \propto \frac{1}{\sqrt{1-\frac{4p_T^2}{s}}}\, \frac{s^2}{(s-M_W^2)^2 + \Gamma_W^2 M_W^2}\ . \qquad (9.14)$$

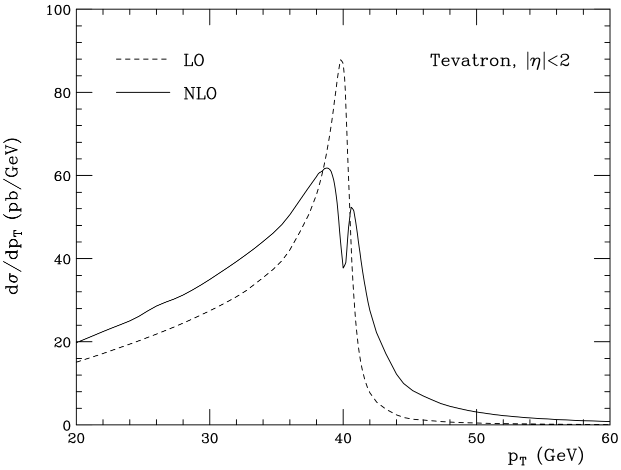

Figure 9.2: LO (dashed) and NLO (solid) cross sections for ℓ^+ production through W boson exchange in $p\bar{p}$ collisions at $\sqrt{S} = 1.96$ TeV.

Since the width of the W boson is much smaller than its mass, the Breit-Wigner distribution is very narrowly peaked around $s = M_W^2$. As a result, the square root factor produces an (integrable) divergence at $p_T = \sqrt{s}/2 \approx M_W/2$. In the limit $\Gamma_W \to 0$ (narrow-width approximation), this singularity is exactly at $p_T = M_W/2$, since in this case we may write

$$\frac{1}{(s - M_W^2)^2 + \Gamma_W^2 M_W^2} \to \frac{\pi}{\Gamma_W M_W}\, \delta(s - M_W^2) \; . \tag{9.15}$$

The Jacobian peak would then become directly visible in the lepton's transverse-momentum spectrum. For finite Γ_W, the convolution with the parton distribution functions smears out the singularity, leaving behind a finite, but narrow, peak near $p_T = M_W/2 \approx 40$ GeV. This will be shown also in our phenomenological results below. The exact shape of the Jacobian peak is very sensitive to the width Γ_W as well as to QCD and even electroweak corrections.

9.3 Phenomenological Results

In order to check the validity of our analytical results and their numerical evaluation, we have performed extensive comparisons to high-statistics runs of the NLO code presented in [269]. We have found excellent agreement in each case. A representative example is shown in Fig. 9.1, where we show the comparison for the case of ℓ^+ production in pp-collisions at LHC, $\sqrt{S} = 7$ TeV, in the vicinity of the Jacobian peak. We have used the parton distributions of [115] for both codes, and the renormalization and factorization scales $\mu_R = \mu_F = p_T$, and we have adopted the values $M_W = 80.398$ GeV, $\Gamma_W = 2.141$ GeV for the W mass and width. As one can see, the agreement of the two calculations is excellent. Since our results are largely analytical whereas the code of [269] is based on a standard Monte-Carlo integration with numerical cancelation of singularities, our new code produces the result shown in

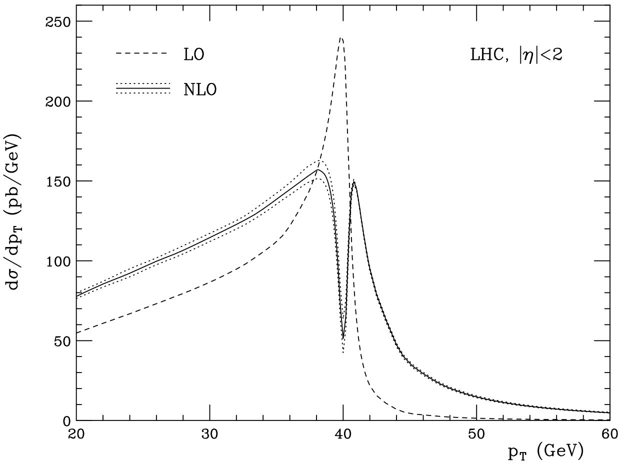

Figure 9.3: LO (dashed) and NLO (solid) cross sections for ℓ^+ production through W boson exchange in pp collisions at $\sqrt{S} = 7$ TeV. The dotted lines show the NLO for factorization and renormalization scales $p_T/2$ (lower) and M_W (upper).

about two orders of magnitude less time. We will comment below on the features of the cross section seen in the figure.

We now present a few phenomenological applications of our results for pp scattering the LHC ($\sqrt{S} = 7$ TeV) and $p\bar{p}$ scattering at the Tevatron ($\sqrt{S} = 1.96$ TeV). We use the NLO MSTW parton distributions from [115]. Again, we choose the renormalization and factorization scales as $\mu_R = \mu_F = p_T$. Figure 8.3 in Chapter 8 shows our LO (dashed) and NLO (solid) results for the cross section $d\sigma/dp_T$ for ℓ^+ and ℓ^- production at RHIC. We have integrated the lepton's rapidity over $|\eta| \leq 1$. One notices that the NLO corrections are significant everywhere. The have moderate size below and around the peak and become very large well above the peak.

In Figs. 9.2 and 9.3 we present our results for ℓ^+ production in $p\bar{p}$ collisions at the Tevatron and in pp scattering at the LHC. For the LHC, we also show NLO results for renormalization and factorization scales $\mu_R = \mu_F = p_T/2$ and M_W which demonstrate that the scale dependence is very weak (other scales such as $2p_T$ or $\sqrt{p_T^2 + M_W^2/4}$ give a cross section even closer to the one for our default scale choice). One notices a striking "double-peak" structure near $p_T = M_W/2$, which becomes even more pronounced as one moves up in energy from Tevatron to the LHC. In fact, a close inspection of the results for RHIC shown in Fig. 8.3 reveals a hint of a double-peak structure also there. We found the reason for the double-peak structure to be twofold. First, the $q\bar{q}'$ channel by itself produces at least a "shoulder" in addition to the usual peak, as may be seen from the upper curve/histogram in Fig. 9.1. How this happens is explained by Fig. 9.4: Near $p_T = M_W/2$, two types of terms in Eq. (F.4) contribute significantly. The terms with distributions in w ("plus distributions" or δ-function) make a sizable *positive* contribution, whereas the terms involving the functions J and K are large and *negative*

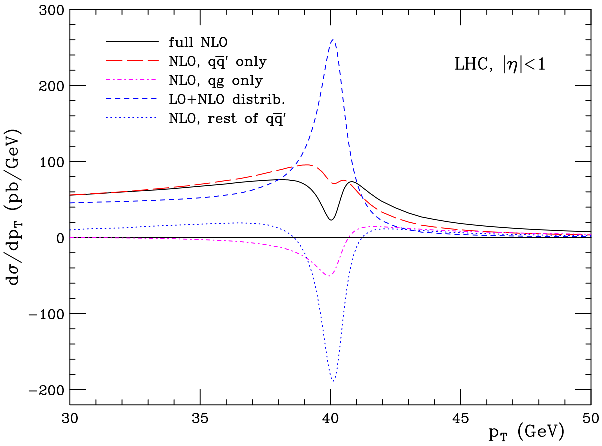

Figure 9.4: Full NLO result (solid) at LHC energy for $|\eta| < 1$ and its decomposition into $q\bar{q}'$ (long-dashed) and qg (dot-dashed) contributions. For the dashed and dotted lines we further break up the $q\bar{q}'$ piece into the distributtion terms (which include the LO term) and the remaining ones.

below $p_T \sim M_W/2$ and then change sign and become positive above. The remaining terms are fairly unimportant. The dashed line in the figure displays the distributional terms (including the LO piece), while the dotted line represents the other NLO terms on the $q\bar{q}'$ channel. The two contributions together give the full $q\bar{q}'$ result at NLO, which is shown by the long-dashed line. One clearly notices the strong cancelations that occur. This means that the $q\bar{q}'$ channel becomes very sensitive to the exact mix of positive and negative contributions, which changes with energy. Secondly, also the qg process makes a negative contribution below and around $p_T = M_W/2$ and then becomes positive, as also shown in the figure. It therefore helps to make the double-peak structure more pronounced, again more so at higher energies where qg scattering becomes more prevalent. The intricate interplay of the various contributions is also the reason why the height of the peak is much reduced at NLO as compared to LO (see Fig. 9.3). Figure 9.5 finally shows how the double peak structure at the LHC varies with rapidity.

These features of the cross section occur of course in a region around $p_T = M_W/2$ whose width is set by $\Gamma_W \sim 2.5$ GeV. This means that the two peaks are rather close together, which explains why they are often not resolved in the NLO studies based on completely numerical evaluations of the cross section (see, however, [282]).

9.4 Discussion and Further Numerical Studies

Given the large size of the corrections in the Jacobian peak region, a NLO calculation cannot be adequate here. Indeed, there has been extensive work on all-order resummations [268, 268] of the cross section. The NLO result yields the usual distributions that become large in the threshold limit $w \to 1$, *c.f.* Eq. (8.36). Usual large-x_T threshold resummation, with $x_T = 2p_T/\sqrt{s}$, would resum logarithms

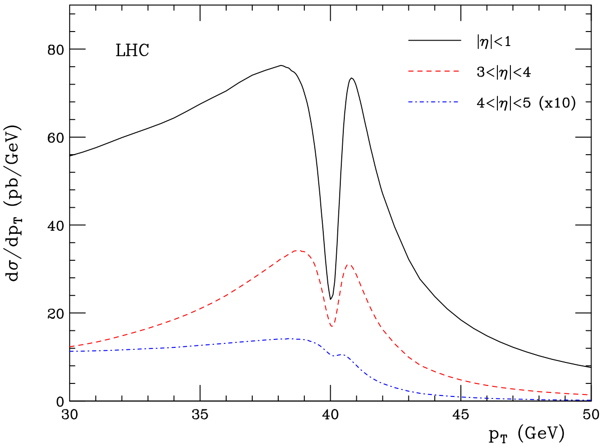

Figure 9.5: Same as Fig. 9.3, but for three different ranges in the lepton's rapidity η. Note that the cross section for $4 \leq |\eta| \leq 5$ has been multiplied by 10 for better visibility.

associated with soft-gluon emission, for $w \to 1$, see [215]. However, we find different kinds of logarithms as well, see Eq. (8.40), which become large in the region of the Jacobian peak around $p_T \sim M_W/2$. The width Γ_W regularizes those logarithms in the sense that they remain finite when the term $(xs - M_W^2)$, see Eq. (8.40), vanishes, which appears in the arguments of $L_{1,2,3}$. It is yet unclear how the behavior around $p_T \sim M_W/2$ connects to the usual threshold limit.

A possible approach is the narrow width approximation. Since the width of the W boson is much smaller than its mass $M_W \gg \Gamma_W$, the denominators P_2 and P_3 given in Eq. (8.38), essentially act as delta functions, setting $s \to M_W^2$. For example, in the case of the denominator P_2, we can make the following approximation

$$\frac{1}{(ws - M_W^2)^2 + g^2} \approx \frac{\pi}{g} \delta(ws - M_W^2). \tag{9.16}$$

With the help of these new delta function, we may perform the w integration in order to end up with a cross section that is differential in p_T only. At the partonic level, we find the following structure

$$\frac{d\hat{\sigma}}{d\hat{p}_T} \sim \frac{1}{\sqrt{1 - \hat{x}_T^2}} \left(a \log^2(1 - \hat{x}_T^2) + b \log(1 - \hat{x}_T^2) + \ldots \right) \tag{9.17}$$

with some coefficients a and b and we have $\hat{x}_T = 2\hat{p}_T/M_W$. The dots in Eq. (9.17) represent additional subleading terms in the large-$\hat{x}_T$ region. In this approximation, we find that all types of logarithmic contributions to the cross section at NLO are equally important in the peak region around $p_T \sim M_W/2$. However, after summing up all logarithmic terms at NLO, using the narrow width approximation, we find that the leading logarithms cancel out, *i.e.* we have $a = 0$.

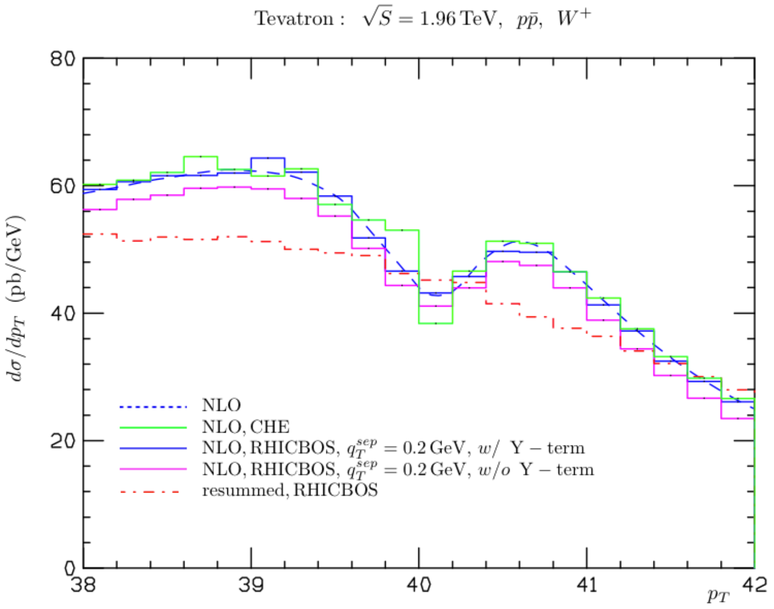

Figure 9.6: Cross sections differential in the lepton's transverse momentum $d\sigma/dp_T$ for Tevatron kinematics. See discussion in the text.

In order to better understand the observed features of the cross section, we performed several numerical studies using different publicly available codes which are CHE [269], RHICBOS [268, 293], DYNNLO [295, 296] and FEWZ [297, 298]. All codes except our new one presented in this Chapter are based on a numerical phase space integration. We start by considering the p_T lepton spectrum at LO, NLO and NNLO. In Fig. 9.6, we start with the production of a W^+ boson for Tevatron kinematics and we integrate the rapidity of the lepton over the interval of $|\eta| < 2$. Here we use the CTEQ6 PDFs from [223]. The lines show the result from our new code whereas histograms are calculated with one of the Monte-Carlo integrators listed above. We find that our NLO result (dashed blue) agrees with the NLO from CHE (solid green) as well as with NLO expansion of RHICBOS in case that the "Y-term" in included (solid blue). Within the framework of q_T resummations, where q_T is the transverse momentum of the produced W boson, the "Y-term" is similar to the NLO matching in threshold resummation taking into account non-singluar terms at a given fixed order. Taking into account only the q_T distributions (solid magenta), we find a significant offset. We would like to stress that RHICBOS is only consistent with the other codes at NLO if we choose the parameter q_T^{sep} of the order of $q_T^{sep} \approx 0.2$ GeV. Furthermore, we note that an additional cut on the W boson transverse momentum q_T such as $q_T < 15$ GeV for example leads to an overall shift of the lepton's p_T distribution. The overall shape remains unaltered. The dash-dot histogram in Fig. 9.6 shows the q_T resummed calculation. In comparison to the other results, it does not have a two-peak structure.

In Fig. 9.7, we show similar results for LHC kinematics. The colors for our NLO and the q_T resummed result are the same. However, now we compare our NLO to the one of FEWZ with which we agree as well. In addition, we plot the NNLO results from FEWZ (solid green) and DYNNLO (solid black).

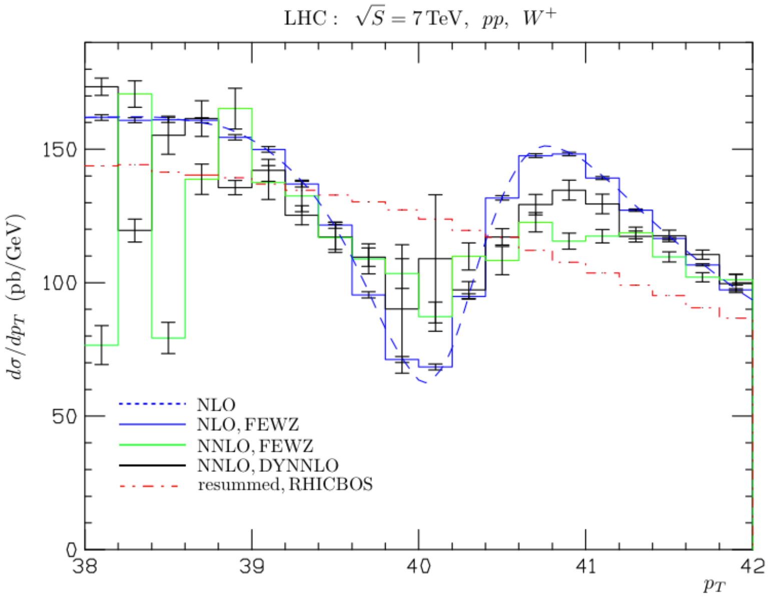

Figure 9.7: Similar to Fig. 9.6 but for LHC kinematics.

Despite numerical uncertainties of the NNLO cross section, we can directly see that the two-peak structure remains also at NNLO even though it appears to be softened to a certain extent. This implies that going beyond NLO does not directly solve the instability issue, where the cross section can get even negative for large values of the c.m.s. energy or for small values of the width Γ_W. Also for LHC energies, the q_T resummed result from RHICBOS is stable.

As a second step, we consider W^+ production cross sections differential in the q_T of the produced W^+ boson in Fig. 9.8 for Tevatron kinematics. In dash dot red, we show the q_T resummed cross section calculated with RHICBOS. In solid blue, we show the NLO expansion (which in principle is the LO for this cross section) with the Y-term and in dashed green without it. Again, we choose the parameter $q_T^{sep} = 0.2$ GeV. As expected the two curves agree very well for low q_T and the difference is not very large even for $q_T = 15$ GeV. In addition, we find a large negative contribution in the smallest q_T bin close to $q_T = 0$ GeV which is due to contributions proportional $\delta(q_T)$. However, this bin is not shown in Fig. 9.8 here. In solid black, we show the full NNLO result from DYNNLO which is closer to the resummed result than the NLO. In general, also CHE and FEWZ fit very well with the presented results even though they are not shown here.

Finally, we show the dependence of the p_T differential NLO cross section on M_W in Fig. 9.9 a). We plot ratios of $d\sigma(M_W \pm 20\,\text{MeV})/d\sigma(M_W)$. In order to measure the M_W mass with an accuracy in the MeV range, the cross section needs to be known with a precision at the percent level. Therefore, we conclude that a solid understanding of the shape around the Jacobian peak is of great importance, see also [299] for example. In Fig. 9.9 b), we show the dependence of the NLO cross section on the width Γ_W. We plot both the standard NLO cross section (solid blue) as well as the cross section with the replacement $\Gamma \to \Gamma_W/10$ (dashed black). We also devide the cross section by a factor of 10 in order

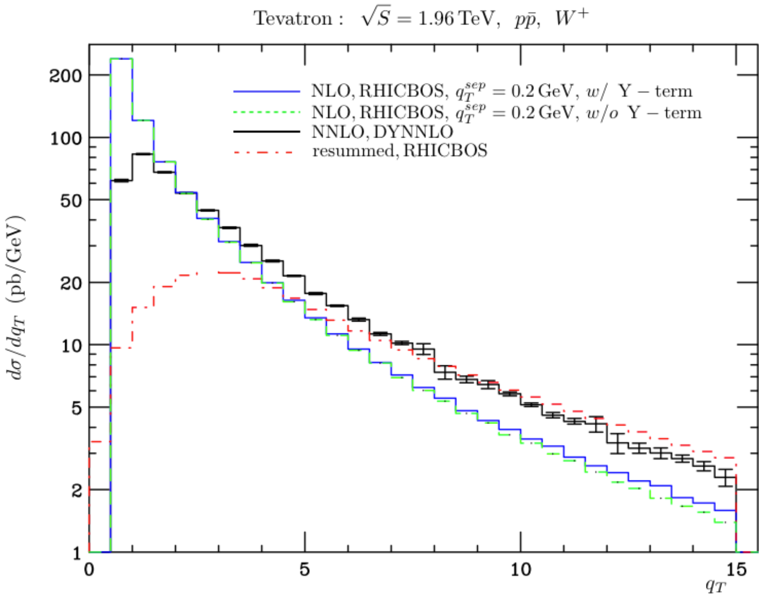

Figure 9.8: Cross sections differential in the transverse momentum of the produced W boson $d\sigma/dq_T$ for Tevatron kinematics. See discussion in the text.

to compensate for the main effects. Note that this corresponds to the narrow width approximation discussed above. As it can be seen, the cross section becomes negative in the peak region.

9.5 Conclusions

We derived a new analytical result for W boson production in hadron-hadron scattering at NLO. With the analytical expression at hand, we were able to identify several types of large logarithmic contributions to the cross section as well as their relevance in the region of the Jacobian peak. A solid understanding of higher order effects is essential for the extraction of M_W at the Tevatron and the LHC. In the next Chapter, we are going to extend our NLO calculation to the polarized case. This will be of great use for the extraction of polarized PDFs from single spin asymmetries involving W bosons at RHIC.

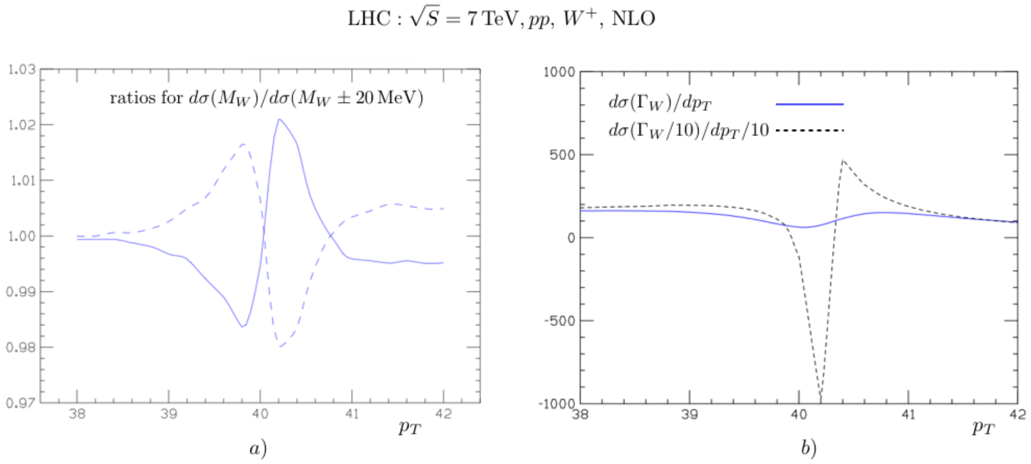

a) *b)*

Figure 9.9: Dependence of the NLO cross section on a) M_W and b) Γ_W for LHC kinematics.

Appendices

APPENDIX A

QCD FEYNMAN RULES

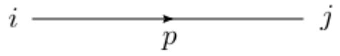

$$= \quad \delta_{ij}\frac{i(\not{p}+m)}{p^2-m^2+i\varepsilon}$$

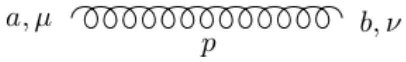

$$= \quad \delta_{ab}\frac{i}{p^2+i\varepsilon}\left(-g^{\mu\nu}+(1-\xi)\frac{p^\mu p^\nu}{p^2+i\varepsilon}\right)$$

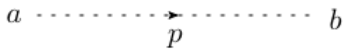

$$= \quad \delta_{ab}\frac{i}{p^2+i\varepsilon}$$

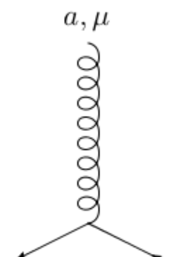

$$= \quad ig\,T^a_{ij}\,\gamma^\mu$$

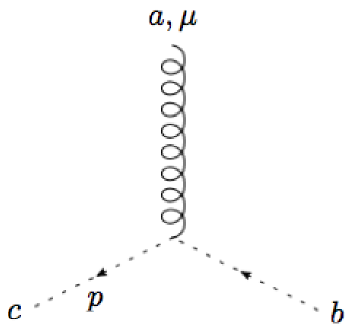

$$= \qquad -g\, f^{abc}\, p^{\mu}$$

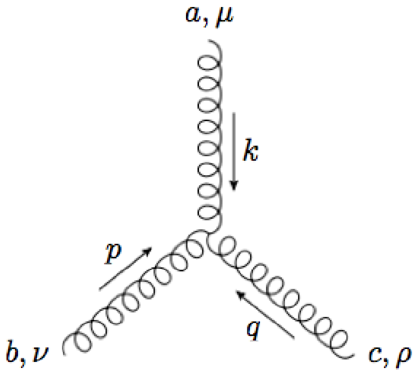

$$= \qquad g\, f^{abc}[g^{\mu\nu}(k-p)^{\rho} + g^{\nu\rho}(p-q)^{\mu} + g^{\rho\mu}(q-k)^{\nu}]$$

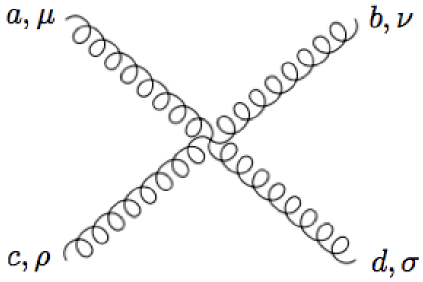

$$= \qquad ig^2[f^{abe} f^{cde}\,(g^{\mu\rho} g^{\nu\sigma} - g^{\mu\sigma} g^{\nu\rho}) + f^{ace} f^{bde}\,(g^{\mu\nu} g^{\rho\sigma} - g^{\mu\sigma} g^{\nu\rho}) + f^{ade} f^{bce}\,(g^{\mu\nu} g^{\rho\sigma} - g^{\mu\rho} g^{\nu\sigma})]$$

Figure A.1: QCD Feynman rules in covariant gauge with quarks (solid), gluons (curly) and ghosts (dotted). See for example [300]. Choosing the gauge parameter $\xi = 1$ ($\xi = 0$) corresponds to Feynman (Landau) gauge.

APPENDIX B

PDF AT LO AND NLO

We give a rather detailed calculation at LO and NLO of the parton distribution function $\phi_{q/q}$ in light-cone gauge $n^2 = 0$, see [65] for example. We start from the operator definition, which is

$$\phi_{q/q}(x) = \frac{1}{4} \sum_{\sigma} \int \frac{dz^-}{2\pi} \, e^{-ixp^+z^-} \, \langle q(p,\sigma)|\bar{\psi}(z^-)\gamma^+\psi(0)|q(p,\sigma)\rangle \; . \tag{B.1}$$

An analogous calculation for $\phi_{g/g}$ may be found in [67] for example.

B.1 Leading Order

We can write the quark states in Eq. (B.1) in terms of quark creation and annihilation operators acting on the vacuum

$$|q(p,\sigma)\rangle = b^{(\sigma)\dagger}(\boldsymbol{p})\,|0\rangle \;, \qquad \langle q(p,\sigma)| = \langle 0|\, b^{(\sigma)}(\boldsymbol{p})\, . \tag{B.2}$$

These operators satisfy the following anticommutation relation

$$\{b^{(r)}(\boldsymbol{p}), b^{(s)\dagger}(\boldsymbol{p}')\} = 2E_p\, \delta_{rs} \delta^{(3)}(\boldsymbol{p}-\boldsymbol{p}') \tag{B.3}$$

and similarly for the corresponding antiquark operators $d, d^\dagger$. With these operators at hand, we are able to write down the free quark field as

$$\psi(z) = \sum_{r=1}^{2} \int \frac{d^3p'}{2E_{p'}} \left(b^{(r)}(\boldsymbol{p}')\, u^{(r)}(p')\, e^{-ip'z} + d^{(r)\dagger}(\boldsymbol{p}')\, v^{(r)}(p')\, e^{ip'z} \right) \; . \tag{B.4}$$

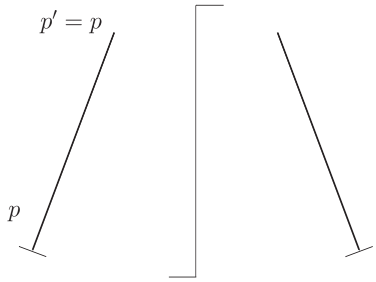

Figure B.1: Quark-quark PDF at LO

Using Eqs. (B.2), (B.4), we may now rewrite Eq. (B.1) as

$$\begin{aligned} \phi^{(0)}_{q/q}(x) &= \frac{1}{4}\sum_{\sigma,r,s}\int\frac{dz^-}{2\pi}\int\frac{d^3p'}{2E_{p'}}\int\frac{d^3p''}{2E_{p''}}\, e^{i(p'^+-xp^+)z^-}\;\bar{u}_i^{(s)}(p'')\gamma^+_{ij}\,u_j^{(r)}(p') \\ &\quad\times \langle 0|b^{(\sigma)}(\boldsymbol{p})\,b^{(s)\dagger}(\boldsymbol{p}'')\,b^{(r)}(\boldsymbol{p}')\,b^{(\sigma)\dagger}(\boldsymbol{p})|0\rangle \\ &= \frac{1}{4}\sum_{\sigma}\int\frac{dz^-}{2\pi}e^{ip^+z^-(1-x)}\,u_j^{(\sigma)}(p)\,\bar{u}_i^{(\sigma)}(p)\gamma^+_{ij} \\ &= \frac{\delta(1-x)}{4p^+}\;\mathrm{tr}[\not{p}\gamma^+] = \delta(1-x)\,. \end{aligned} \tag{B.5}$$

where we have kept the Dirac indices i, j explicit. We can associate the Feynman diagram given in Fig. B.1 with the calculation at LO.

B.2 Next-to-Leading Order

The ψ operators in Eq. (B.1) are Heisenberg operators evolving with the full Hamiltonian. Expanding to a given fixed order in α_s leads to higher order interactions that may be formulated in terms of corresponding Feynman rules. At NLO, we need to consider real and virtual corrections as shown in Fig. B.2. For the real part, we need to consider the following expression

$$\begin{aligned} \phi^{(1),r}_{q/q}(x) &= -\frac{1}{4}g^2\mu^{2\varepsilon}C_F\int\frac{d^dk}{(2\pi)^d}\frac{1}{(2p\cdot k)^2}2\pi\,\delta(k^2)\,\delta(k^+-(1-x)p^+) \\ &\times\;\mathrm{tr}\left[\not{p}\gamma^\mu(\not{p}-\not{k})\gamma^+(\not{p}-\not{k})\gamma^\nu\right]\left(g_{\mu\nu}-\frac{n_\mu k_\nu+n_\nu k_\mu}{n\cdot k}\right)\,, \end{aligned} \tag{B.6}$$

where we are integrating of over the phase space of the gluon crossing the final state cut with momentum k. For simplicity, we treat the two terms in the last bracket separately. Denoting the trace structure by $\mathrm{Tr}^{\mu\nu}$ and working in dimensional regularization $d = 4-2\varepsilon$, we find for the "Feynman term" $\sim g_{\mu\nu}$ the result $\mathrm{Tr}^{\mu\nu}g_{\mu\nu} = -16(1-\varepsilon)\,8(p\cdot k)k^+$. Hence, we may write the real correction as

$$\phi^{(1),r}_{q/q}(x) = \frac{\alpha_s}{\pi}C_F\frac{(4\pi\mu^2)^\varepsilon}{\Gamma(1-\varepsilon)}\,(1-\varepsilon)\,(1-x)\int_0^\infty d|k_T|\,|k_T|^{-1-2\varepsilon}\,, \tag{B.7}$$

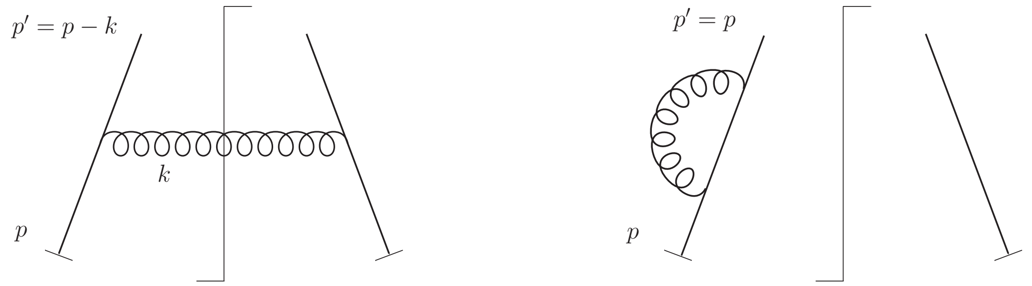

Figure B.2: Quark-quark PDF at NLO; real and virtual corrections.

where we used

$$\delta(k^2) = \frac{1}{2k^+}\delta\left(k^- - \frac{k_T^2}{2k^+}\right) \tag{B.8}$$

and $d^dk = dk^+dk^-d|k_T|\,|k_T|^{d-3}d\Omega_{d-3}$ where $\int d\Omega_{d-3} = 2\pi^{1-\varepsilon}/\Gamma(1-\varepsilon)$. The remaining integral over k_T is divergent. It may be split into an UV and an infrared pole

$$\int_0^\infty d|k_T|\,|k_T|^{-1-2\varepsilon} = \frac{\pi}{\varepsilon} + \frac{\pi}{(-\varepsilon)} + \ldots \tag{B.9}$$

The UV divergence is cancelled by an appropriate $\overline{\text{MS}}$ counterterm, whereas the IR pole remains. In the next step, we need to evaluate the single gauge term in Eq. (B.6). Choosing the principal value prescription and $n = (0, 1, \mathbf{0})$, we find

$$-\operatorname{Tr}^{\mu\nu}\left(\frac{n_\mu k_\nu + n_\nu k_\mu}{n \cdot k}\right) = -32\frac{(p^+)^2k^-}{k^+}(p^+ - k^+)\,. \tag{B.10}$$

Combining both terms, we obtain the following result

$$\phi^{(1),r}_{q/q}(x) = \frac{\alpha_s}{\pi}C_F\,\frac{(4\pi\mu^2)^\varepsilon}{\Gamma(1-\varepsilon)}\left(-\frac{1}{\varepsilon}\right)\left(\frac{1+x^2-\varepsilon(1-x)^2}{1-x}\right), \tag{B.11}$$

where the last term in brackets is indeed proportional to the splitting function $P^<_{q/q}(x)$ in $d = 4 - 2\varepsilon$ dimensions. Here, the superscript $<$ denotes the splitting function without delta function contribution and dropping all "+" prescriptions, cf. Eq. (1.72). The full one-loop quark-quark splitting function is obtained after including also the virtual corrections as shown on the right hand side of Fig. B.2. However, we omit a more detailed calculation for brevity.

APPENDIX C

SIDIS, DIS AND SIA COEFFICIENT FUNCTIONS AT NLO

C.1 SIDIS Coefficient Functions at NLO

In this Appendix we collect the NLO expressions for the spin-averaged partonic SIDIS cross sections. At NLO, we have to consider the processes $\gamma^* q \to qX$, $\gamma^* q \to gX$, and $\gamma^* g \to qX$. For their contributions to the structure function $\mathcal{F}_T^h$ we have in the $\overline{\mathrm{MS}}$ scheme [51, 105–109]:

$$\begin{aligned} C_{qq}^{T,(1)}(\hat{x},\hat{z}) &= e_q^2 C_F \Bigg[-8\delta(1-\hat{x})\delta(1-\hat{z}) + \delta(1-\hat{x}) \left[\tilde{P}_{qq}(\hat{z}) \ln\frac{Q^2}{\mu_F^2} + L_1(\hat{z}) + L_2(\hat{z}) + (1-\hat{z}) \right] \\ &\quad + \delta(1-\hat{z}) \left[\tilde{P}_{qq}(\hat{x}) \ln\frac{Q^2}{\mu_F^2} + L_1(\hat{x}) - L_2(\hat{x}) + (1-\hat{x}) \right] \\ &\quad + \frac{2}{(1-\hat{x})_+(1-\hat{z})_+} - \frac{1+\hat{z}}{(1-\hat{x})_+} - \frac{1+\hat{x}}{(1-\hat{z})_+} + 2(1+\hat{x}\hat{z}) \Bigg], \end{aligned} \tag{C.1}$$

$$\begin{aligned} C_{gq}^{T,(1)}(\hat{x},\hat{z}) &= e_q^2 C_F \Bigg[\tilde{P}_{gq}(\hat{z}) \left(\delta(1-\hat{x}) \ln\left(\frac{Q^2}{\mu_F^2} \hat{z}(1-\hat{z}) \right) + \frac{1}{(1-\hat{x})_+} \right) \\ &\quad + \hat{z}\delta(1-\hat{x}) + 2(1+\hat{x}-\hat{x}\hat{z}) - \frac{1+\hat{x}}{\hat{z}} \Bigg], \end{aligned} \tag{C.2}$$

$$\begin{aligned} C_{qg}^{T,(1)}(\hat{x},\hat{z}) &= e_q^2 T_R \Bigg[\delta(1-\hat{z}) \left[\tilde{P}_{qg}(\hat{x}) \ln\left(\frac{Q^2}{\mu_F^2} \frac{1-\hat{x}}{\hat{x}} \right) + 2\hat{x}(1-\hat{x}) \right] \\ &\quad + \tilde{P}_{qg}(\hat{x}) \left\{ \frac{1}{(1-\hat{z})_+} + \frac{1}{\hat{z}} - 2 \right\} \Bigg], \end{aligned} \tag{C.3}$$

where e_q is the quark's fractional charge, $C_F = 4/3$, $T_R = 1/2$,

$$\begin{aligned}
&\tilde{P}_{qq}(\xi) = \frac{1+\xi^2}{(1-\xi)_+} + \frac{3}{2}\delta(1-\xi), \qquad \tilde{P}_{gq}(\xi) = \frac{1+(1-\xi)^2}{\xi}, \qquad \tilde{P}_{qg}(\xi) = \xi^2 + (1-\xi)^2, \\
&L_1(\xi) = (1+\xi^2)\left(\frac{\ln(1-\xi)}{1-\xi}\right)_+, \qquad L_2(\xi) = \frac{1+\xi^2}{1-\xi}\ln\xi,
\end{aligned} \tag{C.4}$$

and the "+" - distributions are defined as follows:

$$\begin{aligned}
&\int_0^1 d\xi f(\xi)[g(\xi)]_+ \equiv \int_0^1 d\xi\,(f(\xi)-f(1))\,g(\xi), \\
&\int_0^1 d\hat{x}\int_0^1 d\hat{z}\frac{f(\hat{x},\hat{z})}{(1-\hat{x})_+(1-\hat{z})_+} \equiv \int_0^1 d\hat{x}\int_0^1 d\hat{z}\,\frac{f(\hat{x},\hat{z})-f(1,\hat{z})-f(\hat{x},1)+f(1,1)}{(1-\hat{x})(1-\hat{z})}.
\end{aligned} \tag{C.5}$$

Note that we have given expressions in (C.1) for an arbitrary factorization scale μ_F, keeping however the scales the same for the initial and the final state. For the longitudinal structure function F_L^h:

$$\begin{aligned}
C_{qq}^{L,(1)}(\hat{x},\hat{z}) &= 4e_q^2 C_F \hat{x}\hat{z}, \\
C_{gq}^{L,(1)}(\hat{x},\hat{z}) &= 4e_q^2 C_F \hat{x}(1-\hat{z}), \\
C_{qg}^{L,(1)}(\hat{x},\hat{z}) &= 8e_q^2 T_R \hat{x}(1-\hat{x}).
\end{aligned} \tag{C.6}$$

In Mellin-moment space, the NLO results become [110]

$$\begin{aligned}
\tilde{C}_{qq}^{T,(1)}(N,M) = e_q^2 C_F \Bigg[&-8 - \frac{1}{M^2} + \frac{2}{(M+1)^2} + \frac{1}{N^2} + \frac{(1+M+N)^2+1}{M(M+1)N(N+1)} + 3S_2(M) - S_2(N) \\
&+ [S_1(M)+S_1(N)]\left\{S_1(M)+S_1(N) - \frac{1}{M(M+1)} - \frac{1}{N(N+1)}\right\} \\
&+ \left[\frac{1}{N(N+1)} + \frac{3}{2} - 2S_1(N)\right]\ln\left(\frac{Q^2}{\mu_F^2}\right) + \left[\frac{1}{M(M+1)} + \frac{3}{2} - 2S_1(M)\right]\ln\left(\frac{Q^2}{\mu_F^2}\right)\Bigg],
\end{aligned} \tag{C.7}$$

$$\begin{aligned}
\tilde{C}^{T,(1)}_{gq}(N,M) &= e_q^2 C_F\Bigg[\frac{2-2M-9M^2+M^3-M^4+M^5}{M^2(M-1)^2(M+1)^2}+\frac{2M}{N(M+1)(M-1)}\\
&\quad -\frac{2-M+M^2}{M(M+1)(M-1)(N+1)}-\frac{2+M+M^2}{M(M+1)(M-1)}\left[S_1(M)+S_1(N)\right]\\
&\quad +\frac{2+M+M^2}{M(M+1)(M-1)}\ln\left(\frac{Q^2}{\mu_F^2}\right)\Bigg], \qquad \text{(C.8)}
\end{aligned}$$

$$\tilde{C}^{T,(1)}_{qg}(N,M) = e_q^2 T_R\left[\frac{2+N+N^2}{N(N+1)(N+2)}\left(\frac{1}{M-1}-\frac{1}{M}-S_1(M)-S_1(N)+\ln\left(\frac{Q^2}{\mu_F^2}\right)\right)+\frac{1}{N^2}\right], \qquad \text{(C.9)}$$

where

$$S_i(N)\equiv\sum_{j=1}^{N}\frac{1}{j^i}\,. \qquad \text{(C.10)}$$

Note that at large N we have

$$S_1(N)=\ln\bar{N}+\mathcal{O}(1/N),\quad S_2(N)=\frac{\pi^2}{6}+\mathcal{O}(1/N), \qquad \text{(C.11)}$$

where $\bar{N}=N\mathrm{e}^{\gamma_E}$. Furthermore, for the longitudinal structure function,

$$\begin{aligned}
\tilde{C}^{L,(1)}_{qq}(N,M) &= e_q^2 C_F\frac{4}{(M+1)(N+1)}, \qquad \text{(C.12)}\\
\tilde{C}^{L,(1)}_{gq}(N,M) &= e_q^2 C_F\frac{4}{M(M+1)(N+1)}, \qquad \text{(C.13)}\\
\tilde{C}^{L,(1)}_{qg}(N,M) &= e_q^2 T_R\frac{8}{M(N+1)(N+2)}. \qquad \text{(C.14)}
\end{aligned}$$

Here we have corrected a mistake in $\tilde{C}^{L,(1)}_{qg}(N,M)$ in Ref. [110].

C.2 DIS Coefficient Functions at NLO

The DIS coefficient functions up to NLO in the $\overline{\mathrm{MS}}$ scheme are given by [51, 109, 133]

$$\begin{aligned}
\mathcal{C}_q^1(\hat{x}) =& e_q^2\delta(1-\hat{x}) + e_q^2\frac{\alpha_s}{2\pi}C_F\left[(1+\hat{x}^2)\left(\frac{\ln(1-\hat{x})}{1-\hat{x}}\right)_+ - \frac{3}{2}\frac{1}{(1-\hat{x})_+} - \frac{1+\hat{x}^2}{1-\hat{x}}\ln\hat{x} + 3\right.\\
&\left. - \left(-\frac{9}{2}+\frac{\pi^2}{3}\right)\delta(1-\hat{x})\right]\\
\mathcal{C}_q^L(\hat{x}) =& e_q^2\frac{\alpha_s}{2\pi}C_F\,2\hat{x}\\
\mathcal{C}_g^1(\hat{x}) =& e_q^2\frac{\alpha_s}{2\pi}C_F\left[\left(\hat{x}^2+(1-\hat{x})^2\right)\ln\left(\frac{1-\hat{x}}{\hat{x}}\right) - 1 + 4\hat{x}(1-\hat{x})\right]\\
\mathcal{C}_g^L(\hat{x}) =& e_q^2\frac{\alpha_s}{2\pi}C_F\left[4\hat{x}(1-\hat{x})\right]
\end{aligned} \tag{C.15}$$

where $j = q, g$ and $\hat{x} = \xi/x$. The definitions of x and ξ are given in Eqs. (4.5) and (4.6). These coefficients satisfy

$$\mathcal{C}_j^2(\hat{x}) = \mathcal{C}_j^1(\hat{x}) + \mathcal{C}_j^L(\hat{x})\,. \tag{C.16}$$

Concerning Chapter 4, we also would like to point out that these coefficient functions are related to the coefficient functions h_i $(i = 1, 2, L)$ defined in [47] as follows

$$\mathcal{C}^1(\hat{x}) = 2h_1(\hat{x})\,, \quad \mathcal{C}^L(\hat{x}) = 2h_L(\hat{x})\,, \quad \mathcal{C}^2(\hat{x}) = \frac{h_2(\hat{x})}{\hat{x}}\,, \tag{C.17}$$

so that

$$h_L = -h_1 + \frac{h_2}{\hat{x}}. \tag{C.18}$$

The structure function F_i^{AQ} $(i = 1, 2, L)$ presented in the same paper are connected to the ones defined in Eq. (4.15) by the following relations

$$\begin{aligned}
F_1^{\mathrm{AQ}}(x_B, Q^2) &= \frac{\mathcal{F}_1^{\mathrm{TMC}}(x_B, Q^2)}{2} = F_1^{\mathrm{TMC}}(x_B, Q^2)\\
F_2^{\mathrm{AQ}}(x_B, Q^2) &= x_B\mathcal{F}_2^{\mathrm{TMC}}(x_B, Q^2) = F_2^{\mathrm{TMC}}(x_B, Q^2)\\
F_{L,}^{\mathrm{AQ}}(x_B, Q^2) &= \frac{\mathcal{F}_L^{\mathrm{TMC}}(x_B, Q^2)}{2} = \frac{F_L^{\mathrm{TMC}}(x_B, Q^2)}{2x_B}
\end{aligned} \tag{C.19}$$

so that

$$F_L^{\mathrm{AQ}} = \frac{\rho^2}{2x_B}F_2^{\mathrm{AQ}} - F_1^{\mathrm{AQ}}, \tag{C.20}$$

where ρ is defined in Eq. (4.16).

C.3 SIA Coefficient Functions

The coefficient functions up to NLO for SIA in the $\overline{\text{MS}}$ scheme are given by [51, 106, 301, 302]

$$
\begin{aligned}
\hat{\mathcal{C}}_q^1(\hat{z}) =& e_q^2\delta(1-\hat{z}) + e_q^2\frac{\alpha_s}{2\pi}C_F\left[(1+\hat{z}^2)\left(\frac{\ln(1-\hat{z})}{1-\hat{z}}\right)_+ - \frac{3}{2}\frac{1}{(1-\hat{z})_+} + 2\frac{1+\hat{z}^2}{1-\hat{z}}\ln\hat{z} + \frac{3}{2}(1-\hat{z})\right.\\
&\left.+\left(\frac{2}{3}\pi^2-\frac{9}{2}\right)\delta(1-\hat{z})\right]\\
\hat{\mathcal{C}}_q^L(\hat{z}) =& e_q^2\frac{\alpha_s}{2\pi}C_F\\
\hat{\mathcal{C}}_g^1(\hat{z}) =& e_q^2\frac{\alpha_s}{2\pi}C_F\,2\left[\frac{1+(1-\hat{z})^2}{\hat{z}}\ln\left(\hat{z}^2(1-\hat{z})\right) - 2\frac{(1-\hat{z})}{\hat{z}}\right]\\
\hat{\mathcal{C}}_g^L(\hat{z}) =& e_q^2\frac{\alpha_s}{2\pi}C_F\left[4\frac{(1-\hat{z})}{\hat{z}}\right]\ ,
\end{aligned}
\tag{C.21}
$$

where $j = q, g$ and $\hat{z} = \xi_E/z$. The definitions of z and ξ_E are given in Eqs. (4.45) and (4.43). The listed coefficient functions are related by

$$
\hat{\mathcal{C}}_j^2(\hat{x}) = \hat{\mathcal{C}}_j^1(\hat{x}) + \hat{\mathcal{C}}_j^L(\hat{x})\,. \tag{C.22}
$$

APPENDIX D

THE NORMALIZATION OF THE SOFT FUNCTION

The soft matrix S_{LI} in the resumed cross section in moment space, Eq. (7.7), is computed as described in Ref. [80, 81]. Its all-orders form is most conveniently exhibited in moment space, as the ratio of the moments of a fully eikonal cross section $\hat{\sigma}_{LI}^{ab\to cd}$ and four factorized jets, two to absorb the factorizing collinear singularities of the incoming parton lines, and two to absorb the collinear singularities of outgoing lines:

$$\Big(S_{ab\to cd}\left(\alpha_s(\hat{m}^2/\bar{N}^2),\Delta\eta\right)\Big)_{LI} \;=\; \frac{\hat{\sigma}_{LI}^{ab\to cd}\left(\frac{\hat{m}^2}{N^2\mu_R^2},\Delta\eta,\alpha_s(\mu_R^2),\varepsilon\right)}{\prod_{i=a,b}\tilde{\jmath}_{\rm in}^{(i)}\left(\frac{\hat{m}^2}{N^2\mu_R^2},\alpha_s(\mu_R^2),\varepsilon\right)\prod_{j=c,d}\tilde{\jmath}_{\rm out}^{(j)}\left(\frac{\hat{m}^2}{N^2\mu_R^2},\alpha_s(\mu_R^2),\varepsilon\right)}\,. \tag{D.1}$$

As described in Refs. [78, 80, 81], these “in" and “out" jets, $\tilde{\jmath}_{\rm in}$ and $\tilde{\jmath}_{\rm out}$, respectively are defined to match the collinear singularities and radiation phase space in the partonic threshold limit.

The explicit calculation of $(S_{ab\to cd})_{LI}$ at one loop as given here is equivalent to the procedure described in Sec. 5.3.3. The functions on the right of (D.1), as defined in detail below, are normalized and expanded according to

$$\begin{aligned}
\hat{\sigma}_{LI}^{ab\to cd}\left(\frac{\hat{m}^2}{N^2\mu_R^2},\Delta\eta,\alpha_s(\mu_R^2),\varepsilon\right) &= (S_{ab\to cd}^{(0)})_{LI} + \frac{\alpha_s(\mu_R^2)}{\pi}\,\hat{\sigma}_{LI}^{ab\to cd\,(1)} + \mathcal{O}(\alpha_s(\mu_R^2)^2)\,,\\
\tilde{\jmath}_{\rm in}^{(i)}\left(\frac{\hat{m}^2}{N^2\mu_R^2},\alpha_s(\mu_R^2),\varepsilon\right) &= 1 + \frac{\alpha_s(\mu_R^2)}{\pi}\,\tilde{\jmath}_{\rm in}^{(i,1)} + \mathcal{O}(\alpha_s(\mu_R^2)^2)\,,\\
\tilde{\jmath}_{\rm out}^{(j)}\left(\frac{\hat{m}^2}{N^2\mu_R^2},\alpha_s(\mu_R^2),\varepsilon\right) &= 1 + \frac{\alpha_s(\mu_R^2)}{\pi}\,\tilde{\jmath}_{\rm out}^{(j,1)} + \mathcal{O}(\alpha_s(\mu_R^2)^2)\,,
\end{aligned} \tag{D.2}$$

where $S^{(0)}$ is the tree-level soft matrix, defined as in Eq. (5.53). The first-order expansion of the soft matrix is thus,

$$\left(S^{(1)}_{ab\to cd}\right)_{LI} = \hat{\sigma}^{ab\to cd\,(1)}_{LI} - (S^{(0)}_{ab\to cd})_{LI}\left[\sum_{i=a,b} \tilde{\jmath}^{(i,1)}_{\rm in} + \sum_{j=c,d} \tilde{\jmath}^{(j,1)}_{\rm out}\right] . \tag{D.3}$$

At any loop order, the collinear singularities of the eikonal cross section $\hat{\sigma}_{LI}$ match those of properly-defined incoming and outgoing jet functions. At one loop, this will result in a finite soft function by simple cancellation in Eq. (D.3), as seen in Sec. 5.3.3. That is, division by the regularized jet functions plays the role of the collinear factorization of the soft function. It also provides finite, factorizing corrections to the soft function, which depend on the definitions of the jets functions. Here we use jet functions defined directly from the eikonal resummations of Drell-Yan and double inclusive cross sections [191]. The choices, defined below, match collinear singularities of the eikonal cross section, and have the advantage of being Lorentz and gauge invariant. They differ from those made in Refs. [78, 80, 81] by finite terms, but the collinear structure is identical. When restricted to the amplitude level, this is the same formalism that was implemented in Refs. [211–214, 219].

To make the connection to the calculation of the soft function in this paper explicit, we recall that eikonal diagrams are generated by path-ordered exponentials with constant velocities β, which we represent as

$$\Phi^{(f)}_{\beta}(\lambda_2,\lambda_1;x) = P\exp\left(-ig\int_{\lambda_1}^{\lambda_2} d\eta\;\beta{\cdot}A^{(f)}(\eta\beta+x)\right) , \tag{D.4}$$

where superscript f represents the color representation of the parton to which this “Wilson line" corresponds. In terms of these path-ordered exponentials, we define products corresponding to scattering, pair annihilation and pair creation. For the case of 2 → 2 scattering, the ends of two incoming and two outgoing Wilson lines are coupled locally by a constant color tensor $\mathcal{C}_I$,

$$\begin{aligned} w_I^{(ab\to cd)}(x)_{\{j\}} &= \sum_{\{i\}} \Phi^{(d)}_{\beta_d}(\infty,0;x)_{j_d,i_d}\;\Phi^{(c)}_{\beta_c}(\infty,0;x)_{j_c,i_c} \\ &\quad \times\left(\mathcal{C}_I^{(ab\to cd)}\right)_{i_d i_c,i_b i_a}\;\Phi^{(a)}_{\beta_a}(0,-\infty;x)_{i_a,j_a}\Phi^{(b)}_{\beta_b}(0,-\infty;x)_{i_b,j_b}\,. \end{aligned} \tag{D.5}$$

For pair annihilation, two lines in conjugate representations that come from the infinite past are joined by a color singlet tensor, that is, a simple Kronecker delta,

$$w_0^{(a\bar{a})}(x)_{\{j\}} = \sum_{\{i\}} (\delta)_{i_a,i_{\bar{a}}}\;\Phi^{(\bar{a})}_{\beta_{\bar{a}}}(0,-\infty;x)_{i_a,j_a}\Phi^{(a)}_{\beta_a}(0,-\infty;x)_{i_{\bar{a}},j_{\bar{a}}}\,, \tag{D.6}$$

and similarly for pair creation, using color-conjugate lines that emerge from a point, and extend into the infinite future,

$$\hat{w}_0^{(a\bar{a})}(x)_{\{j\}} = \sum_{\{i\}} \Phi^{(\bar{a})}_{\beta_{\bar{a}}}(\infty,0;x)_{i_a,j_a}\Phi^{(a)}_{\beta_a}(\infty,0;x)_{i_{\bar{a}},j_{\bar{a}}}\;(\delta)_{i_a,i_{\bar{a}}}\,. \tag{D.7}$$

In terms of these operators, the eikonal cross section is defined by

$$\begin{aligned}
\hat{\sigma}_{LI}^{ab\to cd}\left(\frac{\hat{m}^2}{N^2\mu_R^2},\Delta\eta,\alpha_s(\mu_R^2),\varepsilon\right) &= \int_0^1 d\tau\;\tau^{N-1}\int\frac{dy^0}{2\pi}\;e^{i\tau\hat{m}y^0} \\
&\quad\times\;\mathrm{Tr}_{\{j\}}\;\langle 0|\,\bar{T}\left(w_L^{(ab\to cd)\dagger}\left((y^0,\vec{0})\right)_{\{j\}}\right)\;T\left(w_I^{(ab\to cd)}(0)_{\{j\}}\right)|0\rangle \\
&= \int_0^1 d\tau\;\tau^{N-1}\sum_{\xi}\;\delta(\tau\hat{m}-p_\xi^0) \\
&\quad\times\;\mathrm{Tr}_{\{j\}}\;\langle 0|\,\bar{T}\left(w_L^{(a\bar{a})\dagger}\,(0)_{\{j\}}\right)|\xi\rangle\,\langle\xi|T\left(w_I^{(a\bar{a})}(0)_{\{j\}}\right)|0\rangle\,,
\end{aligned}\tag{D.8}$$

where T represents time-ordering, $\bar{T}$ anti-time ordering, and p_ξ^0 is the energy of state $|\xi\rangle$. The in jet is defined *in terms of its square* in moment space as

$$\begin{aligned}
\left(\tilde{j}_{\mathrm{in}}^{(a)}\left(\frac{\hat{m}^2}{N^2\mu_R^2},\alpha_s(\mu_R^2),\varepsilon\right)\right)^2 &= \int_0^1 d\tau\;\tau^{N-1}\sum_{\xi}\;\delta(\tau\hat{m}-p_\xi^0) \\
&\quad\times\;\mathrm{Tr}_{\{j\}}\;\langle 0|\,\bar{T}\left(w_0^{(a\bar{a})\dagger}\,(0)_{\{j\}}\right)|\xi\rangle\,\langle\xi|T\left(w_0^{(a\bar{a})}(0)_{\{j\}}\right)|0\rangle\,.
\end{aligned}\tag{D.9}$$

With this choice, $\left(\tilde{j}_{\mathrm{in}}^{(a)}\right)^2$ is exactly the eikonal Drell-Yan cross section. It was computed to two loops in Ref. [303]. The out jet is defined by the same integrals but with the pair of incoming Wilson lines of the operator $w_0(x)$ replaced by the outgoing pair in $\hat{w}_0(x)$, corresponding to double inclusive annihilation [93]:

$$\begin{aligned}
\left(\tilde{j}_{\mathrm{out}}^{(c)}\left(\frac{\hat{m}^2}{N^2\mu_R^2},\alpha_s(\mu_R^2),\varepsilon\right)\right)^2 &= \int_0^1 d\tau\;\tau^{N-1}\sum_{\xi}\;\delta(\tau\hat{m}-p_\xi^0) \\
&\quad\times\;\mathrm{Tr}_{\{j\}}\;\langle 0|\,\bar{T}\left(\hat{w}_0^{(c\bar{c})\dagger}\,(0)_{\{j\}}\right)|\xi\rangle\,\langle\xi|T\left(\hat{w}_0^{(c\bar{c})}(0)_{\{j\}}\right)|0\rangle\,.
\end{aligned}\tag{D.10}$$

It is easy to confirm explicitly in Ref. [303] that the calculation of this quantity depends only on the inner products $\beta_a\cdot\beta_{\bar{a}}$ so that the full two-loop calculation and renormalization of this operator is the same for outgoing as for incoming eikonal jets.

The resummation of logarithms of N in this cross section leads precisely to the functions $\ln\Delta_i^N$ in Eq. (5.25), which summarize factoring NNLL dependence on the moment variable N, as confirmed recently in Ref. [304]. We note, however, that in the NNLL exponentiation as implemented into the expression for the functions Δ_i^N in Eq. (6.7), the Drell-Yan soft function is treated as an overall prefactor evaluated at the hard scale $\hat{m}^2$, rather than at $\hat{m}^2/N^2$. Logarithms at NNLL that are associated with this shift are already incorporated into the exponent by use of the relation [304]

$$S(\alpha_s(\hat{m}^2/N^2)) \;=\; S(\alpha_s(\hat{m}^2))\exp\left[-\frac{1}{2}\int_{\hat{m}^2/N^2}^{\hat{m}^2}\frac{d\mu^2}{\mu^2}\frac{\partial \ln S(\alpha_s(\mu^2))}{\partial \mu^2}\right]\,. \tag{D.11}$$

To match logarithms associated with these factors consistently we include in our definition of Δ_i^N in Eq. (6.7) an extra factor of $1-(3\alpha_s/4\pi)A_i^{(1)}\zeta(2)$, to account for our definitions of the in- and out-jet functions in terms of Drell-Yan and double inclusive cross sections. The combined factors for all four jet functions match the π^2 contribution in (5.92), which in turn arises from the explicit π^2 terms in the integrals $dI_{ij}/d\hat{\tau}$ in (5.90).

APPENDIX E

THE SOFT FUNCTION FOR SINGLE-INCLUSIVE HADRON PRODUCTION AT NLO

For all channels, we choose the color basis of [82]. The leading-order matrices $S^{(0)}$ may be found in [82]. The soft-matrix at NLO for single-inclusive hadron production may be split into a part that is proportional to the LO soft matrix $S^{(0)}$ and a remainder which turns out to be proportional to the matrix $\mathcal{R}_{12}$ introduced in (6.32) and (5.83).

For the channels $qq' \to qq'$ and $qq \to qq$, we obtain the following result

$$\begin{aligned} S^{(1)}_{qq'\to qq'} &= S^{(1)}_{qq\to qq} \\ &= -\frac{C_F}{2}\Big([\ln(1-v)+\ln v]^2 - 2\,\zeta(2)\Big)\,S^{(0)}_{qq'\to qq'} \\ &\quad + C_F \ln(1-v)\ln v \begin{pmatrix} 1 & -C_A \\ -C_A & 0 \end{pmatrix} \end{aligned} \tag{E.1}$$

see also Eq. (6.51). For the channels $q\bar{q}' \to q\bar{q}'$, $q\bar{q} \to q'\bar{q}'$ and $q\bar{q} \to q\bar{q}$, we find

$$\begin{aligned} S^{(1)}_{q\bar{q}'\to q\bar{q}'} &= S^{(1)}_{q\bar{q}\to q'\bar{q}'} = S^{(1)}_{q\bar{q}\to q\bar{q}} \\ &= -\frac{C_F}{2}\Big([\ln(1-v)+\ln v]^2 - 2\,\zeta(2)\Big)\,S^{(0)}_{q\bar{q}'\to q\bar{q}'} \\ &\quad + C_F \ln(1-v)\ln v \begin{pmatrix} 0 & C_A \\ C_A & (C_A^2-2)/2 \end{pmatrix}. \end{aligned} \tag{E.2}$$

For the channels $qg \to qg$ and $gq \to qg$, we find

$$\begin{aligned} S^{(1)}_{qg\to qg} &= S^{(1)}_{gq\to qg} \\ &= \left(-\frac{C_F}{2}\left[\ln(1-v)+\ln v\right]^2 + (C_F - C_A)\ln^2(1-v) + C_F\,\zeta(2)\right) S^{(0)}_{qg\to qg} \\ &\quad + \frac{C_F C_A}{2}\ln(1-v)\ln v \begin{pmatrix} 0 & 0 & -4C_A \\ 0 & C_A^2-4 & 4-C_A^2 \\ -4C_A & 4-C_A^2 & C_A^2 \end{pmatrix}. \end{aligned} \tag{E.3}$$

For the channels $gq \to gq$ and $qg \to gq$, we find

$$\begin{aligned} S^{(1)}_{gq\to gq} &= S^{(1)}_{qg\to gq} \\ &= \left(-\frac{C_A}{2}\left[\ln(1-v)+\ln v\right]^2 + (C_A - C_F)\ln^2 v + C_A\,\zeta(2)\right) S^{(0)}_{gq\to gq} \\ &\quad + \frac{C_F C_A}{2}\ln(1-v)\ln v \begin{pmatrix} 0 & 0 & -4C_A \\ 0 & C_A^2-4 & 4-C_A^2 \\ -4C_A & 4-C_A^2 & C_A^2 \end{pmatrix}. \end{aligned} \tag{E.4}$$

For the channel $q\bar{q} \to gg$, we find

$$\begin{aligned} S^{(1)}_{q\bar{q}\to gg} &= -\frac{C_F}{2}\left(\left[\ln(1-v)+\ln v\right]^2 - 2\,\zeta(2)\right) S^{(0)}_{q\bar{q}\to gg} \\ &\quad + C_F \ln(1-v)\ln v \begin{pmatrix} 4C_F C_A^2 & 0 & 0 \\ 0 & (2C_F - C_A)(C_A^2-4) & 0 \\ 0 & 0 & -C_A \end{pmatrix}. \end{aligned} \tag{E.5}$$

For the channel $gg \to q\bar{q}$, we find

$$\begin{aligned} S^{(1)}_{gg\to q\bar{q}} &= -\frac{C_A}{2}\left(\left[\ln(1-v)+\ln v\right]^2 - 2\,\zeta(2)\right) S^{(0)}_{gg\to q\bar{q}} \\ &\quad + C_F C_A \ln(1-v)\ln v \begin{pmatrix} 4C_A^2 & 0 & 0 \\ 0 & C_A^2-4 & 0 \\ 0 & 0 & C_A^2 \end{pmatrix}. \end{aligned} \tag{E.6}$$

For the channel $gg \to gg$, we find

$$S^{(1)}_{gg\to gg} = -\frac{C_A}{2}\Big([\ln(1-v)+\ln v]^2 - 2\,\zeta(2)\Big)\,S^{(0)}_{gg\to gg}$$
$$+3\ln(1-v)\ln v \begin{pmatrix} 5 & 0 & 0 & 0 & 0 & 0 & 0 & 0 \\ 0 & 5 & 0 & 0 & 0 & 0 & 0 & 0 \\ 0 & 0 & 0 & 0 & 0 & 0 & 0 \\ 0 & 0 & 0 & 0 & 0 & 2 & 0 & 0 \\ 0 & 0 & 0 & 0 & 4 & 4 & 8 & 0 \\ 0 & 0 & 0 & 2 & 4 & 4 & 0 & 6 \\ 0 & 0 & 0 & 0 & 8 & 0 & 20 & 12 \\ 0 & 0 & 0 & 0 & 0 & 6 & 12 & 36 \end{pmatrix}, \tag{E.7}$$

where we chose $C_F = 4/3$ and $C_A = 3$ in the second line.

APPENDIX F

EXPLICIT RESULTS FOR HADRONIC W PRODUCTION AT NLO

In this Appendix, we present some of our explicit NLO results. We first consider the $q\bar{q}'$ channel when an intermediate W^- boson is produced (for example through $d\bar{u}$ scattering), for which effectively $C_1 = 0, C_2 = 8$ in (9.10) (see discussion after Eq. (9.11)). We define the functions

$$\begin{aligned} K(z) &\equiv \arctan\left(\frac{\Gamma_W M_W}{zs - M_W^2}\right) + \pi\,\Theta(M_W^2 - zs)\ , \\ J(z) &\equiv \log\left[\frac{(zs - M_W^2)^2 + \Gamma_W^2 M_W^2}{M_W^4 + \Gamma_W^2 M_W^2}\right] - \frac{2M_W}{\Gamma_W} K(z)\ , \end{aligned} \tag{F.1}$$

with the usual (Heaviside) step function. In addition to the values $z_1 = 1\,, z_2 = w\,, z_3 = (1-v)/(1-vw)$ of Eq. (8.39), we introduce

$$z_0 = 0\,, \quad z_4 = 1 - v + vw\ , \tag{F.2}$$

and we set

$$J_i \equiv J(z_i)\,, \quad K_i \equiv K(z_i)\,. \tag{F.3}$$

We then find for production of a W^-:

$$\begin{aligned}
\frac{s\,d^2\hat{\sigma}^{(1)}_{q\bar{q}'}}{dvdw} &= \frac{|U_{qq'}|^2}{\pi N_c}\left(\frac{G_F M_W^2}{\sqrt{2}}\right)^2 C_F \Bigg[v^2 P_1 \Bigg[2(1+w^2)\left(\frac{\log(1-w)}{1-w}\right)_+ - 2\,\log(1-vw)\,\frac{P_{qq}(w)}{C_F} \\
&+ \left(\pi^2 - 8 + \left(\frac{3}{2} + 2\log(1-v)\right)\log\frac{1-v}{v}\right)\delta(1-w) + \frac{1+w^2}{1-w}\left(J_0 - J_2 - J_3 + J_4 + \kappa(K_0 - K_2 - K_3 + K_4)\right)\Bigg] \\
&- \frac{v}{2}\left(\frac{J_0 - 2J_3 + J_4}{1-vw} - \frac{J_0 - J_4}{1-v+vw}\right) + v^2\Bigg\{P_2\Bigg[(1+w^2)\left(\frac{\log(1-w)}{1-w}\right)_+ - \frac{P_{qq}(w)}{C_F}\log\left(\frac{\mu_F^2}{vs}\right) + 1 - w \\
&- \frac{1}{2}\,\frac{1+w^2}{1-w}\left(J_0 - 2J_2 + J_4 + \frac{\kappa}{w}(K_0 - 2K_2 + K_4)\right)\Bigg]\Bigg\} + \frac{v^3 w^2}{1-vw}\left\{v \to 1-vw, w \to \frac{1-v}{1-vw}\right\}\Bigg], \qquad \text{(F.4)}
\end{aligned}$$

with the splitting function P_{qq} of Eq. (8.32), and with

$$\kappa \equiv \frac{2M_W(\Gamma_W^2 + M_W^2)}{\Gamma_W s}\,. \qquad \text{(F.5)}$$

Note that despite appearance the expression is perfectly well regularized at $w = 1$.

By applying crossing one obtains the corresponding cross section for $\bar{q}'q \to W^- g$. Crossing is achieved by changing $v \to 1 - vw$, $w \to (1-v)/(1-vw)$ and multiplying the result by the Jacobian $v/(1-vw)$. We do not give the crossed result explicitly here.

Writing the NLO partonic $q\bar{q}'$ cross section for general C_1 and C_2 in the form

$$C_1\,d\hat{\sigma}_1^{(1)} + C_2\,d\hat{\sigma}_2^{(1)}\,, \qquad \text{(F.6)}$$

we find that $d\hat{\sigma}_2^{(1)} = [d\hat{\sigma}_1^{(1)}]_{\text{crossed}}$. Since the result for W^+ production is obtained in our calculations by setting $C_1 = 8, C_2 = 0$ (see Sec. 9.2.2), we thus have

$$\begin{aligned}
d\hat{\sigma}^{(1)}_{q\bar{q}'\to W^+ g} &= 8d\hat{\sigma}_1^{(1)} = d\hat{\sigma}^{(1)}_{\bar{q}q'\to W^- g}\,, \\
d\hat{\sigma}^{(1)}_{\bar{q}'q\to W^+ g} &= 8\left[d\hat{\sigma}_1^{(1)}\right]_{\text{crossed}} = d\hat{\sigma}^{(1)}_{q'\bar{q}\to W^- g}. \qquad \text{(F.7)}
\end{aligned}$$

We remind the reader that the $W^\pm$ cross section for a polarized incoming quark differs just by a sign from the corresponding unpolarized one (see Eq. (8.7)) while that for an incoming polarized antiquark involves no sign change. The cross sections for intermediate Z bosons may be constructed from (F.6), using (F.4) and its crossed variant and inserting the appropriate coupling factors C_1 and C_2 in each case.

Secondly, we also present the result for the channel $g\bar{q} \to W^-\bar{q}'$ in the unpolarized and the polarized case:

$$\begin{aligned}
\frac{s\, d^2\hat{\sigma}^{(1)}_{g\bar{q}}}{dvdw} &= \frac{T_R |U_{qq'}|^2}{\pi N_c} \left(\frac{G_F M_W^2}{\sqrt{2}}\right)^2 v^2 P_2 \Bigg\{ 2\,(1-w)w - \; P_{qg}(w) \\
&\qquad \times \left[J_0 - 2J_2 + J_4 + \frac{\kappa}{w}(K_0 - 2K_2 + K_4) + 2\log\left(\frac{\mu_F^2}{v(1-w)s}\right)\right] \Bigg\}\,, \\
\frac{s\, d^2\Delta\hat{\sigma}^{(1)}_{g\bar{q}}}{dvdw} &= -\frac{T_R |U_{qq'}|^2}{\pi N_c} \left(\frac{G_F M_W^2}{\sqrt{2}}\right)^2 v^2 P_2 \Bigg\{ 2\,(1-w) - \; \Delta P_{qg}(w) \\
&\qquad \times \left[J_0 - 2J_2 + J_4 + \frac{\kappa}{w}(K_0 - 2K_2 + K_4) + 2\log\left(\frac{\mu_F^2}{v(1-w)s}\right)\right] \Bigg\}\,, \qquad \text{(F.8)}
\end{aligned}$$

where $T_R = 1/2$ and

$$\begin{aligned}
P_{qg}(x) &= \frac{1}{2}\left(x^2 + (1-x)^2\right)\,, \\
\Delta P_{qg}(x) &= \frac{1}{2}\,(2x-1)\,. \qquad \text{(F.9)}
\end{aligned}$$

We note that the terms in square brackets have a similar structure as the penultimate one in (F.4). Finally, for $qg \to W^- q'$ we find

$$\begin{aligned}
\frac{s\, d^2\hat{\sigma}^{(1)}_{qg}}{dvdw} &= \frac{T_R |U_{qq'}|^2}{\pi N_c} \left(\frac{G_F M_W^2}{\sqrt{2}}\right)^2 \Bigg[\frac{v}{1-vw} \Bigg\{ \frac{2M_W^2}{s}\,(J_0 - 2J_3 + J_4 + \tilde{\kappa}(K_0 - 2K_3 + K_4)) \\
&+ \; P_3\, v^2 w^2 \left[2(1-\tilde{w})\tilde{w} - P_{qg}(\tilde{w})\, \left(J_0 - 2J_3 + J_4 + \frac{\kappa}{\tilde{w}}(K_0 - 2K_3 + K_4) + 2\log\left(\frac{\mu_F^2}{v(1-w)s}\right)\right)\right] \\
&- \; (J_0 - 2J_3 + J_4)\,\frac{1 - v - vw + 2v^2 w - v^2 w^2}{1-vw} - \frac{(1+vw)(1-2v+vw)}{1-vw} \Bigg\} \\
&+ \; \frac{v}{(1-v+vw)^2} \Bigg\{ -\frac{M_W^2}{s}\,(J_0 - J_4 + \tilde{\kappa}(K_0 - K_4))\,\frac{1 - 3v + 2v^2 + 4vw - 3v^2 w + v^2 w^2}{1-v+vw} \\
&+ \; \frac{1}{2}(J_0 - J_4)(1-v)(1-2v+2vw) - v(1-v-2w+vw) \Bigg\} \Bigg]\,, \qquad \text{(F.10)}
\end{aligned}$$

where

$$\tilde{w} \equiv \frac{1-v}{1-vw} \; = z_3\,, \qquad \text{(F.11)}$$

and

$$\tilde{\kappa} \equiv \frac{\Gamma_W^2 + M_W^2}{\Gamma_W M_W}\,. \qquad \text{(F.12)}$$

The corresponding spin-dependent cross section for an incoming polarized quark again just differs by a sign; see (8.7).

ACKNOWLEDGMENTS

I would like to express my gratitude to my supervisor Prof. Dr. Werner Vogelsang for giving me the opportunity to write my Ph.D. thesis in his group. I am very thankful for his enormous support, many helpful discussions and for giving me the opportunity to work on many different and interesting research projects. Thanks to his support I was able to go to several conferences, summer schools and to the Brookhaven National Laboratory for a research stay.

I am grateful to Prof. Dr. Thomas Gutsche for his advice, discussions and for being very helpful all time during my Ph.D.

Furthermore, I would like to thank my office mate and frequent co-worker Daniele Anderle for the nice time working and also traveling together as well as for solving many computer related issues. Many thanks to Patriz Hinderer for the fruitful collaboration on several different projects and for the nice time in Tübingen.

In addition, I would like to thank my other collaborators on projects during my Ph.D. time which are Dr. Alberto Accardi, Prof. Dr. Daniel de Florian, Prof. Dr. Asmita Mukherjee and Prof. Dr. George Sterman. Thanks a lot for their support and the pleasant time working together. I also would like to express my gratitude to Dr. Alberto Accardi for inviting me twice to Jefferson Lab.

I am thankful to Leandro Almeida, Abhay Deshpande, Ciprian Gal, Aude Gehrmann-De Ridder, Alexander Huss, Martin Leitgab, Michael Klasen, Sven Moch, Peter Monaghan, Juan Rojo, Jacques Soffer, Marco Stratmann, Ilmo Sung, Bernd Surrow, Marco Traini and Christian Weiss for very useful communications.

Many thanks to the whole theoretical physics group in Tübingen, including Prof. Dr. Barbara Jäger, Dr. Giuseppe Burgio, Dr. Davide Campagnari, Dr. Valery Lyubovitskij, Dr. Marc Schlegel, Dr. Marco Stratmann, Julien Baglio, Ehsan Ebadati, Jan Heffner, Tom Kaufmann, Matthias Kesenheimer, Martin Lambertsen, Lukas Salfelder, Peter Vastag and Hannes Vogt, for many discussions and a nice working atmosphere. In addition, I would like to thank Dr. Melanie Pfeuffer, Sabine Werner and Ingrid Estiry.

Finally, I would like to thank my girlfriend Jasone for being supportive in many different ways. Many thanks also to my sister Pia and my parents Angelika and Franz for always being there for me.

BIBLIOGRAPHY

[1] E. Bloom, D. Coward, H. DeStaebler, J. Drees, G. Miller, L. Mo, R. Taylor, M. Breidenbach, J. Friedman, G. Hartmann, et al., Physical Review Letters **23**, 930 (1969).

[2] D. Gross and F. Wilczek, Physical Review Letters **30**, 1343 (1973).

[3] H. Politzer, Physical Review Letters **30**, 1346 (1973).

[4] J. C. Collins, D. E. Soper, and G. Sterman, Nuclear Physics B **261**, 104 (1985).

[5] J. C. Collins, D. E. Soper, and G. F. Sterman, Adv.Ser.Direct.High Energy Phys. **5**, 1 (1988).

[6] G. F. Sterman, AIP Conf.Proc. **74**, 22 (1981).

[7] G. F. Sterman, Nuclear Physics B **281**, 310 (1987).

[8] S. Catani and L. Trentadue, Nuclear Physics B **327**, 323 (1989).

[9] CMS Collaboration, Physical Review Letters **107**, 132001 (2011), `1106.0208`.

[10] M. Leitgab, R. Seidl, M. Grosse Perdekamp, A. Vossen, I. Adachi, H. Aihara, D. M. Asner, V. Aulchenko, T. Aushev, A. M. Bakich, et al., Physical Review Letters **111**, 062002 (2013).

[11] J. P. Lees, V. Poireau, V. Tisserand, E. Grauges, A. Palano, G. Eigen, B. Stugu, D. N. Brown, L. T. Kerth, Y. G. Kolomensky, et al., Physical Review D **88**, 032011 (2013).

[12] W. J. Stirling, private communication. (2012).

[13] C. Yang and R. Mills, Physical Review **96**, 191 (1954).

[14] H. Fritzsch, M. Gell-Mann, and H. Leutwyler, Physics Letters B **47**, 365 (1973).

[15] E. Abers and B. Lee, Physics Reports **9**, 1 (1973).

[16] L. Faddeev and V. Popov, Physics Letters B **25**, 29 (1967).

[17] D. E. Soper, p. 54 (1997), `9702203`.

[18] G. Leibbrandt, Reviews of Modern Physics **59**, 1067 (1987).

[19] O. Tarasov, A. Vladimirov, and A. Zharkov, Physics Letters B **93**, 429 (1980).

[20] S. Larin and J. Vermaseren, Physics Letters B **303**, 334 (1993).

[21] S. Bethke, The European Physical Journal C **64**, 689 (2009).

[22] M. Pfeuffer, Ph.D. thesis (2013).

[23] L. Surguladze and M. Samuel, Reviews of Modern Physics **68**, 259 (1996).

[24] R. D. Field, *Applications of Perturbative QCD* (Addison-Wesley, 1995).

[25] M. Stratmann, ECT*, Trento (2012).

[26] T. Lee and M. Nauenberg, Physical Review **133**, B1549 (1964).

[27] T. Kinoshita, Journal of Mathematical Physics **3**, 650 (1962).

[28] G. Sterman, Physical Review D **17**, 2773 (1978).

[29] G. Sterman, Physical Review D **17**, 2789 (1978).

[30] Z. Kunszt and D. E. Soper, Physical Review D **46**, 192 (1992).

[31] E. Farhi, Physical Review Letters **39**, 1587 (1977).

[32] G. Sterman, Physical Review Letters **39**, 1436 (1977).

[33] G. Soyez, Nuclear Physics B - Proceedings Supplements **191**, 131 (2009), `0812.2362`.

[34] G. C. Blazey, J. R. Dittmann, S. D. Ellis, V. D. Elvira, K. Frame, S. Grinstein, R. Hirosky, R. Piegaia, H. Schellman, R. Snihur, et al., pp. 47–77 (2000), `0005012`.

[35] S. D. Ellis, Physical Review D **48**, 3160 (1993).

[36] S. Catani, Y. Dokshitzer, M. Seymour, and B. Webber, Nuclear Physics B **406**, 187 (1993).

[37] Y. Dokshitzer, G. Leder, S. Moretti, and B. Webber, Journal of High Energy Physics **1997**, 001 (1997).

[38] M. Cacciari, G. P. Salam, and G. Soyez, Journal of High Energy Physics **2008**, 12 (2008), `0802.1189`.

[39] A. Mukherjee and W. Vogelsang, Physical Review D **86**, 094009 (2012), `1209.1785`.

[40] B. Jager, M. Stratmann, and W. Vogelsang, Physical Review D **70**, 23 (2004), `0404057`.

[41] M. Furman, Nuclear Physics B **197**, 413 (1982).

[42] F. Aversa, P. Chiappetta, M. Greco, and J. Guillet, Nuclear Physics B **327**, 105 (1989).

[43] A. Mukherjee and W. Vogelsang, Physical Review D **86**, 094009 (2012).

[44] G. Altarelli, R. Ellis, and G. Martinelli, Nuclear Physics B **143**, 521 (1978).

[45] G. Altarelli, R. Ellis, and G. Martinelli, Nuclear Physics B **157**, 461 (1979).

[46] J. C. Collins and D. E. Soper, Nuclear Physics B **194**, 445 (1982).

[47] A. Accardi and J.-W. Qiu, p. 18 (2008), `0805.1496`.

[48] G. Altarelli and G. Parisi, Nuclear Physics B **126**, 298 (1977).

[49] Y. L. Dokshitzer, Sov.Phys.JETP **46**, 641 (1977).

[50] V. Gribov and L. Lipatov, Sov.J.Nucl.Phys. **15**, 438 (1972).

[51] W. Furmanski and R. Petronzio, Zeitschrift für Physik C Particles and Fields **11**, 293 (1982).

[52] S. Moch, J. Vermaseren, and A. Vogt, Nuclear Physics B **688**, 101 (2004).

[53] A. Vogt, S. Moch, and J. Vermaseren, Nuclear Physics B **691**, 129 (2004).

[54] S. Moch, J. Vermaseren, and A. Vogt, Nuclear Physics B **889**, 351 (2014).

[55] K. Olive, Chinese Physics C **38**, 090001 (2014).

[56] W. Vogelsang, Physical Review D **54**, 2023 (1996).

[57] A. Vogt, Computer Physics Communications **170**, 65 (2005).

[58] A. Vogt, Physics Letters B **497**, 228 (2001).

[59] E. Gardi and R. Roberts, Nuclear Physics B **653**, 227 (2003).

[60] G. Corcella and L. Magnea, Phys.Rev. **D72**, 74017 (2005), `hep-ph/0506278`.

[61] G. Grunberg, Physics Letters B **687**, 405 (2010).

[62] S. Schaefer, A. Schäfer, and M. Stratmann, Physics Letters B **514**, 284 (2001).

[63] D. Anderle, F. Ringer, and W. Vogelsang, Physical Review D **87**, 034014 (2013), `1212.2099`.

[64] S. Catani, Nuclear Physics B **478**, 273 (1996).

[65] G. F. Sterman, *An Introduction to quantum field theory* (Cambridge University Press, 1994).

[66] G. F. Sterman, TASI 95 (1995).

[67] T. O. Eynck, Ph.D. thesis (2003).

[68] S. Coleman and R. E. Norton, Il Nuovo Cimento **38**, 438 (1965).

[69] M. E. Peskin and D. V. Schroeder (1995).

[70] J. C. Collins, D. E. Soper, and G. Sterman, Nuclear Physics B **308**, 833 (1988).

[71] D. de Florian, R. Sassot, and M. Stratmann, Phys.Rev. **D75**, 114010 (2007), `hep-ph/0703242`.

[72] D. de Florian, R. Sassot, M. Epele, R. J. Hernandez-Pinto, and M. Stratmann (2014), `hep-ph/1410.6027`.

[73] S. Albino, B. Kniehl, and G. Kramer, Nuclear Physics B **803**, 42 (2008).

[74] M. Epele, R. Llubaroff, R. Sassot, and M. Stratmann, Phys.Rev. **D86**, 74028 (2012), `hep-ph/1209.3240`.

[75] M. Hirai, S. Kumano, T.-H. Nagai, and K. Sudoh, Physical Review D **75**, 094009 (2007).

[76] M. Soleymaninia, A. N. Khorramian, S. M. Moosavi Nejad, and F. Arbabifar, Phys.Rev. **D88**, 54019 (2013), `hep-ph/1306.1612`.

[77] D. de Florian, M. Pfeuffer, A. Schäfer, and W. Vogelsang, Physical Review D **88**, 014024 (2013).

[78] N. Kidonakis and G. Sterman, Nuclear Physics B **505**, 321 (1997).

[79] R. Bonciani, S. Catani, M. L. Mangano, and P. Nason, Physics Letters B **575**, 268 (2003).

[80] N. Kidonakis, G. Oderda, and G. F. Sterman, Nuclear Physics B **525**, 299 (1998).

[81] N. Kidonakis, G. Oderda, and G. Sterman, Nuclear Physics B **531**, 365 (1998).

[82] N. Kidonakis and J. Owens, Physical Review D **63**, 054019 (2001).

[83] L. Almeida, G. Sterman, and W. Vogelsang, Physical Review D **80**, 074016 (2009).

[84] E. Laenen, G. Oderda, and G. Sterman, Physics Letters B **438**, 173 (1998).

[85] H. Contopanagos, E. Laenen, and G. Sterman, Nuclear Physics B **484**, 303 (1997).

[86] J. Botts and G. Sterman, Nuclear Physics B **325**, 62 (1989).

[87] S. Catani, M. Grazzini, and A. Torre, Nuclear Physics B **874**, 720 (2013).

[88] M. Stratmann, talk (2012).

[89] M. Burkardt, C. A. Miller, and W.-D. Nowak, Reports on Progress in Physics **73**, 016201 (2010).

[90] M. Leitgab, pp. 955–958 (2012).

[91] S. Joosten, talk (2011).

[92] N. Makke, CERN-THESIS-2011-279 (2011).

[93] G. F. Sterman and W. Vogelsang, Physical Review D **74**, 114002 (2006).

[94] J. G. M. Gatheral, Phys.Lett. **B133**, 90 (1983).

[95] J. Frenkel and J. Taylor, Nuclear Physics B **246**, 231 (1984).

[96] C. F. Berger, Ph.D. thesis (2003).

[97] E. Laenen, G. Sterman, and W. Vogelsang, Physical Review D **63**, 114018 (2001).

[98] E. Laenen, G. Sterman, and W. Vogelsang, Physical Review Letters **84**, 4296 (2000).

[99] M. Cacciari and S. Catani, Nuclear Physics B **617**, 253 (2001), `0107138`.

[100] J. Blumlein and V. Ravindran, Phys.Lett. **B640**, 40 (2006), `hep-ph/0605011`.

[101] S. Moch and A. Vogt, Physics Letters B **680**, 239 (2009).

[102] M. Procura and W. J. Waalewijn, Physical Review D **85**, 114041 (2012).

[103] G. Bozzi, S. Catani, D. de Florian, and M. Grazzini, Nuclear Physics B **791**, 1 (2008).

[104] W. Vogelsang, in *AIP Conference Proceedings* (AIP, 2005), vol. 747, pp. 9–15.

[105] G. Altarelli, R. Ellis, G. Martinelli, and S.-Y. Pi, Nuclear Physics B **160**, 301 (1979).

[106] P. Nason and B. R. Webber, Nucl.Phys. **B421**, 473 (1994).

[107] D. Graudenz, Nuclear Physics B **432**, 351 (1994).

[108] D. de Florian and W. Vogelsang, Physical Review D **57**, 5811 (1998).

[109] D. de Florian and Y. R. Habarnau, Eur.Phys.J. **C73**, 2356 (2013), `hep-ph/1210.7203`.

[110] M. Stratmann and W. Vogelsang, Physical Review D **64**, 114007 (2001).

[111] G. F. Sterman and W. Vogelsang, JHEP **0102**, 016 (2001).

[112] M. Osipenko, S. Simula, W. Melnitchouk, P. Bosted, V. Burkert, E. Christy, K. Griffioen, C. Keppel, S. Kuhn, and G. Ricco, Physical Review D **71**, 054007 (2005).

[113] T. Becher, M. Neubert, and B. D. Pecjak, Journal of High Energy Physics **2007**, 076 (2007).

[114] S. Kretzer, Physical Review D **62**, 054001 (2000).

[115] A. D. Martin, W. J. Stirling, R. S. Thorne, and G. Watt, The European Physical Journal C **63**, 189 (2009).

[116] D. D'Enterria, private communication (2012).

[117] B. Abelev, A. Abrahantes Quintana, D. Adamová, A. Adare, M. Aggarwal, G. Aglieri Rinella, A. Agocs, A. Agostinelli, S. Aguilar Salazar, Z. Ahammed, et al., Physics Letters B **717**, 162 (2012).

[118] M. Beneke and V. M. Braun, in *Shifman, M. (ed.): At the frontier of particle physics, vol. 3* (2000), pp. 1719–1773, `0010208`.

[119] V. D. Burkert, Conference: C11-06-28.1 p. 29 (2012), `1203.2373`.

[120] L. L. Frankfurt, M. I. Strikman, L. Mankiewicz, A. Schäfer, E. Rondio, A. Sandacz, and V. Papavassiliou, Physics Letters B **230**, 141 (1989).

[121] A. Airapetian, N. Akopov, Z. Akopov, M. Amarian, V. Ammosov, A. Andrus, E. Aschenauer, W. Augustyniak, R. Avakian, A. Avetissian, et al., Physical Review D **71**, 012003 (2005).

[122] M. Alekseev, V. Alexakhin, Y. Alexandrov, G. Alexeev, A. Amoroso, A. Austregesilo, B. Badelek, F. Balestra, J. Barth, G. Baum, et al., Physics Letters B **693**, 227 (2010).

[123] A. Airapetian, N. Akopov, Z. Akopov, A. Andrus, E. Aschenauer, W. Augustyniak, R. Avakian, A. Avetissian, E. Avetissian, S. Belostotski, et al., Physical Review D **75**, 012007 (2007).

[124] M. Alekseev, V. Alexakhin, Y. Alexandrov, G. Alexeev, A. Amoroso, A. Austregesilo, B. Badelek, F. Balestra, J. Ball, J. Barth, et al., Physics Letters B **690**, 466 (2010).

[125] X. Zheng, K. Aniol, D. S. Armstrong, T. D. Averett, W. Bertozzi, S. Binet, E. Burtin, E. Busato, C. Butuceanu, J. Calarco, et al., Physical Review Letters **92**, 012004 (2004).

[126] X. Zheng, K. Aniol, D. S. Armstrong, T. D. Averett, W. Bertozzi, S. Binet, E. Burtin, E. Busato, C. Butuceanu, J. Calarco, et al., Physical Review C **70**, 065207 (2004).

[127] K. Dharmawardane, S. Kuhn, P. Bosted, Y. Prok, G. Adams, P. Ambrozewicz, M. Anghinolfi, G. Asryan, H. Avakian, H. Bagdasaryan, et al., Physics Letters B **641**, 11 (2006).

[128] D. de Florian, R. Sassot, M. Stratmann, and W. Vogelsang, Physical Review Letters **101**, 072001 (2008).

[129] D. de Florian, R. Sassot, M. Stratmann, and W. Vogelsang, Physical Review D **80**, 034030 (2009).

[130] D. de Florian, R. Sassot, M. Stratmann, and W. Vogelsang (2011).

[131] E. Leader, A. V. Sidorov, and D. B. Stamenov, Physical Review D **82**, 114018 (2010).

[132] S. Simula, M. Osipenko, G. Ricco, and M. Taiuti, Physical Review D **65**, 034017 (2002).

[133] M. Glück, E. Reya, M. Stratmann, and W. Vogelsang, Physical Review D **53**, 4775 (1996).

[134] S. Catani, M. L. Mangano, and P. Nason, Journal of High Energy Physics **1998**, 024 (1998).

[135] A. Martin, R. Roberts, W. Stirling, and R. Thorne, The European Physical Journal C - Particles and Fields **28**, 455 (2003).

[136] G. F. Sterman and W. Vogelsang (2000).

[137] E. C. Aschenauer, M. Stratmann, and R. Sassot, Physical Review D **86**, 054020 (2012).

[138] E. Leader, A. Sidorov, and D. Stamenov, Physical Review D **75**, 074027 (2007).

[139] J. Blümlein and H. Böttcher, Nuclear Physics B **841**, 205 (2010).

[140] A. Accardi and W. Melnitchouk, Physics Letters B **670**, 114 (2008).

[141] A. Accardi, T. Hobbs, and W. Melnitchouk, JHEP **0911**, 84 (2009), `hep-ph/0907.2395`.

[142] L. Brady, A. Accardi, T. Hobbs, and W. Melnitchouk, Phys.Rev. **D84**, 074008 (2011).

[143] H. Avakian, S. Brodsky, A. Deur, and F. Yuan, Physical Review Letters **99**, 082001 (2007).

[144] P. Jimenez-Delgado, W. Melnitchouk, and J. F. Owens, J.Phys. **G40**, 93102 (2013), `hep-ph/1306.6515`.

[145] S. Forte and G. Watt, Ann.Rev.Nucl.Part.Sci. **63**, 291 (2013), `hep-ph/1301.6754`.

[146] S. Albino, Rev.Mod.Phys. **82**, 2489 (2010), `hep-ph/0810.4255`.

[147] J. F. Owens, A. Accardi, and W. Melnitchouk, Phys.Rev. **D87**, 94012 (2013), `hep-ph/1212.1702`.

[148] H.-L. Lai, M. Guzzi, J. Huston, Z. Li, P. M. Nadolsky, and Others, Phys.Rev. **D82**, 74024 (2010), `hep-ph/1007.2241`.

[149] R. D. Ball and Others (2014), `hep-ph/1410.8849`.

[150] A. Accardi, Mod.Phys.Lett. **A28**, 1330032 (2013), `hep-ph/1308.2906`.

[151] S. Chatrchyan and Others, Phys.Rev. **D87**, 112002 (2013), `hep-ph/1212.6660`.

[152] G. Aad, B. Abbott, J. Abdallah, A. A. Abdelalim, A. Abdesselam, O. Abdinov, B. Abi, M. Abolins, H. Abramowicz, H. Abreu, et al., Physical Review D **86**, 014022 (2012).

[153] R. J. Holt and C. D. Roberts, Rev.Mod.Phys. **82**, 2991 (2010), `nucl-th/1002.4666`.

[154] A. Courtoy and S. Liuti, Phys.Lett. **B726**, 320 (2013), `hep-ph/1302.4439`.

[155] J. Dudek, R. Ent, R. Essig, K. S. Kumar, C. Meyer, and Others, Eur.Phys.J. **A48**, 187 (2012), `hep-ex/1208.1244`.

[156] S. Alekhin, J. Blumlein, and S. Moch, Phys.Rev. **D86**, 54009 (2012), `hep-ph/1202.2281`.

[157] J. Blumlein, H. Bottcher, and A. Guffanti, Nucl.Phys. **B774**, 182 (2007), `hep-ph/0607200`.

[158] A. D. Martin, R. G. Roberts, W. J. Stirling, and R. S. Thorne, Eur.Phys.J. **C35**, 325 (2004), `hep-ph/0308087`.

[159] N. Sato, Ph.D. thesis, Florida State U. (2014).

[160] A. Fantoni, N. Bianchi, and S. Liuti, Eur.Phys.J. **A24S1**, 35 (2005), `hep-ph/0501126`.

[161] H. Georgi and H. D. Politzer, Phys.Rev. **D14**, 1829 (1976).

[162] I. Schienbein, V. A. Radescu, G. P. Zeller, M. E. Christy, C. E. Keppel, and Others, J.Phys. **G35**, 53101 (2008), `hep-ph/0709.1775`.

[163] D. P. Anderle, F. Ringer, and W. Vogelsang, Phys.Rev. **D87**, 94021 (2013), `hep-ph/1304.1373`.

[164] D. P. Anderle, F. Ringer, and W. Vogelsang (2013).

[165] S. Albino, B. Kniehl, G. Kramer, and W. Ochs, Physical Review D **73**, 054020 (2006).

[166] O. Nachtmann, Nucl.Phys. **B63**, 237 (1973).

[167] J.-W. Qiu, Phys.Rev. **D42**, 30 (1990).

[168] E. L. Berger, ANL-HEP-CP-87-45 (1987).

[169] P. J. Mulders, AIP Conf.Proc. **588**, 75 (2001), `hep-ph/0010199`.

[170] S. Kretzer and M. H. Reno, Phys.Rev. **D69**, 34002 (2004), `hep-ph/0307023`.

[171] M. A. G. Aivazis, F. I. Olness, and W.-K. Tung, Phys.Rev. **D50**, 3085 (1994), `hep-ph/9312318`.

[172] N. Michel and M. V. Stoitsov, Computer Physics Communications **178**, 535 (2008).

[173] Y. Liang and Others (2004), `nucl-ex/0410027`.

[174] S. P. Malace and Others, Phys.Rev. **C80**, 35207 (2009), `nucl-ex/0905.2374`.

[175] F. D. Aaron and Others, JHEP **1001**, 109 (2010), `hep-ex/0911.0884`.

[176] L. W. Whitlow, E. M. Riordan, S. Dasu, S. Rock, and A. Bodek, Phys.Lett. **B282**, 475 (1992).

[177] J. J. Aubert and Others, Nucl.Phys. **B259**, 189 (1985).

[178] A. Accardi, M. E. Christy, C. E. Keppel, P. Monaghan, W. Melnitchouk, and Others, Phys.Rev. **D81**, 34016 (2010), `0911.2254`.

[179] P. Monaghan, A. Accardi, M. E. Christy, C. E. Keppel, W. Melnitchouk, and Others, Phys.Rev.Lett. **110**, 152002 (2013), `1209.4542`.

[180] we thank P. Monaghan for kindly providing us with the bin-centered data points., *No Title*.

[181] W. Melnitchouk, R. Ent, and C. Keppel, Phys.Rept. **406**, 127 (2005), `hep-ph/0501217`.

[182] J. Blumlein and A. Tkabladze, Nucl.Phys. **B553**, 427 (1999), `hep-ph/9812478`.

[183] M. E. Christy, J. Blumlein, and H. Bottcher (2012), `hep-ph/1201.0576`.

[184] A. Accardi, D. P. Anderle, and F. Ringer, *in preparation*.

[185] C. F. Berger and G. Sterman, Journal of High Energy Physics **2003**, 058 (2003).

[186] S. Catani, D. de Florian, M. Grazzini, and P. Nason, Journal of High Energy Physics **2003**, 028 (2003).

[187] V. Ahrens, T. Becher, M. Neubert, and L. L. Yang, The European Physical Journal C **62**, 333 (2009).

[188] M. Bonvini and S. Marzani, Journal of High Energy Physics **2014**, 7 (2014).

[189] S. Catani, L. Cieri, D. de Florian, G. Ferrera, and M. Grazzini, Nuclear Physics B **888**, 75 (2014).

[190] C. Anastasiou, C. Duhr, F. Dulat, E. Furlan, T. Gehrmann, F. Herzog, and B. Mistlberger, Physics Letters B **737**, 325 (2014).

[191] M. Czakon, A. Mitov, and G. Sterman, Physical Review D **80**, 074017 (2009).

[192] L. L. Yang, C. S. Li, J. Gao, and J. Wang (2014).

[193] W. Beenakker, T. Janssen, S. Lepoeter, M. Krämer, A. Kulesza, E. Laenen, I. Niessen, S. Thewes, and T. Van Daal, Journal of High Energy Physics **2013**, 120 (2013).

[194] A. Broggio, A. Ferroglia, B. D. Pecjak, and Z. Zhang (2014).

[195] C. De Marzo, M. De Palma, C. Favuzzi, G. Maggi, E. Nappi, F. Posa, A. Ranieri, G. Selvaggi, P. Spinelli, A. Bamberger, et al., Physical Review D **42**, 748 (1990).

[196] H. B. White, FERMILAB-THESIS (1991).

[197] H. B. White, K. Streets, G. Boca, C. Georgiopoulos, J. H. Goldman, S. Hagopian, V. Hagopian, K. F. Johnson, D. Levinthal, F. Lopez, et al., Physical Review D **48**, 3996 (1993).

[198] M. Begel, FERMILAB-THESIS (1999).

[199] A. Angelis, H.-J. Besch, B. Blumenfeld, L. Camilleri, T. Chapin, R. Cool, C. del Papa, L. Di Lella, Z. Dimčovski, R. Hollebeek, et al., Nuclear Physics B **209**, 284 (1982).

[200] Z. Kunszt, A. Signer, and Z. Trócsányi, Nuclear Physics B **411**, 397 (1994).

[201] Z. Bern and D. Kosower, Physical Review Letters **66**, 1669 (1991).

[202] Z. Bern and D. A. Kosower, Nuclear Physics B **379**, 451 (1992).

[203] R. Kelley and M. D. Schwartz, Physical Review D **83**, 045022 (2011).

[204] J. Kodaira and L. Trentadue, Physics Letters B **112**, 66 (1982).

[205] S. Catani, E. D'Emilio, and L. Trentadue, Physics Letters B **211**, 335 (1988).

[206] S. Catani, D. de Florian, and M. Grazzini, Journal of High Energy Physics **2001**, 025 (2001).

[207] R. Harlander and W. Kilgore, Physical Review D **64**, 013015 (2001).

[208] T. O. Eynck, E. Laenen, and L. Magnea, Journal of High Energy Physics **2003**, 057 (2003).

[209] E. Laenen and L. Magnea, Physics Letters B **632**, 270 (2006).

[210] M. Sjödahl, Journal of High Energy Physics **2009**, 087 (2009).

[211] S. M. Aybat, L. J. Dixon, and G. Sterman, Physical Review Letters **97**, 072001 (2006).

[212] S. Aybat, L. Dixon, and G. Sterman, Physical Review D **74**, 074004 (2006).

[213] E. Gardi and L. Magnea, Journal of High Energy Physics **2009**, 079 (2009).

[214] T. Becher and M. Neubert, JHEP **0906**, 081 (2009).

[215] D. de Florian and W. Vogelsang, Physical Review D **71**, 114004 (2005).

[216] D. de Florian and W. Vogelsang, Physical Review D **76**, 074031 (2007).

[217] A. Kulesza, G. F. Sterman, and W. Vogelsang, Physical Review D **66**, 014011 (2002).

[218] E. Glover, Nuclear Physics B - Proceedings Supplements **116**, 3 (2003).

[219] G. Sterman and M. E. Tejeda-Yeomans, Physics Letters B **552**, 48 (2003).

[220] S. Catani, Physics Letters B **427**, 161 (1998).

[221] W. Van Neerven, Nuclear Physics B **268**, 453 (1986).

[222] J. Owens, Physical Review D **65**, 034011 (2002).

[223] W. Tung, H. Lai, A. Belyaev, J. Pumplin, D. Stump, and C.-P. Yuan, Journal of High Energy Physics **2007**, 053 (2007).

[224] P. Aurenche, M. Fontannaz, J.-P. Guillet, B. Kniehl, and M. Werlen, The European Physical Journal C **13**, 347 (2000).

[225] B. Kniehl, G. Kramer, and B. Pötter, Nuclear Physics B **597**, 337 (2001).

[226] D. de Florian, W. Vogelsang, and F. Wagner, Physical Review D **78**, 074025 (2008).

[227] P. Hinderer, F. Ringer, G. F. Sterman, and W. Vogelsang (2014).

[228] S. Moch, J. Vermaseren, and A. Vogt, Nuclear Physics B **726**, 317 (2005).

[229] G. Curci, W. Furmanski, and R. Petronzio, Nuclear Physics B **175**, 27 (1980).

[230] G. 't Hooft and M. Veltman, Nuclear Physics B **153**, 365 (1979).

[231] D. Duke and J. Owens, Physical Review D **26**, 1600 (1982).

[232] L. E. Gordon and W. Vogelsang, Physical Review D **48**, 3136 (1993).

[233] B. Jäger, A. Schäfer, M. Stratmann, and W. Vogelsang, Physical Review D **67**, 054005 (2003).

[234] C. Meyer, Conference: C12-05-27.1 p. 4 (2013), `1310.2946`.

[235] C. Mesropian, Conference: C11-03-20 p. 4 (2011), `1106.3119`.

[236] A. Gehrmann-De Ridder, T. Gehrmann, E. Glover, and J. Pires, Physical Review Letters **110**, 162003 (2013).

[237] J. Currie, A. G.-D. Ridder, E. W. N. Glover, and J. a. Pires, Journal of High Energy Physics **2014**, 110 (2014).

[238] M. Kumar and S. Moch, Physics Letters B **730**, 122 (2014).

[239] M. Klasen, G. Kramer, and M. Michael, Physical Review D **89**, 074032 (2014).

[240] M. Cacciari, G. P. Salam, and G. Soyez, The European Physical Journal C **72**, 1896 (2012).

[241] M. Dasgupta and G. Salam, Physics Letters B **512**, 323 (2001).

[242] A. Banfi and M. Dasgupta, Journal of High Energy Physics **2004**, 027 (2004).

[243] A. Banfi, M. Dasgupta, K. Khelifa-Kerfa, and S. Marzani, Journal of High Energy Physics **2010**, 64 (2010).

[244] N. Kidonakis, E. Laenen, S. Moch, and R. Vogt, Physical Review D **64**, 114001 (2001).

[245] P. Nadolsky, H.-L. Lai, Q.-H. Cao, J. Huston, J. Pumplin, D. Stump, W.-K. Tung, and C.-P. Yuan, Physical Review D **78**, 013004 (2008).

[246] F. Ringer, talk given at the PSR workshop, Münster p. 16 (2014).

[247] S. Carrazza and J. a. Pires, Journal of High Energy Physics **2014**, 145 (2014).

[248] J. Blümlein and S. Kurth, Physical Review D **60**, 014018 (1999).

[249] R. D. Ball, V. Bertone, S. Carrazza, C. S. Deans, L. Del Debbio, and Others, Nucl.Phys. **B867**, 244 (2013), `hep-ph/1207.1303`.

[250] G. Aad, B. Abbott, J. Abdallah, A. A. Abdelalim, A. Abdesselam, O. Abdinov, B. Abi, M. Abolins, H. Abramowicz, H. Abreu, et al., The European Physical Journal C **71**, 1512 (2011).

[251] A. Abulencia and Others, Phys.Rev. **D75**, 092006 (2007).

[252] G. Jones, talk given at Rencontres de Moriond (2012).

[253] S. Moch and A. Vogt, Journal of High Energy Physics **2009**, 081 (2009).

[254] V. Del Duca, G. Falcioni, L. Magnea, and L. Vernazza, Journal of High Energy Physics **2015**, 29 (2015).

[255] CMS Collaboration, CMS-PAS-SMP-12-012 (2013).

[256] E.-C. Aschenauer, A. Bazilevsky, M. Diehl, J. Drachenberg, K. O. Eyser, and Others (2015).

[257] L. Adamczyk, J. K. Adkins, G. Agakishiev, M. M. Aggarwal, Z. Ahammed, I. Alekseev, J. Alford, C. D. Anson, A. Aparin, D. Arkhipkin, et al., Physical Review Letters **113**, 072301 (2014).

[258] PHENIX Collaboration, to be published. (2015).

[259] A. Adare, S. Afanasiev, C. Aidala, N. N. Ajitanand, Y. Akiba, R. Akimoto, J. Alexander, H. Al-Ta,Äôani, K. R. Andrews, A. Angerami, et al., Physical Review Letters **106**, 062001 (2011).

[260] M. M. Aggarwal, Z. Ahammed, A. V. Alakhverdyants, I. Alekseev, J. Alford, B. D. Anderson, C. D. Anson, D. Arkhipkin, G. S. Averichev, J. Balewski, et al., Physical Review Letters **106**, 062002 (2011).

[261] C. Bourrely and J. Soffer, Physics Letters B **314**, 132 (1993).

[262] G. Bunce, N. Saito, J. Soffer, and W. Vogelsang, Annual Review of Nuclear and Particle Science **50**, 525 (2000).

[263] D. de Florian, R. Sassot, M. Stratmann, and W. Vogelsang, Physical Review Letters **113**, 012001 (2014).

[264] B. Kamal, Physical Review D **57**, 6663 (1998).

[265] T. Gehrmann, Nuclear Physics B **534**, 21 (1998).

[266] A. Weber, Nuclear Physics B **403**, 545 (1993).

[267] A. Mukherjee and W. Vogelsang, Physical Review D **73**, 074005 (2006).

[268] P. Nadolsky and C.-P. Yuan, Nuclear Physics B **666**, 31 (2003).

[269] D. de Florian and W. Vogelsang, Physical Review D **81**, 094020 (2010).

[270] C. von Arx and T. Gehrmann, Physics Letters B **700**, 49 (2011).

[271] E. R. Nocera, R. D. Ball, S. Forte, G. Ridolfi, and J. Rojo, Nuclear Physics B **887**, 276 (2014).

[272] P. Aurenche and J. Lindfors, Nuclear Physics B **185**, 274 (1981).

[273] G. 't Hooft and M. Veltman, Nuclear Physics B **44**, 189 (1972).

[274] P. Breitenlohner and D. Maison, Communications in Mathematical Physics **52**, 11 (1977).

[275] M. Jamin and M. E. Lautenbacher, Computer Physics Communications **74**, 265 (1993).

[276] A. J. Buras and P. H. Weisz, Nuclear Physics B **333**, 66 (1990).

[277] M. Ciuchini, E. Franco, L. Reina, and L. Silvestrini, Nuclear Physics B **421**, 41 (1994).

[278] W. Vogelsang, Nuclear Physics B **475**, 47 (1996).

[279] S. Goria, G. Passarino, and D. Rosco, Nuclear Physics B **864**, 530 (2012).

[280] W. Beenakker, H. Kuijf, W. van Neerven, and J. Smith, Physical Review D **40**, 54 (1989).

[281] Z.-B. Kang, J.-W. Qiu, and W. Vogelsang, Physical Review D **79**, 054007 (2009).

[282] S. Dittmaier, A. Huss, and C. Schwinn, Nuclear Physics B **885**, 318 (2014).

[283] J. Smith, W. van Neerven, and J. Vermaseren, Physical Review Letters **50**, 1738 (1983).

[284] C. Balázs, J. Qiu, and C.-P. Yuan, Physics Letters B **355**, 548 (1995).

[285] V. Abazov, B. Abbott, B. Acharya, M. Adams, T. Adams, J. Agnew, G. Alexeev, G. Alkhazov, A. Alton, T. Andeen, et al., Physical Review D **89**, 012005 (2014).

[286] C. Bourrely, J. Soffer, and F. Buccella, The European Physical Journal C - Particles and Fields **23**, 487 (2002).

[287] C. Bourrely, F. Buccella, and J. Soffer, Physics Letters B **726**, 296 (2013).

[288] M. Glück, E. Reya, M. Stratmann, and W. Vogelsang, Physical Review D **63**, 094005 (2001).

[289] M. Gluck and E. Reya, Mod.Phys.Lett. **A15**, 883 (2000).

[290] D. de Florian, G. Navarro, and R. Sassot, Physical Review D **71**, 094018 (2005).

[291] T. Aaltonen, B. Álvarez González, S. Amerio, D. Amidei, A. Anastassov, A. Annovi, J. Antos, G. Apollinari, J. A. Appel, T. Arisawa, et al., Physical Review Letters **108**, 151803 (2012).

[292] V. M. Abazov, B. Abbott, B. S. Acharya, M. Adams, T. Adams, G. D. Alexeev, G. Alkhazov, A. Alton, G. Alverson, M. Aoki, et al., Physical Review Letters **108**, 151804 (2012).

[293] P. Nadolsky and C.-P. Yuan, Nuclear Physics B **666**, 3 (2003).

[294] J. Collins, D. E. Soper, and G. Sterman, Nuclear Physics B **250**, 199 (1985).

[295] S. Catani and M. Grazzini, Physical Review Letters **98**, 222002 (2007).

[296] S. Catani, L. Cieri, G. Ferrera, D. de Florian, and M. Grazzini, Physical Review Letters **103**, 082001 (2009).

[297] R. Gavin, Y. Li, F. Petriello, and S. Quackenbush, Computer Physics Communications **182**, 2388 (2011).

[298] Y. Li and F. Petriello, Physical Review D **86**, 094034 (2012).

[299] G. Bozzi, L. Citelli, and A. Vicini (2015).

[300] R. K. Ellis, W. J. Stirling, and B. Webber, Camb.Monogr.Part.Phys.Nucl.Phys.Cosmol. **8**, 1 (1996).

[301] S. Kretzer, Physical Review D **62**, 054001 (2000), `0003177`.

[302] D. de Florian and W. Vogelsang, Physical Review D **57**, 5811 (1998), `9711387`.

[303] A. Belitsky, Physics Letters B **442**, 307 (1998).

[304] G. Sterman and M. Zeng, Journal of High Energy Physics **2014**, 132 (2014).